Fabrication et caractérisations électriques et mécaniques d'un composite cuivre - carbone à architecture 3D

Oussama Keddache

université PARIS-SACLAY

Fabrication et caractérisations électriques et mécaniques d'un composite cuivre - carbone à architecture 3D

Fabrication of a 3D architecture carbon – copper composite and its electrical and mechanical characterizations

Thèse de doctorat de l'université Paris-Saclay

École doctorale n°579 : Sciences mécaniques et énergétiques, matériaux et géosciences (SMEMaG)
Spécialité de doctorat : Matériaux
Graduate School : Sciences de l'ingénierie et des systèmes
Référent : CentraleSupélec

Thèse préparée dans l'unité de recherche **Laboratoire de Mécanique de Paris-Sacaly** (CentraleSupélec), sous la direction de **Jinbo BAI**, Directeur de Recherche CNRS, la co-direction de **Delong HE**, HDR.

Thèse soutenue à Paris-Saclay, le 31 MAI 2024, par

Oussama KEDDACHE

Composition du Jury

Membres du jury avec voix délibérative

Marie-Christine RECORD Professeure, IM2NP, Univ. Aix-Marseille	Présidente & Examinatrice
Sébastien FONTANA HDR, Institut Jean Lamour, Université de Lorraine	Rapporteur & Examinateur
Christophe LAURENT Professeur, CIRIMAT, Université Toulouse III – Paul Sabatier	Rapporteur & Examinateur
Vincent JI Professeur, ICCMO, Univ. Paris-Saclay	Examinateur
Mingyu ZHOU Chef Ingénieur, GEIRI	Examinateur

THESE DE DOCTORAT

NNT : 2024UPAST066

université PARIS-SACLAY

ÉCOLE DOCTORALE
Sciences mécaniques et énergétiques, matériaux et géosciences (SMEMAG)

Titre : Fabrication et caractérisations électriques et mécaniques d'un composite cuivre - carbone à architecture 3D

Mots clés : Graphène, cuivre, composite cuivre graphène, métallurgie des poudres, propriétés électriques, propriétés mécaniques

Résumé : Cette thèse vise à l'étude des propriétés éléctriques et mécaniques des composites cuivre – graphène. La littérature scientifique a montré, expérimentalement et numériquement, que le dopage des propriétés électriques par le graphène, à condition d'avoir une monocouche voire une bicouche de graphène à l'interface avec le cuivre, était possible. Or cela n'a été fait qu'en utilisant un procédé donnant un matériau anisotrope. Ce procédé consistait à déposer du graphène sur des feuillets de cuivre d'épaisseur micrométrique, de les empiler puis de les presser à chaud. D'autres procédés ont été développés afin d'obtenir du graphène aux joints de grains en frittant des poudres préalablement recouvertes de graphène. De la même manière, les propriétés mécaniques d'un composite cuivre/graphène sont améliorées par blocage des dislocations par le carbone aux joints de grains. Allier cuivre et carbone dans le but de fabriquer un matériau qui améliore les propriétés mécaniques et électriques du cuivre est chose complexe. En effet, le carbone est pratiquement insoluble dans le cuivre. Il faut donc pouvoir maitriser un procédé qui puisse donner un matériau dense et isotrope qui améliore à la fois les propriétés électriques et mécaniques.

Il existe une foison de procédés de fabrication dans la littérature scientifique. Celle retenue pour ce projet a été la fabrication via la métallurgie des poudres. Pour cela, une poudre micrométrique de cuivre est enrobée d'un précurseur contenant du carbone, ici du saccharose. Deux approches ont été abordées, la première en enrobant les particules brutes qui possèdent une couche d'oxide et une seconde en enrobant les particules après avoir préalablement réduit l'oxide. Cette poudre enrobée est ensuite brûlée sous atmosphère optimisée faite d'argon et d'hydrogène. La poudre obtenue est finalement frittée afin d'obtenir le composite. Le composite ainsi obtenu est ensuite étudié en utilisant les techniques usuelles en métallurgie telles que la microscopie électronique à balayage (MEB), la microscopie électronique en transmission (MET), Spectroscopie de perte d'énergie des électrons (EELS), la diffraction des rayons X (DRX), la spectroscopie Raman pour la caractérisation du carbone. Toutes ces techniques visent à la compréhension de l'interaction entre le cuivre son renfort carboné.

Title : Fabrication of a 3D architecture carbon – copper composite and its electrical and mechanical characterizations

Keywords : Graphene, copper, copper graphene composite, powder metallurgy, electrical properties, mechanical properties

The aim of this thesis is to study the electrical and mechanical properties of copper-graphene composites. The scientific literature has shown, both experimentally and numerically, that it is possible to dope electrical properties with graphene, provided that a monolayer or even a bilayer of graphene is present at the interface with the copper. However, this was only achieved using a process that produced an anisotropic material. This process involved depositing graphene on micrometre-thick sheets of copper, stacking them and then hot-pressing them. Other processes have been developed to obtain graphene at grain boundaries by sintering powders previously coated with graphene. Similarly, the mechanical properties of a copper/graphene composite are improved by the carbon blocking dislocations at the grain boundaries. Combining copper and carbon to produce a material that improves the mechanical and electrical properties of copper is a complex task. Carbon is virtually insoluble in copper. So we need to be able to master a process that can produce a dense, isotropic material that improves both electrical and mechanical properties.

There is a wealth of manufacturing processes in the scientific literature. The one chosen for this project was powder metallurgy. A micrometric copper powder is coated with a precursor containing carbon, in this case sucrose. Two approaches have been used, the first involving coating raw particles with an oxide layer and the second involving coating particles after first reducing the oxide. This coated powder is then burnt in an optimised atmosphere of argon and hydrogen. The powder obtained is finally sintered to produce the composite. The resulting composite is then studied using standard metallurgical techniques such as scanning electron microscopy (SEM), transmission electron microscopy (TEM), electron energy loss spectroscopy (EELS), X-ray diffraction (XRD) and Raman spectroscopy to characterise the carbon. All these techniques are aimed at understanding the interaction between copper and its carbon reinforcement.

RESUME EN FRANÇAIS

CHAPITRE 1 – INTRODUCTION ET BIBLIOGRAPHIE

Le chapitre 1 présente une revue de la littérature sur les composites cuivre-graphène. Il commence par souligner l'importance du cuivre dans diverses industries et la demande croissante de matériaux à base de cuivre présentant des propriétés électriques et mécaniques supérieures. Le graphène, avec ses propriétés exceptionnelles, est présenté comme un matériau de renforcement prometteur pour le cuivre. Cependant, la synthèse et l'intégration du graphène dans une matrice de cuivre posent des défis en raison de l'insolubilité du carbone dans le cuivre et de la nécessité d'une dispersion homogène du graphène pour des performances optimales du composite.

Le cuivre est un métal largement utilisé dans l'industrie en raison de ses propriétés remarquables, notamment une conductivité électrique et thermique élevée, une ductilité et une malléabilité importantes. Il joue un rôle essentiel dans de nombreux secteurs, tels que l'électricité, la construction, les transports et l'électronique. La demande mondiale de cuivre est en constante augmentation, stimulée par les progrès technologiques et l'expansion des réseaux électriques à l'échelle mondiale.

L'extraction et le traitement du cuivre s'effectuent principalement par deux procédés métallurgiques : la pyrométallurgie et l'hydrométallurgie. La pyrométallurgie, qui représente environ 80 % de la production mondiale de cuivre, implique la fusion à haute température de minerais sulfurés de cuivre. Ce procédé comprend plusieurs étapes clés, notamment la concentration du minerai par flottation, la fusion dans un four à haute température pour produire un *matte* de cuivre, la conversion du *matte* en un *blister*, le raffinage au feu pour éliminer les impuretés restantes et l'électroaffinage pour obtenir du cuivre de haute pureté (99,99 %).

L'hydrométallurgie, quant à elle, est utilisée pour traiter les minerais oxydés de cuivre et les minéraux sulfurés secondaires. Ce procédé comprend la lixiviation du minerai avec de l'acide sulfurique dilué pour dissoudre le cuivre, l'extraction par solvant pour séparer sélectivement le cuivre de la solution de lixiviation et l'électrolyse pour déposer le cuivre pur sur des cathodes.

Le cuivre se présente sous différentes nuances, chacune ayant des propriétés et des applications distinctes. Le cuivre électrolytique (ETP) est largement utilisédans l'industrie. Le cuivre désoxydé au phosphore (DHP et DLP) et le cuivre sans oxygène (OF et OFC) sont d'autres nuances importantes. La pureté du cuivre est cruciale pour ses applications électriques, car même de petites quantités d'impuretés peuvent réduire considérablement sa conductivité. l'International Annealed Copper Standard (IACS) définit la conductivité d'un fil de cuivre ETP recuit comme référence pour les mesures de conductivité électrique.

La structure électronique du cuivre, caractérisée par sa configuration

électronique, est responsable de sa conductivité électrique élevée. La configuration électronique du cuivre, avec un seul électron dans la couche 4s, permet un flux d'électrons sans entrave lorsqu'un champ électrique est appliqué.

Le cuivre est un très bon conducteur électrique mais il est structurellement faible. Le renforcement du cuivre peut être obtenu par diverses méthodes, notamment le renforcement par écrouissage, le renforcement par affinement des grains, le maclage, la déformation plastique sévère (SPD) et l'alliage. Chacune de ces méthodes présente des avantages et des inconvénients en termes de résistance mécanique et de conductivité électrique. Le renforcement par déformation et par affinage de la taille des grains améliore la résistance mécanique, mais peut réduire la conductivité en raison de la diffusion accrue des électrons. Le renforcement par maclage offre un équilibre entre résistance et conductivité, tandis que le SPD et l'alliage permettent d'obtenir une résistance et une conductivité élevées, mais peuvent nécessiter des processus de fabrication complexes.

Le graphène est un matériau bidimensionnel composé d'une seule couche d'atomes de carbone disposés en réseau hexagonal. Il possède des propriétés remarquables, notamment une résistance mécanique, une conductivité électrique et une conductivité thermique exceptionnelles. Le graphène peut être synthétisé par différentes méthodes, telles que l'exfoliation mécanique, l'exfoliation liquide, le dépôt chimique en phase vapeur (CVD) et la réduction chimique de l'oxyde de graphène.

Les composites cuivre-graphène visent à combiner la conductivité électrique et thermique élevée du cuivre avec la résistance mécanique et les propriétés électriques exceptionnelles du graphène. Cependant, la fabrication de ces composites présente des défis en raison de l'insolubilité du carbone dans le cuivre, ce qui peut entraîner l'agglomération du carbone et compromettre les propriétés souhaitées du composite.

Les premières recherches sur les composites à matrice de cuivre renforcés par du carbone ont porté sur les composites cuivre-nanotubes de carbone (CNT). Les méthodes de traitement des poudres, telles que le broyage à billes, le dépôt chimique, le mélange à l'échelle moléculaire et le frittage, ainsi que la technique d'électrodéposition, ont été utilisées pour fabriquer ces composites. L'électrodéposition a donné de meilleurs résultats en termes de dispersion des CNT, de résistance mécanique et de conductivité électrique.

Les recherches se sont ensuite étendues aux composites cuivre-nanoplaquettes de graphite (GNP), en utilisant des techniques similaires à celles employées pour les composites cuivre-CNT. Ces composites présentaient de meilleures propriétés mécaniques, mais une diminution des propriétés électriques due à l'agglomération des GNP et à l'introduction de défauts. Diverses techniques, telles que le broyage à billes, le dépôt chimique, le mélange à l'échelle moléculaire et le dépôt électrochimique, ont été explorées pour la fabrication de composites cuivre-GNP.

Des progrès ont été réalisés dans le développement d'architectures bidimensionnelles (2D) et tridimensionnelles (3D) pour améliorer les composites

cuivre-graphène. L'architecture 2D, consistant à empiler des couches de graphène et de cuivre, a montré un potentiel d'amélioration de la conductivité électrique, certains composites atteignant une conductivité de 117 % IACS. Cela a été attribué à l'effet de dopage du graphène et à l'amélioration de la correspondance du réseau entre le graphène et la matrice de cuivre.

Les études sur l'architecture 3D ont démontré la possibilité d'une croissance in situ de graphène sur des particules de cuivre avant le frittage, ce qui améliore la dispersion du graphène et les propriétés mécaniques. Toutefois, la plupart des publications font état de la présence de carbone amorphe plutôt que de graphène cristallin dans ces structures, ce qui peut limiter les améliorations de conductivité.

En conclusion, le chapitre 1 met en évidence les défis et les progrès réalisés dans la synthèse et la caractérisation des composites cuivre-graphène. Il souligne la nécessité de poursuivre les recherches pour combiner les avantages des architectures 2D et 3D, en mettant l'accent sur la croissance de graphène monocouche de haute qualité directement sur les particules de cuivre. Une meilleure compréhension de l'interaction entre le graphène et le cuivre au niveau moléculaire est essentielle pour optimiser les performances électriques et mécaniques de ces composites et surmonter les défis actuels liés à la qualité du carbone et à la dispersion dans la matrice de cuivre.

CHAPITRE 2 – ELABORATION DE LA POUDRE CUIVRE - CARBONE

Le chapitre 2 de cette thèse porte sur la fabrication de particules de cuivre enrobées de carbone, une étape cruciale dans la production de composites cuivre-graphène. L'objectif principal est de créer des particules de cuivre enrobées de graphène en utilisant du saccharose comme source solide de carbone, qui seront ensuite densifiées par Spark Plasma Sintering (SPS). Deux approches principales ont été explorées :

- Enrobage direct de la poudre de cuivre brute et carbonisation : Cette méthode consiste à enrober directement la poudre de cuivre, qui présente naturellement une couche d'oxyde de cuivre, avec une solution de saccharose. Après séchage à 80 °C à l'air, la poudre est broyée pour assurer l'homogénéité et augmenter la surface disponible pour les réactions ultérieures. La poudre enrobée de saccharose est ensuite carbonisée à 1000 °C sous atmosphère contrôlée d'argon et d'hydrogène pour transformer le saccharose en carbone.
- Réduction de l'oxyde de cuivre, enrobage et carbonisation: Dans cette approche, la poudre de cuivre brute est d'abord traitée thermiquement à 200 °C sous une atmosphère d'argon et d'hydrogène pour réduire la couche d'oxyde de cuivre. La poudre de cuivre réduite est ensuite enrobée de saccharose, séchée à 100 °C sous argon pour éviter l'oxydation, broyée, puis carbonisée à 1000 °C.

Les particules de cuivre enrobées de carbone ont été caractérisées par plusieurs techniques : microscopie électronique à balayage (MEB), microscopie électronique à transmission (MET), spectroscopie Raman, analyse thermogravimétrique (ATG) et diffraction des rayons X (DRX).

L'analyse de la poudre de cuivre a révélé la présence d'oxydes de cuivre (I) et (II), confirmant la nécessité de l'étape de réduction. Cependant, la réduction complète des oxydes s'est avérée difficile, même aux températures de réduction et dans une atmosphère réductrice. La présence de saccharose semble entraver la réduction, probablement en raison de la réaction compétitive de l'hydrogène avec le saccharose plutôt qu'avec les oxydes de cuivre.

L'ATG a montré que le saccharose commence à se décomposer à 200 °C et se transforme complètement en carbone à 600 °C. Cependant, l'analyse Raman des particules de cuivre enrobées de carbone a révélé que le carbone formé était principalement amorphe, avec un faible degré de graphitisation. Cela suggère que la couche d'oxyde initiale et les conditions de graphitisation ont empêché la formation de graphène.

La MET et l'analyse EELS ont confirmé la présence d'oxyde de cuivre résiduel et de carbone amorphe, même après un traitement à 1000 °C sous atmosphère réductrice. L'oxyde de cuivre semble persister en raison de la couche protectrice initiale sur les poudres de cuivre et de la présence de traces d'oxygène dans les gaz utilisés.

Pour améliorer la qualité du carbone, la poudre de cuivre a été réduite avant l'enrobage de saccharose. Cette approche a donné lieu à un enrobage de carbone plus structuré, avec des rides visibles sur les particules de cuivre enrobées de carbone, caractéristiques du graphène. L'analyse Raman a également indiqué une meilleure organisation structurelle du carbone.

L'influence de la concentration initiale en saccharose a également été étudiée. Une concentration de 0,65 % en poids de saccharose a été jugée optimale pour éviter le frittage prématuré des particules de cuivre. Cependant, des temps d'exposition plus longs à haute température ont entraîné un frittage important, en particulier avec de faibles concentrations de saccharose. L'augmentation de la proportion d'hydrogène dans l'atmosphère de graphitisation a également favorisé le frittage.

Différentes concentrations d'hydrogène (0,5%, 5%, 10% et 30%) ont été testées lors de la graphitisation. Les résultats ont montré que des concentrations plus élevées d'hydrogène entraînaient un rétrécissement et un frittage accrus des particules de cuivre, ce qui est indésirable. L'analyse Raman a révélé que l'augmentation de la proportion d'hydrogène diminuait le rapport I(D)/I(G), suggérant une interaction entre l'hydrogène et les couches de carbone qui pourrait influencer le degré de désordre et le processus de graphitisation.

L'augmentation du temps de graphitisation à 60 minutes a entraîné un frittage important des particules de cuivre, en particulier avec une faible concentration de saccharose (0,65 % en poids). En revanche, avec une concentration en saccharose de 2,00 % en poids, le revêtement de carbone était intact.

En conclusion, le chapitre 2 met en évidence les défis liés à la production de particules de cuivre enrobées de graphène de haute qualité. Les résultats montrent que les conditions de traitement, la concentration en saccharose, la réduction de l'oxyde de cuivre, la proportion d'hydrogène et le temps d'exposition sont des facteurs cruciaux pour obtenir un enrobage de graphène. Les recherches futures devront se concentrer sur l'optimisation de ces paramètres afin de favoriser la formation de graphène sur les particules de cuivre. Des pistes d'amélioration comprennent l'utilisation de techniques de réduction de l'oxyde de cuivre à basse température, un contrôle précis de l'apport de carbone, des conditions de graphitisation sous pression réduite, l'utilisation de poudres de cuivre avec différentes morphologies et tailles de particules, et l'exploration d'autres sources de carbone ou de précurseurs de graphène.

CHAPITRE 3 – DENSIFICATION DE LA POUDRE POUDRE CUVIRE – CARBONE

Le chapitre 3 de cette thèse examine la densification de poudres de cuivre pur et de poudres de cuivre enrobées de carbone à l'aide du SPS. L'objectif principal est d'évaluer le comportement de frittage de ces poudres sous différentes conditions et d'analyser l'impact du carbone sur les propriétés du composite résultant.

Deux ensembles de paramètres de frittage ont été utilisées : 800°C et 50 MPa, et 900°C et 100 MPa. Les poudres de cuivre pur réduites à 200°C et 300°C (rCu200C et rCu300C), les poudres de cuivre enrobées de carbone (rCu200C@0.65% et rCu200C@2.00%) et des mélanges de poudre de cuivre pur et de poudre enrobée de carbone (Cu-CuC@0.50%, Cu-CuC@1.00%, Cu-CuC@5.00% et Cu-CuC@25.0%) ont été densifiés.

L'analyse des courbes SPS a révélé une densification sans accroc pour tous les échantillons. Un dégagement gazeux, probablement de l'hydrogène, a été observé lors du frittage des échantillons de cuivre pur. Les échantillons de cuivre pur et le composite rCu200C@0.65% ont atteint des densités élevées (8,79 g/cm³ à 8,86 g/cm³ pour le cuivre pur et 8,85 g/cm³ à 8,86 g/cm³ pour le composite), tandis que le composite rCu200C@2.00% a montré des densités plus faibles (8,75 g/cm³ et 8,74 g/cm³). Cela met en évidence l'impact de la teneur en carbone sur la densité.

L'augmentation des paramètres de frittage a amélioré la densité du cuivre pur, mais a eu un effet négligeable sur les composites en raison de la présence de carbone aux joints de grains, qui limite la croissance des grains. La dissolution de la matrice de cuivre dans les composites a révélé des défauts dans le squelette de carbone, indiquant des problèmes structurelles.

L'analyse nanostructurale a montré que le frittage pouvait favoriser la cristallisation du carbone aux joints de grains, mais une ségrégation du carbone a également été observée, probablement due aux contraintes de cisaillement interfaciales. Cette ségrégation explique la densité plus faible du composite rCu200C@2.00% par rapport au rCu200C@0.65%.

Les mélanges de cuivre pur et de cuivre enrobé de carbone ont montré des densités variables en fonction de la teneur en carbone. Les mélanges à faible teneur en carbone (Cu-CuC@0.50% et Cu-CuC@1.00%) présentaient des densités plus faibles, tandis que les mélanges à teneur plus élevée (Cu-CuC@5.00% et Cu-CuC@25.0%) présentaient des densités plus élevées, comparables à celles des échantillons rCu200C@2.00%.

Les observations au MEB ont confirmé ces résultats, révélant des grains équiaxes et une absence de porosités visibles dans les composites rCu200C@0.65%. En revanche, les échantillons rCu200C@2.00% présentaient des agrégats de carbone importants aux joints de grains, ce qui explique leur densité plus faible.

En conclusion, le chapitre 3 met en évidence la complexité de la densification des composites cuivre-carbone et l'importance de contrôler la teneur en carbone et les paramètres de frittage pour obtenir les propriétés souhaitées. Les recherches futures devront se concentrer sur l'optimisation de la qualité et de la distribution du carbone

dans la matrice de cuivre, ainsi que sur l'exploration de paramètres de frittage alternatifs pour améliorer les propriétés mécaniques et électriques de ces composites.

CHAPITRE 4 – PROPRIETES PHYSIQUES DU COMPOSITE CUVIRE – CARBONE

Le chapitre 4 de cette thèse examine les propriétés physiques, notamment la conductivité électrique et la dureté, de composites cuivre-carbone obtenus par frittage de poudres de cuivre pur et de poudres de cuivre enrobées de carbone. L'objectif est d'évaluer l'impact de l'incorporation de carbone et des conditions de frittage sur ces propriétés.

Les résultats montrent que les échantillons de cuivre pur (rCu200C et rCu300C) présentent des conductivités électriques supérieures à celles des échantillons composites (rCu200C@0.65% et rCu200C@2.00%), ce qui est attribué à la qualité inférieure du carbone dans les composites. Cependant, l'augmentation de la température et de la pression de frittage améliore la conductivité électrique, tant pour le cuivre pur que pour les composites.

En ce qui concerne la dureté, les échantillons composites présentent des valeurs plus élevées que les échantillons de cuivre pur, ce qui indique un renforcement de la matrice par le carbone. De manière surprenante, les composites frittés à une température et une pression plus faibles (800°C - 50MPa) montrent une dureté supérieure à ceux frittés à 900°C - 100MPa. Cela pourrait être dû à une diminution des contraintes de cisaillement interfaciales à des températures plus basses, préservant ainsi l'intégrité structurelle du carbone aux joints de grains.

L'analyse des indentations de dureté révèle que le carbone absorbe efficacement la déformation, ce qui contribue à la dureté du composite. Les échantillons composites ne présentent pas de caractéristiques de déformation visibles autour des indentations, contrairement au cuivre pur, ce qui suggère que le carbone répartit uniformément la contrainte de déformation.

Les mélanges de cuivre pur et de cuivre enrobé de carbone (Cu-CuC) présentent des conductivités électriques variables en fonction de la teneur en carbone. Le mélange Cu-CuC@5.00% présente la conductivité la plus élevée, tandis que Cu-CuC@0.50% et Cu-CuC@1.00% ont des conductivités plus faibles, probablement en raison d'une densification insuffisante. Cu-CuC@25.0% présente une dureté accrue grâce à sa teneur en carbone, ce qui met en évidence l'équilibre entre conductivité et résistance mécanique dans les compositions mixtes.

L'analyse des facies de rupture des composites révèle une rupture fragile, en particulier le long des joints de grains où le carbone est présent. Cela suggère que bien que le carbone améliore la dureté, il peut compromettre la ductilité du composite.

En conclusion, le chapitre 4 souligne l'impact complexe des paramètres de frittage et de la teneur en carbone sur les propriétés électriques et mécaniques des composites cuivre-carbone. Les résultats mettent en évidence la nécessité d'optimiser l'incorporation du carbone et les conditions de traitement pour développer des composites cuivre-carbone de haute qualité. Les recherches futures devraient se

concentrer sur l'amélioration de la qualité du carbone, l'exploration de techniques de traitement alternatives et l'étude des mécanismes détaillés régissant l'interaction entre le carbone et le cuivre.

CHAPITRE 5 – CONCLUSIONS

Le chapitre 5 conclut la thèse en résumant les principales découvertes et en proposant des perspectives pour de futures recherches.

La thèse a exploré la synthèse, la densification et la caractérisation de composites cuivre-carbone, en se concentrant sur l'influence des conditions de traitement et de l'incorporation de carbone sur les propriétés électriques, mécaniques et microstructurales. Les résultats ont mis en évidence la complexité de la fabrication de particules de cuivre enrobées de graphène de haute qualité et l'importance de contrôler les conditions de traitement, la concentration en saccharose et la réduction de l'oxyde de cuivre pour obtenir un revêtement de carbone structuré.

Le SPS a été utilisé pour densifier les poudres de cuivre pur, les poudres de cuivre enrobées de carbone et leurs mélanges. Les résultats ont montré que la densité et les propriétés microstructurales des composites étaient fortement influencées par la teneur en carbone et les paramètres de frittage. L'augmentation de la température et de la pression de frittage a amélioré la conductivité électrique, mais a eu un effet négligeable sur la densité des composites en raison de la présence de carbone aux joints de grains.

L'analyse des propriétés électriques et mécaniques a révélé un compromis entre la conductivité électrique et la dureté. Les échantillons de cuivre pur présentaient une conductivité électrique supérieure, tandis que les composites présentaient une dureté accrue en raison de la présence de carbone. L'analyse des indentations de dureté a montré que le carbone absorbait efficacement la déformation, contribuant ainsi à la dureté du composite.

Les mélanges de cuivre pur et de cuivre enrobé de carbone ont montré des conductivités électriques variables en fonction de la teneur en carbone, soulignant l'importance d'un équilibre optimal entre la teneur en carbone et la densification pour obtenir des propriétés électriques souhaitables.

L'analyse des facies de rupture a révélé une rupture fragile dans les composites, en particulier le long des joints de grains où le carbone est présent. Cela suggère que bien que le carbone améliore la dureté, il peut compromettre la ductilité du composite.

Les perspectives de recherche future incluent l'optimisation des processus de réduction de l'oxyde de cuivre à basse température, l'amélioration du contrôle de l'apport de carbone pendant la graphitisation, l'utilisation de poudres de cuivre avec différentes morphologies et tailles de particules, et l'étude d'autres sources de carbone ou de précurseurs de graphène. De plus, des études mécanistiques approfondies sur l'interaction entre le cuivre et le carbone, ainsi que des analyses électriques et électroniques détaillées, pourraient fournir des informations précieuses pour la conception et le développement de composites cuivre-graphène de haute

performance.

En somme, cette thèse apporte une contribution significative à la compréhension des composites cuivre-graphène et ouvre la voie à de nouvelles recherches pour améliorer leurs performances et élargir leurs applications potentielles dans divers domaines technologiques et industriels.

CONTENT

CHAPTER 1 – INTRODUCTION AND LITTERATURE REVIEW

1.1 CONTEXT AND MOTIVATION

The field of material science and engineering is perpetually evolving, driven by the ceaseless quest for materials that surpass the current benchmarks of efficiency, durability, and performance. In this context, the exploration of new composites, particularly those combining metals with graphene, represents a frontier of immense scientific interest and technological potential. Copper graphene composites, embodying the union of two vastly researched materials, stand at the forefront of this exploration due to their prospective applications and the unique synergy of their intrinsic properties.

Copper, with its old history and indispensable role in electrical engineering, remains a material of choice for a multitude of applications, primarily due to its high electrical and thermal conductivity. It serves as the backbone of modern electrical infrastructure, from microelectronics to large-scale power transmission systems [1]. The global demand for copper is continuously rising, propelled by advancements in technology and the expansion of electrical networks worldwide[1]. However, despite its widespread use, the performance thresholds of pure copper are being challenged by the increasing demands of modern applications, necessitating the development of new materials that can sustain higher currents, endure more extreme conditions, and exhibit superior mechanical properties.

Enter graphene, a material that has captivated the scientific community since its groundbreaking isolation in 2004 [2]. Characterized by its two-dimensional structure, exceptional mechanical strength, and unprecedented electrical properties, graphene has been heralded as a 'wonder material' [3]. Its potential to revolutionize a myriad of fields, from electronics to energy storage, has sparked an intense research effort to integrate it into practical applications. Yet, graphene's integration into materials such as copper remains a challenging endeavor due to issues like synthesis scalability, material compatibility, and the retention of its properties when mixed with copper.

The fusion of copper and graphene into a composite material is envisaged to synergize their respective strengths: the unparalleled electrical conductivity of copper among non-precious metals [4] combined with the mechanical robustness and electrical properties of graphene [2], [5], [6]. Such composites could not only enhance the performance of existing copper-based materials but also open new avenues for applications in fields as diverse as electronics, thermal management, and structural materials. The promise of copper-graphene composites lies in their potential to transcend the limitations of their constituent materials, offering new solutions to long-standing challenges.

This research aims to delve into the electrical and mechanical study of copper-graphene composites, a venture that is as challenging as it is promising. The scientific community's growing interest in these composites is fueled by their potential to

combine the best of two worlds: the reliability and conductivity of copper with the strength and versatility of graphene. However, the path to realizing this potential is fraught with technical hurdles, from the synthesis of high-quality graphene to its integration with copper without compromising the properties that make each material desirable in the first place.

The motivation behind this PhD thesis is rooted in the aspiration to contribute to the advancement of composite materials, bridging the gap between theoretical potential and practical utility. By investigating the electrical and mechanical properties of copper-graphene composites, this study aims to uncover insights that could lead to the development of materials with unprecedented capabilities, addressing the needs of evolving technologies and paving the way for future innovations.

1.2 OBJECTIVES

The primary objective of this PhD thesis is to investigate the electrical and mechanical properties of copper-graphene composites with an aim to understand and quantify the synergistic effects of combining copper with graphene. The research focuses on elucidating how the integration of graphene influences the overall performance of copper and how these composites can be optimized for various applications. Specifically, the study aims to:

1. Characterize the microstructural features of copper-graphene composites, including grain size, distribution of graphene within the copper matrix, and the interface between copper and graphene.
2. Assess the mechanical properties of the composites, such as hardness, and compare these with those of pure copper and other copper-based composites.
3. Evaluate the electrical properties of the composites, particularly their conductivity in comparison to standard copper used in electrical applications.
4. Explore the effects of various synthesis and processing techniques on the properties of copper-graphene composites to identify optimal manufacturing conditions.

1.3 HYPOTHESIS

The hypotheses guiding this research are based on the premise that the incorporation of graphene into a copper matrix can lead to enhanced electrical and mechanical properties due to the attributes of graphene. It is hypothesized that:

1. The dispersion of graphene within the copper matrix will significantly improve the mechanical strength of the composites due to load transfer mechanisms and the inhibition of grain growth during processing.
2. The electrical conductivity of copper-graphene composites will be superior to that of pure copper due to the high conductivity of graphene and the potential for reduced electron scattering at grain boundaries.
3. The processing and synthesis techniques of the carbon – copper powders, including reduction of copper oxides and graphene formation, will have significant impacts on the composite microstructure, and thus their final properties.

1.4 PLAN OF THE THESIS

This thesis is organized into five main chapters to provide a comprehensive study of copper-graphene composites:

1. Introduction and literature review: this chapter sets the stage by discussing the motivation behind the study, outlining the research objectives and hypotheses, and providing an extensive review of the relevant literature on copper, graphene, and their composites.
2. Preparation of copper/graphene powders: this chapter describes the experimental methods used to synthesize copper-graphene composite powders, including the different approaches and treatments applied.
3. Densification of powders and microstructural analysis: details the process of converting the synthesized powders into solid discs using Spark Plasma Sintering and analyzes the resulting microstructures.
4. Physical properties of the composites: explores the electrical and mechanical properties of the composites in depth, comparing them to those of pure copper and discussing the impact of different variables.
5. Conclusion and future perspectives: summarizes the findings of the research, discusses the implications of these results, and suggests directions for future research.

1.5 LITTERATURE REVIEW

This literature review is structured into three comprehensive sections. The first section provides an in-depth examination of copper, encompassing its extraction and refinement from ores to pure copper, the classification of different copper grades, and the various techniques employed to enhance its mechanical strength. The second section delves into graphene, presenting a detailed description of its properties and the methodologies for its synthesis. The final section is dedicated to copper-graphene composites, outlining the diverse fabrication routes and analyzing the properties and performance characteristics of the resultant composite materials.

1.5.1 Copper

Copper is one of the oldest metals known to humanity, with a history of use dating back over 10,000 years [7]. Its extensive use through history has been primarily due to its natural occurrence in pure form and its array of desirable properties, such as high thermal and electrical conductivity, ductility, and malleability. The extraction and processing of copper have evolved significantly, from early smelting processes to the modern techniques of electrorefining and electrowinning.

The global demand for copper is driven by its critical role in a variety of industries, including electrical, construction, transportation, and electronics [1]. The production of copper involves several key steps, starting from the extraction of copper ores such as chalcopyrite and chalcocite, followed by concentration, smelting, and refining processes to produce pure copper metal [8].

Copper predominantly occurs in the form of sulfide ores, specifically chalcopyrite ($CuFeS_2$) and chalcocite (Cu_2S), which characteristically contain copper in concentrations ranging from approximately 0.3% to 1.7%. In contrast, copper's presence in oxidized mineral forms—such as carbonates, oxides, hydroxysilicates, and sulfates—is comparatively less substantial. The direct extraction of copper via melting is deemed economically impracticable due to the low concentration of copper within these ores [8].

Therefore, to facilitate the extraction of copper from these low-grade ores, two principal metallurgical processes are employed: pyrometallurgy and hydrometallurgy. Pyrometallurgy, which accounts for approximately 80% of the copper produced, primarily involves the smelting of copper sulfide ores at high temperatures, followed by various refining processes to produce pure copper. On the other hand, hydrometallurgy, contributing to around 20% of copper production, encompasses a series of aqueous chemical processes, including leaching, solvent extraction, and electrowinning, to extract and refine copper from its ores [8]. These methodologies mark the adaptability of extraction techniques to the specific chemical and physical nature of copper ores, optimizing yield in the production of this metal.

The subsequent discussion delineates the various processing methodologies deployed to produce copper of the highest purity, alongside a comprehensive examination of the existent grades of this metal. The quality of copper is paramount in

harnessing its superior electrical and thermal properties to their fullest extent.

1.5.1.1 The processing of copper through Pyrometallurgy

The pyrometallurgical process of copper production is an important component of modern copper metallurgy, embodying an series of stages designed to extract, concentrate, and refine copper from its sulfide ores. This process spans from the initial isolation of ore using froth flotation through to the steps of smelting, conversion, fire-refining, and electrorefining, culminating in the production of highly pure copper. Throughout this procedure, various gases play pivotal roles, numerous impurities are systematically targeted and eliminated, and copper concentrations undergo transformations, reflecting the efficiency and complexity of the extraction process [8].

The initiation of copper extraction begins with the isolation of copper-bearing ore through the process of froth flotation. This technique involves the grinding of ore to a fine particulate form, facilitating the liberation of copper minerals from the surrounding gangue. The resultant finely ground ore is then suspended in water, forming a slurry to which specific reagents (usually xanthate but others such as dithiophosphates, mercaptans, and thiocarbamates, are also used), are added, inducing the hydrophobic properties of the copper-bearing minerals. Upon the introduction of air into the slurry, bubbles form, adhering to the hydrophobic particles and elevating them to the surface as froth. This froth, enriched with copper minerals, is skimmed off, resulting in a concentrate that significantly increases the copper content from the initial ore, typically from 0.3%-1.7% to about 20%-30%. The air employed in this stage serves a purpose, facilitating bubble formation and the subsequent attachment of copper particles. The primary impurities, such as silica, alumina, iron, and other sulfide minerals, are left behind in the aqueous solution, separated from the concentrated copper due to their hydrophilic nature [8].

Transitioning from concentration to extraction, the smelting process represents the next stage. In this phase, the concentrate, now a mixture of copper sulfides and other materials, is subjected to high temperatures (1250°C) in a furnace, inducing reactions facilitated by the introduction of oxygen. This oxidative environment plays a vital role in separating the copper from its sulfides, converting iron sulfides into iron oxide which combines with silica to form slag, and sulfur into sulfur dioxide, a gas that is either captured for industrial use or released into the atmosphere under controlled conditions. The smelting process not only isolates copper in the form of molten matte, typically containing 40%-70% copper, but also effectively eliminates significant amounts of iron and sulfur from the concentrate [8].

Following smelting, the conversion or oxidation process further refines the copper matte into blister copper in a Peirce-Smith converter at 1220°C. In this stage, air or pure oxygen is blown into the molten matte within a converter, instigating a series of reactions that oxidize the remaining iron and sulfur. This stage is demanding as it transitions the copper from sulfide forms in the matte to elemental copper in the blister copper, albeit still intermingled with impurities and characterized by its blister-like appearance due to escaping sulfur dioxide gases during solidification. Here, gases

such as oxygen play a dual role: facilitating the oxidation of impurities and propelling the metallurgical reactions towards the formation of blister copper, with typical copper concentrations elevating to approximately 98%-99% [8].

As the process progresses to fire-refining, the impure blister copper undergoes further refinement through heating in an oxidizing atmosphere. The application of air during this stage assists in the oxidation of residual sulfur and the removal of remaining metallic impurities through slagging or volatilization. Controlled oxidation also reduces the oxygen content within the copper, preparing it for the subsequent and final purification step. This fire-refining process elevates copper purity to approximately 99.5%, while selectively targeting the removal of remaining elements such as arsenic, antimony, and lead, which are less noble than copper and hence oxidize and separate more readily [8].

Electrorefining stands as the culmination of the copper purification process. The fire-refined copper is cast into large slabs, known as anodes, and subjected to an electrochemical process where they are dissolved in an electrolytic solution comprising copper sulfate and sulfuric acid. Through the application of an electric current, copper ions migrate from the anodes to cathodes, depositing pure copper at a purity level of 99.99%. Throughout this stage the process removes soluble impurities which remain in the electrolyte, while insoluble impurities, including precious metals, accumulate as anodic slimes, offering additional value through their subsequent recovery [8].

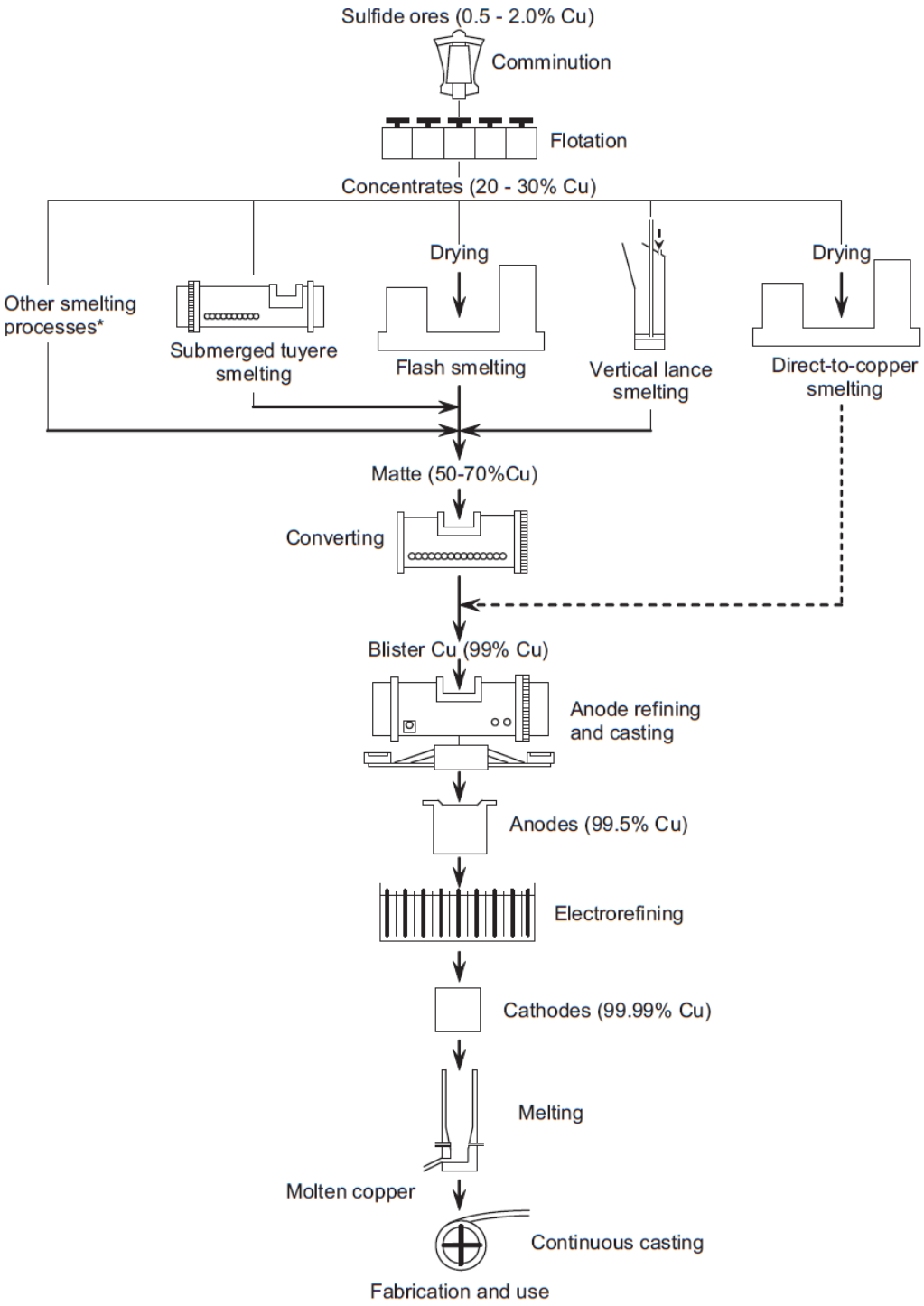

*Figure 1.1 Main processes for extracting copper from sulfide ores. Parallel lines indicate alternative processes. *Principally Mitsubishi and Vanyukov smelting [8].*

1.5.1.2 The processing of copper through Hydrometallurgy

The hydrometallurgical process for copper extraction represents a refined methodology applied predominantly to copper oxide ores, such as carbonates, oxides, hydroxysilicates, and sulfates, as well as secondary sulfide minerals like chalcocite. This process is characterized by three primary stages: leaching, solvent extraction, and electrowinning. Each stage is crucial for the efficient extraction, purification, and concentration of copper, transitioning from raw ore to pure copper sheets [8].

The initial phase of copper extraction involves the leaching of copper from broken or crushed ore using dilute sulfuric acid, resulting in an impure copper-bearing aqueous solution. The choice of sulfuric acid is predicated on its efficacy in dissolving copper oxides and its reactivity with sulfide minerals to produce copper sulfate. The reaction mechanisms are influenced by factors such as acid concentration, temperature, and ore particle size. Optimal leaching occurs when these variables facilitate the complete dissolution of available copper ions into the solution [8].

Copper oxide ores, are just dissolved by the sulfuric acid while for sulfides like chalcocite, the leaching involves a two-step process, initially involving the oxidation of copper sulfides to sulfate, followed by acid dissolution [8].

The leaching time varies depending on the ore type and operational conditions, typically spanning several weeks to months. This extended duration ensures the thorough percolation of acid through the ore heap, facilitating complete copper extraction. The initial copper concentrations in the solution depend on the ore's copper content and the leaching efficiency, typically ranging from 1 to 8 grams per liter [8].

Following leaching, the impure leach solution, termed Pregnant Leach Solution (PLS), undergoes solvent extraction (SX) to transfer copper from the aqueous solution into a copper-specific organic extractant. This stage is pivotal for separating copper from other dissolved metals and impurities. The process hinges on the selective affinity of the organic extractant for copper ions over other impurities such as iron, manganese, and zinc [8].

The separation process in SX involves two principal steps: extraction, where copper ions are selectively transferred to the organic phase, and stripping, where the copper-loaded organic is contacted with a high-strength acid solution to reverse the extraction, concentrating copper into a rich electrolyte. The organic extractant typically contains a chelating agent that forms a complex with copper ions, allowing their selective removal from the PLS [8].

The duration of the solvent extraction process is contingent on the volume of PLS and the operational efficiency of the SX plant, typically ranging from hours to days. The process effectively increases copper concentrations from the initial 1-8 grams per liter in the PLS to 30-45 grams per liter in the electrolyte solution prepared for electrowinning [8].

The concentrated electrolyte solution from the solvent extraction process is subjected to electrowinning, where copper ions are reduced to metallic copper and deposited onto cathodes, forming pure copper sheets. Electrowinning contrasts with electrorefining primarily in the types of electrodes used. In electrowinning, inert

anodes, typically made of lead alloys, are employed, unlike the soluble copper anodes used in electrorefining. This distinction highligths the different objectives: electrowinning aims to extract pure copper from a solution, whereas electrorefining purifies crude copper metal. In electrowinning, copper ions are reduced at the cathode [8].

The impurities, such as iron and selenium, are left in the solution or precipitate as sludge that requires further treatment. The process's duration varies, typically taking a week to complete, influenced by factors such as the current density and the desired thickness of the copper deposit. The copper concentrations in the final cathodes are typically over 99.99% pure [8].

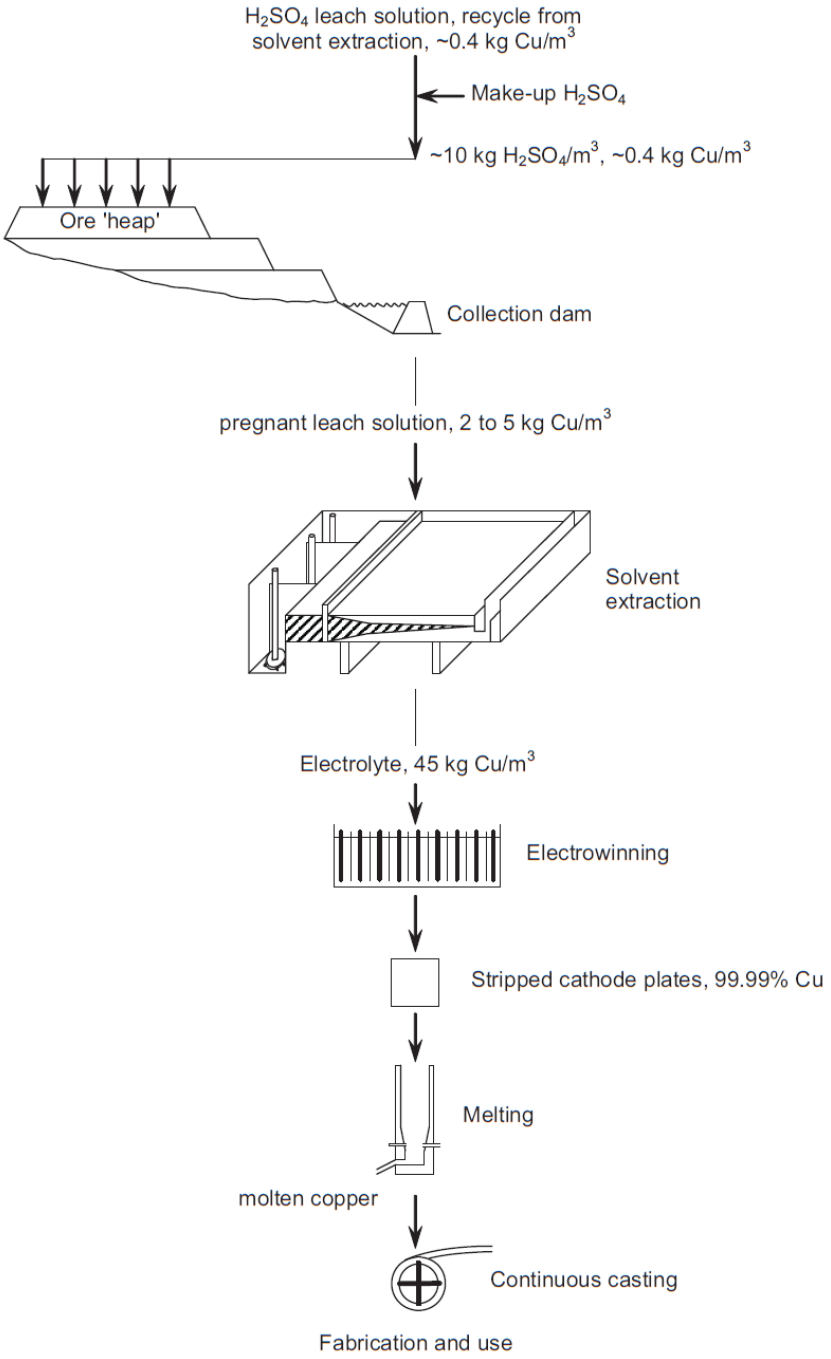

Figure 1.2 Flowsheet for leaching oxide and Cu2S ores. The dissolved Cu is recovered by solvent extraction purification followed by electrowinning. Leaching accounts for ~20% of primary (from ore) copper production [8].

1.5.1.3 Type of copper products

Decisions regarding the melting and casting technologies for copper are influenced by three main factors: the quality of the copper being used as raw material, the specific chemical composition required for the finished product, and the form of the finished product, such as wires or tubes [8].

The Unified Numbering System acknowledges 45 different varieties of wrought copper (all containing at least 99.3% copper) and six types of cast copper. Some of these copper varieties are slightly alloyed with phosphorus to enhance their welding properties by enabling the phosphorus to react with oxygen. This phosphorus is also used to react with the oxygen that is introduced in the melted copper [8].

Pure copper is categorized broadly into two groups. The first group includes electrolytic tough pitch copper (ETP), which intentionally incorporates between 100-650 ppm of oxygen. The oxygen serves two purposes: it helps eliminate unwanted hydrogen absorbed during melting through a reaction ($O+2H \rightarrow H_2O$) that prevents porosity from water vapor during welding and casting. Furthermore, it reacts with metallic impurities to form oxides at the grain boundaries, which are less detrimental to the copper's drawability compared to other possible compounds. This purification process also enhances the copper's conductivity [8]. Most copper production in this category involves casting and fabricating as ETP, chemically refined tough pitch (CRTP), or fire-refined high conductivity copper (FRHC).

The second category is made up of oxygen-free copper varieties, such as oxygen-free copper (OFC) or oxygen-free high conductivity copper (OFHC), which have exceptionally low oxygen levels and show no visible Cu_2O formations in their microstructure. OFC Grade 2 allows a maximum of 10 ppm oxygen, while the best copper grade, oxygen-free electronic (OFE) Grade 1, allows only up to 5 ppm. The absence of Cu_2O precipitates enhances the electrical conductivity of OFC, making it preferable for electrical applications including bus tubes and waveguides. Its enhanced properties also decrease the likelihood of wire breakage during the production of fine magnet wire. Although ETP copper is an alternative for such applications if the impurity levels are adequately controlled, OFC is increasingly being chosen for this purpose. Since phosphorus can be added into the copper to react with oxygen it can be considered as an oxygen-free copper so Phosphorus deoxidised high residual phosphorus (DHP) and phosphorus deoxidised low residual phosphorus (DLP) are part of this category [8].

The different types of copper grades are listed in the table 1 below for more clarity.

1.5.1.4 Copper grades

Table 1. Physical properties of copper that are impacted by impurities [4]

Physical properties of copper grades					
	ETP	DHP	DLP	OF	OFC
Melting point (°C)	1065 to 1083	1083	1083	1084	1084
Density at 20°C (g/cm^3)	8.89 to 8.92	8.94	8.94	8.94	8.94
Thermal conductivity at 20°C (W/(m.K))	389	328	362	389	392
Electrical conductivity at 20°C (% IACS)	100	70 to 90	85 to 98	100	101
Electrical resistivity at 20°C (10^{-8} Ohm.m)	1.7	2.2	1.9	1.7	1.7

ETP regoups ETP, CRTP, FRTP and FRHC.

1.5.1.5 The International Annealed Copper Standard (IACS)

The ETP grade has a composition defined by a minimum copper content of 99.90% and is chosen to be the standard for electrical conductivity measurements with a minimum electrical conductivity in the annealed state at 20°C, of 100% IACS. Its resistivity is $1.7241.10^{-8}$ Ohm.m. This value, which corresponds to a resistance of 0.15328 Ohm for a wire 1 m long weighing 1.0g, was retained in 1913 by the International Electrotechnical Commission as a resistivity standard. The electrical conductivity of copper at 100% IACS is 58 MS/m [9].

1.5.1.6 Copper electronic structure

The intrinsic properties of copper, specifically its electrical conductivity, have positioned it as a material of choice for a myriad of electrical applications, from basic wiring and electrical components to sophisticated electronic devices. This superior conductivity is not merely a fortunate coincidence but is rooted in the electronic structure and the purity of the metal [10], [11]. To fully appreciate the relationship between copper's purity and its electrical performance, it is essential to dig into the atomic underpinnings that facilitate its conductive properties.

Copper's electronic structure is distinguished by its electron configuration, $1s^2 2s^2 2p^6 3s^2 3p^6 4s^1 3d^{10}$ [12]. The presence of a single electron in the 4s orbital, which is at a higher energy level compared to the fully occupied 3d orbitals, is pivotal. It is important to say that this 4s layer does not take part in the chemical reactions in which copper may be involved [13]. The conductivity of a material is a measure of how freely electrons can move through its conductive band. In the case of copper, the half-filled 4s shell acts as a spacious conduit, allowing electrons to flow. Besides, the Fermi level cuts through the 4s band leaving "space" for electrons to flow when an electric field is applied.

However, the conductivity of copper is not solely a function of its electron configuration. The level of purity significantly influences its ability to conduct electricity. In its purest form, copper can achieve a conductivity level exceeding 100% IACS, as evidenced by specialized single crystal copper wires that have demonstrated conductivity rates of 113% IACS [14]. Or in polycrystalline copper like OFHC copper achieving as much as 104% IACS [4]. These figures indicate the role of purity and grain size in maximizing copper's electrical performance. Impurities, even in minute quantities, can drastically alter the conductive performance of copper by introducing scattering centers for conduction electrons. Elements such as iron, zinc, or nickel, when present as impurities, can impede the flow of electrons, thereby reducing the material's overall conductivity.

The refinement process of copper, aimed at eliminating these impurities, is both an art and a science. Starting from copper ores that contain as little as 0.5% copper, a series of extraction and refining techniques are employed to concentrate and purify the metal. Through processes such as froth flotation, smelting, and electrorefining, copper is refined to achieve a purity level of 99.99%. This level of purity is essential to get the desired electrical properties of the final product.

The deleterious impact of impurities on copper's conductivity is not merely a linear phenomenon but can exhibit a disproportionately large effect relative to the concentration of the impurity. For instance, a 0.01% presence of oxygen in copper can lead to a significant reduction in conductivity, illustrating the sensitivity of electrical performance to material purity. This sensitivity is a testament to the delicate balance that governs the interaction between free electrons and the atomic lattice of copper. Impurities disrupt this balance by introducing irregularities in the lattice structure, which serve as obstacles to electron movement. These obstacles, depending on their nature and distribution, can significantly hinder the efficiency of electron flow, manifesting as a reduction in conductivity.

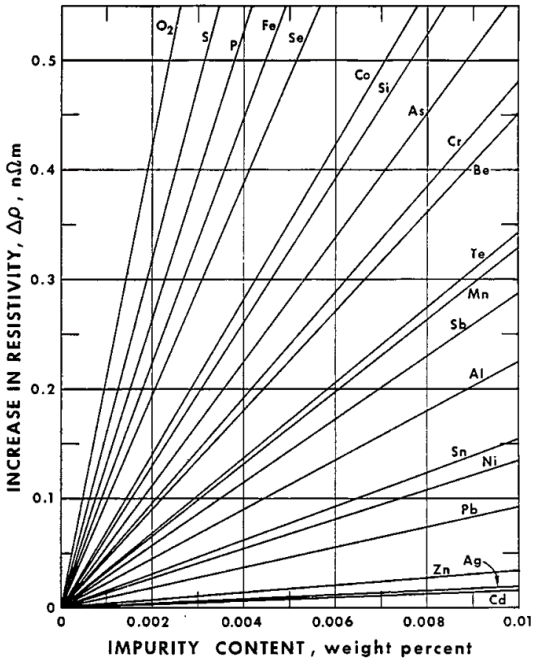

Figure 1.3. Increase of the electrical resistivity of copper as a function of the concentration of different impurities. For comparison, the electrical resistivity of copper at room temperature is about 15.5 nΩm [15]

1.5.1.7 Copper strengthening

The enhancement of the mechanical properties of copper through deformation strengthening, fine grain strengthening, severeplastic deformation (SPD), twinning and alloying is highly important in materials science, particularly because of the implications these processes have on the metal's electrical conductivity and on its strength.

1.5.1.7.1 Deformation strengthening and fine grain strengthening

Deformation strengthening, also known as work hardening or strain hardening, is a process that involves the mechanical manipulation of copper's microstructure to improve its hardness and tensile strength. This phenomenon occurs when copper is subjected to plastic deformation, such as rolling, hammering, or bending, which results in the generation of dislocations within the crystal lattice of the metal. These dislocations impede the movement of other dislocations, thereby increasing the material's resistance to further deformation [12].

At the atomic level, the mechanism of deformation strengthening can be understood through the dislocation theory. Dislocations are linear defects within the crystal structure, and their movement is a primary mode of plastic deformation in metals. When copper undergoes deformation, the density of these dislocations increases, leading to an interaction among them that hampers their mobility. This immobilization of dislocations necessitates the application of greater external force for further deformation, manifesting as increased hardness and strength of the material [12].

Fine grain strengthening, alternatively known as grain boundary strengthening, is another technique employed to augment the mechanical properties of copper. This method relies on the principle that reducing the grain size of the metal increases the total area of grain boundaries, which act as barriers to dislocation movement. Smaller grains mean that dislocations have a shorter mean free path before they are obstructed by grain boundaries, thus requiring a higher stress to propagate through the material [12].

The Hall-Petch relationship provides a quantitative description of the impact of grain size on the yield strength of a metal, indicating that a decrease in grain size leads to an increase in yield strength. The process of achieving fine grain structures in copper typically involves plastic deformation to increase the dislocation density and thermal treatments such as annealing to induce recrystallization, followed by rapid cooling (quenching), which suppresses the growth of grains, leading to a finer microstructure [12].

While deformation strengthening and fine grain strengthening significantly enhance the mechanical properties of copper, they have inverse effects on its electrical conductivity. The increase in dislocation density and the augmentation of grain boundaries, which are beneficial for mechanical strength, act as scattering centers for electrons, thereby impeding the flow of electrical current [10], [11].

Copper's outstanding electrical conductivity is attributed to its crystalline

structure, which allows for the free movement of electrons. However, the introduction of dislocations and grain boundaries disrupts this orderly arrangement, increasing the electrical resistivity of the metal. Consequently, there exists a trade-off between the mechanical strength and electrical conductivity of copper, necessitating a careful optimization of the strengthening processes to achieve the desired balance for specific applications.

The mechanical properties of copper is not significantly influenced by the grade of the material or, to a large extent, by the form of the product, whether it be rolled products, tubes, or bars. Instead, these properties are predominantly affected by the degree of work hardening and, to a lesser extent, by the final dimensions of the product. The average values of these mechanical properties can be summarized as follows:

Table 2. Mechanical properties of annealed and hardened copper [16]

State	Elastic modulus (GPa)	Tensile strength (MPa)	Yield strength (MPa)	Elongation (%)	Vickers Hardness
Annealed	120	220	69	50	50
Quarter hard	120	270	220	22	80
Half hard	120	290	260	14	100
Full hard	120	320	280	20	110
Extra hard	120	360	340	3.3	115
Spring tempered	120	410	390	1.5	130

1.5.1.7.2 Twinning strengthening

Copper hardening through twinning is a sophisticated metallurgical process that exemplifies the interplay between material microstructure and mechanical properties [17].

Twinning in copper refers to the formation of a mirror-like crystallographic orientation within the grains of the metal. This phenomenon is a form of plastic deformation distinct from dislocation movement, which is more commonly associated with the hardening of metals [12]. When copper is subjected to stress, twinning occurs as an alternative mechanism to accommodate strain, especially under conditions of high strain rates or at low temperatures where the movement of dislocations is hindered.

Twin boundaries, the interfaces between the twinned and untwined portions of the grain, serve as obstacles to dislocation motion. The presence of these boundaries within the crystal structure effectively impedes the glide of dislocations across the grain, thus requiring a higher stress to deform the material. This resistance to deformation manifests as an increase in the hardness and strength of the copper.

While twinning improves the mechanical properties of copper, its effect on the metal's electrical conductivity is nuanced. Unlike other hardening mechanisms, such as deformation strengthening and fine grain strengthening, which can significantly increase electrical resistivity due to the proliferation of dislocation density and grain boundaries, twinning does not introduce as many scattering centers for electrons. Consequently, the adverse impact on electrical conductivity is relatively minimized, making twinning an attractive hardening mechanism for applications where maintaining electrical performance is crucial.

However, it is important to note that the extent of hardening through twinning and its impact on electrical conductivity can vary depending on the specific conditions under which the twinning is induced and the overall composition of the copper alloy in question. Therefore, an optimization of the twinning process is essential to achieve the desired mechanical and electrical properties.

Lu et al. [17] enhanced pure copper's tensile strength to 1068 MPa—over ten times that of conventional copper—while maintaining high electrical conductivity, nearly matching that of pure copper. This was achieved by synthesizing copper with nanoscale growth twins through a pulsed electrodeposition technique. These twins effectively block dislocation motion to increase strength without significantly impacting conductivity. The resultant copper's electrical resistivity (96.9%IACS) closely approached the standard for oxygen-free high-conductivity copper, demonstrating a minimal trade-off between strength and conductivity.

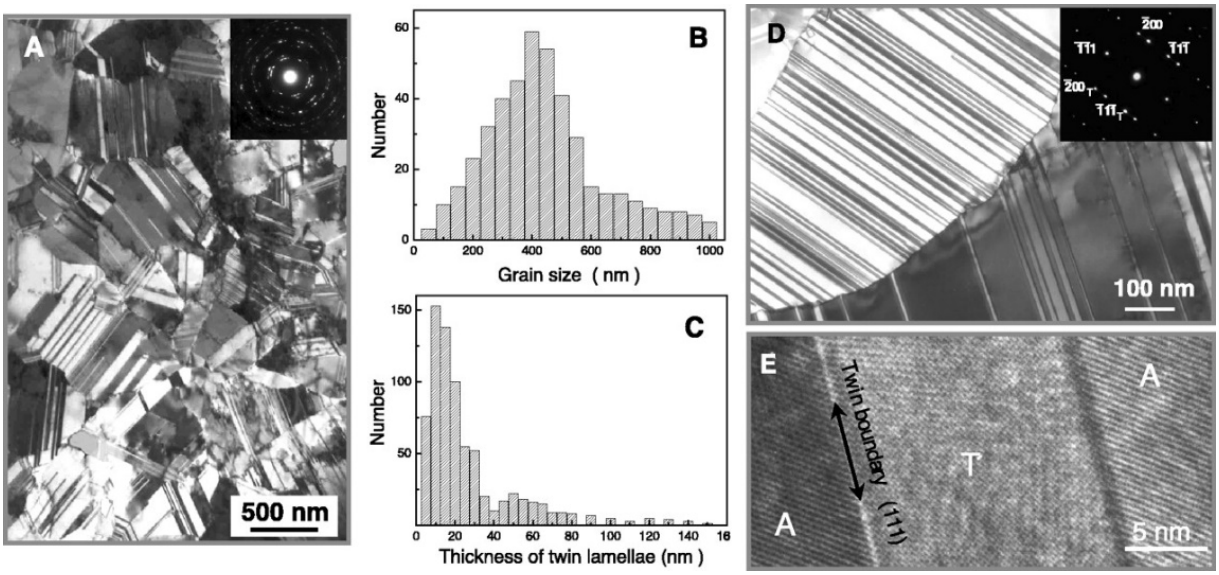

*Figure 1.4. TEM observations of the typical microstructure in an as-deposited Cu sample. A bright-field TEM image (**A**) and the electron diffraction pattern (inset) show roughly equiaxed submicrometer-sized grains with random orientations separated by high-angle GBs. The statistical distributions for grain size (**B**) and for thickness of the twin/matrix lamellae (**C**) were obtained from the many TEM images of the same sample. Electron diffraction patterns [inset in (D)] indicate that the twins in each grain are parallel to each other in {111} planes (**D**), and high-resolution TEM images (**E**) show that the twins follow a sequence of ATATA..., with twinning elements. [17]*

1.5.1.7.3 Severe plastic deformation strengthening (SPD)

Copper hardening through SPD [18], [19], [20], [21], [22], [23], [23] is a metallurgical technique that bridges the conceptual and practical domains between deformation strengthening and fine grain strengthening in copper and other metals. This technique harnesses the intrinsic benefits of both approaches, leveraging the intensive application of plastic deformation to not only introduce a high density of dislocations—akin to the process of deformation strengthening—but also to significantly refine the grain structure to the submicron or even nanometer level, reminiscent of the outcomes sought in fine grain strengthening. Through the imposition of severe strain, SPD promotes the rearrangement of dislocations into new, low-energy configurations, precipitating the formation of ultrafine grains. This dual-action mechanism effectively enhances the material's strength and hardness by impeding dislocation motion and reducing the mean free path of dislocations through an increased number of grain boundaries. SPD techniques, including Equal-Channel Angular Pressing (ECAP), High-Pressure Torsion (HPT), and Accumulative Roll Bonding (ARB).

The refinement of grain size and the increase in dislocation density associated with SPD could, in theory, detrimentally affect the electrical conductivity of copper. This is because both grain boundaries and dislocations serve as scattering centers for conduction electrons, potentially increasing the material's electrical resistivity. However, the actual impact on copper's conductivity depends on the specific SPD technique employed and the conditions under which it is applied. In some instances, the optimized microstructure obtained through SPD can minimize the adverse effects on conductivity, maintaining copper's utility in electrical applications.

1.5.1.7.3.1 Accumulative roll bonding (ARB)

Hosseini and Manesh [22] explored the effects of the accumulative roll-bonding (ARB) process on commercial pure copper (98.51% Cu) strips, aiming to achieve high strength and high conductivity through ultra-fine grain development. Utilizing transmission electron microscopy, they observed the evolution of microstructures with grains as fine as ~180 nm after eight ARB cycles, accompanied by an increase in tensile strength and microhardness. The tensile strength escalated to 723.56 MPa, which is significantly higher than the starting material, while maintaining a slight increase in elongation after the initial drop. Notably, the electrical conductivity exhibited a decrease during the first six cycles of ARB but interestingly increased after eight cycles, suggesting a recovery phenomenon likely due to dynamic recovery effects and temperature rises from the process.

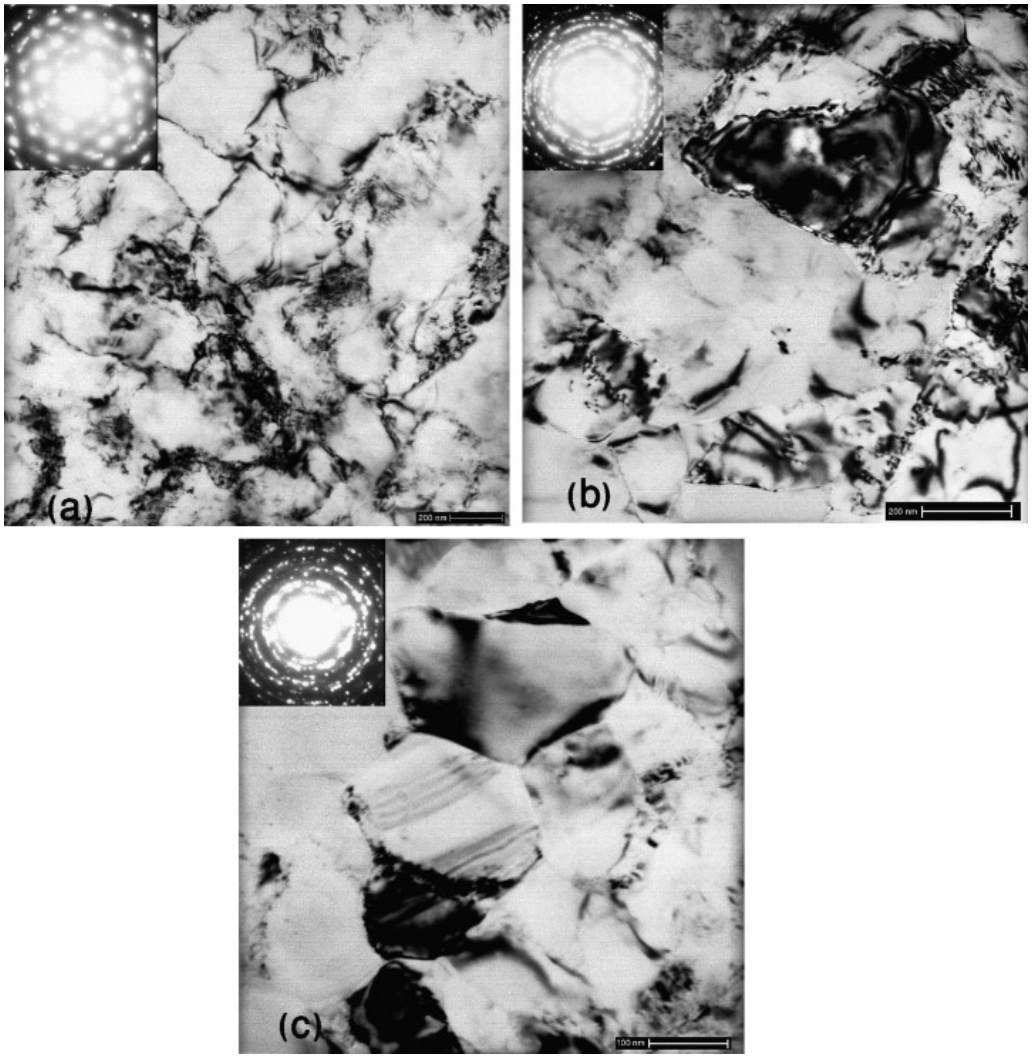

Figure 1.5. TEM micrograph and corresponding SAD patterns of commercial pure copper after RT-ARB process, (a) 4 cycles, 38kx, (b) 6 cycles, 99kx and (c) 8 cycles,115kx. [22]

1.5.1.7.3.2 Equal channel angular rolling (ECAR)

Habibi et al. [18] developed nano-grained pure copper using the Equal Channel Angular Rolling (ECAR) process, which involved ten passes with a specific rotation technique to ensure uniform grain structure. This severe plastic deformation technique refined the grains to sizes between 70-200 nm. The ECAR process significantly improved mechanical properties, where after the first pass, the yield strength increased by approximately 85%, and tensile strength rose by 6%. Despite a significant reduction in ductility, particularly after the first three passes, the materials maintained a slight variation in electrical conductivity, with a slight decrease initially but a minor improvement after seven passes.

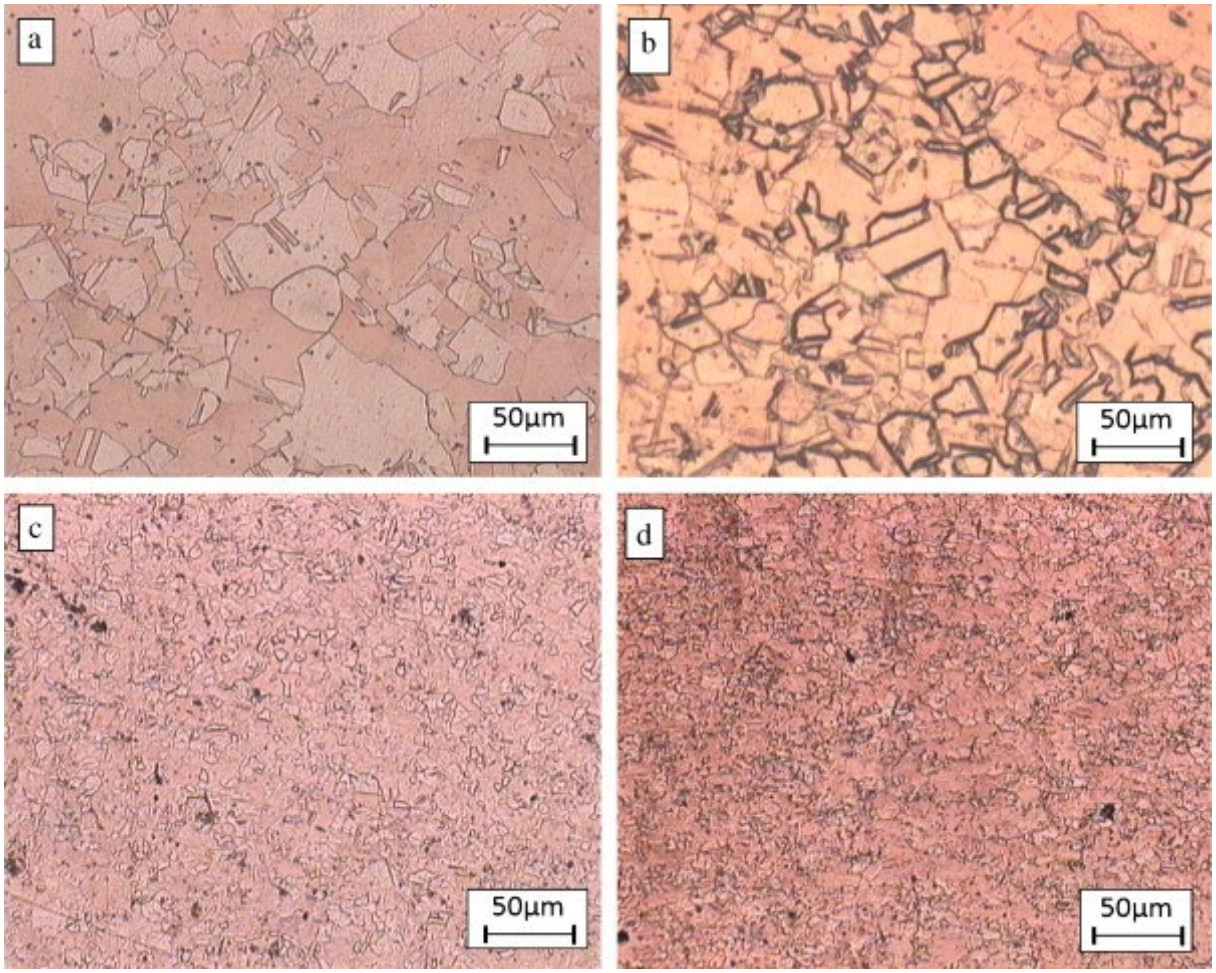

Figure 1.6. Optical micrographs of the (a) as-annealed, (b) 1-pass ECAR'ed, (c) 7-pass ECAR'ed and (d) 10-pass ECAR'ed specimens. [18]

1.5.1.7.3.3 Friction stir processing

Surekha et al. [19] explored the development of high strength, high conductivity copper via friction stir processing (FSP) on a three-millimeter thick pure copper plate, achieving fine grains by varying the travel speed from 50 to 250 mm/min at a constant rotation speed of 300 rpm. The process resulted in a decreased grain size from 9 to 3 μm and an increase in hardness from 102 to 114 HV, demonstrating that tensile strength, yield strength, and hardness are enhanced with the reduction of grain size. Notably, the yield strength followed the Hall–Petch relationship $\sigma_s = 223.8 + 0.07d^{1/2}$, indicating a direct correlation between grain size and yield strength. The highest recorded ultimate tensile strength reached 328 MPa. Moreover, the study found that electrical resistivity at room temperature remained unchanged, measured at 1.72×10^{-8} Ω.m (100% IACS), compared to the base metal, thus achieving the aim of enhancing mechanical properties without affecting electrical conductivity.

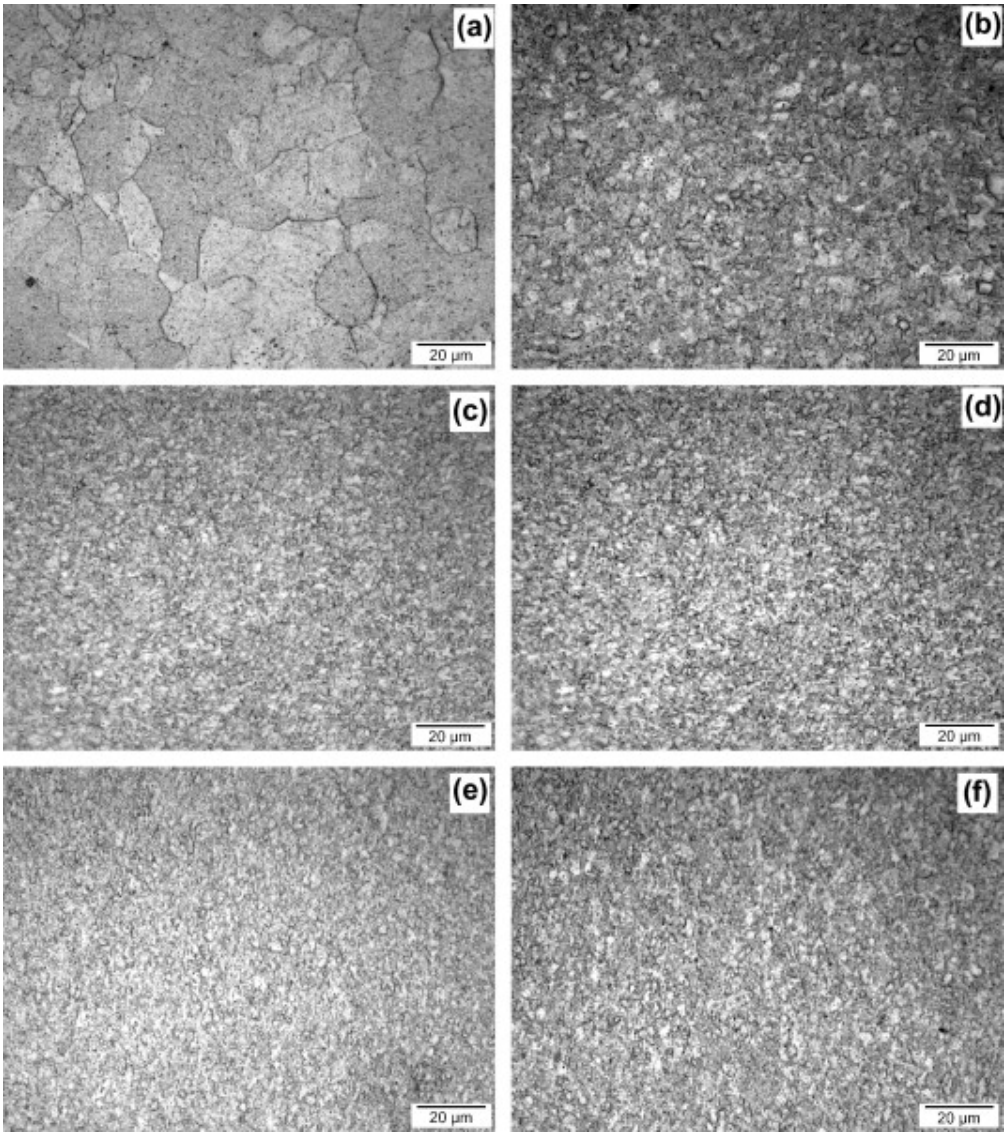

Figure 1.7. Optical micrographs of (a) BM and (b)–(f) nugget regions of processed samples at (b) 50, (c) 100, (d) 150, (e) 200 and (f) 250 mm/min. [19]

1.5.1.7.4 Alloying

HuiYa et al. [24] conducted a comprehensive review focusing on high strength and high conductivity (HSHC) copper alloys, which are pivotal in fields demanding materials that combine excellent electrical conductivity with substantial mechanical strength. Their analysis spans across multiple copper (Cu) alloy systems, namely Cu-Cr-Zr, Cu-Ni-Si, Cu-Ag, Cu-Mg, and Cu-Nb, each offering unique properties and applications based on their composition and treatment processes.

Cu-Cr-Zr System: The Cu-Cr-Zr alloys are primarily known for their precipitation strengthening mechanism. A composition within this system, the Cu-0.55Cr-0.05Zr (wt.%) alloy, demonstrates an impressive combination of strength, recorded at 131 HV, alongside an electrical conductivity reaching 85.3%IACS. This balance is achieved through controlled aging treatments that precipitate finely dispersed phases, thereby enhancing the alloy's strength without significantly compromising its conductivity. The incorporation of Zr not only refines the microstructure but also contributes to the stability of properties under elevated temperatures, making the Cu-Cr-Zr alloy suitable for applications requiring both high strength and conductivity under challenging conditions.

Cu-Ni-Si System: Cu-Ni-Si alloys stand out for their aging-strengthening capabilities. The system utilizes the precipitation of the δ-Ni_2Si phase to achieve a harmonious balance between mechanical strength and electrical conductivity. The aging process facilitates the precipitation of the strengthening phase from a supersaturated solid solution, which, in turn, obstructs dislocation movement and enhances the alloy's strength. Simultaneously, the reduction in solute atoms within the Cu matrix diminishes electron scattering, improving conductivity. This system's adaptability is further enhanced by microalloying with elements such as Ti, Cr, Fe, and Mg, each adding to the alloy's comprehensive mechanical properties while minimally affecting its conductivity.

Cu-Ag System: The Cu-Ag alloys are celebrated for their exceptional strength and good conductivity, benefiting significantly from cold work and optimized heat treatments. For instance, the Cu-71.9Ag (wt.%) alloys have demonstrated yield strengths of approximately 400 MPa, with specific processing methods leading to nano-scale Cu-Ag composite materials with tensile strengths reaching up to 1420 MPa. The unique feature of this system lies in its ability to form a fine, dense micro composite structure upon cold working, significantly enhancing the material's strength. Additionally, when combined with intermediate heat treatment, these alloys can maintain relatively high conductivity alongside their remarkable strength.

Cu-Mg System: This alloy system focuses on the modest influence of Mg on the electrical conductivity of Cu. By leveraging the precipitation strengthening effect and maintaining Mg content below 1%, the Cu-Mg alloys exhibit significant improvements in both tensile strength and electrical conductivity, with minimal impact on machining performance. This balance makes the Cu-Mg alloy particularly valuable for applications such as electrified railway contact wires, where both high electrical conductivity and mechanical strength are crucial.

Cu-Nb System: Widely investigated for its high strength, conductivity, and workability, the Cu-Nb system exemplifies the synergy between microstructural refinement and the intrinsic differences in crystal structures of Cu and Nb. This system's strength is often attributed to the refinement of microstructures and the formation of Nb nanoribbons within the Cu matrix. For example, Cu-16Nb (vol.%) composites have achieved tensile strengths of 932 MPa and electrical conductivities as high as 73%IACS, showcasing the potential of this alloy system for high-field magnet technology and similar demanding applications.

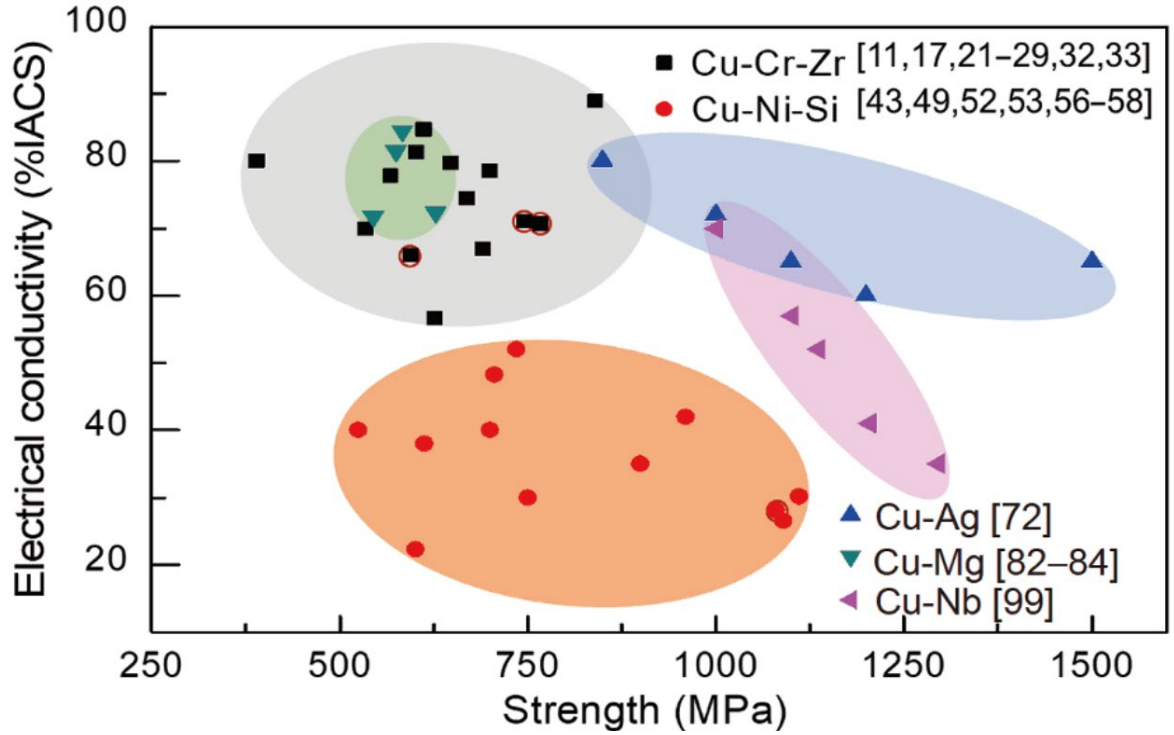

Figure 1.8. (Color online) The electrical conductivity versus the strength of Cu alloys and Cu matrix composites (some strength values are calculated as 3.5 times of the hardness values, marked with red circle). [24]

1.5.2 Graphene

Graphene, represents one of the most intriguing advancements in material science over the past few decades. Initially conceptualized as a theoretical construct, graphene's real-world isolation in 2004 [2] marked a significant milestone in nanotechnology and materials science, opening the door to a vast array of research into two-dimensional materials.

The foundational structure of graphene is simple yet profoundly intricate: a single layer of carbon atoms, each bonded to three others, forming a flat, two-dimensional honeycomb lattice. This structure can be imagined as an infinite array of fused hexagonal rings or, more colloquially, as "chicken wire" made entirely of carbon. Despite its simplicity, the isolation of such a structure, a mere atom thick, posed significant experimental challenges. The breakthrough came relatively recently, demonstrating the difficulty of working at such atomic scales [13], [25].

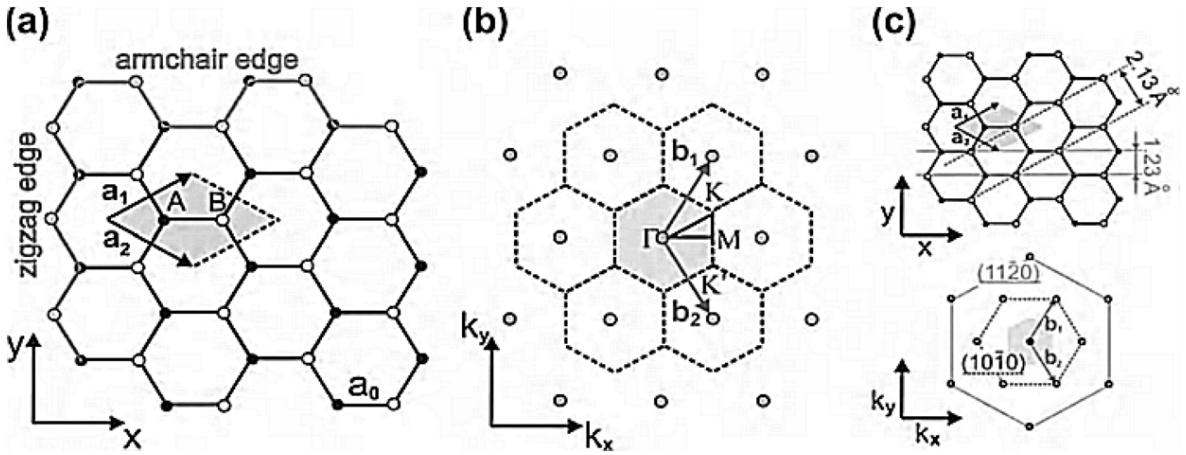

Figure 1.9 Crystal structure of graphene: (a) 2D hexagonal lattice of graphene in real space with basis vectors a1 and a2. The unit cell is highlighted in grey. It contains two nonequivalent carbon atoms A and B, each of which span a triangular sublattice as indicated with black and white atoms, respectively. An armchair and a zigzag edge are highlighted in grey. (b) Reciprocal lattice (dashed) with reciprocal lattice vectors b1 and b2. The first Brillouin zone is marked grey and the high symmetry points G, M, K and K0 are indicated. (c) Demagnified views of the real (upper panel) and reciprocal lattice (lower panel), respectively. Two sets of lattice planes with d = 2.13Å and d = 1.23Å are highlighted with dotted and full lines in the real space lattice. In the reciprocal lattice the corresponding diffraction spots are marked with a dotted and full hexagon, accordingly [25].

Graphene's atomic composition and arrangement confer upon it a set of exceptional properties. Each carbon atom in graphene is sp^2 hybridized, meaning that it shares electrons with three neighboring atoms in a plane, forming strong covalent bonds. This configuration grants graphene its great strength. Moreover, the delocalized

electrons from these bonds form π bands, which are crucial to graphene's unique electronic properties [13], [25].

In terms of electronic structure, graphene is a zero-gap semiconductor or a semimetal. Its conduction and valence bands meet at the Dirac points, locations in momentum space that are fundamental to graphene's electronic behavior. Near these points, the charge carriers—electrons and holes—exhibit linear energy-momentum relations, differing substantially from the parabolic relations observed in conventional semiconductors. This distinction leads to several remarkable electronic properties, including very high electrical conductivity and mobility [13], [25].

Graphene's high electron mobility is particularly remarkable, with values surpassing those of other known materials. This high mobility means that electrical charges can travel through graphene with minimal resistance, a property highly desirable in electronic devices. Furthermore, this mobility remains nearly constant, even as carrier concentrations increase, a stark contrast to the behavior observed in traditional semiconductors. The physical and electronic structures of graphene also allow for ballistic transport, where charge carriers move through the material without scattering, even at room temperature [25].

1.5.2.1 The importance of the number of layers

The structure and properties of graphene exhibit significant variation depending on the number of layers present, and these differences are crucial for its application in various fields. Single-layer graphene (SLG) consists of a single atomic layer of carbon atoms arranged in a two-dimensional hexagonal lattice. The carbon atoms in SLG are bonded together by strong in-plane covalent bonds known as sigma (σ) bonds, formed from electrons in the 2s, $2p_x$, and $2p_y$ valence orbitals. The fourth valence electron occupies the $2p_z$ orbital, which interacts with the $2p_z$ orbitals of neighboring atoms to form pi (π) bonds. These π bonds result in delocalized π and π* bands, which are crucial for the unique electronic properties of SLG. The delocalized electrons in these bands contribute to graphene's exceptional electrical conductivity and high electron mobility. SLG is also a zero-gap semiconductor, meaning it does not have an energy gap between the valence and conduction bands, leading to its unique electronic properties, such as the ability to conduct electricity with minimal resistance [25].

Bi-layer graphene (BLG), on the other hand, consists of two layers of graphene stacked together. The electronic properties of BLG differ significantly from those of SLG due to the interactions between the two layers. The most common stacking arrangement in BLG is the AB (Bernal) stacking. In this arrangement, one layer's carbon atoms are positioned directly over half of the second layer's carbon atoms, while the other half of the carbon atoms are located above the centers of the hexagonal rings in the second layer. This arrangement leads to the splitting of the π and π* bands, introducing a small band gap under an applied electric field, which is not present in SLG. This tunable band gap makes BLG suitable for certain electronic applications where a band gap is desirable, such as in transistors and other semiconductor devices. Additionally, the Raman spectrum of BLG shows a broader 2D peak compared to SLG,

indicating the presence of multiple sub-peaks due to the band splitting [25].

Multi-layer graphene (MLG) consists of three or more layers of graphene stacked together. When the number of layers exceeds ten, the material begins to exhibit properties similar to bulk graphite. The electronic properties of MLG depend on both the number of layers and the stacking sequence. In few-layer graphene (FLG), which consists of three to fewer than ten layers, the band structure becomes more complex, with the conduction and valence bands starting to overlap. This overlap introduces additional charge carriers, which affects the electronic properties of the material. As the number of layers increases, the electronic properties transition from those of SLG to those of bulk graphite. This transition is marked by changes in the thermal and electrical conductivity of the material. The thermal conductivity of graphene decreases with an increasing number of layers due to the interlayer interactions that hinder phonon transport. Phonons, which are quasiparticles of lattice vibrations and primary carriers of heat in materials, face increased scattering and reduced mobility in MLG, leading to lower thermal conductivity compared to SLG [25].

1.5.2.2 Graphene oxide and reduced graphene oxide

Graphene oxide (GO) is a derivative of graphene that has been oxidized, resulting in a structure that contains various oxygen-containing functional groups such as epoxides, hydroxyls, and carboxyls. These groups are typically located on the basal plane and edges of the graphene sheets. The oxidation process disrupts the pristine lattice structure of graphene, introducing significant disorder and defects. The production of GO is relatively scalable and involves the oxidation of graphite powder in the presence of strong acids and oxidants. This method yields a product with a layered structure similar to graphite, but with a higher degree of functionalization. The typical C atomic ratio in GO ranges from 2.0 to 2.9. Due to the presence of oxygen functionalities, GO is hydrophilic and can be dispersed in water, making it useful for various applications such as coatings, composites, and sensors [25].

Reduced graphene oxide (rGO) is produced by the chemical or thermal reduction of graphene oxide. This reduction process aims to remove the oxygen-containing functional groups, partially restoring the structure and properties of pristine graphene. However, the reduction is typically incomplete, and some functional groups and defects remain, which can influence the properties of rGO. The reduction process often involves the use of reducing agents such as hydrazine, hydrogen, or thermal annealing. Despite the reduction, rGO generally retains some of the defects introduced during the oxidation of graphite, which can degrade its electrical properties compared to pristine graphene. For example, the conductivity of rGO is often lower than that of mechanically cleaved graphene. rGO finds applications in areas where high conductivity is not critical, such as in certain composites and coatings. Moreover, rGO can serve as a nanofiller to enhance the mechanical properties of polymers, where the presence of some functional groups can improve dispersion and interfacial adhesion within the polymer matrix [25].

1.5.2.3 Fabrication of graphene

Graphene's production methods vary in terms of cost, scalability, and quality of the produced material. Techniques such as mechanical exfoliation, liquid exfoliation, chemical vapor deposition (CVD), and chemical reduction of graphene oxide are commonly employed, each with its own advantages and limitations. High-quality graphene is essential for applications requiring optimal performance, as defects, layer number, and impurities significantly affect its properties.

1.5.2.3.1 Graphene fabrication through CVD

CVD represents a cornerstone technique in materials science, particularly in the synthesis of graphene, due to its ability to produce high-quality, uniform films over large areas. At its core, the CVD process involves the deposition of a material from a gaseous state to a solid state on a substrate through a chemical reaction. This method is particularly suited for graphene synthesis due to its scalability and the high quality of the graphene produced. The process parameters, such as chemical reactions, gas precursors, CH_4 to H_2 ratios, temperature settings, and substrate choices, play pivotal roles in determining the morphology, structural integrity, and mechanical properties of the resultant graphene [26].

One of the primary advantages of CVD is its ability to produce large, continuous graphene films, which are essential for applications in transparent conductive electrodes, flexible electronics, and other technologies requiring uniform material properties over large areas. Unlike mechanical exfoliation, which produces small, randomly scattered flakes, CVD can cover entire wafers with a single layer of graphene [25]. The quality of graphene produced via CVD is also high. The process allows for precise control over the number of layers, and with optimization, it is possible to produce predominantly single-layer graphene. The graphene films obtained are generally free of significant defects, providing excellent electronic properties, such as high carrier mobility and conductivity [25].

The choice of substrate plays a crucial role in the CVD process. Copper is favored due to its low carbon solubility, which promotes the growth of single-layer graphene. In contrast, nickel, with its higher carbon solubility, can lead to the formation of multi-layer graphene upon cooling and carbon precipitation. After graphene growth, the metal substrate is often etched away, leaving a free-standing graphene film that can be transferred to another substrate for further use [25].

1.5.2.3.1.1 Fundamental Principles of CVD for Graphene Synthesis

The synthesis of graphene via CVD involves decomposing hydrocarbon gas precursors (e.g., methane, ethylene) at elevated temperatures on a catalytic metal substrate (commonly copper or nickel), leading to the deposition of carbon atoms on the substrate's surface. The chemical reaction can be generally represented as follows: $CH_4 \rightarrow C$ (graphene) + $2H_2$, where methane (CH_4) is decomposed into solid carbon

(graphene) and hydrogen gas. This reaction requires precise control over temperature, which typically ranges from 900°C to 1100°C for copper substrates, to ensure the proper dissociation of the gas molecules and subsequent formation of a graphene layer [26], [27].

1.5.2.3.1.2 Low-Pressure Chemical Vapor Deposition (LPCVD)

LPCVD operates under reduced pressure conditions, enhancing the uniformity and quality of the graphene film by facilitating a more uniform gas flow and reducing undesirable gas-phase reactions. Operating at lower pressures also allows for a higher mean free path of gas molecules, contributing to the formation of uniform graphene layers. Temperature conditions in LPCVD are crucial; too high a temperature may lead to the formation of multilayer graphene, while too low a temperature may not efficiently decompose the gas precursors. The choice of substrate, with copper being the most popular due to its ability to catalyze the growth of monolayer graphene, significantly influences the efficiency and quality of graphene synthesis in LPCVD processes [27].

1.5.2.3.1.3 Atmospheric Pressure Chemical Vapor Deposition (APCVD)

APCVD is conducted at atmospheric pressure, simplifying the process setup compared to LPCVD and potentially making the process more accessible for large-scale production. The operation at atmospheric pressure can lead to faster reaction rates, which, while beneficial for production speed, may compromise layer uniformity due to the turbulent flow of gases. APCVD requires control over temperature and gas flow rates to ensure the deposition of uniform and high-quality graphene layers. Despite these challenges, APCVD has demonstrated significant potential in the scalable production of graphene, particularly when optimizations are applied to control gas flow dynamics and reaction kinetics effectively [27], [28].

1.5.2.3.1.4 Plasma-Enhanced Chemical Vapor Deposition (PECVD)

PECVD introduces plasma into the CVD process, enabling graphene synthesis at significantly lower temperatures than traditional CVD methods. The plasma, generated by an electromagnetic field, provides energy that facilitates the decomposition of gas molecules and the formation of graphene, even at these lower temperatures. This method's ability to operate at lower temperatures widens the range of possible substrates, including those sensitive to high temperatures. PECVD can offer superior control over the growth process, potentially leading to the deposition of graphene with fewer defects and higher uniformity. However, the introduction of plasma also adds complexity to the process, requiring careful optimization of plasma power, gas flow rates, and temperature to achieve the desired graphene quality [27], [28].

1.5.2.3.1.5 Growth of graphene using solid carbon sources as precursor in CVD-like setup

Graphene can also be grown from solid carbon sources such as PMMA, sucrose

or amorphous carbon [29], [30].

Ji et al. [29], successfully grew high-quality monolayer graphene on copper foil using amorphous carbon as the starting material and hydrogen gas as a key facilitator. They propose that hydrogen reacts with the amorphous carbon at high temperatures to produce hydrocarbon gases, which then serve as the actual carbon source for graphene growth on the copper surface. The resulting graphene exhibited uniformity, large area coverage, low defect concentration, and excellent electrical properties.

Sun et al. [30], present a method for growing graphene using solid carbon sources, such as polymers like PMMA (polymethyl methacrylate) and small molecules like fluorene and sucrose, on metal catalyst substrates like copper and nickel. The process involves heating the carbon source-coated metal substrate in a hydrogen and argon atmosphere at temperatures as low as 800°C. The hydrogen acts as both a reducing agent and a carrier gas, facilitating the transformation of the solid carbon into graphene while removing excess carbon atoms. By adjusting parameters like gas flow rates and temperature, the researchers could control the thickness of the resulting graphene, producing monolayer, bilayer, or few-layer graphene films.

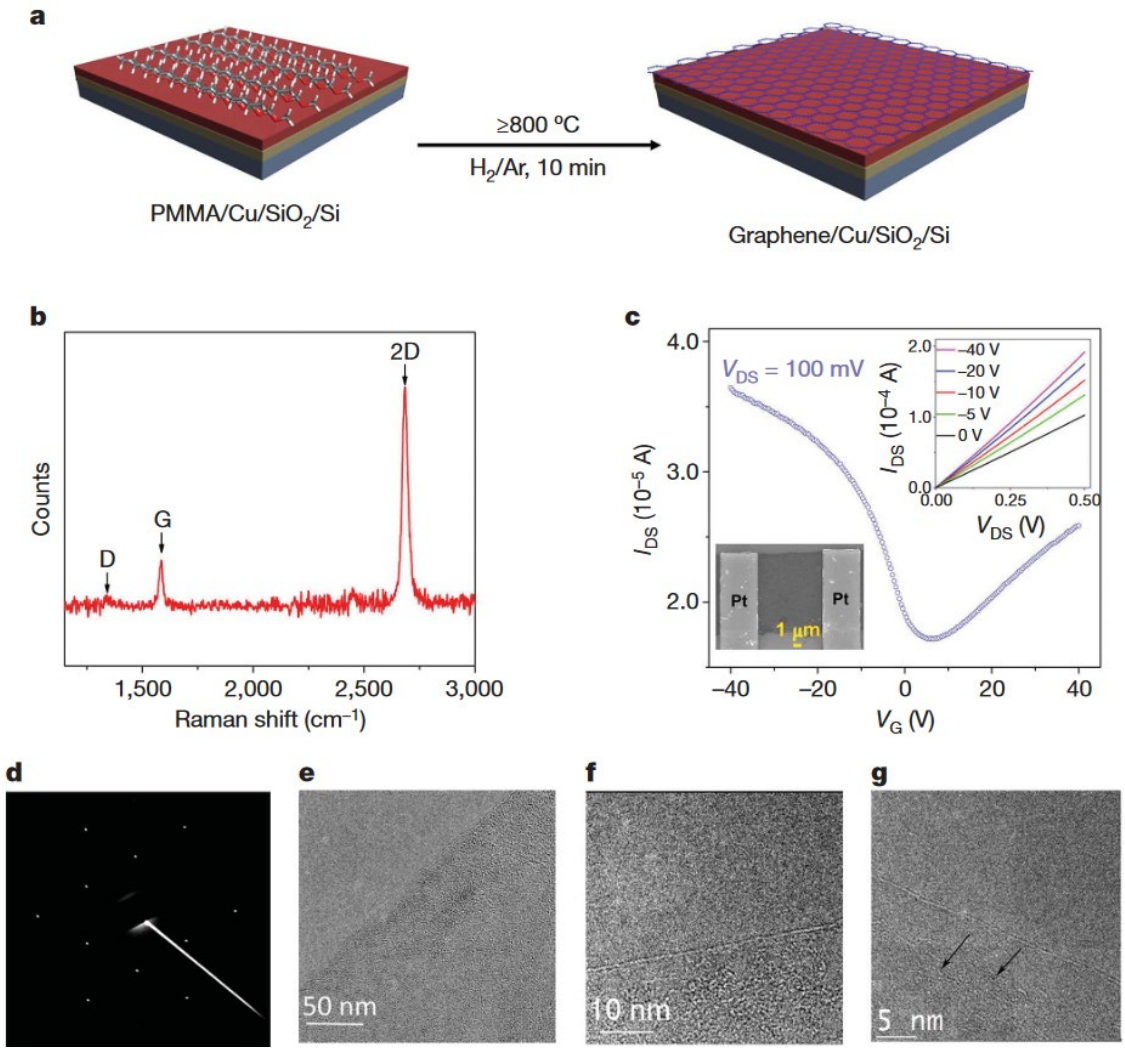

Figure 1.10 ynthetic protocol, spectroscopic analysis and electrical properties of PMMA-

derived graphene. a, Monolayer graphene is derived from solid PMMA films on Cu substrates by heating in an H2/Ar atmosphere at 800 uC or higher (up to 1,000 uC). b, Raman spectrum (514 nm excitation) of monolayer PMMA-derived graphene obtained at 1,000 uC. See text for details. c, Room temperature IDS–VG curve from a PMMA-derived graphene-based back-gated FET device. Top inset, IDS–VDS characteristics as a function of VG; VG changes from 0 V (bottom) to 240 V (top). Bottom inset, SEM (JEOL-6500 microscope) image of this device where the PMMA-derived graphene is perpendicular to the Pt leads. IDS, drain–source current; VG, gate voltage; VDS, drain–source voltage. d, SAED pattern of PMMA-derived graphene. e–g, HRTEM images of PMMA-derived graphene films at increasing magnification. In g, black arrows indicate Cu atoms [30].

1.5.2.3.2 Mechanical exfoliation

Mechanical exfoliation, also known as the "Scotch tape method," is a straightforward and cost-effective technique used to produce graphene from bulk graphite. This method was famously used by Andre Geim and Konstantin Novoselov in 2004 to isolate single-layer graphene, a breakthrough that earned them the Nobel Prize in Physics in 2010. The process involves attaching adhesive tape to the surface of a graphite crystal and then peeling it off, which results in thin layers of graphene adhering to the tape. These layers can then be transferred onto a silicon wafer or another substrate [25].

The primary advantage of mechanical exfoliation is its ability to produce high-quality, defect-free graphene sheets with excellent electronic properties, suitable for fundamental research and prototype device fabrication. However, the method is not scalable for large-scale production because it typically yields only small flakes of graphene, varying in thickness and lateral dimensions [25].

The technique is limited by the manual nature of the process, which is labor-intensive and not suitable for industrial applications. Additionally, the graphene layers produced can sometimes have wrinkles or folds due to the peeling process, which may affect their properties. Despite these limitations, mechanical exfoliation remains a popular method in research settings due to its simplicity and the high quality of graphene it can produce, providing an essential tool for studying the fundamental properties of graphene and developing initial applications in electronics and materials science [25].

1.5.2.3.3 Liquid-phase exfoliation (Chemical exfoliation)

Liquid-phase exfoliation is a widely used method for producing graphene from bulk graphite through dispersion and ultrasonic treatment in a solvent. This technique involves dispersing graphite in a solvent such as N-methyl-2-pyrrolidone (NMP) or water with surfactants, and then applying ultrasonic energy to exfoliate the graphite into graphene sheets. The high-energy ultrasonic waves create cavitation bubbles in the solvent, which collapse and generate shock waves that break apart the graphite

layers into individual graphene sheets [25].

One of the main advantages of liquid-phase exfoliation is its scalability, making it suitable for producing large quantities of graphene at a relatively low cost. This method can yield graphene sheets of various sizes and thicknesses, depending on the processing conditions and the nature of the solvent used. The graphene produced by this method is often few-layered and can contain some defects, but it is adequate for many applications where pristine, single-layer graphene is not required [25].

The resulting graphene dispersion can be processed further to concentrate and purify the graphene sheets, often through centrifugation to separate the larger graphite particles from the smaller graphene flakes. The dispersions can be used directly in applications such as inks for printing, composite materials, and coatings [25].

Despite its advantages, liquid-phase exfoliation has some limitations. The graphene sheets produced are typically smaller and may have more defects compared to those produced by mechanical exfoliation or chemical vapor deposition. Additionally, the process can introduce surfactant residues or solvent contamination that need to be removed for certain applications [25].

1.5.2.3.4 Chemical reduction of reduced Graphene Oxide

Chemical reduction of graphene oxide (GO) is a widely used method for producing reduced graphene oxide (rGO), which serves as a practical alternative to pristine graphene. This process begins with the oxidation of graphite to create graphene oxide, a material rich in oxygen-containing functional groups such as hydroxyl, carboxyl, and epoxy groups. These groups make GO hydrophilic and easily dispersible in water, facilitating its use in various applications [25].

The reduction of GO involves chemical agents such as hydrazine, sodium borohydride, or hydroquinone, which remove the oxygen functionalities, partially restoring the graphene lattice and improving its electrical conductivity. Thermal reduction methods, where GO is heated at high temperatures in an inert or reducing atmosphere, are also commonly employed. Although the reduction process significantly decreases the oxygen content, some functional groups and defects usually remain, distinguishing rGO from pristine graphene [25].

One of the main advantages of this method is its scalability and cost-effectiveness, enabling the production of large quantities of graphene-like materials. rGO retains many of the beneficial properties of graphene, such as high surface area and mechanical strength, but its electronic properties are somewhat compromised due to residual defects and oxygen groups. These remaining functionalities, however, can be advantageous for certain applications, such as in sensors, composite materials, and energy storage devices, where they enhance chemical reactivity and interaction with other materials [25].

1.5.2.4 Characterization of graphene

1.5.2.4.1 Raman spectroscopy

Raman spectroscopy is a technique that relies on the inelastic scattering of monochromatic light, usually from a laser, to study vibrational, rotational, and other low-frequency modes in a material. When light interacts with the material, most photons are elastically scattered (Rayleigh scattering), maintaining the same energy as the incident photons. However, a small fraction of photons is inelastically scattered, either gaining or losing energy, which corresponds to the vibrational energy levels of the molecules in the material. This inelastic scattering is known as Raman scattering, and the energy shift provides a unique spectral fingerprint that can be used to identify and characterize materials [25], [31].

The G band is one of the most prominent features in the Raman spectrum of graphene and other graphitic materials. Located around 1580 cm^{-1}, the G band corresponds to the in-plane vibration of sp^2-bonded carbon atoms. This mode is a first-order Raman-allowed process involving the stretching of the carbon-carbon bonds in the hexagonal lattice. The G band is a critical indicator of the presence of graphitic structures and is typically strong in all sp^2 carbon systems. In graphene, the G band appears as a single, sharp peak, and its position and intensity can provide insights into the doping level and strain in the graphene lattice [25], [31].

The D band, found around 1350 cm^{-1}, is associated with the presence of defects and disorder in the graphene lattice. This band arises from a second-order process involving a defect-mediated intervalley double resonance. Unlike the G band, the D band is not present in pristine graphene and only appears when there are defects such as vacancies, edges, or functional groups disrupting the sp^2 carbon network. The intensity of the D band relative to the G band (I(D)/I(G) ratio) is a commonly used measure to quantify the defect density in graphene. A higher I(D)/I(G) ratio indicates a higher level of defects [25], [31].

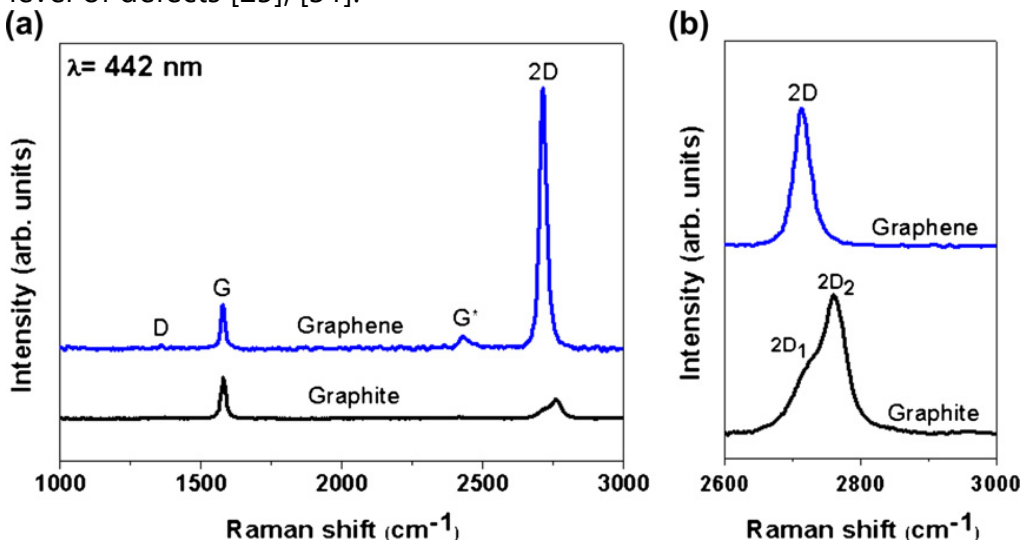

Figure 1.11 (a) Raman spectra of graphene and graphite, showing the main Raman features, the D, G, G and 2D bands taken with a 442 nm laser. (b) Zoomed 2D*

region of graphene and graphite [25].

The 2D band, also known as the G' band, is located around 2700 cm^{-1} and is a second-order overtone of the D band, but unlike the D band, it does not require the presence of defects to be active. The 2D band results from a two-phonon, double-resonance Raman scattering process. In single-layer graphene, the 2D band appears as a single, sharp, symmetric peak, whereas in multi-layer graphene, it splits into multiple sub-peaks due to interlayer interactions. The shape, position, and intensity of the 2D band are sensitive to the number of graphene layers, making it a valuable feature for determining layer thickness [25], [31].

The intensity ratio of the D band to the G band (I(D)/I(G)) is a crucial parameter in assessing the quality of graphene. This ratio provides a quantitative measure of the defect density in the material. In pristine graphene, the D band is nearly absent, resulting in a very low I(D)/I(G) ratio. As defects are introduced, the D band intensity increases, and consequently, the I(D)/I(G) ratio rises. This ratio can be used to monitor the effects of processes such as chemical functionalization, thermal treatment, and mechanical deformation on graphene. For example, an increase in I(D)/I(G) ratio after chemical treatment indicates the introduction of defects, whereas a decrease after thermal annealing suggests defect healing.

1.5.2.4.2 Transmission Electron Microscopy of graphene

Transmission Electron Microscopy (TEM) is a critical technique for the morphological and structural characterization of graphene. TEM provides high-resolution images and allows for detailed analysis of graphene's atomic structure, layer number, defects, and chemical composition.

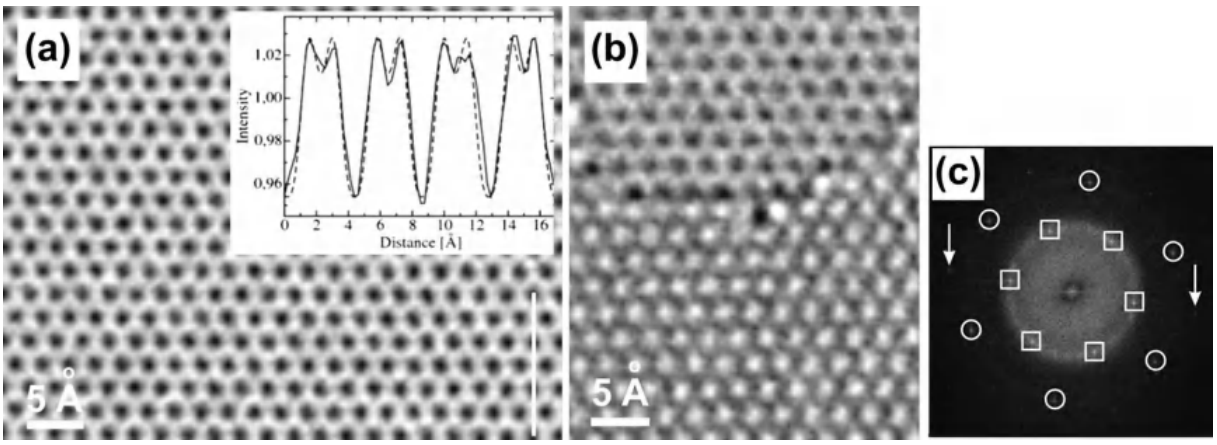

Figure 1.12 (a) Atomic resolution TEM image of monolayer graphene. The carbon atoms appear with white contrast. Inset: measured (solid line) and simulated (dashed line) contrast profile of monolayer graphene. (b) Atomic resolution TEM micrograph of a monolayer (top) next to a bilayer graphene region (bottom). (c) FFT of a graphene bilayer region with the reflections corresponding to an information transfer of 2.13Å, 1.23 Å and

1.06 Å marked with squares, circles and arrows, respectively [25].

One of the primary uses of TEM in graphene research is to determine the number of layers in a graphene sample. This can be done by examining the edges of graphene sheets. By tilting the sample, it is possible to count the number of lines of contrast at the folded edges, providing a cross-sectional view of the layers. High-resolution TEM (HRTEM) images can also reveal the number of layers and the quality of stacking in multi-layer graphene [25].

TEM can provide atomic-resolution images, allowing for the detailed study of defects within the graphene lattice. Defects such as vacancies, dislocations, grain boundaries, and other structural irregularities can significantly affect graphene's electronic and mechanical properties. Advanced TEM techniques, such as aberration-corrected TEM, enable the visualization of these defects at the atomic level, offering insights into how they influence the material's behavior [25].

In addition to imaging, TEM can be used for electron diffraction and spectroscopy. Electron diffraction provides information about the crystallographic structure of graphene, including the orientation and spacing of the atomic planes. This is particularly useful for studying the quality of graphene crystals and identifying different crystalline phases [25].

Energy-dispersive X-ray spectroscopy (EDS) and electron energy loss spectroscopy (EELS) can be performed within a TEM to analyze the elemental composition and chemical state of the atoms in graphene. EELS, in particular, is sensitive to light elements like carbon and can provide detailed information about the electronic structure and bonding environment in graphene [25].

1.5.2.4.3 Other techniques for graphene characterization

In addition to Transmission Electron Microscopy (TEM) and Raman spectroscopy, several other characterization techniques are essential for analyzing the properties and quality of graphene. Scanning Electron Microscopy (SEM) is widely used to study the surface morphology of graphene, providing images that reveal features such as wrinkles, folds, and overall domain structures. Atomic Force Microscopy (AFM) offers high-resolution topographical mapping and can determine the number of graphene layers, assess surface roughness, and identify mechanical properties at the nanoscale. Scanning Tunneling Microscopy (STM) provides atomic-level imaging and insights into the electronic properties by mapping the local density of states [25], [32].

Fourier Transform Infrared Spectroscopy (FTIR) is used to identify chemical bonding and functional groups in graphene, particularly useful for characterizing graphene oxide and reduced graphene oxide. X-ray Photoelectron Spectroscopy (XPS) analyzes the elemental composition and chemical state of graphene, providing information about the types and amounts of functional groups present. Thermogravimetric Analysis (TGA) measures the thermal stability and composition of graphene materials by monitoring weight changes as a function of temperature, which

helps in understanding the decomposition and oxidation behaviors [25], [32].

1.5.3 Copper – Graphene composites

Copper, with its distinguished status as an exceptional conductor of electricity and heat, stands as a material of choice for numerous industrial applications. However, its inherent mechanical properties—particularly its strength—leave much to be desired when juxtaposed against the rigorous demands of modern engineering applications. The quest to fortify copper's mechanical strength through conventional strategies such as deformation strengthening, fine grain enhancement, or alloying invariably encounters a significant trade-off: a discernible diminution in its electrical conductivity. This inherent dichotomy between enhancing mechanical strength and preserving electrical conductivity presents a substantial challenge.

Conversely, graphene emerges as a material of profound interest, boasting an array of remarkable properties including unparalleled mechanical strength, exceptional electrical conductivity, and superior thermal conductivity. Despite these attributes, the direct utilization of graphene within composite materials encounters formidable challenges, primarily due to its synthesis, integration, and the maintenance of its intrinsic properties when interfaced with metals such as copper.

The past two decades have marked a period of intense research and development, initially focusing on the creation of copper and CNTs composites. These endeavors laid the groundwork for the subsequent exploration into copper-graphene composites, propelled by the aspiration to merge the electrical and thermal conductivity of copper with the mechanical robustness and electrical properties of graphene. However, the journey towards achieving a harmonious copper-graphene composite is fraught with complexities. A primary obstacle arises from carbon's insolubility in copper, which predisposes the composite to issues of carbon agglomeration if the fabrication process is not optimized. While this insolubility facilitates the deposition of graphene on copper substrates for CVD, it poses a considerable challenge in achieving a homogeneous distribution of graphene within a copper matrix—a prerequisite for an effective composite.

Achieving a uniformly dispersed carbon species within the copper matrix necessitates a deep understanding of the interfacial interactions and compatibility between copper and graphene. This understanding begins with a retrospective look at the foundational studies involving CNTs, which served as a precursor to the current explorations into copper-graphene composites. The insights gleaned from these initial studies provide a valuable context for navigating the complexities of graphene integration.

This discourse will proceed to delineate the various methodologies employed in the synthesis of copper-graphene composites, highlighting the innovative approaches and technological advancements that have emerged. These processes, ranging from powder metallurgy – which includes powder processing through physical mixing, electroless deposition, molecular level mixing and in situ graphene growth from gaseous or solid carbon feedstock – to electrochemical deposition each present unique challenges and opportunities in the quest to embed graphene within a copper matrix effectively.

Subsequent sections will dig into the specific enhancements in mechanical properties achieved through the introduction of graphene into copper. This analysis will explore how graphene's tensile strength and elasticity contribute to the overall fortification of the composite, potentially mitigating the trade-offs associated with traditional copper strengthening techniques.

Finally, the discourse will address the advancements in electrical properties conferred by graphene incorporation. Despite the challenges posed by carbon's insolubility, the integration of graphene promises not only to maintain but potentially to enhance the electrical conductivity of copper, thereby realizing the potential for high-performance copper-graphene composites.

1.5.3.1 CNTs reinforced copper composites

This section will just enumerate what was done in the literature for the fabrication of CNTs – copper composites since it is not the core subject of the thesis but rather a retrospective look. Since the techniques used for CNTs – copper composites are the same than graphite nanoplatelets copper (GNPs) composites the different methods will be detailed in the dedicated sections.

When examining the scientific literature, two predominant methodologies have been identified for the synthesis of CNTs reinforced copper matrix composites: firstly, the processing of CNTs-copper powder mixtures through ball milling, electroless deposition, ultrasonication, molecular level mixing [33], [33], [34], [35], [36], [37], [38], [39], [40], [41], [42], [43], [44], [45], [46], [47], [48], [49], [50], [51], [52], [53], [54], [55], [56], [57], [58], [59], which typically involves subsequent sintering procedures, and secondly, the electrodeposition technique [60], [61], [62], [63], [64], [65], [66], [67], [68], [69], [70], [71], [72], [73], [74], [75], [76], [77], [78], [79], [80], [81], [82]. The latter encompasses the deposition of copper ions from an electrolytic solution onto a cathode template composed of CNTs or the co-deposition of both CNTs and copper ions, with the constituents being dispersed within an electrolytic solution.

Upon the examination of the literature about CNTs – copper composite the technique that seems to show the best results in term of CNTs dispersion, mechanical strength and electrical conductivity is the fabrication through electrochemical deposition.

Subramaniam et al. [74] present an approach to fabricating CNTs–copper composites with significantly enhanced current-carrying capacity (ampacity) while maintaining high electrical conductivity. Vertically aligned single-walled CNTs forests were first densified using a liquid densification technique with copper ions. A two-stage electrodeposition process was then employed, involving initial nucleation of copper seeds on the CNTs surface in an organic solution followed by growth of the seeds in an aqueous solution to fill the mesopores. This method resulted in a homogeneous CNTs–Cu composite with a CNTs volume fraction of 45% and a density of 5.2 $g.cm^{-3}$. The composite exhibited a room temperature conductivity of 4.7×10^{5} $S.cm^{-1}$ (81% IACS), comparable to that of pure copper, and a temperature coefficient of resistivity an order of magnitude lower than copper. Remarkably, the CNTs–Cu composite demonstrated an ampacity of 6×10^{8} $A.cm^{-2}$, 100 times higher than that of copper, attributed to the suppression of surface and grain boundary diffusion pathways for copper atoms by the CNT network. Failure analysis revealed that the primary failure mechanism was copper electromigration, with an activation energy of 2.03 eV for copper diffusion in the composite, similar to that of bulk diffusion in copper.

1.5.3.2 GNP reinforced copper composites

The initial phase of investigations into graphene-reinforced copper matrix composites involved the utilization of graphite nanoplatelets. These nanoplatelets, characterized by their composition of 10 to 30 layers of graphene, were employed as a primary material for the fabrication of the composites. The methodologies applied in the development of these composites are analogous to those utilized in the production of CNTs copper composites. These methodologies encompass a range of techniques including powder processing through ball milling, electroless deposition, and molecular level mixing, as well as electrochemical deposition [83], [84], [85], [86], [87], [88], [89], [90], [91], [92], [93], [94], [95], [96], [97], [98], [99], [100], [101], [102], [103], [104], [105], [106], [107], [108], [109], [110], [111], [112], [113], [114], [115], [116], [117], [118], [119], [120], [121], [122], [123], [124], [125], [126]. Those approaches helped the integration of graphene into the copper matrix, aiming to enhance the composite's mechanical and electrical properties.

1.5.3.2.1 Ball milling

Ball milling is a mechanical processing technique used extensively across the industry, including in the fabrication of composites in powder state for bulk applications [83], [84], [85], [86], [87], [88], [89], [90], [91], [92], [93]. The process involves placing balls and particles within a container and then rotating it. The powder is usually placed into a shaker mill, planetary mill or attritor and grinded with steel balls. This method is praised for its simplicity and low operational cost. In the context of manufacturing Cu-GNP composites, ball milling plays a role in dispersing GNPs over a copper base, aiding in the incorporation of GNPs into the matrix material. The action of ball milling helps to disperse the GNPs within the copper matrix and facilitates the deformation of copper particles into flaky shapes, which is beneficial for achieving a well-distributed composite material.

Varol et al. [87] investigated the effects of GNPs content on the properties of copper matrix nanocomposites synthesized using flake powder metallurgy. Gas atomized copper powder and GNPs particles were ball milled for 5 hours to produce composite powders with varying GNPs weight percentages (0.5-5 wt%). The ball milling process transformed the spherical copper powder into a flakes, with GNPs particles embedded and dispersed within the copper flakes. Increasing GNPs content led to a decrease in the average particle size of the composite powders, attributed to the reduced plastic deformation caused by the presence of GNPs. The green density of the composites decreased with increasing GNPs content, with the 0.5 wt% GNPs composite exhibiting the highest green density of 8.08 g/cm^3 (90.7% relative to pure copper). Sintering at 950°C for 2 hours under an argon atmosphere resulted in increased density for all composites, with the 0.5 wt% GNPs composite again showing the highest sintered density of 8.74 g/cm^3 (98.1% relative to pure copper). The electrical conductivity of both green and sintered composites decreased with increasing GNPs content, attributed to increased porosity and agglomeration of GNPs particles

hindering the formation of conductive paths. The 0.5 wt% GNPs composite displayed the highest conductivity of 78.5% IACS. Similarly, the hardness of the composites decreased with increasing GNPs content due to the soft nature of GNPs and the presence of agglomerates.

1.5.3.2.2 Electroless deposition

Electroless deposition between GNPs and copper is a process designed to enhance bonding between the GNPs and the copper matrix [94], [95], [96], [97], [98], [99], [100], [101], [102], [103], [104], [105], [106]. This process involves the chemical deposition of copper on the surface of GNPs without the need for an external electrical power source. The key to this method is achieving a uniform coating of copper on the GNPs, which can significantly improve the interfacial compatibility between the GNPs and the copper matrix. This compatibility is crucial for the effective transfer of load and stress from the copper matrix to the GNPs, leading to composites with enhanced tensile strength compared to pure copper. The technique has been explored in several studies, where GNPs are first treated with copper and nickel plating to improve their wettability with the copper matrix, followed by mixing and sintering to create the composite material.

Tang et al. [103] reported a method for enhancing the mechanical properties of copper matrix composites using GNPs decorated with nickel nanoparticles (Ni NPs) as reinforcement. GNPs–Ni hybrids were synthesized via in situ chemical reduction of graphene oxide (GO) and nickel ions, resulting in a homogeneous distribution of Ni NPs with an average size of 8 nm on the GNP surface. These hybrids were then incorporated into a copper matrix at 0.5 vol% and 1.0 vol% GNP concentrations and consolidated using spark plasma sintering. The resulting GNS–Ni/Cu composites exhibited a remarkable improvement in mechanical properties, with the 1.0 vol% GNP composite demonstrating a 61% increase in Young's modulus (132 GPa) and a 94% increase in yield strength (268 MPa) compared to pure copper. The enhanced mechanical performance is attributed to the synergistic effects of the GNP–Ni hybrids, including the improved dispersion of GNPs in the copper matrix due to the presence of Ni NPs acting as spacers, and the strengthened GNP–Cu interfacial bonding facilitated by the formation of a Cu–Ni solid solution. The experimental results were consistent with a modified shear-lag model, indicating the presence of an efficient load transfer mechanism. Furthermore, the strengthening efficiency of GNP–Ni hybrids was found to be significantly higher than that of bare GNPs, CNTs, and other traditional reinforcements.

1.5.3.2.3 Molecular level mixing

Molecular level mixing (MLM) between graphene nanoplatelets (GNP) and copper involves a process where GNPs are integrated into the copper matrix at a very fine, molecular scale, which ensures a homogeneous distribution and strong interfacial bonding. This technique often includes precoating GNPs with copper nanoparticles to

prevent their aggregation, which enhances their dispersion within the copper matrix [107], [108], [109], [110], [111], [112], [113], [114], [115].

Chen et al. [110] investigated the impact of GNPs on the microstructure and properties of copper matrix composites fabricated using a molecular-level mixing process and SPS. GNPs were initially dispersed in an alcoholic solution of copper nitrate and then co-precipitated with copper oxide (Cu_2O) using glucose as a reducing agent. The resulting Cu_2O/GNPs composite powder was subsequently reduced in a hydrogen atmosphere to obtain Cu/GNPs composite powders with varying graphene contents (0.2-4.0 vol%). SPS consolidation at 700°C and 50 MPa yielded bulk Cu/GNPs composites with a relative density exceeding 98%. Microstructural analysis revealed a homogeneous distribution of GNPs within the copper matrix for composites with low graphene content (≤ 0.8 vol%), while higher graphene content led to the alignment of GNPs perpendicular to the SPS consolidation force. The addition of GNPs resulted in significant strengthening of the copper matrix, with the 0.6 vol% GNP composite exhibiting the highest yield strength of 310 MPa, a 118% increase compared to pure copper. However, further increasing the GNP content led to a decrease in strength due to the transition from plastic to brittle fracture behavior. Thermal diffusivity decreased with increasing GNP content, attributed to reduced heat carrier mean-free path and increased interfacial thermal resistance. Electrical conductivity also decreased slightly with increasing GNP content but remained above 85% of the reference copper value even at 4.0 vol% GNPs. Tribological tests demonstrated a significant improvement in wear resistance and friction reduction with increasing GNP content, with the 4.0 vol% GNP composite exhibiting a 60% reduction in the coefficient of friction compared to pure copper.

1.5.3.2.4 Electrochemical deposition

Electrochemical deposition between GNPs and copper involves creating a composite material that combines copper with graphene or GNPs through an electrodeposition process [116], [117], [118], [119], [120], [121], [122], [123], [124], [125], [126]. This technique uses a composite electrolyte consisting of graphene or GNPs, sulfuric acid, and copper sulfate. The GNPs, are dispersed in the electrolyte. The electrodeposition is performed using both pulse power and DC power supplies, where a copper foil acts as the cathode and a pure copper sheet serves as the anode. This process allows for the effective incorporation of GNPs into the copper matrix, producing a composite material with enhanced properties.

Pavithra et al. [122] present an approach for synthesizing copper-graphene (Cu-Gr) nanocomposite foils using pulse reverse electrodeposition (PRED). Electrochemically exfoliated graphene oxide (GO) nanosheets, consisting of 1-5 layers and with diameters ranging from 500 nm to 1 µm, were dispersed in a copper sulfate electrolyte at a concentration of 0.5 g/L. PRED was employed to co-deposit copper and GO onto a titanium substrate, with optimized pulse parameters leading to a uniform distribution of GO sheets throughout the copper matrix. The resulting Cu-Gr composite

foils exhibited a high hardness of approximately 2.5 GPa, roughly double that of pure copper, and an increased elastic modulus of around 137 GPa, approximately 1.2 times higher than that of pure copper. The enhanced mechanical properties are attributed to the fine grain size of the copper matrix, the presence of twins, and the reinforcing effect of the well-dispersed GO sheets, which act as barriers to dislocation motion and promote load transfer through covalent bonding with the copper matrix. Annealing of the Cu-Gr composite foils at 300°C resulted in minimal grain growth and no significant decrease in hardness or modulus, further demonstrating the effectiveness of GO as a reinforcement and grain growth inhibitor. The electrical resistivity of the as-deposited Cu-Gr composite foils was measured to be around 3.4×10^{-6} Ω.cm, slightly higher than that of pure copper, but decreased to 2.3×10^{-6} Ω cm upon annealing.

1.5.3.3 Graphene reinforced copper composites

In prior investigations, graphene (or GNPs)—whether in single or multiple layers—has been dispersed randomly and individually within a copper matrix. The production of composites through this fabrication process effectively enhanced the mechanical properties like yield strength or tensile strength but ductility is lowered and the GNPs tend to agglomerate. Moreover, the presence of nickel nanoparticles or defects induced by ball milling within these nanostructures may inevitably introduce defects into the final composites. Such defects could potentially decrease the electrical conductivity by scattering the electrons, thereby impairing the material's overall performance.

To benefit mostly their excellent properties, it could be better to construct 2D or 3D continuous network at macroscale level. "…to fully exert its outstanding in-plane properties of graphene for macroscopic applications, the advanced architecture design of the graphene composites at multiple length scales from the atomic to the macro level is of the first priority to be required…".

In this effort, researchers have investigated the layer-by-layer assembly or two-dimensional (2D) architecture [127], [128], [129], [130]. In this method, graphene is synthesized on copper substrates and subsequently layered to create a composite resembling a sandwich structure. This approach has been explored by various research groups and has culminated in the attainment of extraordinary electrical conductivity, reaching 117% IACS [128]. Computational simulations have corroborated these findings [127], demonstrating that the integration of graphene within metallic matrices can significantly enhance electrical conductivity.

Additionally, advancements have been made in the development of three-dimensional (3D) architectures [131], [132], [133], [134], [135], [136], [137], [138], [139]. A critical review of the literature reveals that in these structures, the material present at the grain boundaries is not graphene per se but rather sp^2-bonded amorphous carbon. Only two research groups successfully grown graphene on copper prior to the fabrication of the composite [136], [137]. This distinction is crucial as it sits at the grain boundaries, increasing or decreasing electron mobility. Moreover, it enhances carbon dispersion and augments the mechanical properties of the composite.

1.5.3.3.1 Copper graphene 2D

Cao et al. [128] focused on enhancing the electrical conductivity of copper by embedding graphene (Gr) through a process involving CVD and hot pressing. Graphene was deposited onto copper foils using a CVD process, where the foils were heated to 1000°C in a hydrogen/argon atmosphere, followed by the introduction of methane for graphene growth. Subsequently, multiple layers of these graphene-coated copper foils were stacked and hot pressed at 900°C and 50 MPa for 20 minutes to create bulk Gr/Cu composites. The study revealed that the electrical conductivity of the composites increased with a higher volume fraction of graphene, reaching a peak conductivity of 68.2×10^6 $S.m^{-1}$, equivalent to approximately 117.4% IACS, surpassing the conductivity of pure silver. This enhancement was attributed to a combination of graphene's intrinsic electrical properties and microstructural changes in the copper matrix induced by the CVD process, as evidenced by the strong Cu(111) orientation and grain coarsening observed in EBSD images. Further investigation using PF-AFM mapping revealed that the electrical conductivity of embedded graphene was significantly influenced by the lattice matching between graphene and the copper matrix, with Cu(111)/Gr/Cu(111) exhibiting the highest conductivity due to its superior lattice match. Additionally, first-principles calculations based on density functional theory suggested that the high electrical conductivity arose from a doping effect, leading to an increased carrier density of approximately 4.3×10^{14} cm^{-2} and a high carrier mobility of about 8×10^5 $cm^2\ V^{-1}\ s^{-1}$ in the embedded graphene.

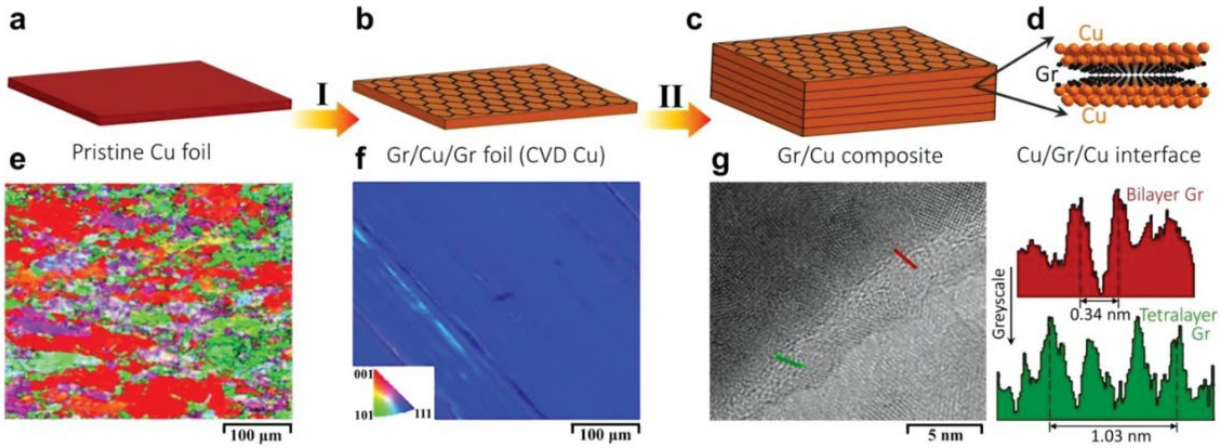

Figure 1.13. Fabrication of Gr/Cu composites with aligned CVD graphene. a–c) Stacking method for multilayered composites: I) Depositing graphene on both sides of pristine polycrystalline Cu foil via a CVD process; II) stacking i layers of Gr/Cu/Gr foils and hot pressing at 50 MPa and 900 °C. d) Schematic of the Cu/Gr-layers/Cu interface structure. e,f) EBSD images of the Cu foils before and after graphene deposition. g) TEM image of the Cu/Gr/Cu interface, showing mostly bilayer graphene as well as some trilayer or tetralayer graphene, as indicated by the grayscale section analyses of the two high-intensity peaks (red) and four high-intensity peaks (blue) separated by an expected interplanar spacing of 0.34 nm. [128]

Kim et al. [129] explored the strengthening effect of single-atomic-layer graphene in metal-graphene nanolayered composites, specifically focusing on copper and nickel matrices. Graphene was synthesized using CVD on copper foils, where the foils were exposed to methane and hydrogen gas at 1000°C, resulting in predominantly single-layer graphene with a Raman G/2D ratio of 1/2.15. These graphene layers were then transferred onto metal-deposited substrates via a PMMA support layer, creating alternating layers of metal and graphene with varying repeat layer spacings. The mechanical properties of the composites were evaluated using nanopillar compression testing, revealing significantly enhanced strengths compared to bulk single-crystal metals. For instance, copper-graphene composites with a 70 nm repeat layer spacing exhibited a flow stress at 5% plastic strain of 1.5 GPa, while nickel-graphene composites with a 100 nm repeat layer spacing demonstrated a flow stress of 4.0 GPa. These ultra-high strengths were attributed to the effective constraint of dislocation motion by the graphene layers, as confirmed by ex situ and in situ TEM analyses, which showed dislocation pile-up at the metal-graphene interfaces. Molecular dynamics simulations further corroborated these findings, indicating that the high intrinsic strength and bending stiffness of graphene prevented dislocations from penetrating the interface, leading to their confinement within the metal layers. The study also highlighted the potential influence of interfacial shear strength on the deformation behavior of metal-graphene multilayers, with density functional calculations suggesting higher interfacial shear strengths for Ni-graphene compared to Cu-graphene.

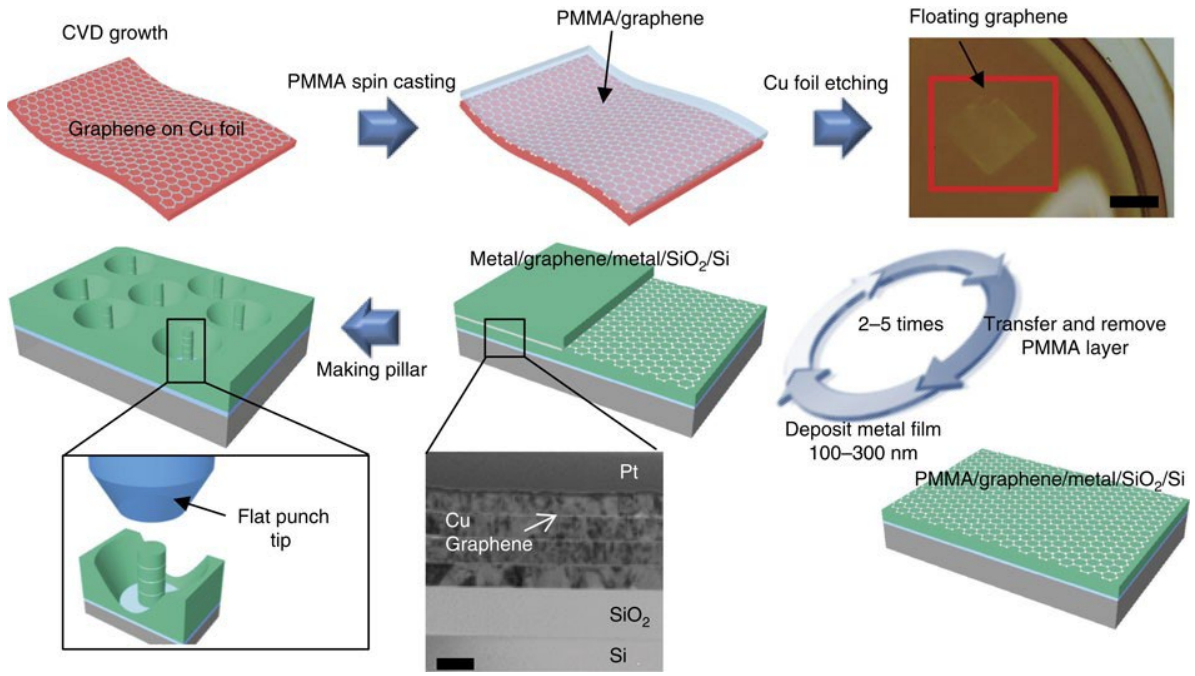

Figure 1.14. Graphene is first grown using CVD and transferred onto the evaporated metal thin film on an oxidized Si substrate. The PMMA layer is then removed, and the next metal thin film layer is evaporated. By repeating the metal deposition and graphene transfer processes, Cu–graphene nanolayered composites are synthesized with different repeated metal thicknesses of 70, 125 and 200 nm, and Ni–graphene

nanolayered composites are synthesized with repeated metal thicknesses of 100, 150 and 300 nm. The mechanical properties were studied by compression testing of nanopillars etched by FIB. The scale bar for the floating graphene is 10 mm and that for the TEM is 200 nm. [129]

Subedi et al. [127] employed density functional theory (DFT) calculations to investigate the electronic transport properties of copper-graphene (Cu-G) composites, focusing on the impact of interfacial distance between copper and graphene layers. A Cu/G/Cu interface model was constructed with a (111) copper surface and graphene positioned in a top-fcc configuration, where one sub-lattice site of graphene was placed above the first layer of copper and the other above the third layer. The electronic conductivity of the models was computed using the Kubo-Greenwood formula, revealing an increase in conductivity with decreasing Cu-G distance, reaching a saturation point below a threshold distance of approximately 2.23 Å. Bader charge analysis indicated an increasing charge transfer between interfacial copper atoms and graphene as the Cu-G distance decreased, suggesting enhanced interaction and potential for improved conductivity. Analysis of the electronic density of states showed that both copper and carbon atoms contributed to an increased density of states near the Fermi level with decreasing Cu-G distance, further supporting the observed conductivity enhancement. Space-projected conductivity calculations provided a spatial perspective on the conduction process, demonstrating that graphene formed a bridge for electronic conduction between copper atoms at the interfacial layers, particularly at short Cu-G distances. The study also explored the influence of varying Cu-Cu distances in an orthorhombic copper model, finding that conductivity increased with decreasing Cu-Cu distance up to a certain point, after which it declined due to increased disorder in the copper lattice.

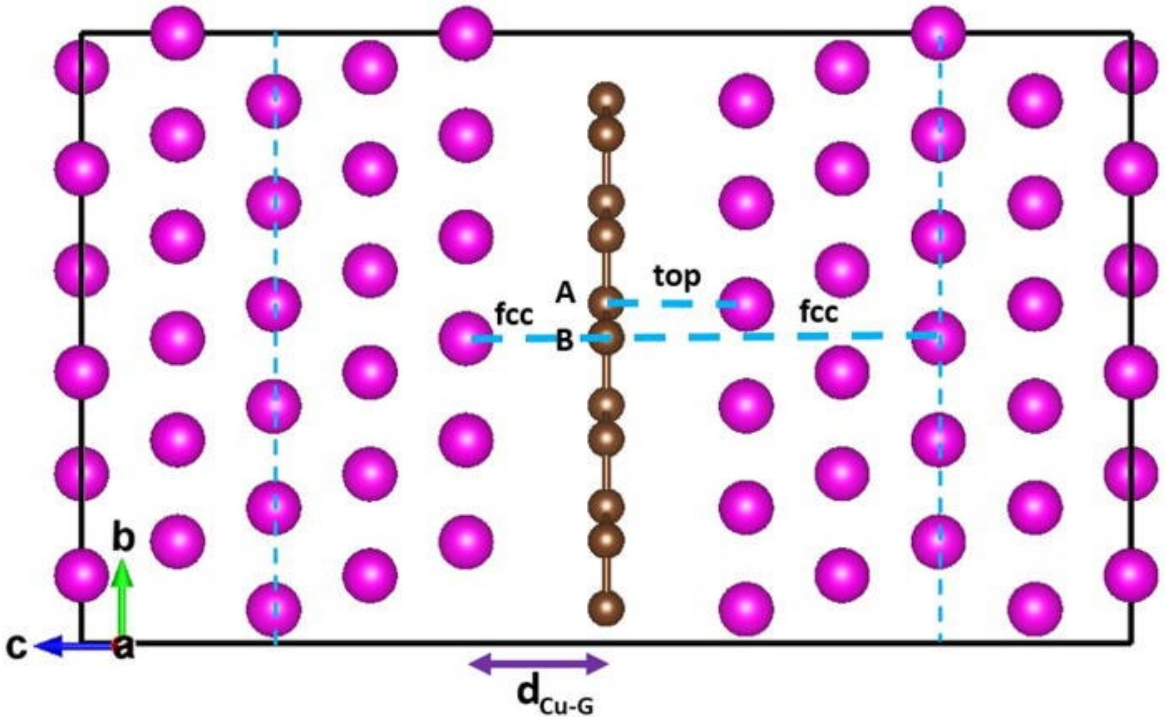

Figure 1.15. Geometry of the Cu/G/Cu model with d_{Cu-G} representing the Cu–G distance. Top–fcc configuration of graphene above the Cu 111 surface with A and B representing sub-lattice sites above the Cu atom at first and third layers, respectively. The pink and brown colored spheres represent Cu and C atoms, respectively. [127]

1.5.3.3.2 Copper graphene 3D

Li et al. [137] investigated a novel approach to fabricate copper-graphene composites with enhanced mechanical properties while maintaining high electrical conductivity. The processing route involved the in-situ growth of 3-5 layers of high-quality graphene on the surface of copper wires using CVD at 1020°C with a controlled gas environment. Subsequent steps included hot extrusion and cold drawing to refine the microstructure and induce texture. The presence of graphene during CVD led to abnormal grain coarsening due to its thermal conductivity anisotropy, limiting heat dissipation and extending grain growth time. However, the subsequent severe plastic deformation processes effectively refined the grains, with the composite wire achieving an average grain size of 8.55 μm. The tensile strength of the composite wire reached 595 MPa, representing a 23.4% increase compared to the original copper wire (482 MPa), while maintaining a comparable electrical conductivity of 5.46×10^7 S/m (98% of the original copper wire). This enhancement was attributed to the uniform dispersion of graphene fragments within the copper matrix, acting as obstacles to dislocation movement and grain boundary sliding, along with the formation of a conductive graphene network that mitigated the negative impact of grain refinement on electrical conductivity.

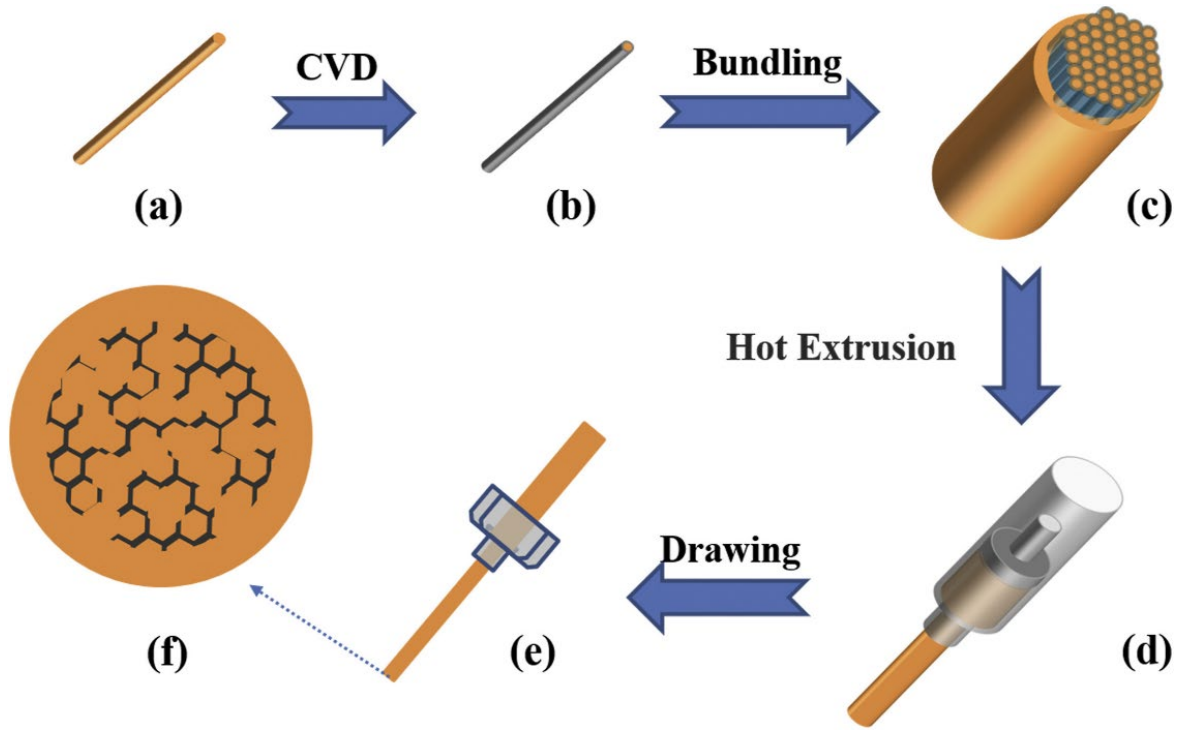

Figure 1.16. Schematic fabrication process of graphene/copper composites. (a) copper wires. (b) graphene coated copper wires. (c) blank prepared for hot extrusion. (d) rod prepared by hot extrusion. (e) wires prepared by following cold drawing. (f) the structure of the material on the cross section. [137]

Li et al. [136] employed chemical vapor deposition (CVD) to synthesize few-layer graphene (1-5 layers) directly onto the surface of liquid copper powder, capitalizing on the enhanced growth dynamics of graphene on molten copper substrates. This approach facilitated uniform graphene coverage, addressing dispersion challenges often encountered in graphene-copper composites. Subsequent processing involved vacuum hot pressing to consolidate the powder, followed by hot extrusion and cold drawing to refine the microstructure and induce texture. Notably, the presence of graphene during vacuum hot pressing inhibited grain growth, resulting in a finer grain structure compared to pure copper. The composite block exhibited a tensile strength of 176.4 MPa and an electrical conductivity of 52.0 MS/m. Hot extrusion further refined the grains through recrystallization while causing partial agglomeration of graphene. However, the composite rod's mechanical properties improved significantly, with a tensile strength of 239.4 MPa and conductivity reaching 58.3 MS/m. The final cold drawing process aligned both copper grains and graphene along the drawing direction, leading to a remarkable tensile strength of 573.3 MPa and conductivity of 57.9 MS/m in the 1mm diameter wire.

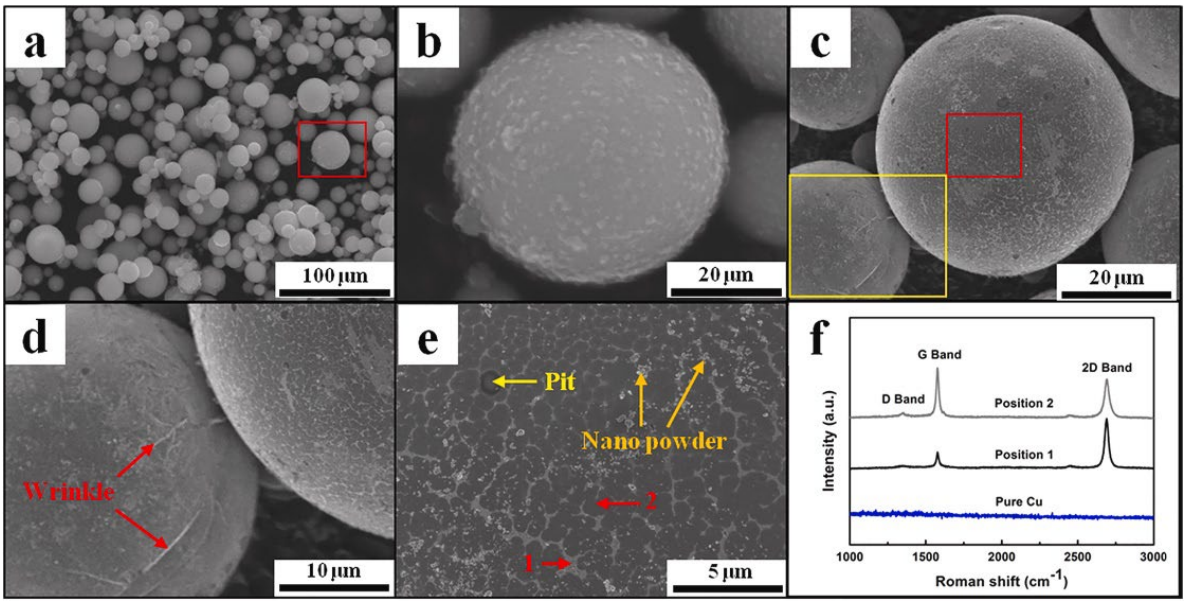

Figure 1.17. (a–b) The SEM image and high magnification image of the pure copper powder, (c–e) High magnification image of graphene coated copper powder, (f) Roman spectra of the original copper powder and the graphene in e. [136]

Zhang et al. *[138]* introduced a powder-metallurgy-based approach to fabricate three-dimensional graphene-like network/copper (3D-GLNN/Cu) composites, leveraging thermal-stress-induced welding for improved mechanical and functional properties. Graphene-like nanosheets (GLNs) were grown on copper powder surfaces using an ambient-pressure rapid thermal annealing (RTA) process at 800°C with sucrose as the carbon source. The GLNs/Cu composite powders were then hot-pressed at 800°C and 50 MPa, during which the GLNs were welded together due to the

coefficient of thermal expansion (CTE) mismatch between GLNs and copper, forming a continuous 3D network. The resulting 3D-GLNN/Cu composites exhibited exceptional mechanical performance, with a yield strength of 292 ± 21 MPa, ultimate tensile strength of 319 ± 30 MPa, and fracture elongation of 25.4 ± 5.6%, surpassing both pure copper and reduced graphene oxide (RGO)/Cu composites. This enhancement was attributed to the 3D network architecture, which promoted grain refinement, dislocation pinning, and enhanced load transfer due to a significantly higher interfacial shear stress compared to 2D graphene/Cu. The composites also demonstrated superior thermal conductivity, reaching 413 W $m^{-1}.K^{-1}$ at room temperature, exceeding that of pure copper. This improvement was attributed to the interconnected copper matrix and the additional thermal transport channels provided by the 3D-GLNN, which effectively reduced electron and phonon scattering. Furthermore, the composites exhibited an electrical conductivity of 60.0±0.5 MS m^{-1}, exceeding the IACS standard by 3.4%, indicating the formation of efficient electron pathways.

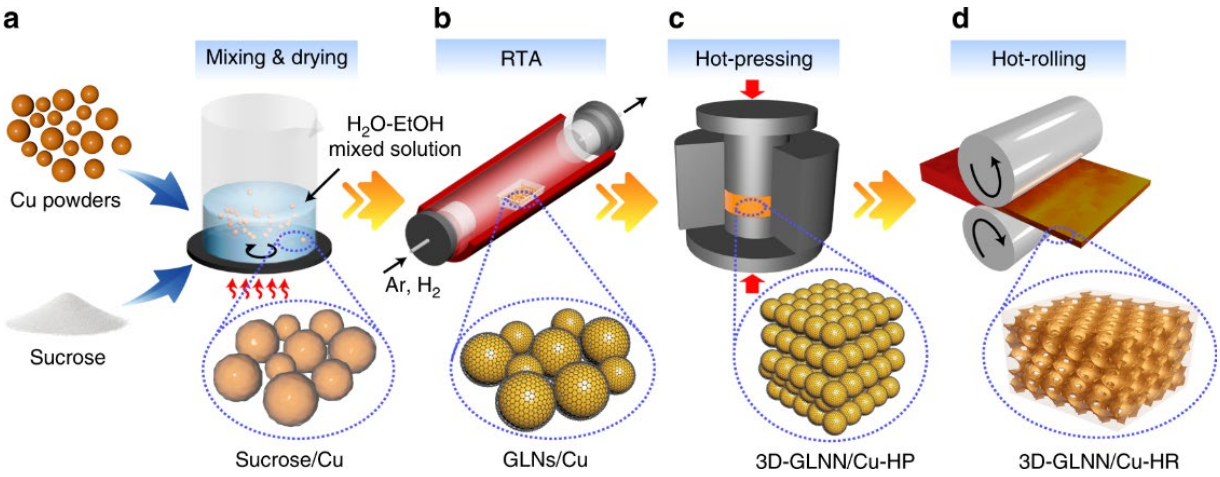

Figure 1.18. ***a*** *The Cu powders were first coated with sucrose as a hybrid precursor.* ***b*** *The hybrid precursor was then subjected to RTA process for growing GLNs.* ***c*** *The GLNs were interconnected into a continuous network structure in the Cu matrix by using hot-pressing.* ***d*** *The fully-densified 3D-GLNN/Cu bulk composites were fabricated by hot-rolling. [138]*

1.5.4 Conclusions

This review was dedicated to enhancing the understanding of copper's fundamental characteristics, its production processes, refinement techniques, and methods for its reinforcement. It has been observed that the electrical conductivity of copper correlates positively with its purity. This enhanced conductivity is attributable to the half-filled 4s orbital, which facilitates electron flow under an electric field. Even minimal impurities can significantly impact electrical conductivity by introducing defects into the copper lattice.

Furthermore, methods employed to augment the mechanical properties of copper frequently result in the introduction of lattice defects, which, in turn, lead to electron scattering. Consequently, this scattering diminishes the material's electrical conductivity. In response to this challenge, contemporary research has focused on integrating carbon-based reinforcements, such as graphene and CNTs, into copper matrices. The objective of this integration is to synergistically enhance both the mechanical and electrical properties of copper, leveraging the unique advantages of carbon's structural and conductive properties.

This dual approach aims to reconcile the trade-offs between electrical and mechanical enhancements by exploring innovative composite materials that harness the complementary characteristics of both copper and carbon-based reinforcements.

In the evolutionary trajectory of carbon-reinforced copper matrix composites, the initial materials developed were CNTs-reinforced copper composites. These were fabricated through methods such as powder processing and sintering, alongside electrochemical deposition, with the latter method exhibiting superior outcomes. Subsequently, the advent of graphene prompted the application of similar techniques utilizing GNPs for the production of composites. These composites demonstrated enhancements in mechanical properties; however, they exhibited a decline in electrical properties.

The exploration then expanded to include both two-dimensional and three-dimensional architectures. The investigations into 2D architecture revealed potential for improving electrical conductivity, while studies into 3D architecture demonstrated the feasibility of in situ growth of graphene on copper particles prior to sintering. It is important to note that most publications report the presence of sp^2-bonded amorphous carbon rather than crystalline graphene in these structures.

There is a pressing need for further research aimed at synthesizing the benefits observed in electrical conductivity from 2D architectures with the mechanical enhancements derived from 3D architectures. Specifically, future studies should focus on the cultivation of monolayer graphene directly on copper particles to optimize the synergistic properties of these composites. This approach necessitates a refined understanding of the interaction between graphene and copper at the molecular level to achieve a balance between electrical and mechanical performance enhancements.

CHAPTER 2 – FABRICATION OF THE CARBON COATED COPPER PARTICLES

2.1 INTRODUCTION

In this Chapter 2, the objective is to synthesize graphene-coated copper particles using sucrose as a solid carbon source for subsequent densification via SPS.

This chapter details two primary methodologies. The first approach involves directly coating the raw copper powder, which possesses an inherent copper oxide layer, followed by graphitization. The second approach entails an initial reduction of the oxide layer, followed by the coating of the reduced copper particles and subsequent graphitization. One of the main difficulties is to avoid any premature sintering of the copper particles, otherwise the powder will lost its particular characteristics and the subsequent densified composite will be porous.

The characterization techniques utilized include SEM, TEM, Raman spectroscopy, TGA, and XRD, which provide insights into the morphological, structural, and compositional attributes of the carbon – coated copper particles.

The ensuing sections delineate a presentation of the results, commencing with an examination of the raw copper powder. This initial assessment encompasses an analysis of the powder's morphology, particle distribution, and chemical composition.

Subsequently, the focus shifts to the oxidative behavior of copper. This segment elucidates the conditions under which copper is oxidized, followed by an exploration of the reduction process of the copper oxide. This sequence is replicated using a finer grade of copper powder to discern the effects of particle size on the oxidation and reduction phenomena.

Given the employment of sucrose as a carbon precursor, an initial investigation is conducted on its thermal decomposition characteristics using Thermogravimetric Analysis (TGA). This preliminary analysis is imporant for understanding the thermal behavior and decomposition kinetics of sucrose under controlled conditions.

Following the characterization of the sucrose, the study proceeds with the coating of the raw copper powder with a 2.00wt% sucrose. This step aims to ensure that a sufficient amount of carbon is deposited onto the copper particles. The thermal behavior of the resulting copper-sucrose powder mixture is then analyzed at two distinct temperatures, 200°C and 300°C, under a reducing atmosphere comprising a flow of argon and hydrogen gases. This analysis helps in understanding the interaction between copper, sucrose and the copper oxides at reduction temperatures and under reducing environments.

The copper-sucrose powder, now coated, is subsequently subjected to a graphitization process at a temperature of 1000°C. This phase of the research is designed to elucidate the structural evolution of the carbon layer into graphene under high-temperature conditions.

The experimental narrative extends further to describe the graphitization

process of copper-sucrose powder, where, in a variant approach, the copper oxide is reduced prior to the graphitization step. This alteration in the procedural sequence serves to investigate the effects of pre-reduction of copper oxide on the efficiency and quality of the subsequent graphitization process.

With optimal flow rates and gas proportions established, the investigation delves into the modulation of the sucrose content at 0.65wt%, reducing it below the initial 2.00wt% threshold. The objective here is to ascertain the minimum quantity of sucrose requisite for effective carbon coating while mitigating premature sintering of the copper particles. The influence of varying time durations and gas mixtures on the graphitization outcome is then examined, aiming to delineate the parameters that most significantly impact the structural integrity and quality of the carbon layer.

2.2 MATERIALS AND EQUIPMENT

The materials employed in this study were obtained to ensure high purity and uniformity in order to maintain consistency and reliability in experimental results. Copper micro-powders, with an average particle size ranging from 3.25 µm to 4.75 µm and a purity of 99.9%, were procured from Alfa Aesar. Another powder, with an average particle size ranging from 0.50 µm to 1.50 µm and a purity of 99%, from the same supplier was purchased for the purpose of comparison. Similarly, sucrose ($C_{12}H_{22}O_{11}$) of 99.9% purity was also obtained from Alfa Aesar, ensuring that reagents of high purity were utilized throughout the experimental procedures. Alumina boats, possessing a volume of 24.5 mL, were acquired from Almath Crucibles to facilitate the sample heating processes.

Raman spectroscopic analysis was executed utilizing a Labram system from Horiba, equipped with a laser spot size of 1.5 µm and employing an excitation wavelength of 532 nm. TEM observations were conducted with the advanced TITAN microscope from FEI, facilitating high-resolution imaging at the atomic level. Additionally, SEM observations were performed utilizing both the Leo 1550 with the Gemini column from Zeiss and the Helios 660 from FEI.

Thermoanalytical measurements, specifically Thermogravimetric Analysis (TGA) and Differential Scanning Calorimetry (DSC), were performed using the NETZSCH STA 443 F3. Particle size distributions were determined employing laser granulometry, facilitated by the Malvern Mastersizer 3000, which is equipped with both red (632.8 nm) and blue (470 nm) lasers.

Sonication processes were executed utilizing the VCX500 ultrasonic processor from Sonics, operating at 225W. Sieving operations employed sieves with mesh sizes of 20, 40, 80, and 100 µm, sourced from Linker Industrietechnik, to achieve particle size segregation.

The processes of carbonization and graphitization were carried out in a controlled chemical vapor deposition (CVD)-like setup, incorporating a quartz tube of 1200 mm in length and 45 mm in inner diameter, to ensure uniform thermal treatment of samples under controlled atmospheric conditions.

The bottle used for the CVD were provided by AirLiquide under the name ALPHAGAZ 1 with purity levels of 99,999 %. The concentrations of impuirities are $H_2O \leq 3$ ppm, $O_2 \leq 2$ ppm, $C_nH_m \leq 0.5$ ppm.

2.3 METHODS

The synthesis of copper/carbon powders was undertaken utilizing two distinct procedural approaches, each designed to assess the influence of preparatory conditions on the material characteristics.

In the first approach, raw copper powders were initially coated with a sucrose solution, followed by a drying phase conducted at 80°C in ambient air to remove moisture content. Subsequently, the dried powders were subjected to a grinding process to ensure uniformity and enhance surface area for subsequent reactions. The final stage in this approach involved the graphitization of the sucrose-coated copper powders, executed at a temperature of 1000°C to induce the formation of carbon structures from the decomposed sucrose.

Conversely, the second approach incorporated an initial treatment step wherein the copper powders were thermally treated at 200°C under a controlled atmosphere composed of argon and hydrogen. The primary aim of this initial heating phase was to reduce the oxide layers present on the surfaces of the copper particles, thereby enhancing the copper's reactivity and surface properties for subsequent graphitization. Following this reduction process, the powders were then coated with sucrose, dried at 100°C, but distinctly under an argon atmosphere to prevent oxidation and maintain the reduced state of the copper. The subsequent steps of grinding and graphitization at 1000°C were then performed analogously to the first method.

These delineated processing routes were executed to enable a comparative analysis of the effects of initial surface conditions and atmospheric controls on the final copper/carbon composite characteristics. The following sections will elaborate in detail on the methodologies, experimental setups, and analytical techniques employed throughout these distinct synthesis routes, providing a foundation for subsequent discussions on material properties, structural analyses, and potential applications

2.3.1 Raw copper powder coating and carbonization

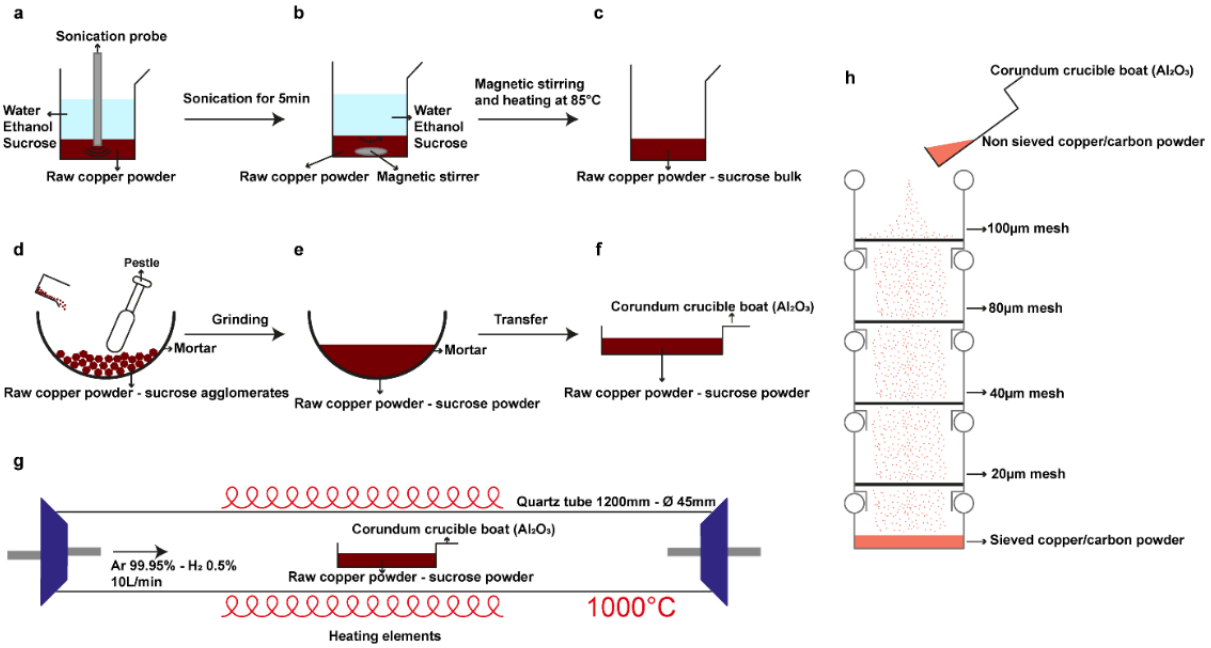

Figure 2.1 – Schematics of the processing of the sucrose coated raw copper particles

The raw copper powder is weighed along with sucrose to achieve a predetermined sucrose to copper ratio. This quantification is followed by a dry mixing process to guarantee an even distribution of sucrose crystals in the cooper powder.

Following the preparation of the dry mixture, the copper-sucrose blend is then dissolved in a 1:1 volumetric mixture of water and ethanol. The incorporation of ethanol is deliberate, exploiting its enhanced dispersing capabilities to achieve a more homogeneous mixture and better particle dispersion compared to water alone. This solution is then subjected to ultrasonic dispersion for five minutes using a sonication probe.

Post-sonication, the suspension is heated to 80°C under continuous magnetic stirring. This heating and stirring step is crucial for facilitating the gradual evaporation of the solvent, ensuring that the sucrose is uniformly deposited onto the copper particles as the solvent dissipates. The magnetic stirring is maintained until the complete evaporation of the liquid phase, after which the stirring is ceased but the powder is kept under heat to ensure full solvent removal and to achieve a dry powder.

The dried copper-sucrose powder is then manually reduced to a finer consistency using a mortar. This manual milling serves not only to break down any residual agglomerates but also to enhance the surface area for the subsequent carbonization process. The finely milled powder is subsequently placed in an alumina crucible and set in the central region of a quartz tube, which is then inserted into a tubular furnace.

A preparatory purge with argon gas at a flow rate of 1.0 L/min is performed for ten minutes to establish an inert atmosphere within the furnace, essential for

preventing any oxidation during the carbonization process. The temperature is then elevated and maintained at 600°C for a minimum duration of five minutes under an argon flow, facilitating the complete carbonization of the sucrose and ensuring a uniform carbon coating on the copper particles.

The final stage of the process is explained at the end of the methods section.

2.3.2 Copper (I) oxide and copper (II) oxide reduction

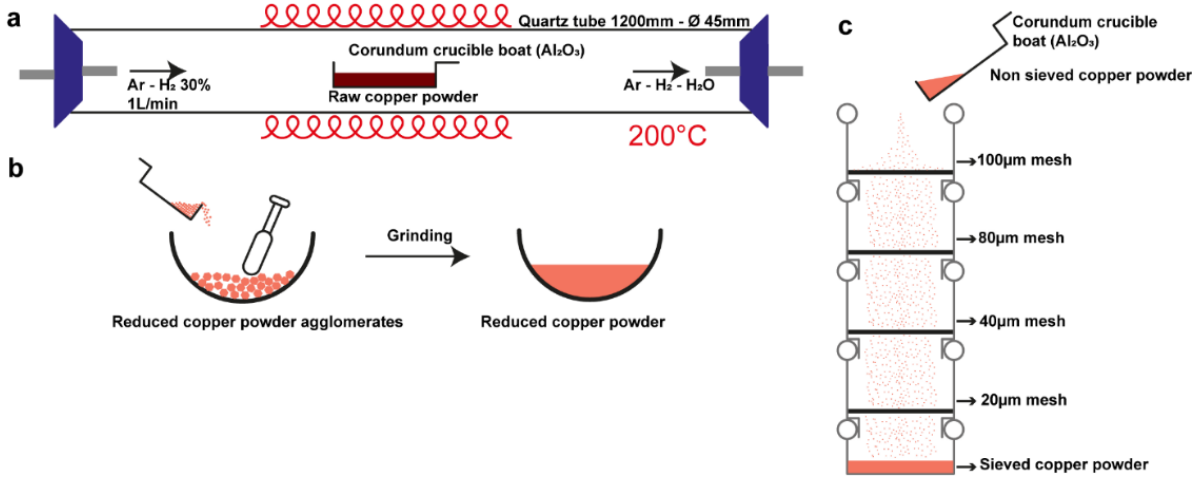

Figure 2.2. Schematics of the reduction process

Initially, the needed mass of raw copper powder is measured and placed within an alumina crucible boat. This crucible is then positioned centrally within a quartz tube, which in turn is inserted into the chamber of a tubular furnace, establishing a controlled environment for the reduction process.

To initiate the reduction procedure, a controlled atmosphere is established within the quartz tube by introducing a gas mixture consisting of argon (0.7 L/min) and hydrogen (0.3 L/min), achieving a total flow rate of 1.0 L/min. This gas mixture is injected into the system for a duration of ten minutes at ambient temperature (approximately 20°C), serving to purge any residual air from the tube. This step is imporant for preventing oxidation of the copper during the subsequent heating process and ensuring that the reduction reaction occurs under optimal conditions.

Following the purging phase, the furnace temperature is elevated to and maintained at 200°C for a period of thirty minutes.

Upon completion of the reduction phase, the furnace is allowed to cool to a manageable temperature under the same protective atmosphere to prevent re-oxidation of the copper. The reduced copper powder is then removed from the tube and subjected to mechanical grinding to break down any agglomerates formed during the reduction.

Finally, the grinded powder is subjected to a sieving process utilizing sieves of different mesh sizes. This sieving is employed to segregate the copper particles by size, removing any oversized aggregates and ensuring a homogeneous powder suitable for further experimental procedures.

2.3.3 Reduced copper powder coating and carbonization

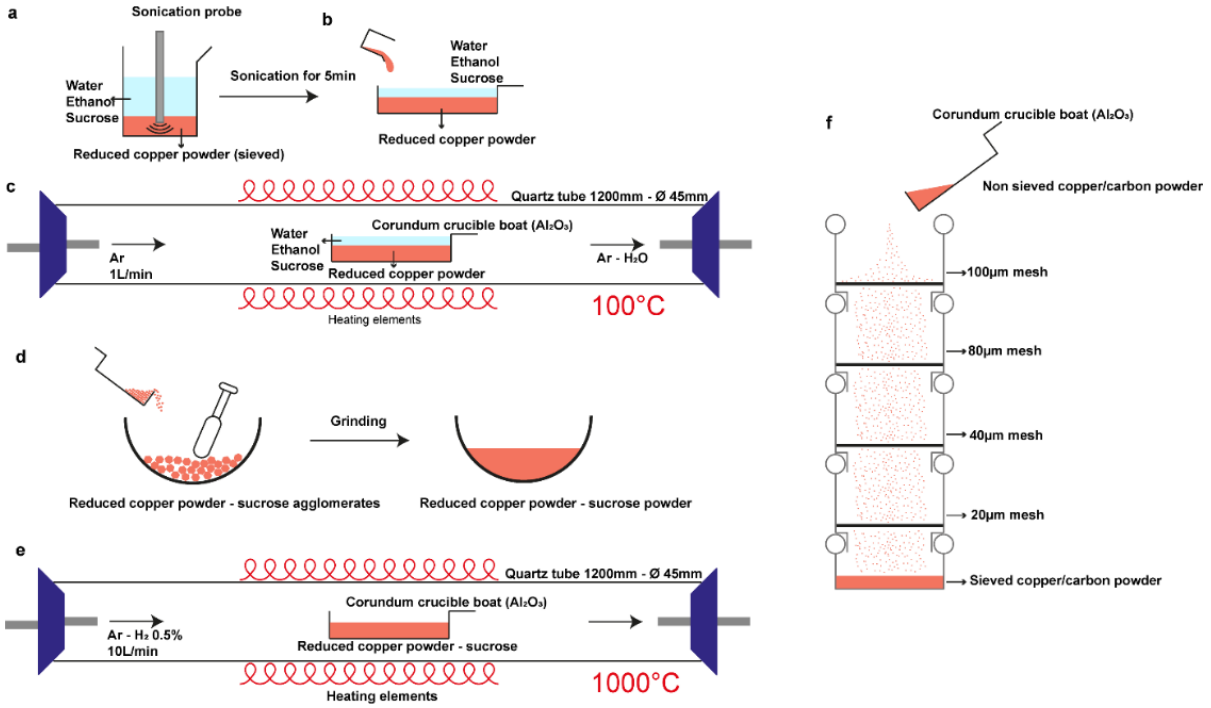

Figure 2.3. Schematics of the sucrose coated reduced copper powder

Sucrose is solubilized in a solvent comprising 10 mL of water and ethanol. Following this, the previously reduced copper powder is integrated with the sucrose solution.

Subsequently, this mixture of reduced copper and sucrose is transferred into an alumina crucible boat, which is then positioned within a quartz tube. This assembly is introduced into the tubular furnace for the drying process. Prior to heating, the furnace atmosphere is purged with an argon flow of 1.0 L/min for ten minutes to purge any residual air, thereby preventing any oxidation.

The temperature within the furnace is then maintained at 100°C to facilitate the complete drying of the reduced copper/sucrose mixture.

Once the drying phase is complete, the resultant material is then grined to produce a fine powder, enhancing the surface area for more effective carbonization. The finely ground powder is then returned to the alumina crucible boat and reintroduced into the quartz tube and furnace for subsequent thermal treatment.

The furnace is again purged with argon, this time at a flow rate of 0.95 L/min for ten minutes, to ensure the removal of air and maintain an inert atmosphere. The temperature is then elevated and stabilized at 600°C for five minutes.

Following carbonization, the gas atmosphere is modified by introducing hydrogen at a flow rate of 0.05 L/min, resulting in a final gas mixture of 5.0 vol.% hydrogen in argon, with a total flow rate maintained at 1.0 L/min. Here hydrogen is sent so that it can diffuse in the tube before the graphitization step.

The final stage of the protocol involves the graphitization of the carbon-coated

copper powder. The temperature is escalated and held constant at 1000°C for thirty minutes under a modified gas flow, where the argon flow rate is adjusted to 9.95 L/min and hydrogen to 0.05 L/min, achieving a total flow rate of 10 L/min with a 0.5 vol.% hydrogen concentration.

Upon the completion of the graphitization process, the copper/carbon powder is subjected to sieving, utilizing a series of sieves to segregate the powder by particle size. This final step is essential for removing any agglomerates formed during the process, thereby ensuring a uniform particle size distribution suitable for subsequent applications or investigations

Powders reduced at 200°C and 300°C will be named rCu200C and rCu300C. Raw copper powder coated with 2.00wt% sucrose and graphitized at 1000°C will be named Cu@2.00% and reduced copper powders coated with 2.00wt% and 0.65wt% will be named rCu200C@2.00% and rCu200C@0.65% respectively.

2.3.4 Temperature profile

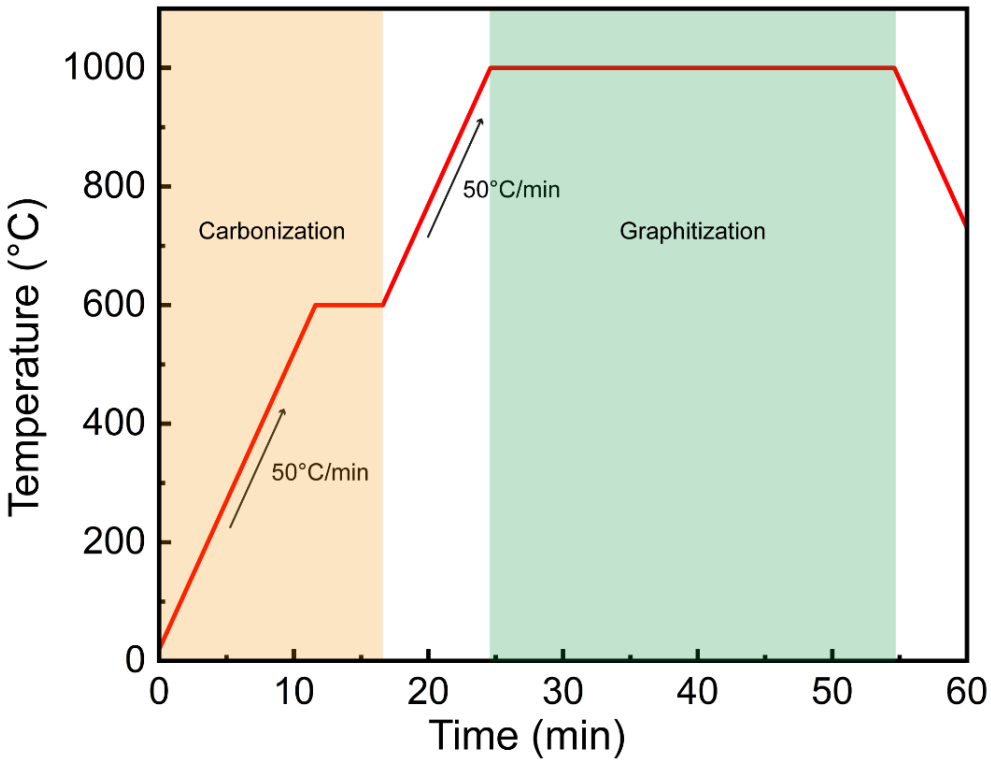

Figure 2.4. Schematics of the temperature program

Initially, the powder is subjected to a heating regime starting from ambient temperature, 20°C, elevating to 600°C. This temperature increase is managed at a heating rate of 50°C per minute. The carbonization stage, maintained for a duration of five to ten minutes at the target temperature of 600°C. Following the carbonization phase, the process transitions to the graphitization stage, necessitating a further

increase in temperature from 600°C to 1000°C. This temperature elevation is again conducted at a rate of 50°C per minute. The temperature is then held steady at 1000°C for a period of 30 minutes.

2.4 RESULTS AND DISCUSSIONS

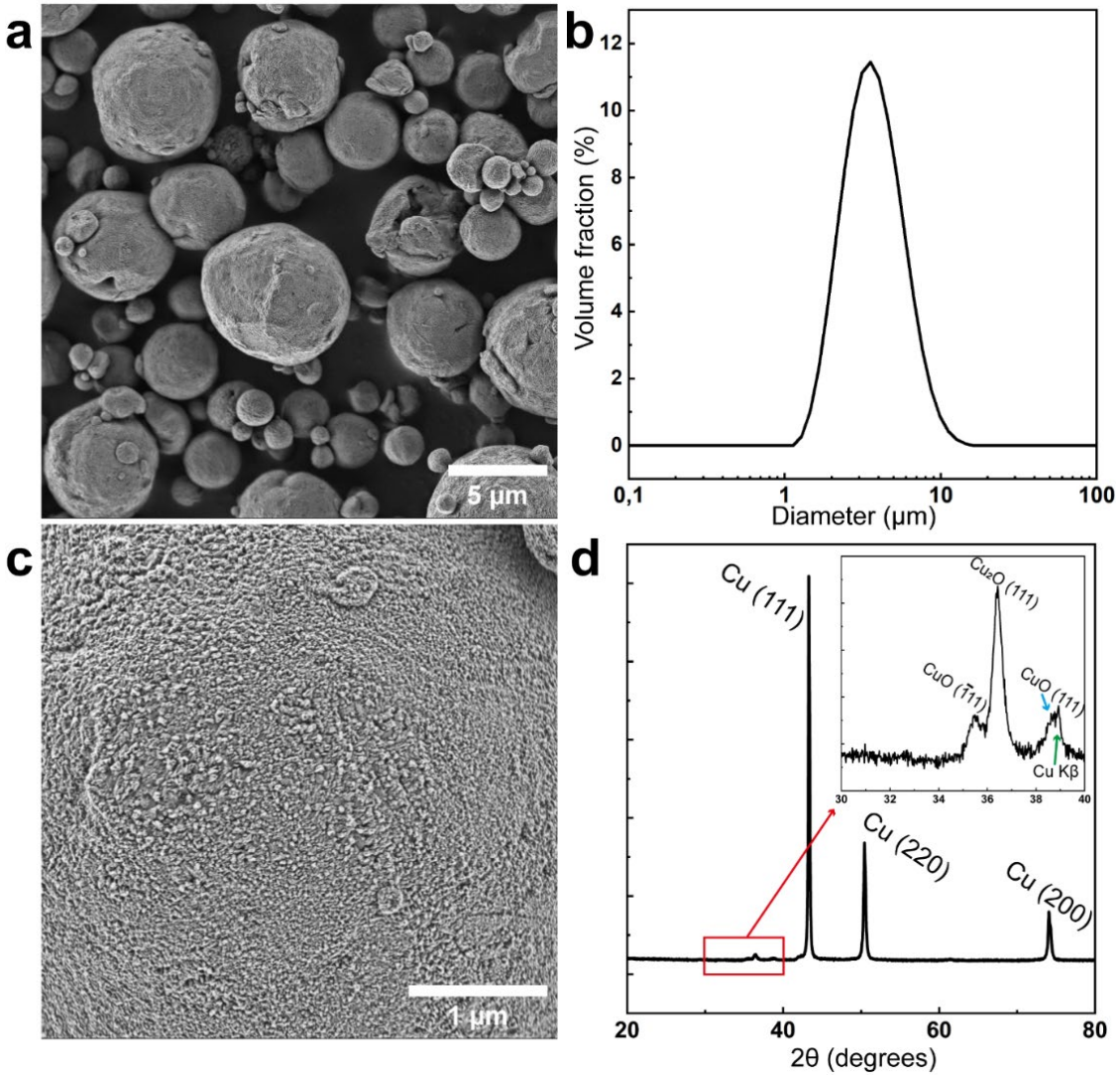

Figure 2.5 – characterization of the copper powder: ***a*** *SEM morphology,* ***b*** *laser granulometry,* ***c*** *SEM zoom on a copper particle showing the copper oxide and* ***d*** *XRD pattern of the copper powder showing copper, copper oxide (I) and (II)*

Figure 2.5 provides a basic morphological characterization of the commercial spherical copper micro-particles utilized in this study. Figure 2.5(a) depicts the micro-particles, which, according to the laser granulometry results shown in figure 2.5(b), has an average particle size distribution ranging from 3.25 µm to 4.75 µm. The Gaussian distribution curve illustrates a pronounced frequency peak around 3.50 µm, indicative of the median particle size, with 50% of the particle volume comprising particles with diameters up to 5 µm.

The selection of these commercial copper micro-powders was motivated by the aim to optimize the grain boundary interactions within the copper/graphene composite post-sintering. The size distribution was chosen to facilitate comprehensive electron microscopy investigations, thereby enabling detailed examination of the copper/graphene composite interfaces. Moreover, adhering to the Hall-Petch

relationship, the utilization of a particle size distribution centered around 5 µm is anticipated to enhance the material's strength due to the presence of finer grains. The non-monodispersed nature of the powder, encompassing a blend of smaller and larger particles, is predicted to contribute to achieving near-full density in the sintered composite.

As reported by the supplier, the copper powder has a purity level of 99.9%. However, an examination reveals that a fraction of the particles exists in oxidized forms, namely Copper (I) oxide and Copper (II) oxide, or Cu_2O and CuO respectively, as visually documented in figure 2.1(c) through SEM. This imagery elucidates alterations in the particles' surface due to the formation of nano-oxides crystals, giving a reddish-brown hue to the powder – a direct consequence of surface oxidation.

Figure 2.5(d) presents the XRD diffractogram of the raw copper powder. The spectrum features distinct peaks at 2θ angles of 36.5° and 38.9°, corresponding respectively to the crystalline phases of Cu_2O and CuO, alongside other peaks characteristic of copper's face-centered cubic (FCC) crystal structure. The oxide layers on these commercial microparticles predominantly consist of Cu_2O, formed under low-temperature aerobic conditions, and CuO, which arises under more elevated thermal conditions. It is important to note that the device used for XRD sends a beam of electrons onto a copper target with sufficient energy to interact with the K alpha and K beta layers of the target, and a nickel filter is placed after the target to absorb the signal emitted by the K beta layer. The problem is that this K beta falls on the peak corresponding to CuO and is not fully absorbed.

The oxides present on the particles, which appear to be a protective layer, present a major problem because they will prevent the carbon from later crystallizing during the carbonization of the sucrose which will coat the particles. Thus, it is important to reduce oxides on the particle surface. It is possible to reduce these oxides in a reducing atmosphere using a mixture of argon and hydrogen. The reducing specie being hydrogen.

The two oxides begin to react with hydrogen around 200°C. However, an incubation time is necessary where the hydrogen must accumulate in the oxide to react, but a little reduction still takes place. The reaction is relatively slow even if it is easier to reduce CuO than to reduce Cu2O this is explained by a lower activation energy for the reduction of CuO than of Cu2O, 14.5 kcal/mol and 27.4 kcal/mol, respectively. The reduction is also very dependent on the kinetics, rapid heating (greater than 40°C/min) will produce Cu2O rather than Cu while relatively slow heating (less than 10°C/min) will reduce the CuO directly to Cu. Under the experimental conditions, at 200°C – 10°C/min – 30% hydrogen, CuO is reduced directly to Cu by following the following reaction:

$$CuO_{(s)} + H_{2(s)} \rightarrow H_2O_{(g)} + Cu_{(s)}$$

Same thing for Cu2O but the reduction is much slower following the following reaction:

$$Cu_2O_{(s)} + H_{2(g)} \rightarrow 2Cu_{(s)} + H_2O_{(g)}$$

The higher the temperature, the faster the reduction. Thus, a temperature of at

least 300°C is necessary to reduce the two oxides in relatively reasonable times. It is important to note that the reduction of CuO does not form an oxide intermediate under these conditions. Whereas during the oxidation of copper at room temperature in air and at atmospheric pressure, Cu_2O is an intermediate oxide, following this sequence: Cu → Cu_2O → CuO. It is therefore essential to reduce Cu_2O at the risk of seeing CuO reappear. In addition, most of the oxide on the surface must consist of CuO while at depth Cu_2O dominates [140].

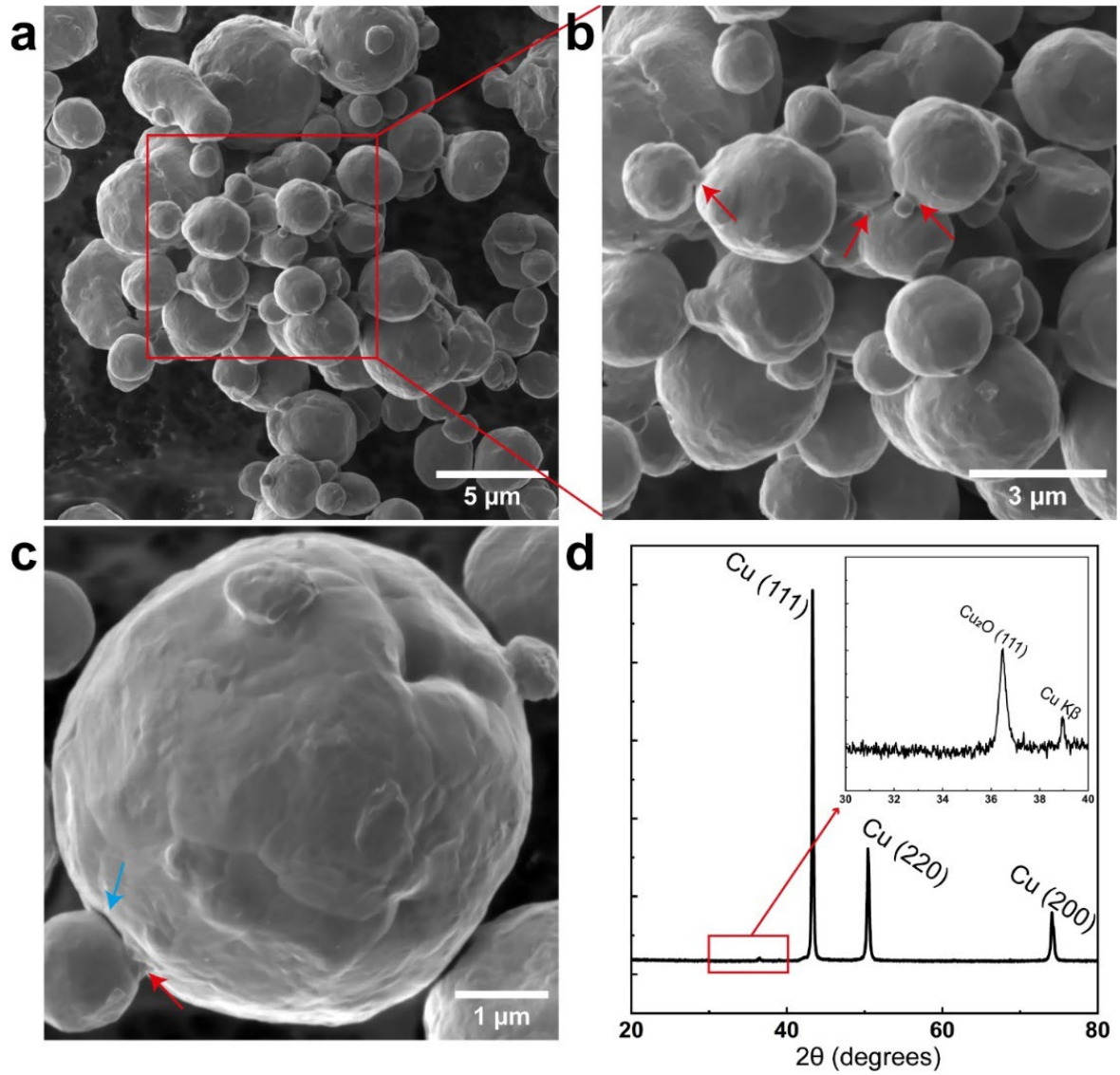

*Figure 2.6 - Characterization of rCu200C: **a** general SEM picture of the powder, **b** zoom on the particles, the red arrows show where the particles begin to sinter but sintering is partial, **c** SEM picture of a reduced particle, the red arrow shows partial sintering and the blue arrow shows a gap and **d** XRD diagram of the powder after reduction at 200°C*

The temperatures of 200°C and 300°C for copper oxide reduction can be challenging when utilizing copper microparticles. Due to their high specific surface area, these particles exhibit a lowered threshold for the initiation of sintering, a

phenomenon corroborated by empirical observations. This characteristic, can presents a significant problem during the densification process of the powder. As the particles begin to sinter prematurely, there is a pronounced risk of aggregate formation, potentially leading to the introduction of porosities within the material after sintering. Such porosities are detrimental as they undermine the structural integrity and reduce the physical properties of the resultant material.

Figure 2.6 provides a characterization of the powder subsequent to a 10-minute reduction process conducted at 200°C. Post-reduction, there is a noticeable alteration in the surface state of the particles; the previously prevalent oxides are, visually, largely eradicated, yielding a predominantly smooth surface, as delineated in figure 2.6 (c).

Conversely, the reduction in oxide layers renders the particles susceptible to diffusion phenomena, with partial sintering becoming evident even at the modest temperature of 200°C, as illustrated by the red arrows in figure 2.6 (b). This partial sintering imparts a certain roughness to the particles, attributed primarily to the mechanical disruption occurring during the powder grinding process post-reduction. Specifically, figure 2.6 (c) highlights a particle showcasing partial sintering, where the red arrow indicates a nascent sintering bridge while the blue arrow points to an ensuing void.

Furthermore, figure 2.6 (d) delves into the XRD analysis, showcasing peaks corresponding to the (111), (220) and (200) planes. Despite the reduction process, it is evident that the complete eradication of oxides is not achieved, as deduced from the residual peaks at 36.5° and 38.9°, attributed to Cu_2O and Cu K_β respectively. Although these oxide signatures are diminished in intensity, their presence signals that a 10-minute reduction span at 200°C may not suffice for the total removal of copper oxides.

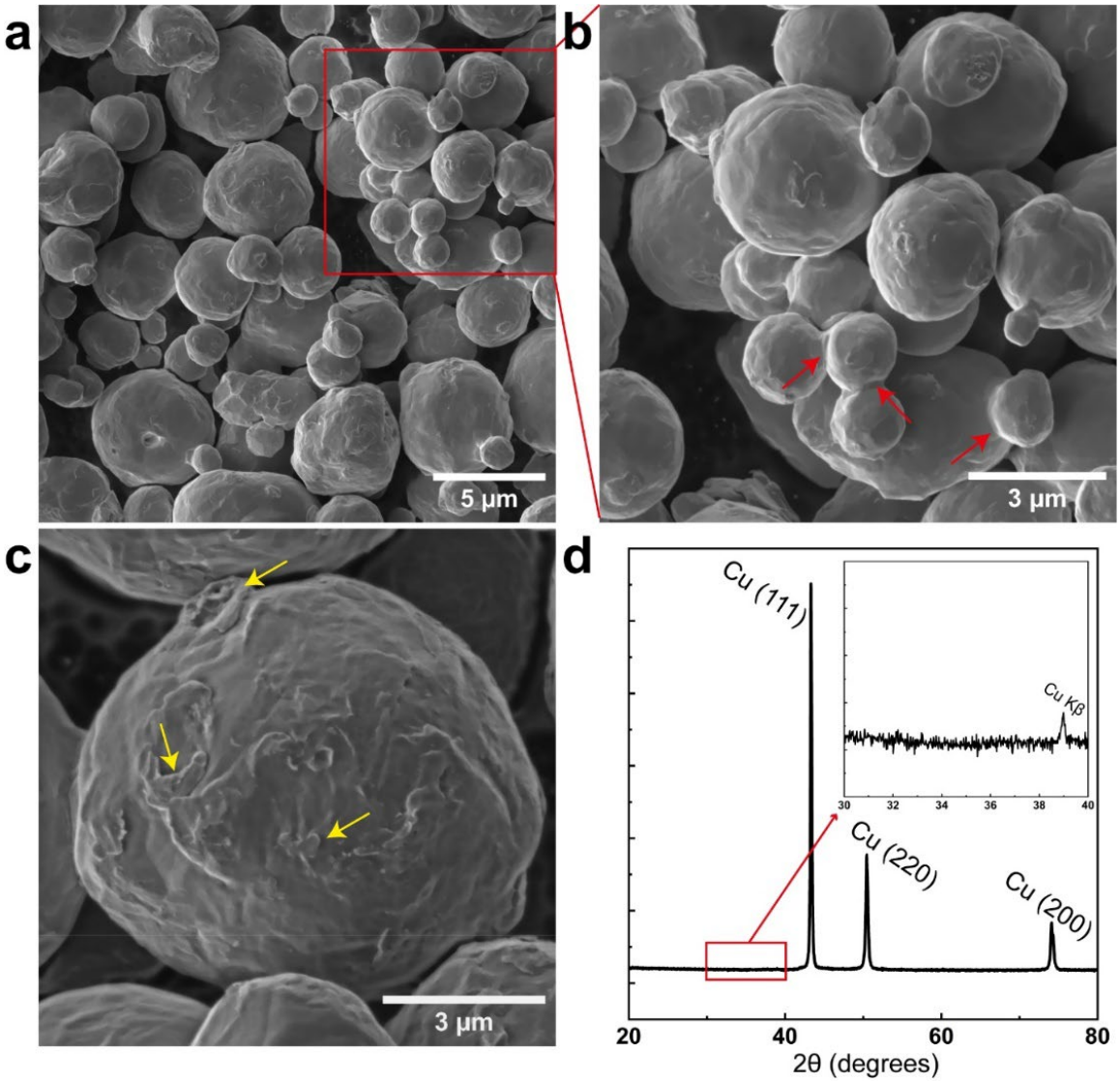

*Figure 2.7 - Characterization of rCu300C: **a** general SEM picture of the powder, **b** zoom on the particles, the red arrows show where the particles begin to sinter, **c** SEM picture of a reduced particle, the yellow arrows show where partially sintered particles were torn apart and **d** XRD diagram of the powder after reduction at 300°C*

Figure 2.7 provides a characterization of the powder subjected to a reduction process at 300°C for a duration of 10 minutes. This treatment resulted in significant alterations in the surface state of the particles, analogous to those observed with the reduction at 200°C. Notably, there is a marked visual disappearance of oxides, as depicted in figure 2.7 (c), indicating effective reduction under increased temperature conditions. In contrast to the reduction at 200°C, the particles exhibited a more pronounced tendency towards sintering at this temperature, as evidenced in figure 2.7 (b). Here, red arrows highlight regions where particle sintering has occurred, indicating an escalation in the agglomeration. Despite this increased sintering, subsequent mechanical grinding of the powder appears to disrupt the initial sintering clusters, indicative of the brittle nature of these nascent sintered forms. It is important to note that after the reduction of the powder at 300°C, the powder is harder to grind. The

resultant surface condition post-grinding is depicted in Figure 2.7 (c), where yellow arrows point to rough surface areas characterized by distinct tear marks resembling half-moons. These features suggest a substantial alteration in the particle morphology due to the mechanical forces applied during grinding, resembling the early stages of sintering akin to those identified in Figure 2.6 (c). Furthermore, figure 2.7 (d) presents XRD pattern for the powder after reduction at 300°C for 10 minutes. The only peaks detected are those corresponding to the diffracting copper planes, which are the (111), (200) and (220) planes, showing that the oxide has been completely reduced after ten minutes of reduction at 300°C.

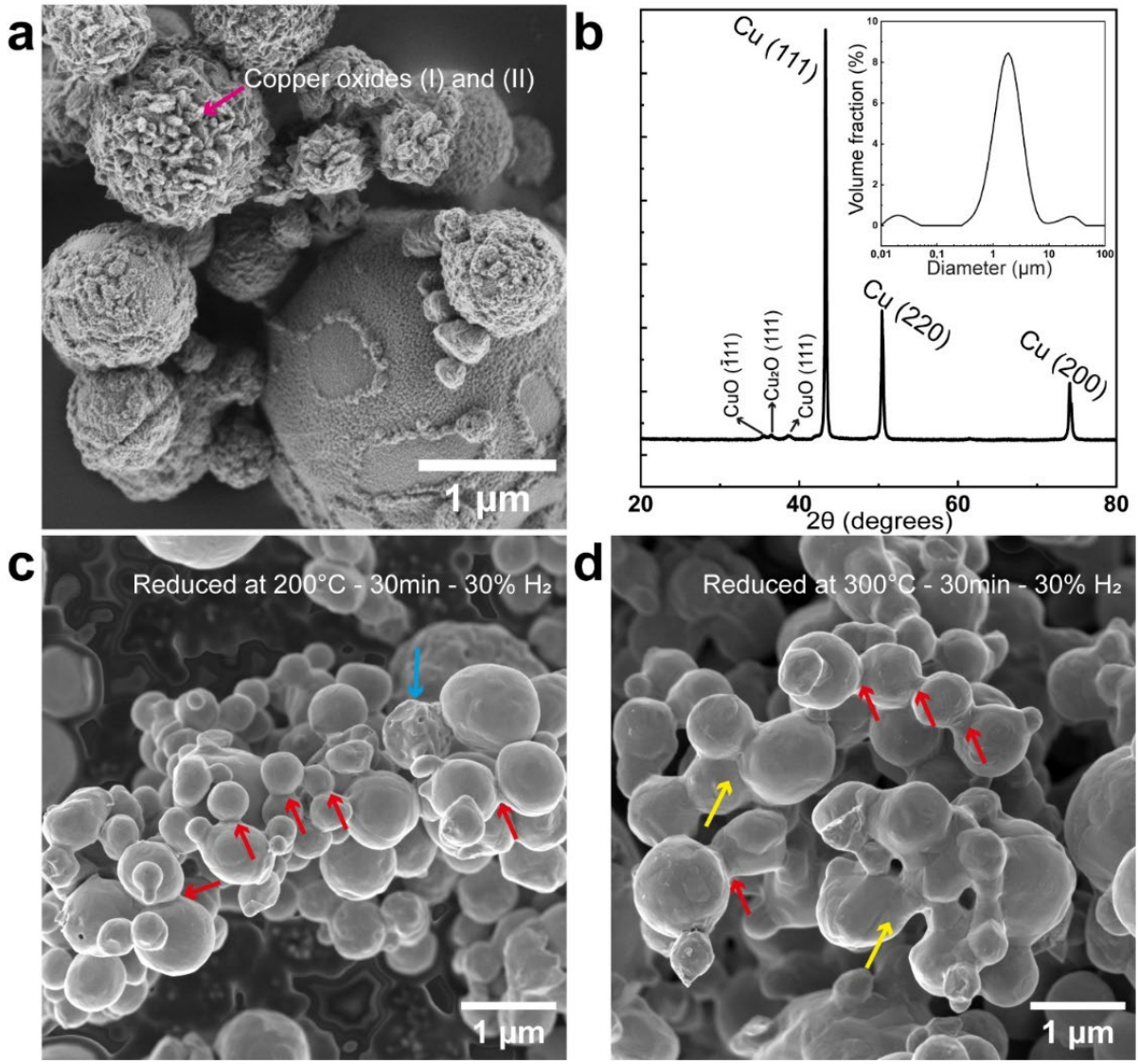

Figure 2.8 – general characterization of another copper powder with smaller particles: ***a*** *general SEM view of the particles where oxide can be seen, the inset is the laser granulometry,* ***b*** *XRD diagram showing copper, copper oxide (I) and (II),* ***c*** *SEM image of the powder after reduction at 200°C and* ***d*** *SEM image of the powder after reduction at 300°C*

The impact of sintering on particle distribution varies significantly depending on the specific size range of the particles involved. While larger particles, as characterized in figure 2.6 and 2.7, display a resilience to sintering effects under the examined conditions, finer particles present a contrasting scenario. Figure 2.8 digs into the behavior of particles with an average diameter spanning between 0.5µm and 1.5µm, as highlighted in the inset of figure 2.8 (a). These finer particles exhibit an enhanced susceptibility to sintering, a phenomenon that becomes particularly pronounced following reduction treatments at 200°C and 300°C for a duration of 10 minutes.

Post-reduction observations, as depicted in figures 2.8 (c) and (d), reveal that despite subsequent grinding efforts, the particles tend to form robust aggregates. These aggregates prove to be resilient against further mechanical breakdown, which

will lead to the introduction of porosities within the densified material.

Moreover, the finer powder exhibits a higher degree of oxidation compared to its coarser counterparts discussed in earlier sections. The XRD pattern, presented in figure 2.8 (b), illustrates this observation with peaks indicative of more pronounced oxide formations. This increased oxidation propensity further complicates the processing and application potential of these finer particles, emphasizing the need for careful consideration of particle size and distribution in the context of sintering and material consolidation processes.

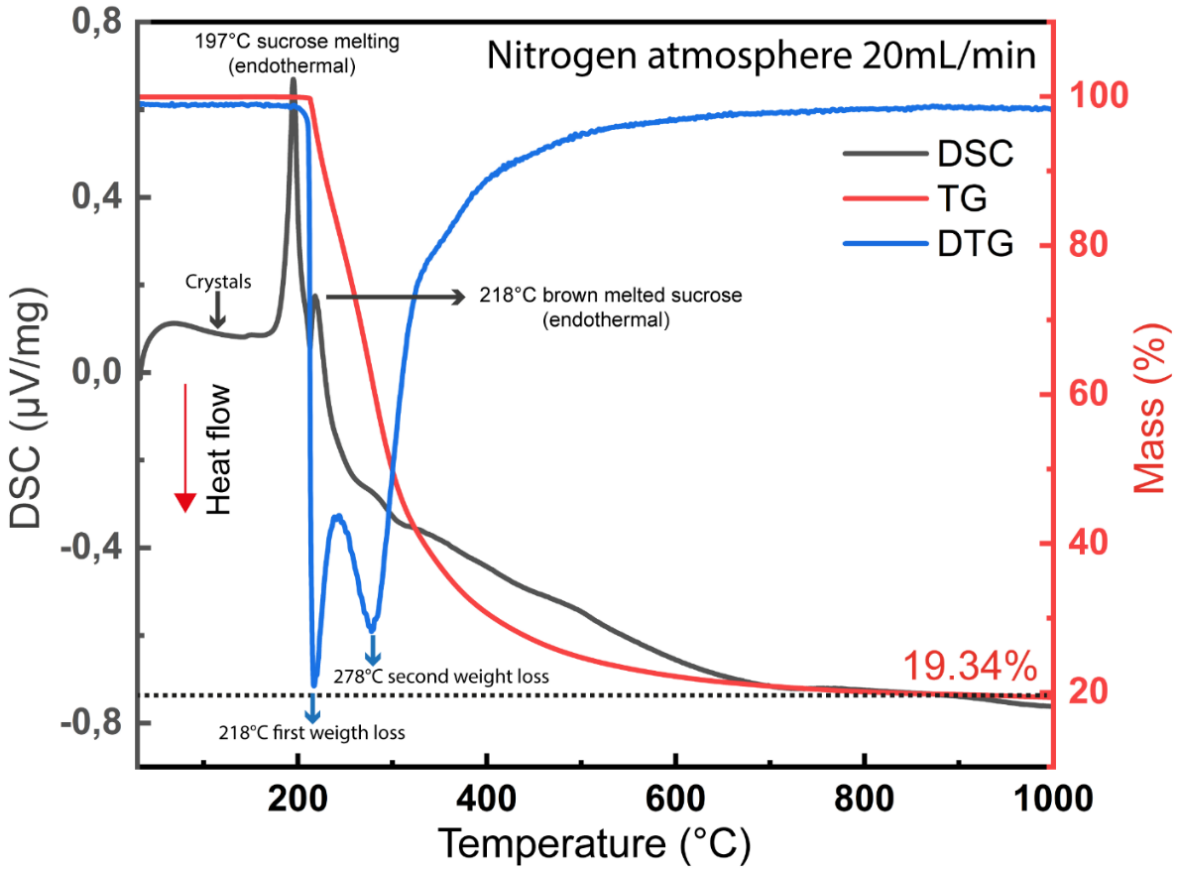

Figure 2.9 – DSC, TG and DTG curves, in grey, red and blue, respectively, of the sucrose under nitrogen atmosphere

Figure 2.9 illustrates the DSC curves in grey, TG curves in red, and differential thermogravimetry (DTG) curves in blue, all of which were obtained under a nitrogen atmosphere. Remarkably, the DSC profile of sucrose exhibited distinct endothermic peaks at around 197°C and 218°C, signifying significant thermal events. Upon visual examination, it was evident that the sucrose crystals underwent a phase change, transitioning from its solid crystalline form to a brown liquid, thereby confirming that the endothermic peak at 197°C represents the melting process. Additionally, the dehydration and condensation of sucrose were observed to occur at the temperature of 218°C.

Interestingly, when sucrose was subjected to the thermal decompostion, a series of reactions ensued as the temperature increased. Specifically, sucrose underwent

decomposition, resulting in the formation of carbon monoxide, carbon dioxide, hydrogen, methane, and water. Intriguingly, at a temperature of approximately 310°C, a distinctive broad exothermic peak emerged, which can be attributed to the decomposition of sucrose into amorphous carbon. It is noteworthy that beyond a temperature of 600°C, the carbonization of sucrose was nearly complete, and no further endothermic or exothermic phenomena were observed.

Thus, it can be deduced that under this inert atmosphere, the decomposition of sucrose predominantly involved its own carbonization process. The TG and DTG curves of sucrose under nitrogen atmospheres were highlighted in red and blue, respectively. Notably, the primary pyrolysis event of sucrose occurred within the temperature range of 200 to 310°C. Particularly, in the initial stage (<200°C), the thermal treatment led to the melting of sucrose, accompanied by the liberation of physically adsorbed moisture from the sucrose structure. Subsequently, in the second stage (200–220°C), the combination of certain hydrogen and hydroxyl groups facilitated the removal of structural water. The third stage (230–280°C) was characterized by the occurrence of a free radical reaction involving sucrose, which subsequently resulted in the release of carbon dioxide, carbon monoxide, and methane. Evidently, as the temperature continued to rise, the carbonization of sucrose became more pronounced, ultimately leading to an approximately 80% weight loss with a final mass of 19.34% of the initial mass.

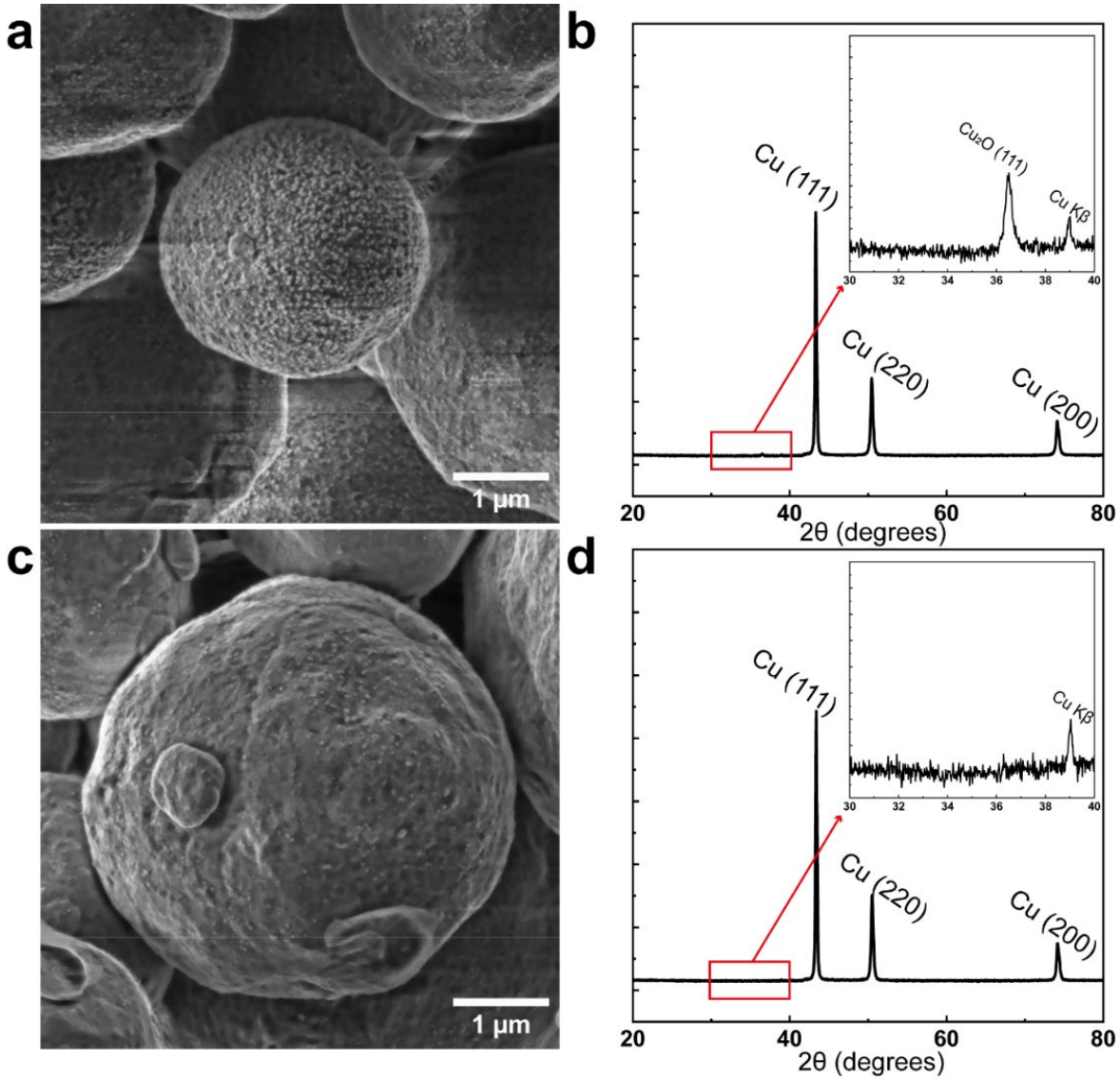

*Figure 2.10 – Characterization of the Cu@2.00% and treated under hydrogen at 200°C and 300°C for 30min: **a** SEM image of the powder after coating and reduction at 200°C, the white spots are copper oxide, **b** its associated XRD diagram, **c** SEM image of the powder after coating and reduction at 300°C, the white spots are copper oxide and **d** its associated XRD diagram*

As the TGA was able to show in figure 2.9, sucrose begins to decompose thermally under an inert atmosphere at 200°C. Between 200 and 230°C the hydrogen in the sugar reacts with the hydroxyl groups to form water, between 230 and 290°C the oxygen in the sugar reacts with the carbon and the carboxyl groups to form either carbon dioxide/monoxide carbon or other. Above 300°C, it carbonizes while gradually separating from the remaining oxygen. However, the different phases of thermal decomposition of sucrose are superimposed on the phases of reduction of copper oxides which, remember, also begin at 200°C. It is therefore possible that when the hydroxyl groups of sucrose begin to react with the hydrogen of sucrose, the injected hydrogen also begins to react with these hydroxyl groups, slowing down the reduction of copper oxides.

Likewise, it is possible that the hydrogen reacts with the oxygen of the sucrose, also slowing down the reduction. Thus, raw powder was coated with sucrose and thermally treated at 200°C and 300°C for 30min in a 70% argon/30% hydrogen mixture to see if the injected hydrogen had the capacity to reduce the oxides onto particles' surface. Figure 2.10(a) and (b) shows SEM observation and associated XRD pattern of the coated and reduced powder at 200°C respectively.

A visual observation is sufficient to see that the oxide is still present, but it is confirmed by the presence of CuO and Cu_2O on the XRD diagram. Figure 2.10 (c) and (d) shows SEM observation and associated XRD pattern of the coated and reduced powder at 300°C respectively. This time, the oxides are less visible but still present as evidenced by the XRD diagram. While when the particles are not coated and after a reduction of 10 min at 200°C and 300°C, it is immediately visible that the oxides have been largely reduced, this is absolutely not the case when the particles are coated with sucrose. It is possible that hydrogen reacts with sucrose rather than reacting with oxides, which could hinder the crystallization of carbon at higher temperatures.

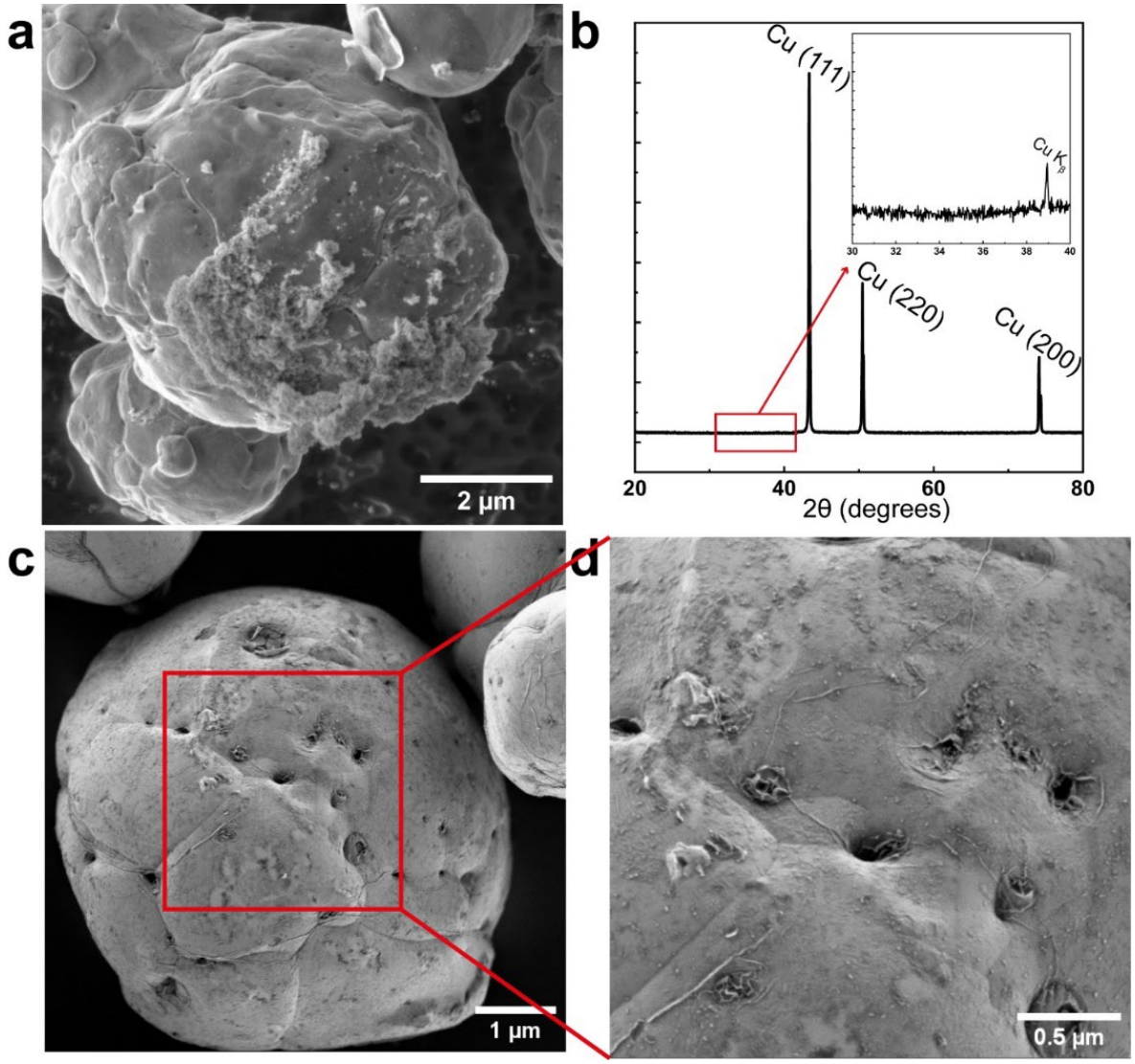

Figure 2.11 - characterization of theCu@2.00% powder and heated at 800°C for 10min: ***a*** *SEM image of the powder after coating and heating at 800°C, the white agregates are copper oxide,* ***b*** *its associated XRD diagram,* ***c*** *SEM image of the powder after coating and reduction at 800°C, the white spots are copper oxide and* ***d*** *its associated magnification*

Figure 2.11 shows the results from SEM observations alongside XRD analysis conducted at an intermediary temperature of 800°C, maintained for 10 minutes, under an atmosphere composed of argon (90%) and hydrogen (10%) at a flow rate of 1.0L/min. The SEM images, depicted in figures 2.11 (a), (b) and (c), provide visual evidence indicating that the copper particles exhibit residual oxidation; this is discernible from the presence of copper oxide nanoparticles, despite the reducing atmosphere provided during the heat treatment. However, there appears to be a discrepancy between the microscopic observations and the XRD analysis results. The latter does not exhibit sufficient resolution or sensitivity to detect the subtle presence of copper oxide phases within the sample. This limitation in the XRD analytical method marks the necessity for more sensitive or complementary analytical techniques to

accurately identify and quantify the extent of oxidation in such nuanced scenarios. For example, by using Electron Energy Loss Spectrometry (EELS) with atomic resolution. Additionally, the SEM analysis reveals a noteworthy structural transformation of the copper particles post-treatment. Notably, the emergence of holes within the particles, absent prior to the thermal treatment, suggests a significant crystalline rearrangement. This observation points towards the occurrence of a morphological evolution under the applied thermal conditions, likely driven by the dynamics of oxidation-reduction reactions and the diffusion processes at elevated temperatures.

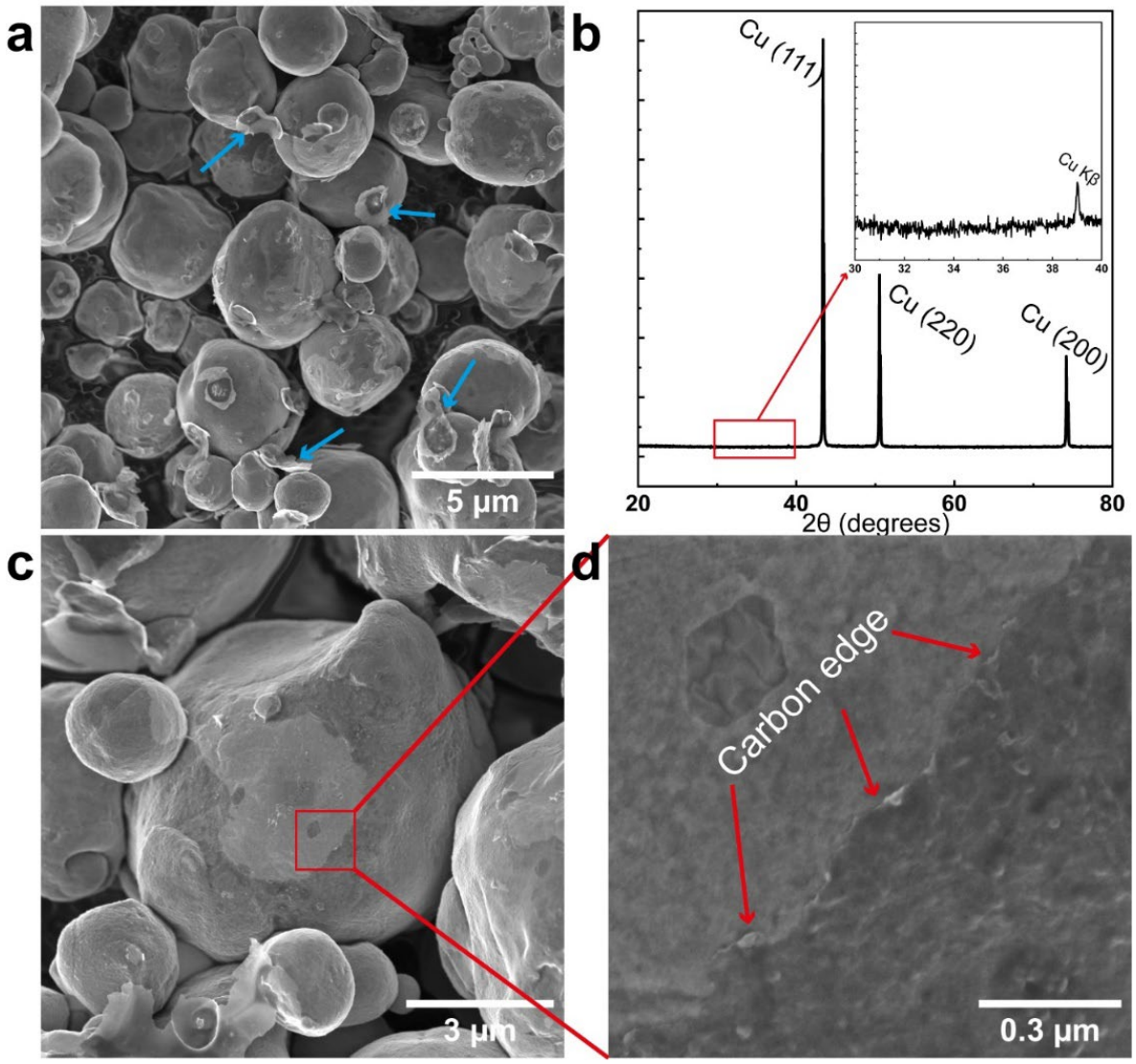

*Figure 2.12 – General characterization of the Cu@2.00% powder after graphitization at 1000°C: **a** SEM image the particles where the carbon shells are pointed by blue arrows, **b** the associated XRD diagram, **c** SEM image showing a particle covered with a carbon layer and **d** the associated magnification*

Figure 2.12 elucidates the characterization outcomes for the Cu@2.00% powder post-graphitization, conducted at a temperature of 1000°C for a duration of 30 minutes

under an atmosphere composed of argon (99.5%) and hydrogen (0.5%), employing SEM and XRD for analysis. The SEM observations in figure 2.12 (a) are revealing, where blue arrows highlight the presence of carbon shells that have evidently detached from their corresponding particles. This phenomenon suggests that the adhesion between the carbon layers and the copper particles is suboptimal, leading to the detachment of the carbon shells. Such a detachment could be indicative of insufficient interaction between the carbon and the metal surface or could result from the grinding after graphitization.

Further, Figure 2.12 (b) displays the XRD pattern obtained from the treated powder. Similar to the observations in Figure 7, no oxide phases are detected within the powder post-graphitization. This absence of oxide peaks in the XRD analysis may reaffirm the effectiveness of the reducing environment provided during the high-temperature treatment, although, as previously mentioned, it also highlights the limitations of XRD in detecting minute quantities or thin layers of oxides.

The SEM images, specifically Figure 2.12 (c) and its magnified counterpart 2.12 (d), provide a detailed view of a particle that is coated with carbon. These images reveal that the carbon layer enveloping the particle appears brittle and is assessed to be of poor quality. The brittleness and apparent poor quality of the carbon coating are significant as they may adversely affect the mechanical and electrical properties of the composite material. The presence of such defects in the carbon layer could be attributed to a variety of factors, including the nature of the carbon precursor, the graphitization conditions, or the compatibility between the carbon and the copper substrate.

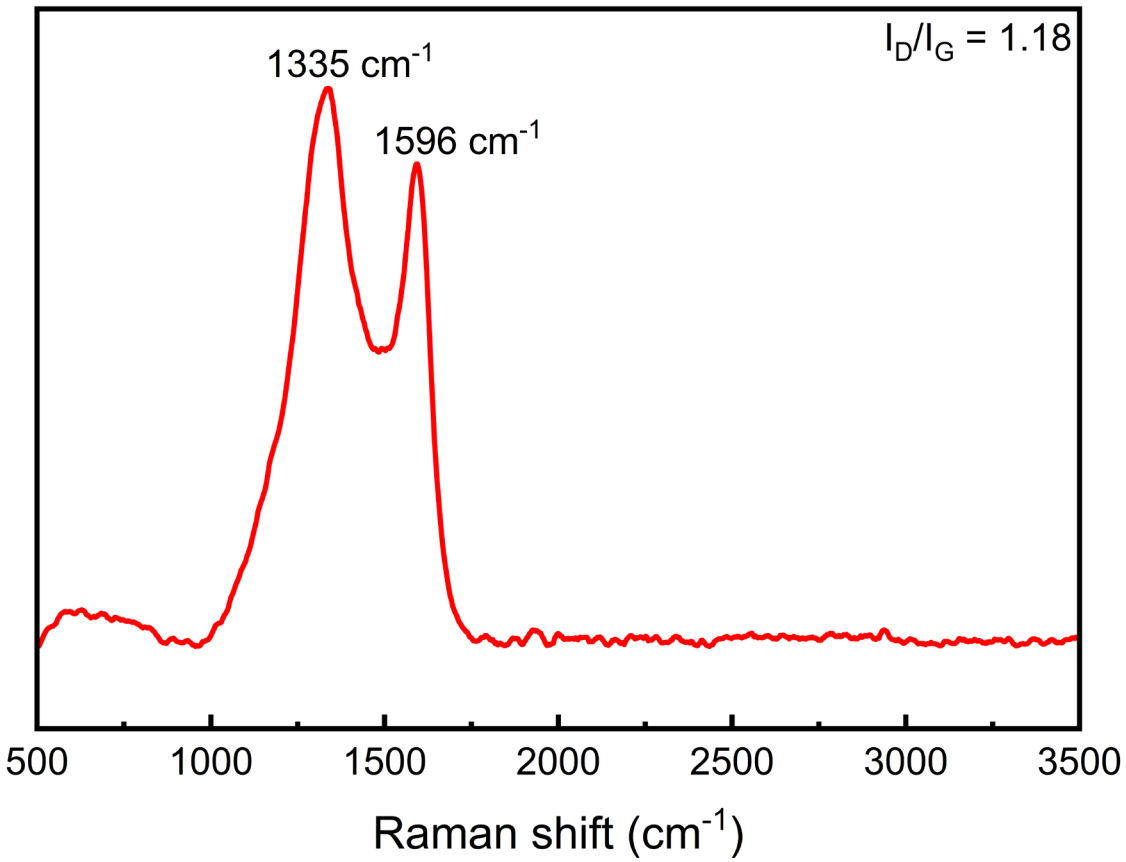

Figure 2.13 – Raman spectra of the Cu@2.00% powder

Figure 2.13 delineates the results from the Raman spectroscopic analysis pertaining to the powder characterized in Figure 2.12. This analytical technique is instrumental in evaluating the structural integrity and quality of carbonaceous materials. The Raman spectrum of the examined powder showcases the presence of the characteristic D and G bands, which are characteristic of carbon material.

The D band, located at 1335 cm^{-1}, is traditionally associated with the presence of defects and disorder within the carbon lattice, typically arising from structural imperfections. On the other hand, the G band, observed at 1594 cm^{-1}, is indicative of the crystalline graphitic structures, corresponding to the in-plane vibrations of sp^2-hybridized carbon atoms.

The intensity ratio of these peaks, denoted as I(D)/I(G), is a widely recognized metric for assessing the quality of carbon materials, particularly in terms of their crystallinity and the extent of structural defects. In the context of the current analysis, this ratio is calculated to be 1.18, which notably suggests a dominance of disordered or defective structures within the carbon matrix, thereby denoting a lower quality of the carbon present. Such a high ratio typically signifies an increased presence of amorphous carbon relative to crystalline graphene, aligning with the SEM observations which highlighted the brittleness and suboptimal quality of the carbon coating.

Furthermore, the absence of additional peaks within the Raman spectrum reinforces the conclusion that the carbon material is predominantly amorphous. This lack of crystalline signatures, coupled with the high I(D)/I(G) ratio, consolidates the

assessment that the carbon synthesized under the specified conditions does not achieve a high degree of graphitization, necessitating further optimization of the synthesis process or the use of alternative precursors and conditions to enhance the crystallinity and overall quality of the carbon produced.

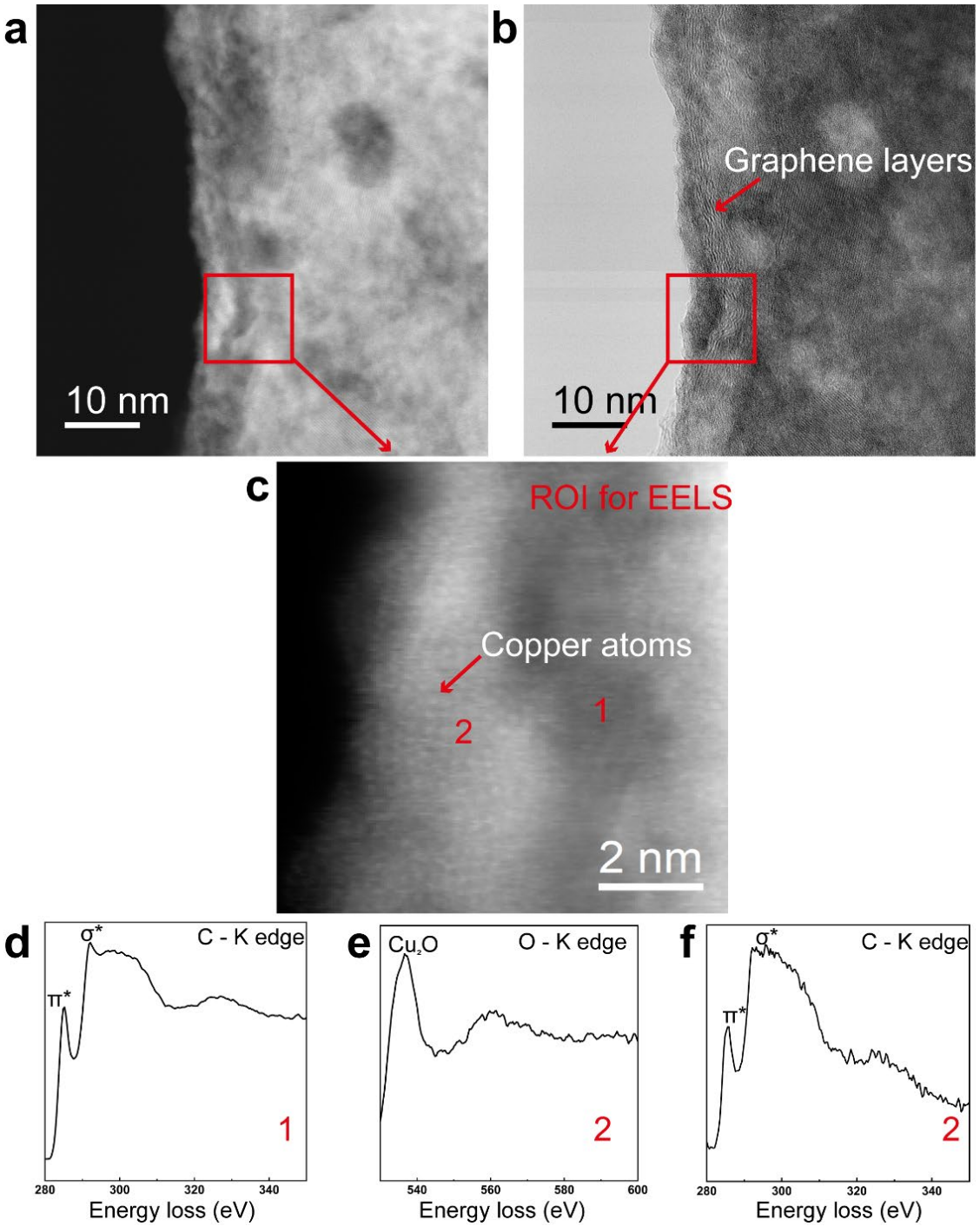

*Figure 2.14 – TEM obervations and EELS analysis of the Cu@2.00% powder: **a** HAADF observation, (**b**) bright field observation, (**c**) ROI for EELS analysis the numbers 1 and 2 denotes the location of gathered specific EELS, (**d**) EELS of the zone 1, (**e**) and (**f**) EELS of the zone 2*

Figure 2.14 provides an examination of the powder subsequent to the dissolution of copper using a solution of iron chloride and hydrochloric acid, to isolate the carbon structure for analysis. This figure presents TEM observations alongside EELS analysis. In the High-Angle Annular Dark-Field (HAADF) TEM imaging, shown in figure 2.14 (a), the analysis reveals varying degrees of crystallization within the carbon structures. The HAADF technique, known for its sensitivity to atomic number variations, enables the differentiation of chemical compositions within the sample. Notably, the white spots visible in the image are identified as copper atoms, indicating the presence of residual copper despite the dissolution process. This residual copper, attributable to the innate oxide layer originally present on the raw copper powder, reflects the challenges in completely removing copper content without affecting the carbon matrix.

Complementary to the HAADF imagery, the bright field TEM imaging, depicted in Figure 2.14 (b), further corroborates the crystalline development within the carbon layers, allowing for the enumeration of distinct layers. This visualization features the partial crystallization achieved under the applied conditions.

The specificity of the structural investigation is enhanced through the designated Region of Interest (ROI) for EELS analysis, marked in Figure 2.14 (c), with distinct areas labeled 1 and 2 earmarked for detailed spectral collection. Figure 2.14 (e) presents the EELS spectrum obtained from zone 1, illustrating characteristics synonymous with graphite, indicative of localized areas of higher crystallinity within the carbon matrix.

Conversely, the EELS spectra derived from zone 2, illustrated in Figures 2.14 (f) and (g), reveal a significantly different scenario. Here, the presence of copper oxide (I), denoted as Cu_2O, is detected alongside an associated amorphous carbon structure. This observation suggests a complex interplay between copper oxidation and carbon structural formation, where areas adjacent to copper oxide exhibit a lack of crystalline carbon development.

The persistence of copper oxide even after treatment at a high temperature of 1000°C under a reducing atmosphere can be ascribed not only to the protective oxide layer initially present on the raw copper powders but also to the operational conditions during graphitization. Despite the reducing environment intended to facilitate copper reduction and carbon graphitization, the presence of trace oxygen, potentially up to 2 ppm in the argon and hydrogen gases used, may contribute to the incomplete reduction of copper oxide.

The previous findings show the complex interplay between the inherent oxide layer on raw copper powders and the subsequent crystallization behavior of carbon upon the powder surfaces. It has been discerned that while the protective oxide layer serves as a protection, it concurrently impedes the effective crystallization of carbon, a phenomenon decisive for the development of graphene. The employment of a reducing atmosphere, utilizing hydrogen at temperatures of 200°C and 300°C, has been identified as a viable strategy for the rapid reduction of the copper oxide layer, typically within a span of approximately 10 minutes. However, this reduction process is not devoid of challenges; the removal of the oxide layer initiates copper diffusion, potentially inciting sintering phenomena at atmospheric pressure and culminating in the undesired formation of aggregates.

Further analytical investigations, employing TGA and DSC, have established that sucrose commences its decomposition at 200°C, transitioning to a fully carbonized state by 600°C. Nonetheless, when the sucrose-coated raw copper powder is subjected to thermal treatments at 200°C, 300°C, and subsequently 800°C, under a reductive atmosphere constituted of argon and hydrogen, the persistence of the oxide layer is evident. It is not until the application of a temperature regime reaching 1000°C that conventional detection methods such as SEM and XRD fail to identify the presence of the oxide

Contrastingly, TEM observations, including HAADF imaging, bright field imaging, and EELS analysis, reveal the residual presence of oxide at the atomic scale. This finding is corroborated by Raman spectroscopic analysis, which indicates that the carbon layer deposited on the copper particles predominantly exhibits an amorphous structure.

In response to these observations, another methodological approach was adopted for the coating and subsequent analysis of the copper powders. Initially, the raw copper powder was thermally reduced with hydrogen at 200°C to facilitate oxide layer reduction, followed by mechanical grinding and sieving to ensure uniform particle size and surface characteristics. Subsequently, the treated powder was coated under a protective argon atmosphere, in order to avoid oxidation of the surface prior to graphitization. The final step involves graphitization at 1000°C, intended to enhance the crystalline quality of the carbon coating.

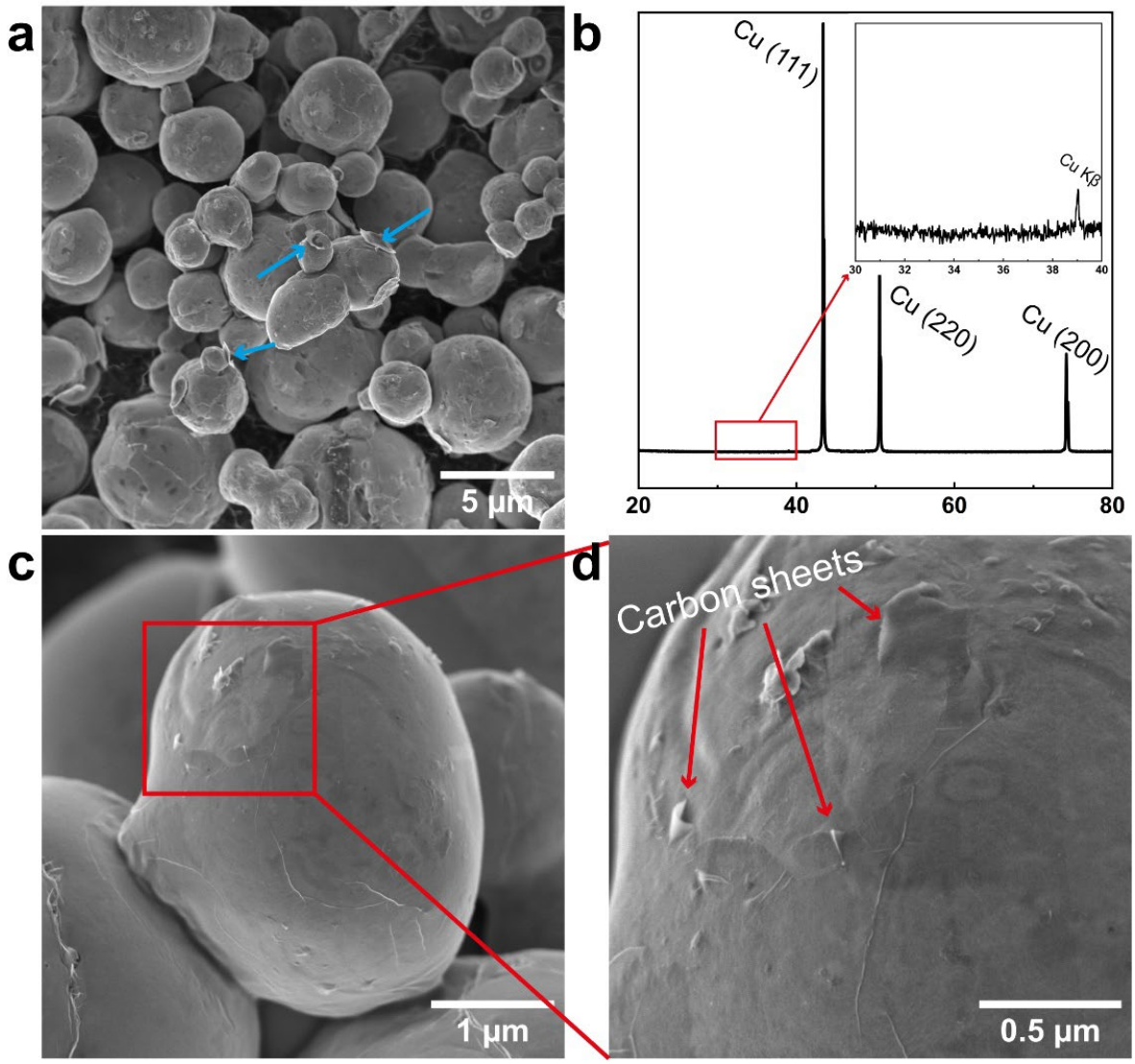

*Figure 2.15 – General characterization of the rCu200C@2.00% powder after graphitization at 1000°C: **a** SEM image the particles where the carbon is pointed by blue arrows, **b** the associated XRD diagram, **c** SEM image showing a particle still covered carbon sheet and **d** the associated magnification*

Figure 2.15 provides a presentation of SEM observations and XRD analysis, conducted in the manner with previous experimental setups. In SEM figure 2.15 (a), blue arrows are utilized to denote instances of carbon shells that have detached from their originating particles. This observation is set against a broader view of the powder, which notably retains most of its original particular characteristics.

Figure 2.15 (b) delineates the results of the XRD analysis. This phase identification process does not reveal the presence of oxide phases, indicating that the preparatory measures taken prior to the graphitization process may have effectively mitigated the formation or retention of copper oxide. But as we said, this technique is not sufficiently precise.

In further detail, SEM figure 2.15 (c) showcases a copper particle that has been successfully coated with a carbon layer. This is subsequently explored at a higher magnification in image 2.15 (d), where the carbon coating is discernible with visible wrinkles – a characteristic often associated with graphene. Moreover, the enhanced structure of the carbon is evidenced by the visibility of sheet-like formations on the surface of the copper particle. These carbon sheets, however, appear to exhibit signs of disruption, as indicated by areas where the layers seem to have been torn apart. This fragmentation might be a consequence of the grinding post graphitization.

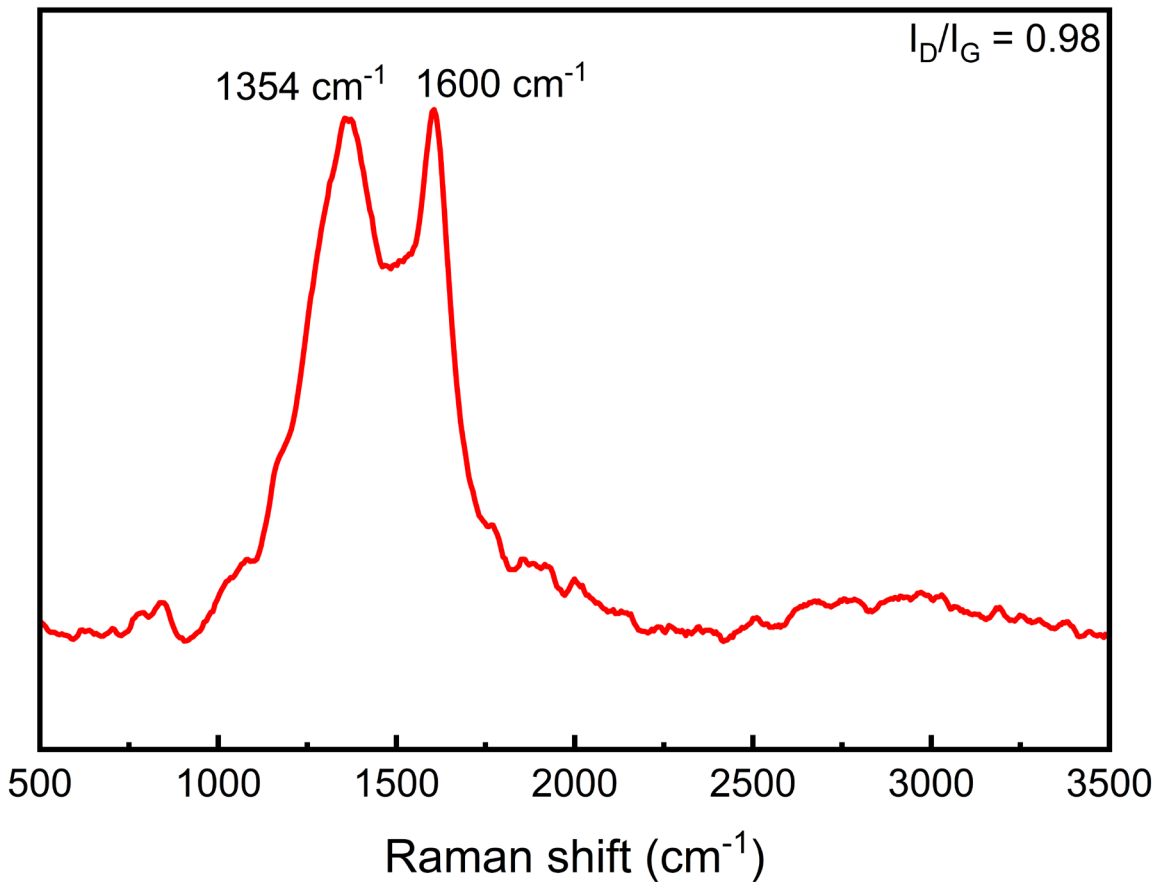

Figure 2.16 – Raman spectra of the rCu200C@2.00% powder after graphitization at 1000°C

Figure 2.16 delineates the results derived from the Raman spectroscopic analysis conducted on the aforementioned powder. Again, the Raman spectra reveals the presence of the characteristic D and G bands, quintessential to the structural analysis of carbon-based materials. The D band, is discerned at 1354 cm^{-1}, whereas the G band, is observed at 1600 cm^{-1}.

The ratio of the intensities of these two peaks, I(D)/I(G), is calculated to be 0.98. This value, being less than unity, is suggestive of a reduced level of structural disorder of the carbon layer, compared to the previous Raman analysis of Cu@2.00%, and implies a some degree of graphitic character.

Additionally, the Raman spectrum exhibits a broad peak extending beyond 2500 cm^{-1}. This feature potentially represents the superposition of several distinct peaks,

specifically those conventionally located at 2700 cm^{-1}, 2950 cm^{-1}, and 3200 cm^{-1}. Such peaks are typically associated with second-order Raman scattering processes in graphitic materials.

Drawing from the analysis of the spectral data, it can be inferred that the carbon coating the particles shows exhibits some sp^2 bonding. However, the amorphous nature suggested by the relatively balanced I(D)/I(G) ratio, coupled with the broad feature in the higher wavenumber region, delineates a structure that, while sp^2-bonded, does not conform to a perfectly crystalline graphitic framework.

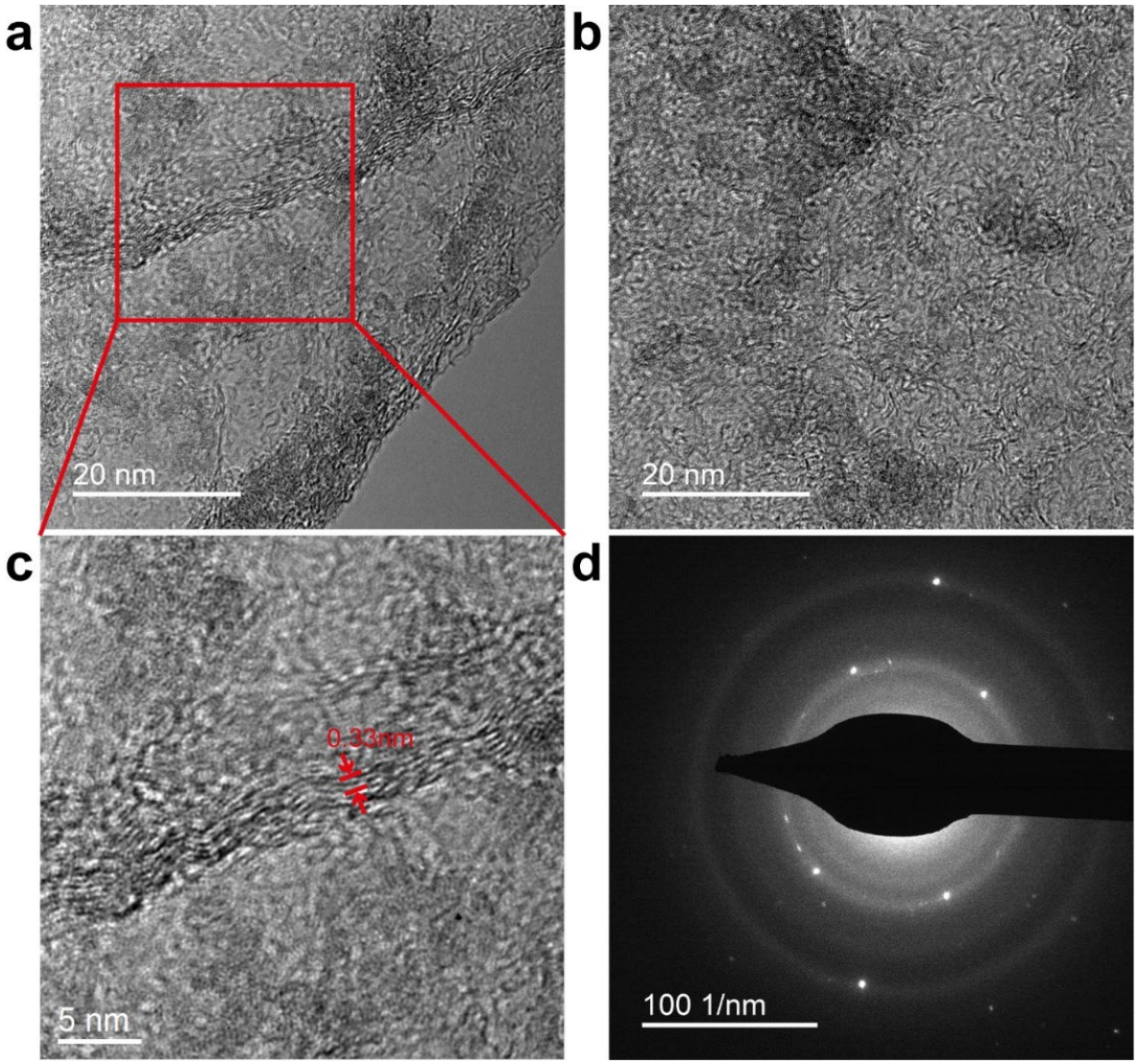

Figure 2.17 – TEM analysis of rCu@2.00% after its dissolution in ferric chloride

Figure 2.17 shows the TEM observations conducted on the rCu@2.00% powder subsequent to the dissolution of copper using a solution of iron chloride ($FeCl_3$) and hydrochloric acid (HCl).

In TEM image 2.17 (a), the visual focus is directed towards the periphery of a carbon shell. Subsequently, Figure 2.17 (c) delves into a higher magnification view of this edge. Within this magnified part of the shell, distinct layers within the carbon

structure become discernible, with an interlayer spacing measured at approximately 0.33 nm.

However, the continuity of these carbon layers is compromised, as evidenced by the presence of disjointed or 'dashed' lines, rather than continuous, unbroken structures. This observation is indicative of a substantial degree of structural disorder within the carbon matrix, an aspect that deviates from the ideal, highly ordered crystalline structure of pristine graphene.

Further inspection, as detailed in Figure 2.17 (b), within the broader context of the carbon shell, reiterates these findings. Here, despite the discernible semblance of order in certain regions, the structure remains predominantly amorphous.

Compounding these morphological assessments, Figure 2.17 (d) presents a Selected Area Electron Diffraction (SAED) pattern derived from the carbon shell. Notably, this diffraction pattern reveals the presence of partial crystallinity, interspersed within the predominantly amorphous carbon. Furthermore, the SAED pattern confirms the residual presence of copper oxide, an outcome that persists despite prior efforts aimed at reducing the copper oxide layer before the carbon coating procedure.

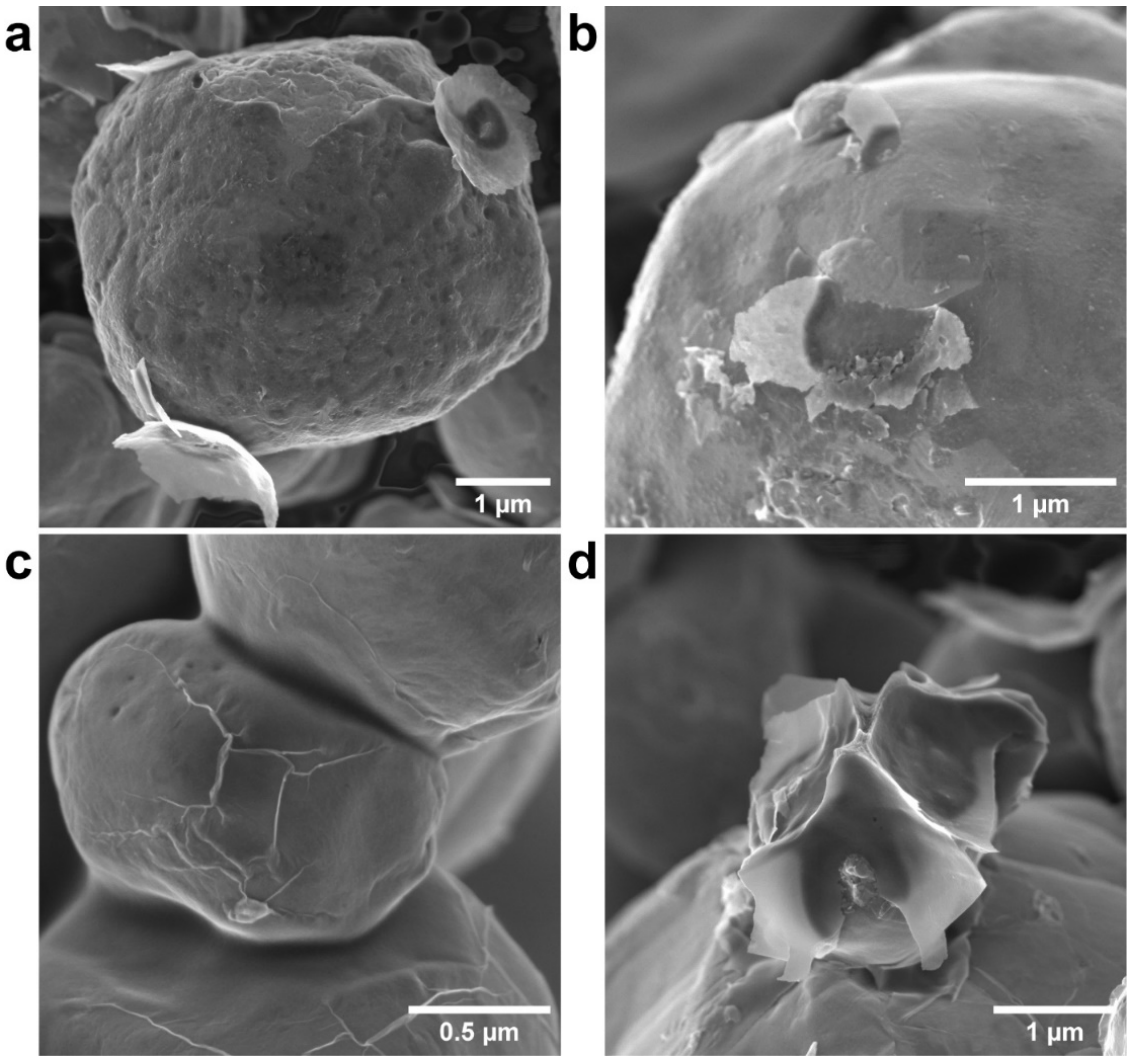

*Figure 2.18 – supplementary SEM observations: **a** and **b** Cu@2.00%, **c** and **d***

rCu200C@2.00%

Figure 2.18 serves as an supplementary visual compilation, providing SEM observations that facilitate a comparative analysis between Cu@2.00% and rCu200C@2.00% subjected to graphitization. The figure is segmented into four parts: Figure 2.18 (a) and (b) display the morphology of Cu@2.00% powder post-graphitization at 1000°C for a duration of 30 minutes. In these images, the carbon coating appears to exhibit a brittle nature, and the surfaces of the copper particles are characterized by a pronounced roughness, indicating a poor quality carbon layer.

Conversely, Figure 2.18 (c) and (d) delineate the morphology of rCu200C@2.00% powder, also following graphitization under identical conditions. These images reveal a discernible contrast in the carbon structure's quality; the carbon layer demonstrates enhanced structural integrity, evident from the visible wrinkles, a characteristic of graphene. Moreover, the overall morphology suggests a more organized and structured carbon deposition on the copper particles.

The juxtaposition of these observations italicizes the impact of preliminary copper surface treatments on the quality and morphology of the resulting carbon coatings. The enhanced structure and apparent increase in uniformity of the carbon layers in the latter set of samples (Figures 2.18 (c) and (d)) suggest that the reduction of copper oxides prior to sucrose coating improves the graphitization outcome, leading to a more consistent and potentially conductive carbon layer.

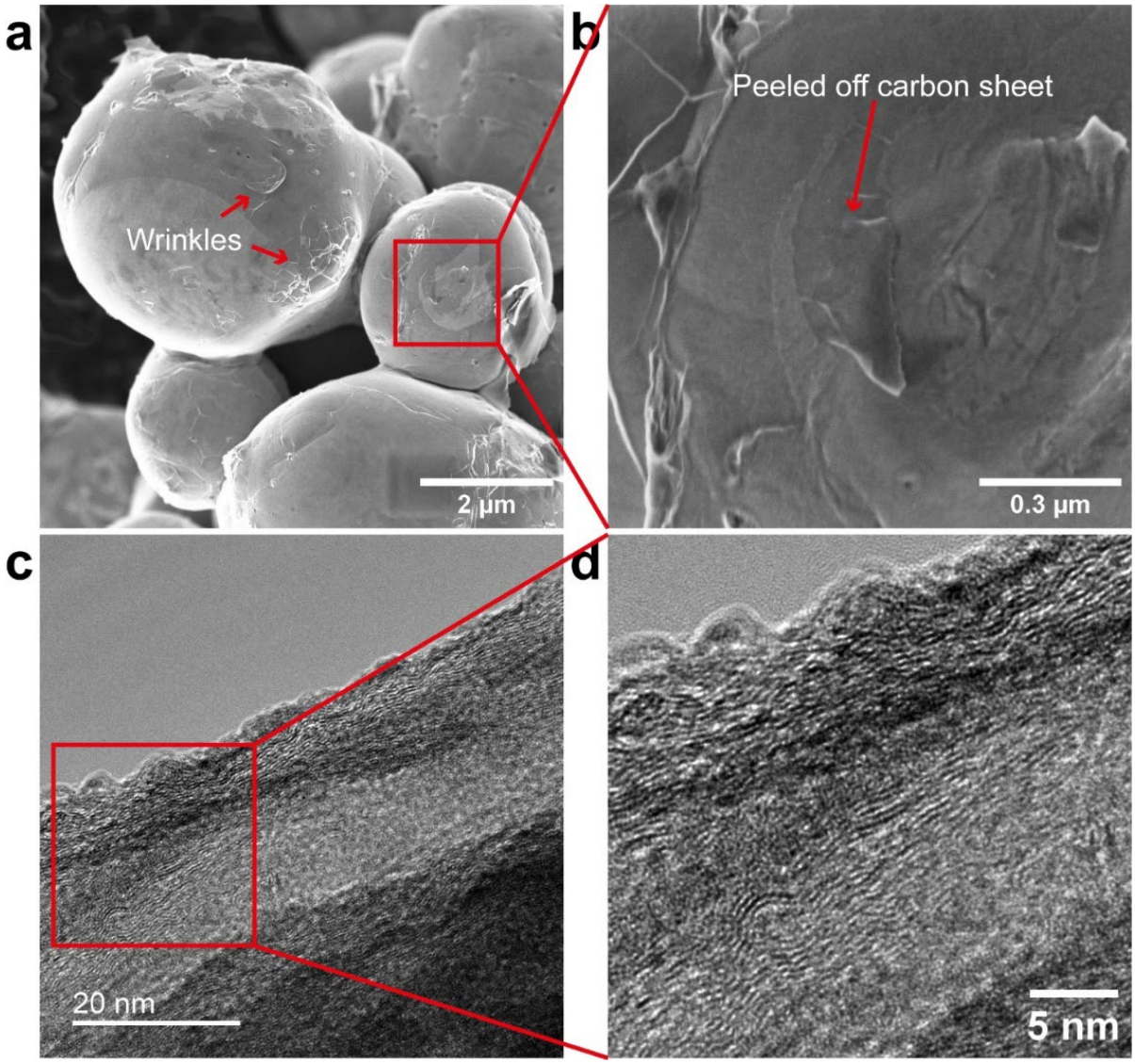

*Figure 2.19 – general characterization of rCu200C@0.65%: **a** low magnification of the powder, **b** its associated magnification, **c** TEM observation and **d** its associated magnification*

Upon establishing the experimental protocol, the next phase involved fine-tuning the initial sucrose concentration to ascertain the minimal quantity necessary to prevent sintering of the copper particles, which is notably dependent on the specific surface area of the powder. Empirical determinations under these procedural conditions and utilizing the specified powder revealed that an optimal initial sucrose concentration for this purpose is 0.65 wt%. Subsequently, the powder was subjected to the refined experimental protocol to assess the effectiveness of this reduced sucrose content in producing a structured carbon coating while preventing sintering.

Figure 2.19 provides a detailed examination through both SEM and TEM analyses of the resultant powder. These imaging techniques were deemed sufficient for the investigation given the established understanding of the factors influencing carbon crystallization.

Figures 2.19(a) and (b) depict SEM observations and their corresponding

magnifications, respectively. The images prominently feature numerous wrinkles across the carbon-coated surfaces, indicative of the formation of a structured carbon layer reminiscent of graphene. Specifically, Figure 2.19 (b) illustrates a carbon sheet that appears to have detached or 'peeled off' from the underlying substrate, suggesting the presence of a structured carbon layer.

Further insights are provided by the TEM analyses displayed in Figures 2.19 (c) and (d), which showcase the carbon shell following the dissolution of copper via a ferric chloride and hydrochloric acid. The TEM images allow for the enumeration of distinct carbon layers, indicating a reduction in disorder compared to previous experimental outcomes. This layered structure is more evident in the magnified view provided by Figure 2.13(d), which highlights the improved organization and delineation of the carbon layers.

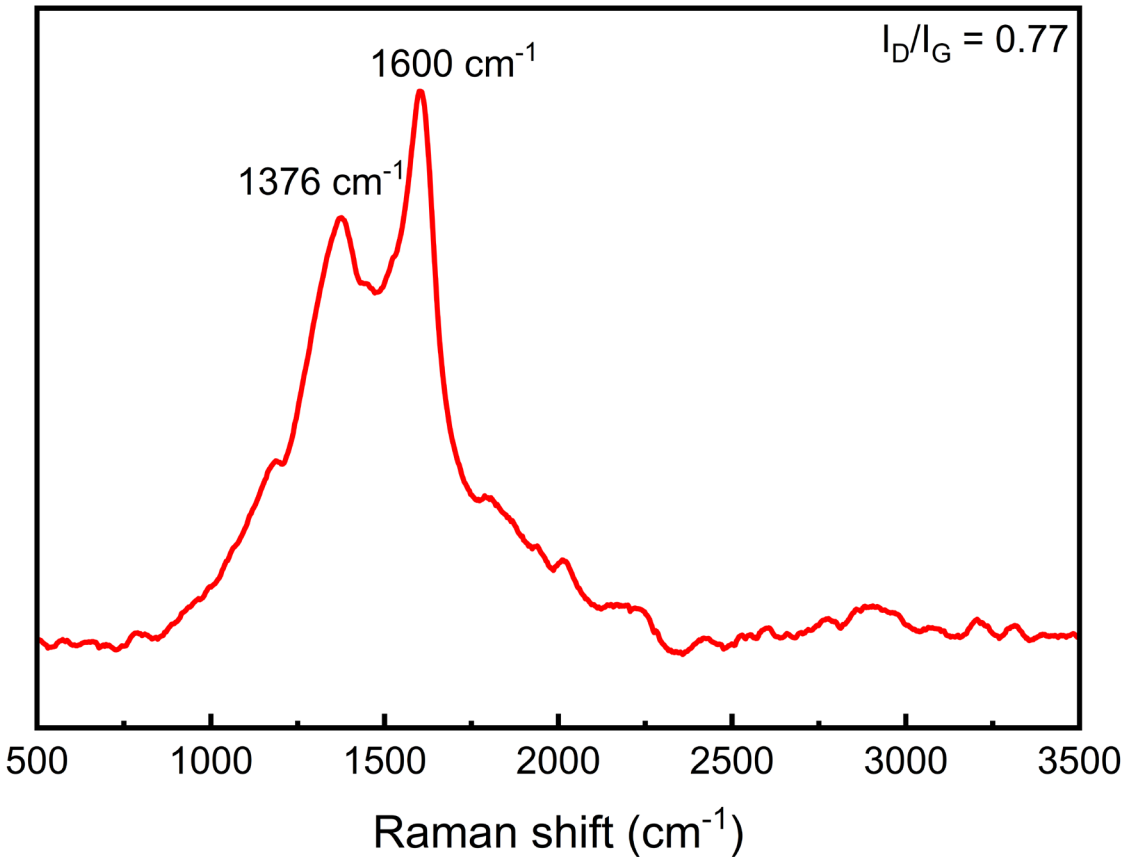

Figure 2.20 – Raman spectra of the rCu@0.65% powder

The structural characteristics of the carbon-coated copper particles, postulated from the SEM and TEM observations, are further confirmed through Raman spectroscopic analysis, as illustrated in Figure 2.20. In Figure 2.20, the Raman spectrum reveals the presence of the two usual peaks: the D peak, situated at 1376 cm^{-1}, and the G peak, located at 1600 cm^{-1}. The ratio of the intensities of these two peaks, I(D)/I(G) is calculated to be 0.77, suggesting a moderate level of disorder that aligns with the partial structuring observed in the TEM images. This points towards a better degree of graphitization and structural organizatio. Additionally, the spectrum identifies a broad

peak discernible beyond 2500 cm^{-1}, typically ascribed to the 2D band in graphene and related materials. The presence and shape of this band are informative regarding the layering of the carbon structures; in this context, the broadness of the peak suggests variations in layer stacking or interactions between multiple graphene layers.

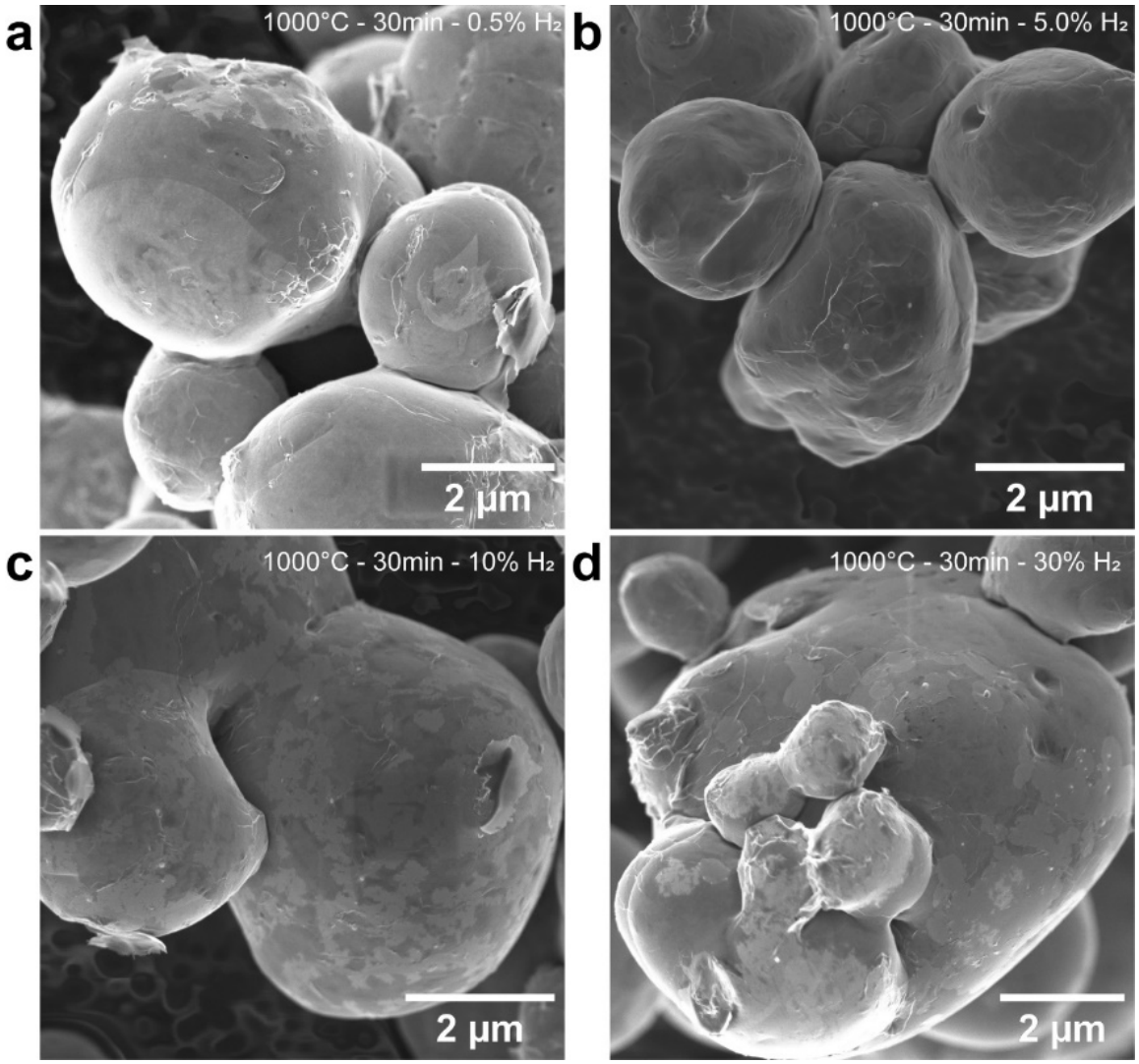

*Figure 2.21 – SEM observations of the rCu@0.65% powder with varying hydrogen proportions: **a** H_2 0.5 vol%, **b** H_2 5 vol%, **c** H_2 10 vol%, and **d** H_2 30 vol%*

So far, the volumetric proportion of hydrogen utilized within the gas mixtures has been maintained at 0.5%. This specific concentration was selected to minimize the risk of excessive hydrogenation of the carbon layers, which could potentially lead to the formation of hydrocarbons. Such a reaction is undesirable as it may lead to the sintering of the copper particles, thereby compromising the particular character of the powder. Figure 2.21 provides an evaluation of the copper powder treated with a sucrose weight of 0.65wt%, under varying hydrogen concentrations in the atmosphere during the graphitization process. The exeriments were conducted with hydrogen proportions set at 0.5%, 5%, 10%, and 30% to investigate the impact of increased

hydrogen content on the behavior of the powder during and post-graphitization. The observations, discernible in the series of SEM images, reveal a progressive change in the physical state of the powder as the proportion of hydrogen is increased. A noticeable trend emerges, wherein the degree of particle shrinkage and the propensity for sintering are evidently augmented with higher hydrogen concentrations. This shrinkage is indicative of the hydrogenation effects on the carbon coating, which can lead to the sintering of the copper particles. Particularly noteworthy is the scenario depicted in Figure 2.21 (d), which showcases the effects at a 30% hydrogen concentration. Here, the SEM images clearly illustrate the onset of some sintering among copper particles, a phenomenon not as apparent or severe at the lower hydrogen proportions.

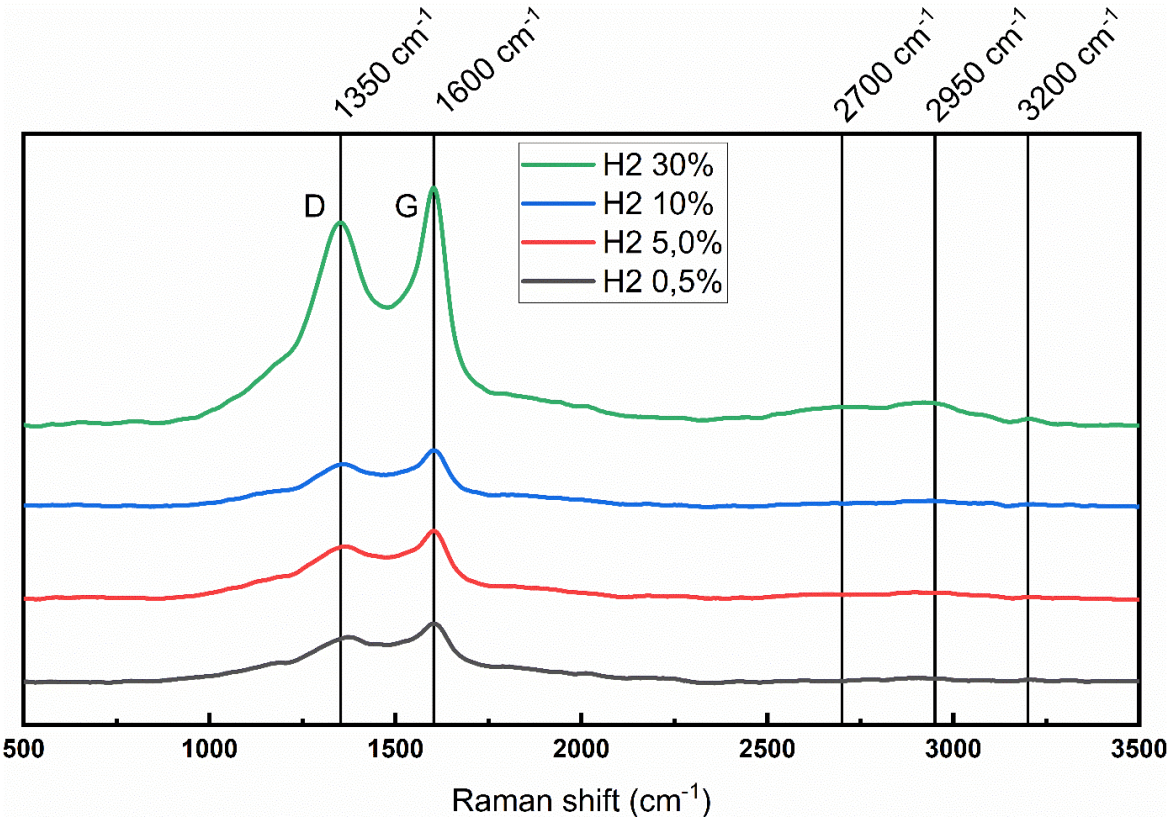

Figure 2.22 – Stacked Raman spectrums of the rCu@0.65% powder with varying hydrogen proportions: H_2 30 vol% in green, H_2 10 vol% in blue, H_2 5 vol% in red and H_2 0.5 vol% in grey

Subsequent to the experimental variations in hydrogen proportions during the synthesis process, Raman spectroscopic analysis was conducted to investigate the structural implications on the resultant copper powders. Figure 2.22 showcases the compiled Raman spectra obtained from powders subjected to hydrogen proportions of 0.5%, 5.0%, 10%, and 30%, providing a comparative insight into the structural dynamics under varying chemical environments. Across all samples, the characteristic D and G peaks, were observed. The G peak remained consistent at 1600 cm^{-1} for all samples. Conversely, a notable shift in the position of the D peak, was observed with

increasing hydrogen proportions. For the powder treated with 0.5% hydrogen, the D peak was located at 1376 cm^{-1}, progressively shifting to 1361 cm^{-1} for those with 5% and 10% hydrogen, and ultimately reaching 1350 cm^{-1} for the sample exposed to 30% hydrogen. The intensity ratio of these peaks, I(D)/I(G), provides further insights into the degree of disorder within the carbon matrices. The calculated ratios were 0.85 for 0.5% hydrogen, reducing to 0.76 and 0.77 for 5% and 10% hydrogen respectively, and remaining at 0.77 for 30% hydrogen. This decrease in the I(D)/I(G) ratio with increasing hydrogen concentration suggests an interaction between hydrogen and the carbon layers, potentially influencing the degree of disorder and the graphitization process. Additionally, the presence of broad peaks at 2700 cm^{-1}, 2950 cm^{-1}, and 3200 cm^{-1}, was detected across the spectra. These peaks were particularly pronounced and better defined in the sample with 30% hydrogen proportion, suggesting enhanced structural changes or interactions within the carbon structure at higher hydrogen concentrations.

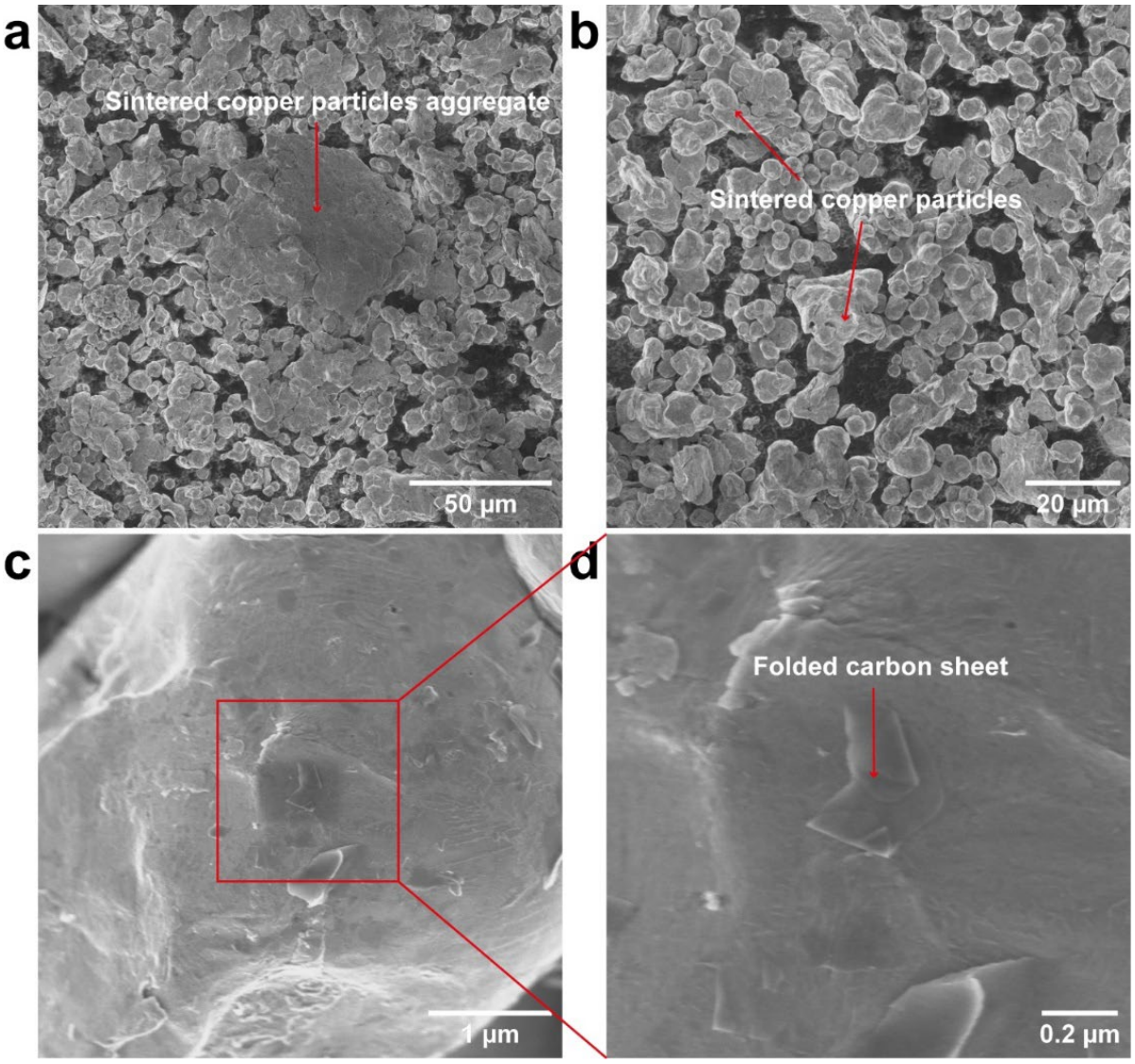

Figure 2.23 – General SEM characterization of the rCu200C@0.65% after 60min

of graphitization: ***a*** *and* ***b*** *broad observations of the powder,* ***c*** *and* ***d*** *observation of a particle and its associated magnification*

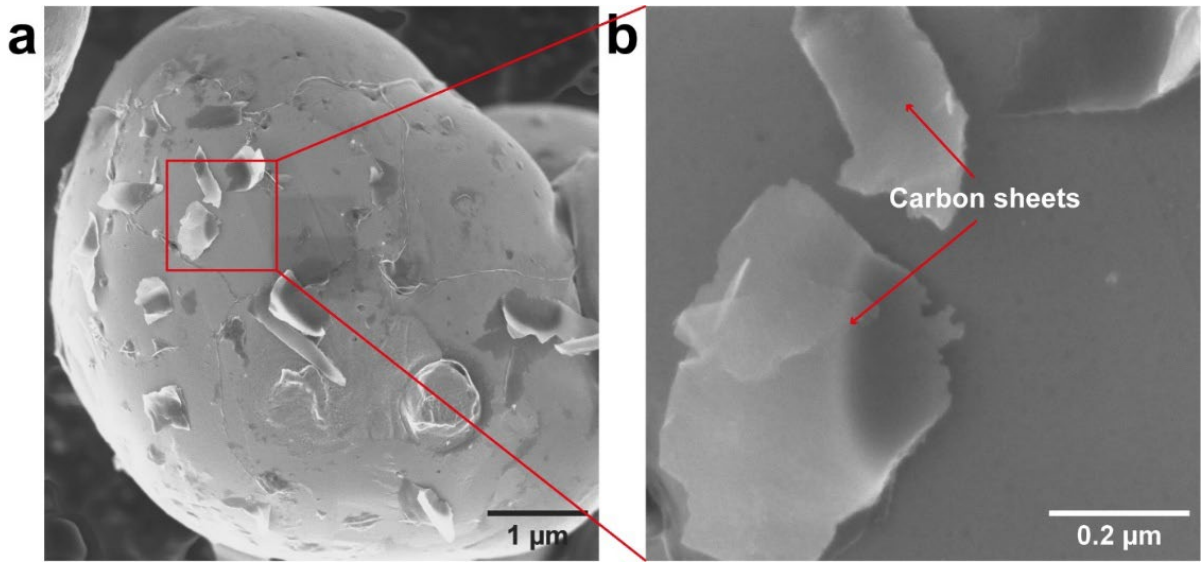

Figure 2.24 – General SEM characterization of the rCu200C@2.00% after 60min of graphitization: ***a*** *observation of a particle and* ***b*** *its associated magnification*

Figures 2.23 and 2.24 provide an examination through SEM of the outcomes resulting from the graphitization of copper powders coated with sucrose concentrations of 0.65wt% and 2.00wt%, respectively, each subjected to a 60 minutes graphitization process.

In the case of the rCu200C@0.65% powder, Figure 2.23 illustrates the challenges encountered post-graphitization. Figures 2.23 (a) and (b) depict the aftermath of the treatment, where the powder predominantly underwent sintering, necessitating substantial mechanical grinding to disaggregate the material. This intensive processing resulted in the loss of the distinct powdery nature of the material, leading to the formation of several sintered copper particle aggregates. The surfaces of these particles exhibit considerable roughness, a direct consequence of the grinding. Figure 2.23 (c) showcases a particle that has experienced a loss of its carbon coating, with Figure 2.23 (d) providing a magnified view where a folded carbon sheet is discernible. These observations suggest that the reduced sucrose content coupled with extended exposure to high temperatures adversely affects the structural integrity and morphology of the powder.

Conversely, Figure 2.24 focuses on rCu200C@2.00% powder. Figure 2.24 (a) presents a close-up view of a particle from this batch, revealing the presence of multiple carbon sheets adorning its surface. The associated magnification in Figure 2.24 (b) further highlights these carbon structures, providing evidence of a more substantial and intact carbon coating compared to the rCu200C@0.65% powder.

The observed phenomena, particularly with the lower sucrose concentration leading to significant sintering, can be attributed to several factors. Prolonged exposure

to the graphitization temperature of 1000°C may facilitate the decomposition of the carbon coating, particularly under suboptimal sucrose concentrations, leading to the exposure and subsequent sintering of the copper particles. The hypothesis that atmospheric argon molecules may contribute to the dislodging of carbon from the particle surfaces under these conditions warrants consideration. Additionally, the potential presence of oxygen traces in the argon and hydrogen gases used could catalyze the oxidation of the carbon to form CO_2 or CO, further exacerbating the loss of carbon coverage and promoting the sintering process.

2.5 CONCLUSIONS

In this study, carbon-coated copper microparticles were synthesized with the primary objective of generating graphene-coated copper microparticles, thereby facilitating the creation of a high-quality copper-graphene composite material. The experimental investigations captioned the pivotal role of temperature and duration in the effective reduction of copper oxide layers present on the surface of the particles. Notably, these parameters were found to significantly influence the extent of oxide reduction, highlighting the necessity for temperature management to prevent premature sintering of the particles. Elevated temperatures were observed to complicate the subsequent mechanical processing steps, such as grinding and sieving, thereby potentially introducing defects and impurities into the powder.

Comparative analysis of the synthesis routes revealed distinct outcomes concerning the carbon structure on the copper particles. The first approach predominantly yielded an amorphous carbon coating, whereas the second route facilitated an enhancement in carbon quality, indicating the impact of the synthesis pathway on the final material properties.

Modifications in the initial sucrose content, hydrogen flow rates, and exposure times were explored to assess their effects on the carbonization and graphitization processes. These parameters were found to have implications for the structural integrity and quality of the resultant carbon coatings.

Despite the progress made, the results indicate that further work is necessary to achieve the deposition of high-quality, monolayer graphene on the copper microparticles. To this end, several strategies are proposed for future research directions:

The reduction of copper oxide should be approached at lower temperatures, potentially employing plasma-enhanced techniques or chemical reduction within a solution, to mitigate the risk of particle sintering and maintain particle integrity.

For a more authentic CVD process and to ensure a continuous supply of carbon, the introduction of methane should be precisely controlled during the graphitization phase, potentially enhancing the formation of high-quality graphene layers.

Operating under reduced pressure conditions could serve to diminish the oxygen content within the reaction environment, thereby minimizing unwanted reactions and improving the overall quality of the carbon coatings.

In summary, the findings from this study contribute to the understanding of the parameters influencing the synthesis of graphene-coated copper microparticles. The proposed future directions aim to address the existing challenges and pave the way for the successful integration of graphene and copper in high-performance composite materials.

CHAPTER 3 – DENSIFICATION OF THE CARBON COATED COPPER PARTICLES USING SPS

3.1 INTRODUCTION

In the previous chapter, carbon coated copper particles were made instead of graphene coated copper particles. The fabrication of graphene remains challenging.

The core objective of this Chapter 3 is to evaluate and compare the sintering behaviors of pure copper powders and carbon-coated copper powders. Through observing the microstructures and measuring the relative densities achieved, this research seeks to ascertain the effectiveness of SPS under two specific parameter sets: 800°C with 50 MPa pressure and 900°C with 100 MPa pressure. These conditions were chosen to optimize the density and incease the electrical conductivity by reducing the interfacial distances between copper and carbon.

The initial part of this section focuses on the interpretation of monitoring curves generated during the SPS densification process, encompassing temperature, pressure, vacuum, and displacement rate. These parameters are crucial for understand the dynamics of the SPS process, offering insights into the interplay between these variables and the consequent properties of the densified discs.

Following this, an assessment of the density for each sintered disc is conducted, with comparative analysis against the standard reference of Cu-ETP. This comparison is instrumental in evaluating the relative success of the densification efforts, providing a quantitative measure of the achieved material density vis-à-vis that of standard pure copper.

In further detail, the microstructural characteristics of both the pure copper and carbon-coated samples are scrutinized utilizing BS) imaging techniques, specifically employing electron channeling contrast to discern crystalline features. This approach allows for a precise examination of the crystalline structure and phase distributions within the sintered samples, highlighting the distinct microstructural elements that arise from the incorporation of carbon and the sintering process.

Lastly, the section advances into nanostructural analyses conducted through Transmission Electron Microscopy (TEM). This investigation aims to explore the grain boundaries and the distribution of carbon within the composite samples at the nanoscale. By delving into the nanostructural realm, the TEM analysis sheds light on how carbon interfaces with copper at an atomic level, influencing the overall structural and mechanical properties of the composites.

3.2 METHODS AND MATERIALS

3.2.1 Methods

The consolidation and densification processes of the synthesized powders were executed employing the Dr. Sinter 515S apparatus, provided by FUJI.

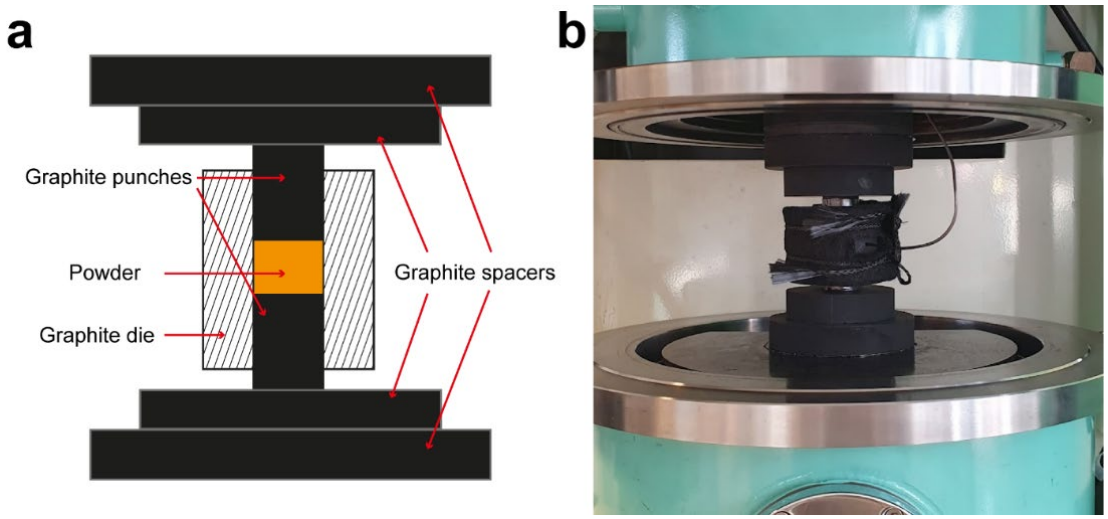

*Figure 3.1 – **a** schematics of the SPS process and **b** digital image of the setup*

Pure copper powders previously reduced at 200°C and 300°C, carbon-coated copper particles, and mixtures of pure copper powder with carbon-coated powder were densified to evaluate the effects of pretreatments and various densification parameters on the resultant discs. The samples derived from pure copper powders subjected to thermal reduction are designated as rCu200C and rCu300C, corresponding to reduced copper powders at 200°C and 300°C, respectively.

Additionally, carbon-coated copper powders are labeled as rCu200C@0.65% and rCu200C@2.00%, representing the copper powders reduced at 200°C and subsequently coated with 0.65wt% and 2.00wt% sucrose, respectively. Furthermore, the mixtures of pure copper powder with carbon-coated copper powder are identified as Cu-CuC@0.50%, Cu-CuC@1.00%, Cu-CuC@5.00%, and Cu-CuC@25.0%, indicating varied compositions; these consist of pure copper powder combined with 0.50%, 1.00%, 5.00%, and 25.0% carbon-coated copper powder, respectively.

Each disc, whether composed of pure copper powder or copper-carbon composite powders, was prepared from 6.0 g of the respective powder. Utilizing a graphite die with a 20 mm internal diameter, accompanied by two graphite punches, the densification process yielded discs measuring 20 mm in diameter and 2.0 mm in thickness. This standardized geometry facilitates uniformity across experimental samples and ensures comparability of results.

The initial stage of the densification involves pre-compression of the powders at 10 MPa. This pre-compression is important to establish adequate contact between

the powder and the punches, thereby facilitating the effective transmission of pulsed electrical current through the sample during subsequent sintering processes. Following pre-compression, two distinct sintering parameter sets were employed:

The first set involves heating to a temperature setpoint of 800°C at a rate of 100°C/min. Upon reaching the designated temperature, the powder is then subjected to a compression pressure of 50 MPa for a duration of 10 minutes, ensuring the consolidation and densification of the disc.

The second parameter set targets a higher temperature setpoint of 900°C, with the same heating rate of 100°C/min. Once the temperature of 880°C is attained, the compression pressure is increased to 100 MPa, maintained for 10 minutes to facilitate the sintering process.

Upon completion of the densification phase, the resultant discs undergo a cleaning process using silicon carbide paper to remove any surface irregularities or residual debris. This step is essential for achieving a smooth surface finish, imperative for accurate density measurements and subsequent analyses.

3.2.2 Characterizations

The determination of the density of the sintered specimens was conducted using the ALJ 160-4NM density measurement system from Kern, equipped with an Archimedes' kit. This is a simple but efficient method for assessing the porosity and the overall quality of the densification process, providing data on the structural integrity of the consolidated powders. Those density evaluations were conducted employing this kit, with a total of five measurements taken to ensure statistical reliability and accuracy. This series of measurements allows for the calculation of an average density, providing critical data on the effectiveness of the sintering parameters and the material's porosity.

Furthermore, to establish a benchmark density for pure copper, a reference sample was extracted from a commercial plate of Electrolytic Tough Pitch Copper (Cu-ETP). This sample underwent the same density measurement protocol, with five individual readings taken to ascertain an accurate reference value. This reference density serves as a comparator for assessing the relative densities of the sintered discs, enabling a comprehensive understanding of the densification outcomes in relation to the theoretical maximum for pure copper.

Microstructural analyses were carried out employing Transmission Electron Microscopy (TEM) utilizing the TITAN microscope from FEI. This instrument facilitated high-resolution imaging and detailed examination of the nanoscale structures within the materials, providing insights into the morphological characteristics and crystalline architecture.

Furthermore, Scanning Electron Microscopy (SEM) and Focused Ion Beam (FIB) techniques were employed for surface and cross-sectional analyses of the specimens. These investigations were conducted using the Leo 1550 system with the Gemini column from Zeiss, and the SEM/FIB HELIOS 660 system from FEI, respectively. The SEM analysis utilized secondary electron (SE) and backscattered electron (BSE) detectors to yield topographical and compositional information. Meanwhile, the FIB was utilized not only for precision sample machining but also for generating secondary electron images resulting from ion-sample interactions, thereby providing a multifaceted characterization of the microstructures.

3.3 Results and Discussions

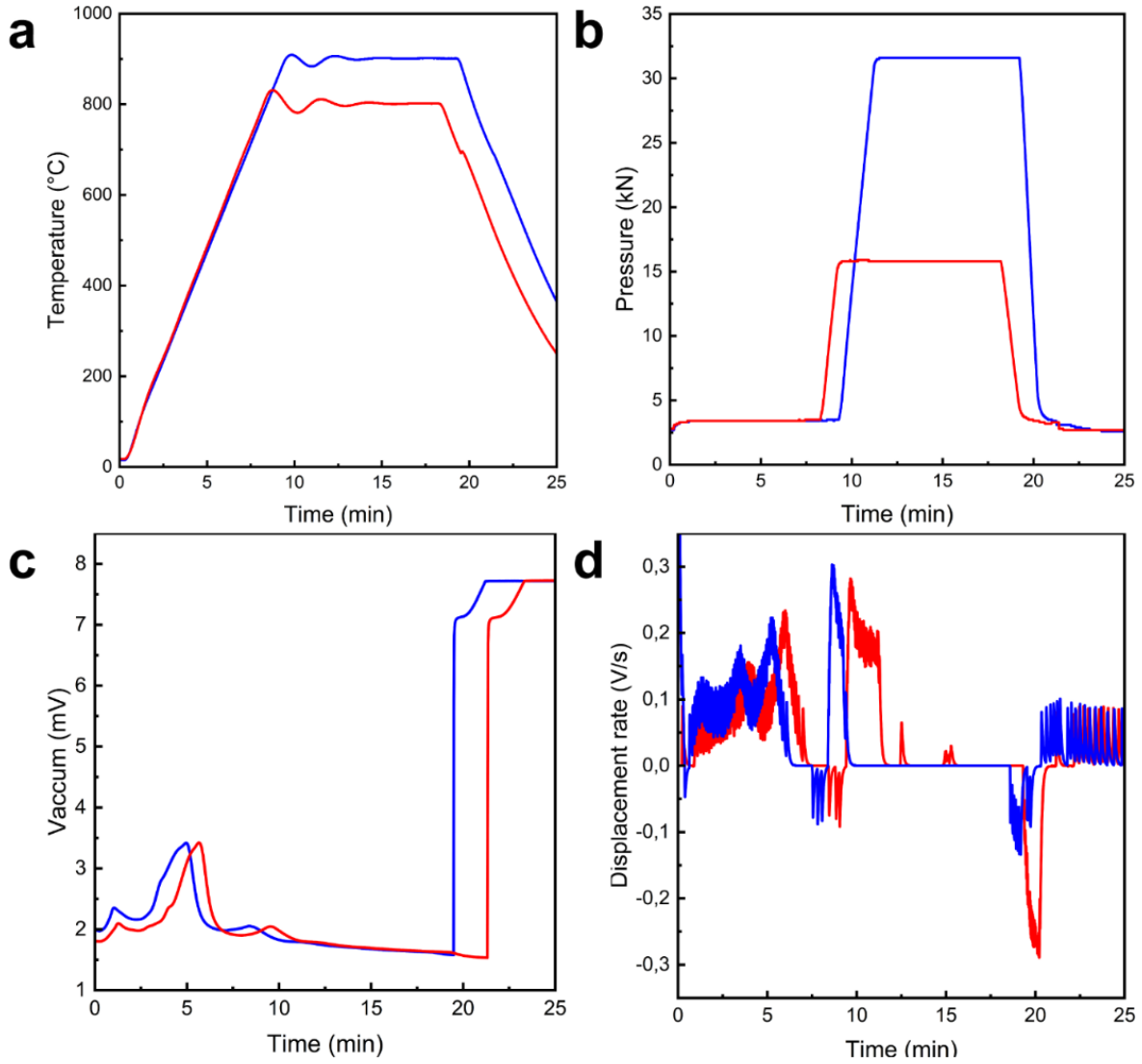

*Figure 3.2 – SPS curves for sintering rCu200C powders under the following conditions: 800°C – 50MPa and at 900°C – 100MPa **a** Temperature, **b** Pressure, **c** Vacuum level and **d** Displacement rate*

Figure 3.2 delineates the SPS densification monitoring curves for the pure copper samples, denoted as rCu200C, with an analogous behavior observed for the rCu300C samples but the figures are not displayed here. These curves represent the dynamic responses under two distinct sintering parameter sets: 800°C with 50MPa and 900°C with 100MPa. The monitoring parameters, including sintering temperature, pressure, vacuum level, and displacement rate, are systematically presented across Figure 3.2 (a) to (d). Notably, both samples exhibited adherence to the predefined temperature and pressure trajectories without any significant deviations. A peculiar observation was made between the temperatures of 250°C and 550°C, where gas release was detected during the sintering process. This phenomenon is postulated to be attributable to the liberation of hydrogen, possibly sequestered within the copper lattice, a consequence of prior exposure to a reducing atmosphere rich in hydrogen.

For the initial sintering parameter set, densification commenced at 800°C, maintaining a hold time of 10 minutes. However, the displacement rate curve indicated that densification effectively concluded after only 1.68 minutes. Conversely, under the second parameter set, despite initiating compression at 880°C with a similar hold duration, the displacement rate suggested that the densification process extended to 2.38 minutes, a slight increase attributable to the programmed compression duration of two minutes.

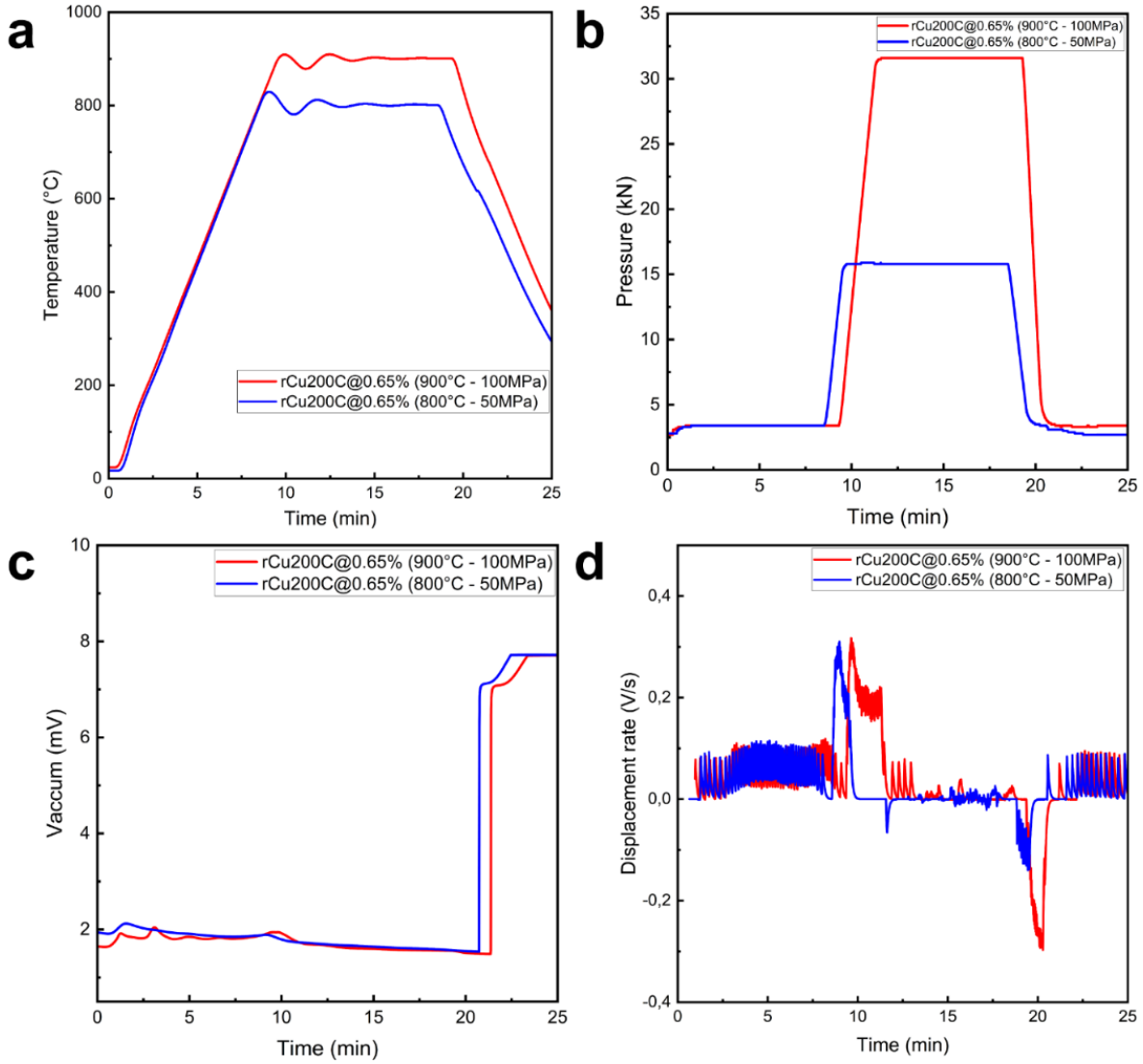

Figure 3.3 – SPS curves for sintering rCu200C@0.65% under the following conditions: 800°C – 50MPa and at 900°C – 100MPa ***a*** *Temperature,* ***b*** *Pressure,* ***c*** *Vacuum level and* ***d*** *Displacement rate*

Figure 3.3 portrays the SPS densification monitoring curves for the composite samples, specifically rCu200C@0.65%, with consistent observations for the rCu200C@2.00% samples which are not displayed here. Similar to the pure copper powders, these composites were evaluated under the two aforementioned sintering

conditions. In contrast to the pure copper samples, no gas release was observed between 250°C and 550°C during sintering, which may reflect the different physicochemical interactions occurring in the presence of the carbon component. Under the first set of sintering conditions for the composite samples, densification initiated at 800°C with a designated holding time of 10 minutes, yet the displacement data indicated completion of densification after merely 1.57 minutes. In the scenario with the second set of sintering parameters, the densification onset at 880°C also culminated slightly earlier than the set hold time, concluding after 2.35 minutes, again reflecting the tailored compression timeline. These observations reveal that, aside from the specific gas release phenomena observed in pure copper samples, the densification behaviors of both the pure copper and carbon-coated copper powders were similar under equivalent processing conditions.

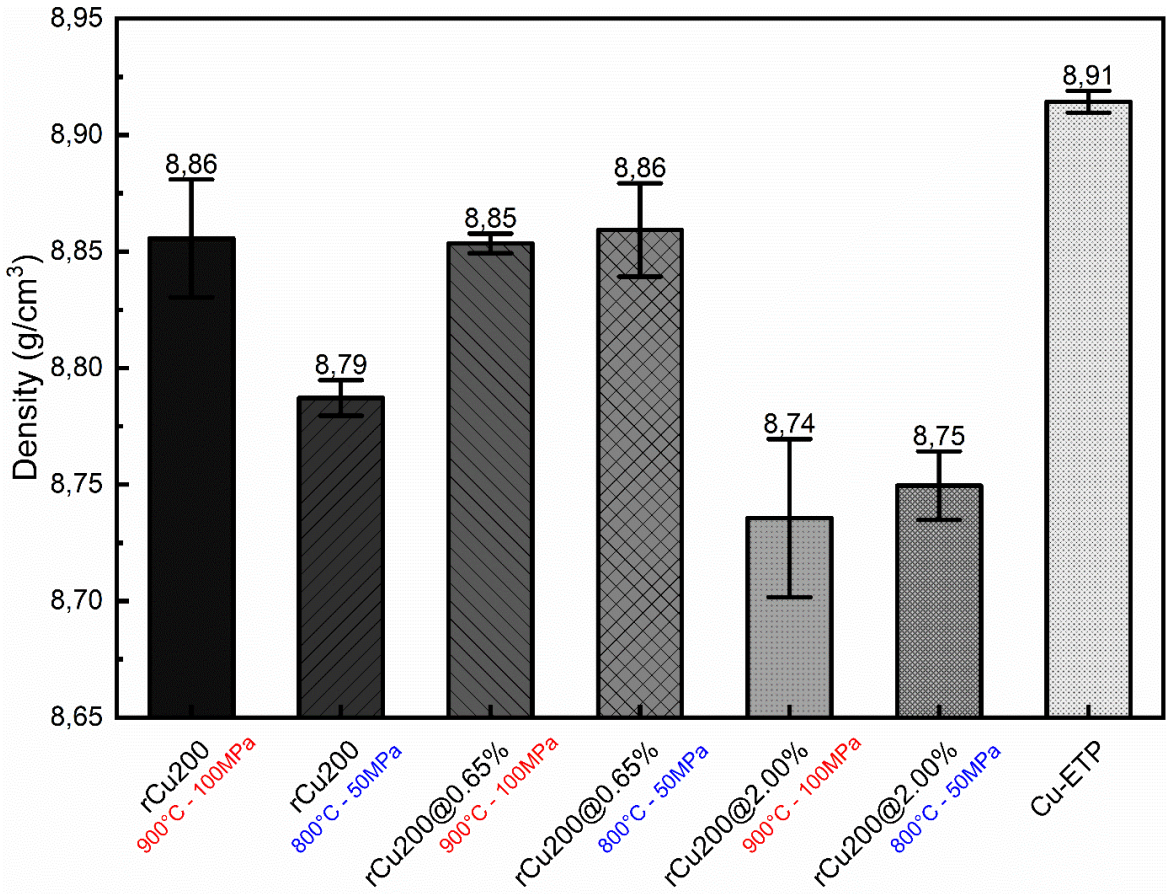

Figure 3.4 – Chart of the measured densities of the composite samples versus the Cu-ETP sample

Subsequent to the densification process, the density values of the sintered samples were determined. Figure 3.4 encapsulates the comparative analysis of the densities obtained for the pure copper samples, rCu200C, against those of the composite samples, rCu200C@0.65% and rCu200C@2.00%, juxtaposed with the benchmark density of commercial copper, specifically Cu-ETP.

For the pure copper samples, densities were observed to increment from 8.79 g/cm³ to 8.86 g/cm³ as the sintering parameters escalated, corresponding to 98.57%

and 99.34% of the Cu-ETP density, respectively. This enhancement in density with elevated sintering parameters shows the effectiveness of the densification process in approaching the theoretical maximum density of copper

In contrast, the composite sample designated as rCu200C@0.65% exhibited densities of 8.85 g/cm^3 and 8.86 g/cm^3 under the sintering conditions of 800°C with 50MPa and 900°C with 100MPa, respectively. These values translate to 99.38% and 99.31% of the Cu-ETP standard density. The negligible discrepancy of merely 0.065% between these two conditions suggests that the densification of this composite variant remains relatively stable across the differing sintering parameters.

Similarly, the second composite configuration, rCu200C@2.00%, manifested densities of 8.75 g/cm^3 and 8.74 g/cm^3, achieving 98.15% and 97.99% of the Cu-ETP density under the same respective sintering conditions. The minor variance of 0.16% between these densities suggests a consistency in the material's response to the sintering parameters, albeit at a slightly reduced densification level compared to the rCu200C@0.65% samples.

Analyzing these findings, it is evident that the pure copper samples exhibit an increase in density with elevated sintering parameters, indicating that higher temperatures and pressures contribute to more effective particle consolidation. Conversely, the composite samples displayed marginal variations in density with changes in sintering conditions, suggesting a lesser influence of these parameters on the final density. Notably, the sample with a lower carbon content, rCu200C@0.65%, attained a higher density compared to the rCu200C@2.00% variant. This discrepancy can be attributed to the reduced carbon presence, which potentially facilitates a more effective copper particle consolidation, highlighting the impact of carbon content on the densification outcomes of copper-carbon composites.

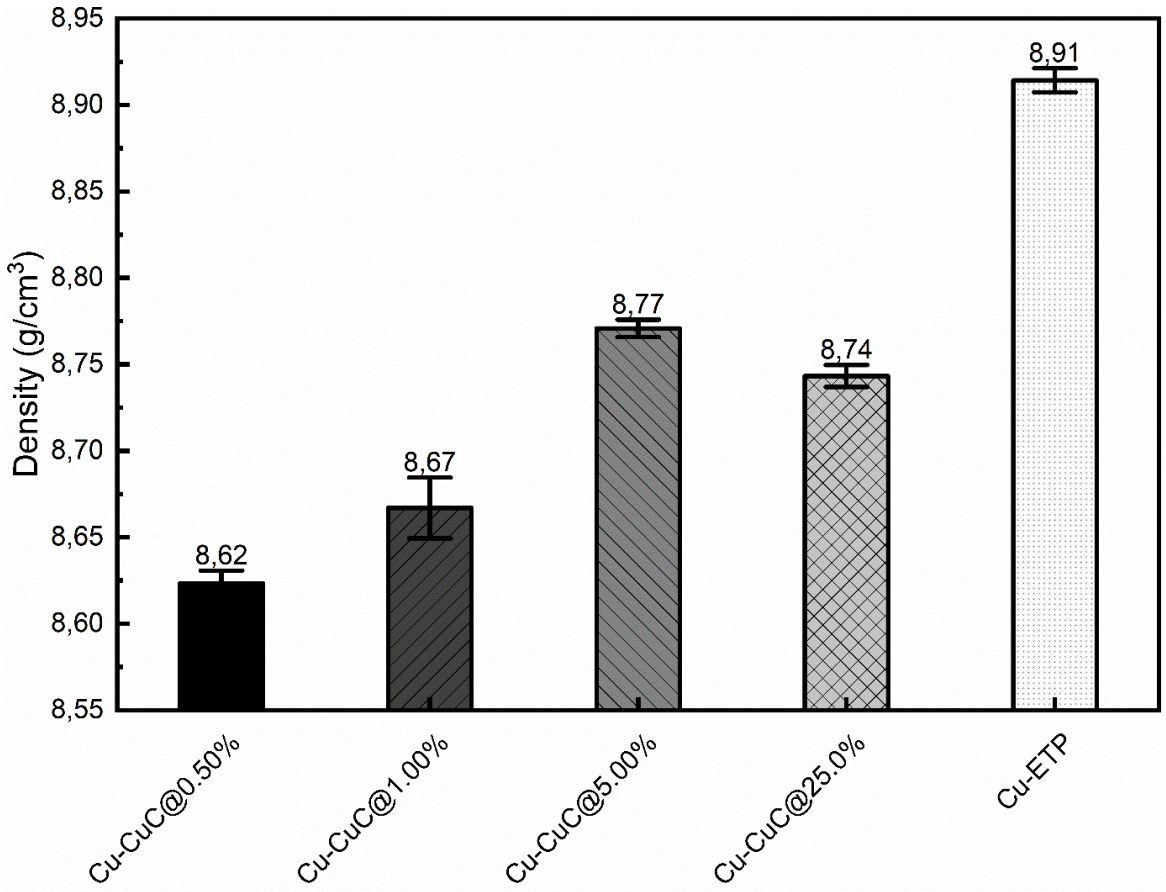

Figure 3.5 – Chart of the measured densities of the mixtures

Subsequently, the densities of various pure copper and carbon-coated copper powder mixtures, specifically designated as Cu-CuC@0.50%, Cu-CuC@1.00%, Cu-CuC@5.00%, and Cu-CuC@25.0%, were evaluated and juxtaposed with the density of Electrolytic Tough Pitch Copper (Cu-ETP). These mixtures were all subjected to a singular set of sintering parameters, specifically 900°C and 100 MPa. Figure 3.5 presents the density measurements derived from these experimental conditions.

Upon examination of the data, a notable observation emerges: Cu-CuC@0.50% and Cu-CuC@1.00%, which contain the lowest proportions of carbon-coated copper particles, exhibit significantly reduced densities of 8.62 g/cm³ and 8.67 g/cm³, corresponding to 96.74% and 97.22% of pure copper density, respectively. This stark contrast in density, particularly when compared to the pure copper, composite, and standard Cu-ETP benchmarks, suggests potential issues within the densification process. The diminished densities in these mixtures could be attributed to suboptimal dispersion of the carbon-coated particles within the copper matrix, potentially leading to particle agglomeration and segregation. Such phenomena would inherently result in the formation of porosities, thereby undermining the overall densification and facilitating undesirable copper recrystallization.

Conversely, Cu-CuC@5.00%, and Cu-CuC@25.0% exhibit appreciably higher densities, recorded at 8.77 g/cm³ and 8.74 g/cm³, translating to 98.39% and 98.08% of the standard copper density, respectively. These values are comparable to the densities

obtained for the rCu200C@2.00% samples, indicating a more successful densification process. Notably, Cu-CuC@5.00% demonstrates a marginally higher density compared to Cu-CuC@25.0%. This variation could be rationalized by the reduced content of carbon-coated copper particles in Cu-CuC@5.00%, suggesting that an optimal balance of carbon content may facilitate better matrix consolidation and reduced porosity, thereby enhancing the overall density.

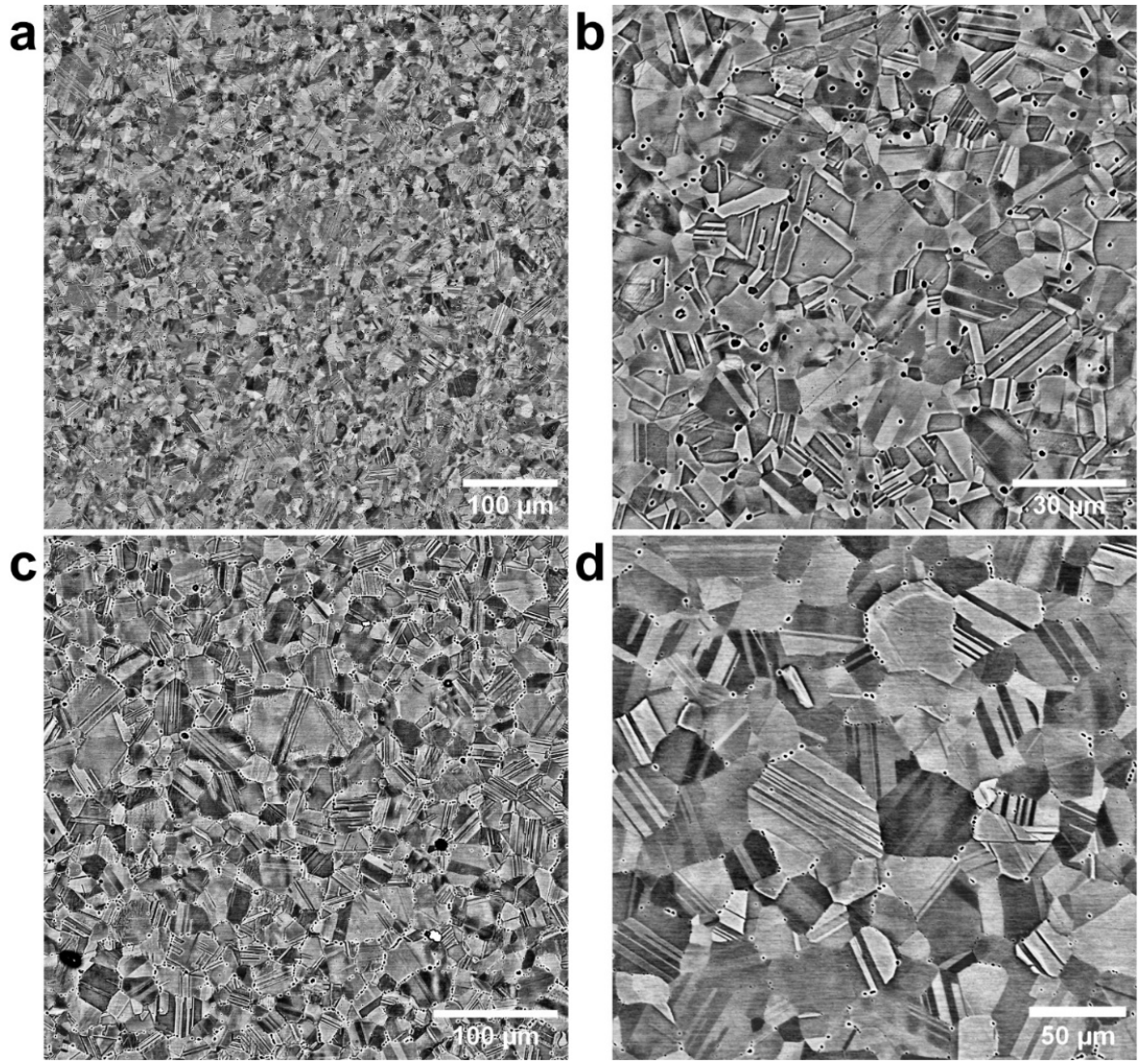

*Figure 3.6 – SEM observations of the microstructures of **a** rCu200C (800°C - 50MPa) and **b** its associated magnification, **c** rCu200C (900°C - 100MPa) and its associated magnification*

Subsequent to the density evaluations, attention is redirected towards the microstructural characteristics of the pure copper samples. Utilizing Electron Channeling Contrast Imaging (ECCI), Figure 3.6 delineates the microstructures of the rCu200C samples subjected to sintering at the conditions of 800°C - 50MPa and 900°C

- 100MPa, respectively.

The microstructural examination reveals a variance in average grain size contingent upon the applied sintering parameters. Specifically, the rCu200C sample sintered at 800°C - 50MPa exhibited an average grain size of approximately 20μm. In contrast, the sample exposed to the heightened sintering condition of 900°C - 100MPa displayed an enlarged average grain size of approximately 30μm. This observation indicates that the escalation in sintering parameters, notably temperature and pressure, correlates with a substantial increase in grain size, estimated at an increment of approximately 10μm.

Further in-depth analysis is provided by Figure 3.6 (b), showcasing a closer view of the rCu200C microstructure post-sintering at 800°C - 50MPa. This image reveals the presence of randomly dispersed porosities within the microstructure. Conversely, Figure 3.6 (d) offers a magnified perspective of the rCu200C sample sintered at 900°C - 100MPa, where porosities appear predominantly localized at the grain boundaries. These distinctions suggest that heightened sintering parameters facilitate the migration of porosities towards the grain boundaries, potentially enhancing the overall density and structural integrity of the material by reducing intra-granular porosity.

Additionally, both samples exhibit a significant presence of twinning within the microstructure. This feature is notable for its potential to reinforce the material, attributed primarily to the application of high pressure during the sintering process. Twinning within the copper grains could contribute to an improved mechanical strength and resistance to deformation, aligning with traditional metallurgical principles.

These microstructural analyses, when correlated with the earlier density measurements, present a coherent narrative. The observed enhancements in density, particularly for the sample sintered at 900°C - 100MPa, are consistent with the microstructural evolution, including grain growth and the localization of porosities at grain boundaries. These findings highlight the interplay between sintering parameters and the resultant microstructural features, offering valuable insights into the mechanisms underpinning the densification and strengthening of pure copper samples during the SPS process.

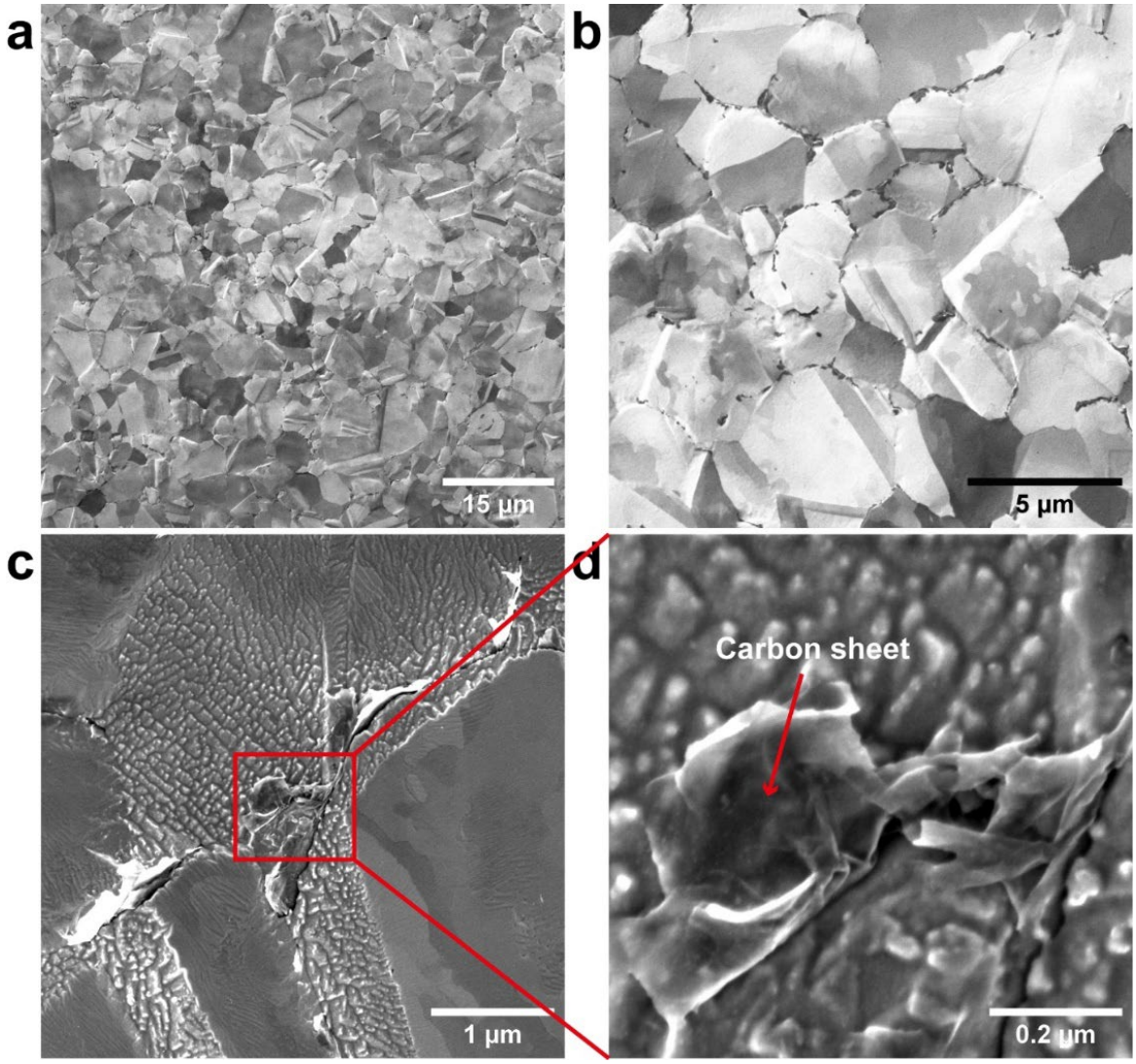

*Figure 3.7 – SEM observations of the microstructure of rCu200C@0.65%(900°C - 100MPa) using ICCI: **a** microstructure of the sample and **b** its associated magnification, **c** observation of a grain boundary and **d** its associated magnification*

In preceding sections, it was noted that the densities of composite samples remained invariant across different sintering parameters, suggesting minimal influence on the overall structural consolidation of these materials. This observation leads to the inference that the microstructural attributes of all composite samples remain consistent, irrespective of the applied sintering conditions. This consistency is due to the presence of carbon at the grain boundaries, which acts as a barrier to copper diffusion, thereby inhibiting crystal growth or recrystallization within the matrix.

Figure 3.7 showcases the microstructure of the rCu200C@0.65% composite sample, which was subjected to sintering at 900°C – 100MPa. The microstructural characterization employed in this instance utilizes Ion Channeling Contrast Imaging (ICCI), as depicted in Figures 3.7 (a) and (b). This observation reveals that the grains within the composite are equiaxed and maintain a circular profile, mirroring the spherical morphology of the initial carbon-coated copper particles. The average grain size within this composite matrix is determined to be approximately 3µm. Notably, this

microstructural examination reveals minimal to no twinning within the grains, distinguishing it from the microstructures observed in pure copper samples. Additionally, it is important to note that no visible porosities were detected within the observed microstructures, indicating a high level of densification and structural integrity within the composite samples.

Further observations of the microstructure is achieved through the use of secondary electrons for ultra-high-resolution imaging, as presented in Figures 7 (c) and (d). These figures focus on a grain boundary and its magnified view. Here, one can distinctly observe a thin carbon layer protruding from the grain boundary, providing direct evidence of the carbon's presence and its role within the sintered matrix. This visualization suggests that the sintering process facilitates the crystallization of the carbon, allowing it to form a definitive boundary that impacts the overall microstructural dynamics of the composite.

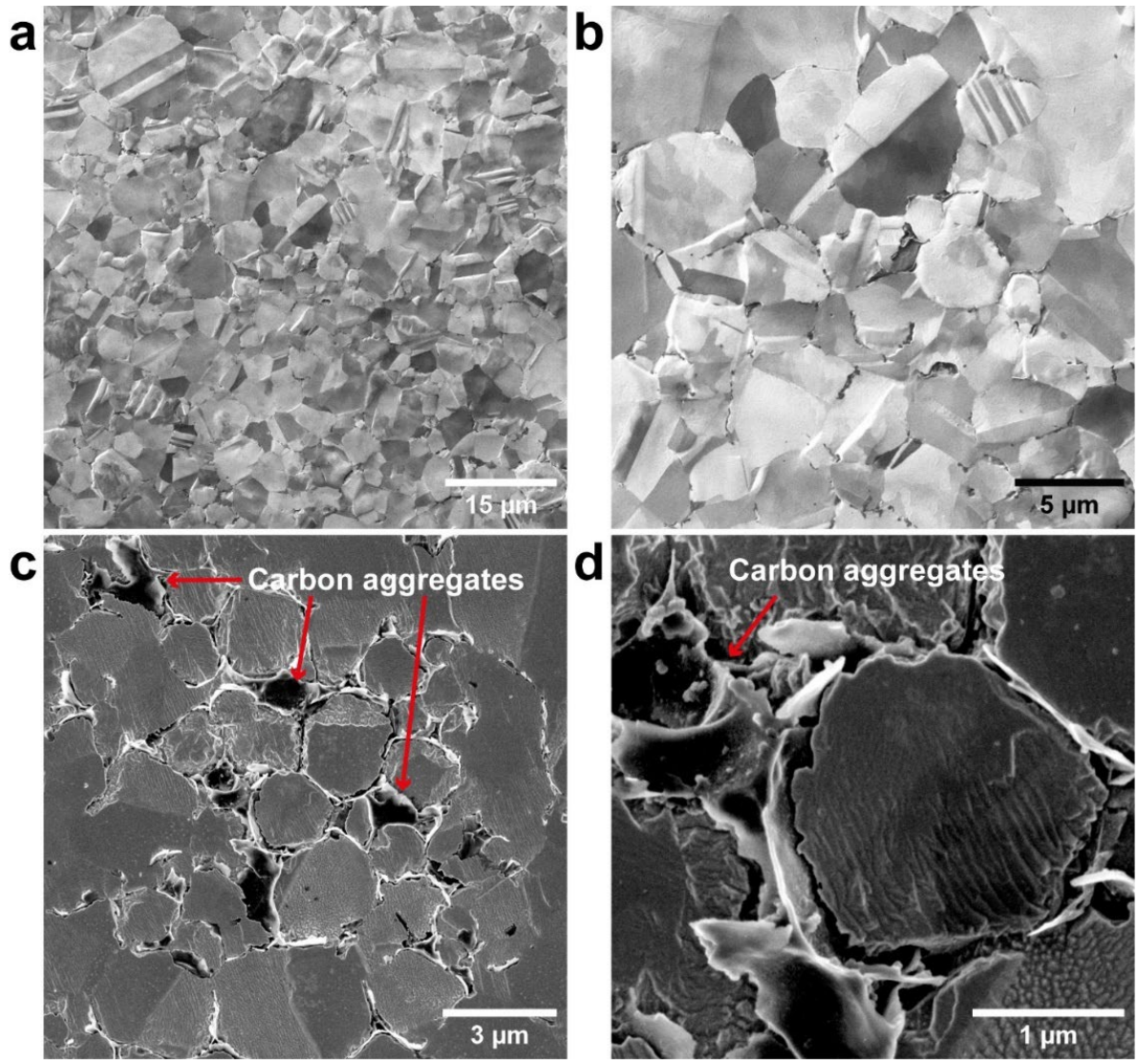

*Figure 3.8 – SEM observations of the microstructure of rCu200C@2.00%(900°C - 100MPa) using ICCI: **a** microstructure of the sample and **b** its associated magnification, **c** observation of a grain boundary and **d** its associated magnification*

Figure 3.8 provides a detailed examination of the microstructure of the rCu200C@2.00% composite sample, which underwent sintering at 900°C – 100MPa, employing identical analytical methodologies as previously described. Observations from Figures 3.8 (a) and (b) reveal that the average grain size remains consistent at approximately 3µm, mirroring the granular dimensions noted in prior analyses. This uniformity in grain size supports the hypothesis that the microstructural stability is maintained across different composite formulations due to the impediment of copper diffusion, thereby restricting grain growth.

Further microscopic investigation is presented in Figures 3.8 (c) and (d), where imaging via secondary electrons and its subsequent magnification provides deeper insight. Notably, in this sample, characterized by a higher carbon content, there is a visible presence of substantial carbon aggregates located at the grain boundaries. The pronounced aggregation of carbon within these regions corroborates the supposition that increased carbon presence contributes to the altered microstructural dynamics observed in this composite variant.

The substantial carbon accumulation at the grain boundaries elucidates the lower density metrics associated with this sample, as compared to its lower carbon-content counterparts. The excessive carbon acts as a barrier to densification, leading to an increase in porosity and a reduction in the overall compactness of the material. This significant presence of carbon, particularly in aggregated form, is anticipated to influence the mechanical, electrical, and thermal properties of the composite, potentially impacting its applicability and performance in intended use cases.

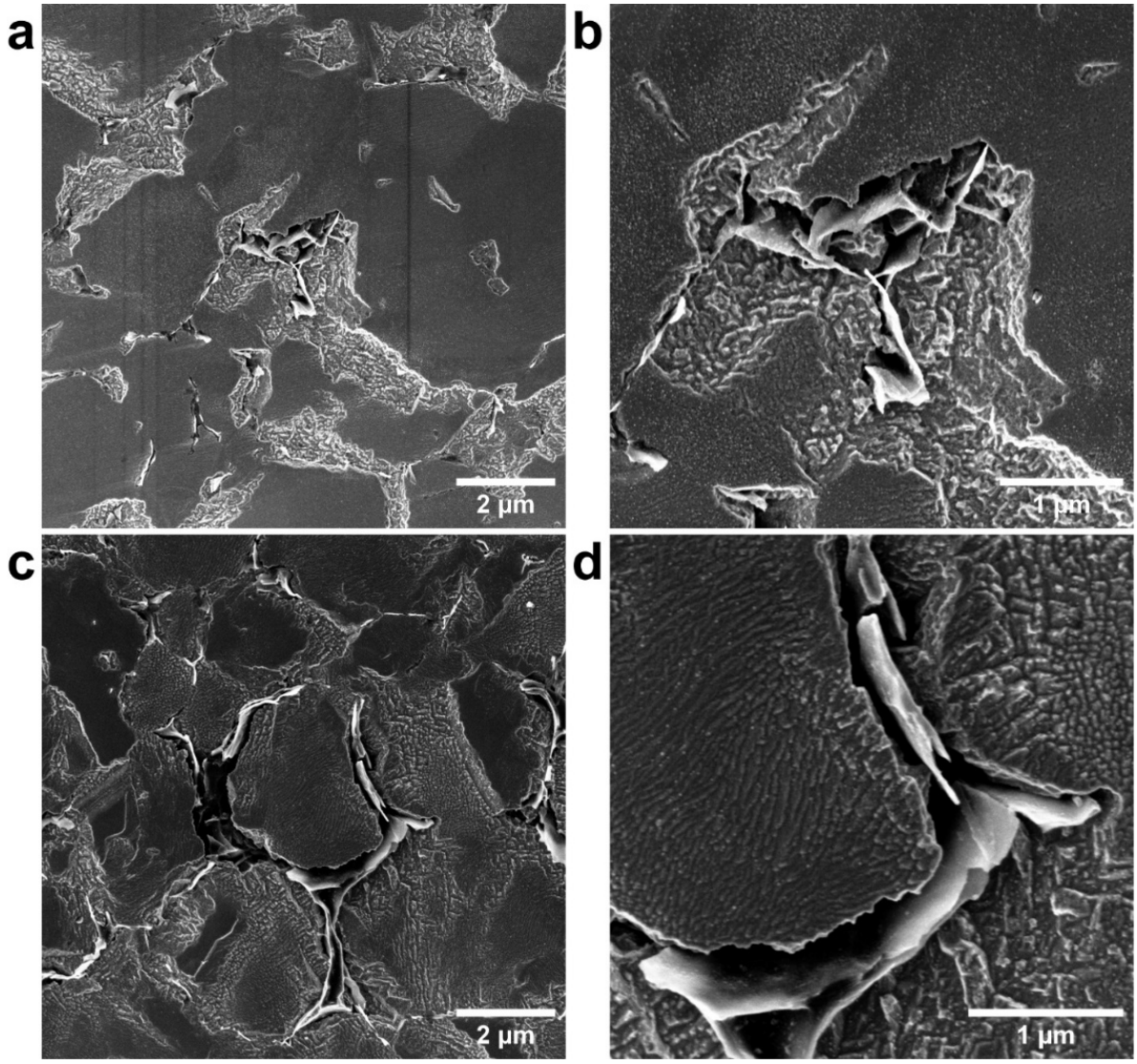

*Figure 3.9 – SEM observations : **a** rCu200C@0.65% and **b** its associated magnification, **c** rCu200C@2.00% and **d** its associated magnification. The powders were sintered at 800°C and 50MPa*

Figure 3.9 offers a detailed portrayal of the microstructures of the rCu200C@0.65% and rCu200C@2.00% composite samples, both of which were subjected to sintering at 800°C and 50MPa. For this set of parameters, the grain size is the same with an average grain size of 3.0µm. The provided micrographs serve to complement and reinforce the analytical insights previously derived, illustrating the microstructural consistency and characteristics that have been discussed in the context of these particular sintering parameters.

These images underscore the distinct microstructural attributes inherent to each composite variation, reflective of their differing carbon contents and the effects of the specific sintering conditions applied. While serving primarily as corroborative visuals, these images validate and reinforce the prior conclusions regarding the role of carbon content in influencing the microstructural integrity, porosity, and overall density of the copper-carbon composites.

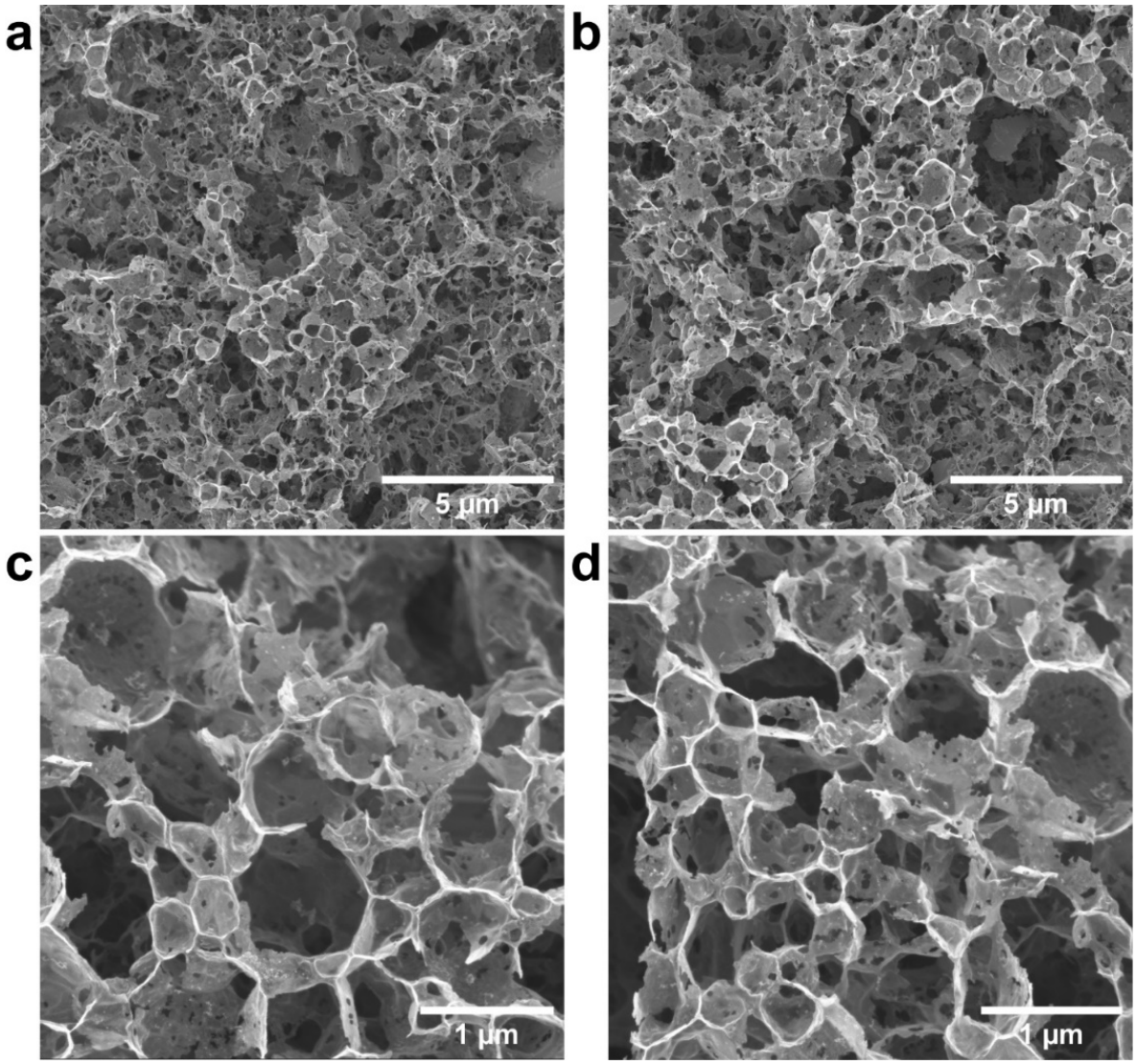

Figure 3.10 – Microstructure of rCu200C@0.65%, each subfigure is an observation at a different location

Figure 3.10 showcases the microstructure of the rCu200C@0.65% sample using SEM following the dissolution of the copper matrix using a solution of ferric chloride and hydrochloric acid. This dissolution unveils the carbon structure formerly interlaced at the grain boundaries, now isolated for in-depth analysis. The SEM images delineated in Figure 3.10 reveal that the carbon maintains a predominantly spherical shape with a distinctive shell-like configuration, indicative of the original morphology of the carbon-coated copper particles used in the composite's fabrication. This morphological characteristic is vital for understanding the structural disposition of carbon within the composite matrix.

Additionally, the SEM analysis brings to light numerous voids within the carbon structure, which may be attributable to interfacial shear stress encountered during the sintering process or potentially derive from the intrinsic qualities of the carbon precursor utilized in the sample's construction. The presence of these voids underscores potential areas of structural weakness within the carbon network.

Furthermore, the microstructural investigation, facilitated by SEM, indicates incomplete fusion between adjacent carbon walls, revealing a discontinuous carbon framework. This particular observation is crucial, as the integrity of these carbon connections is paramount for ensuring cohesive structural support and optimal electrical conductivity within the composite.

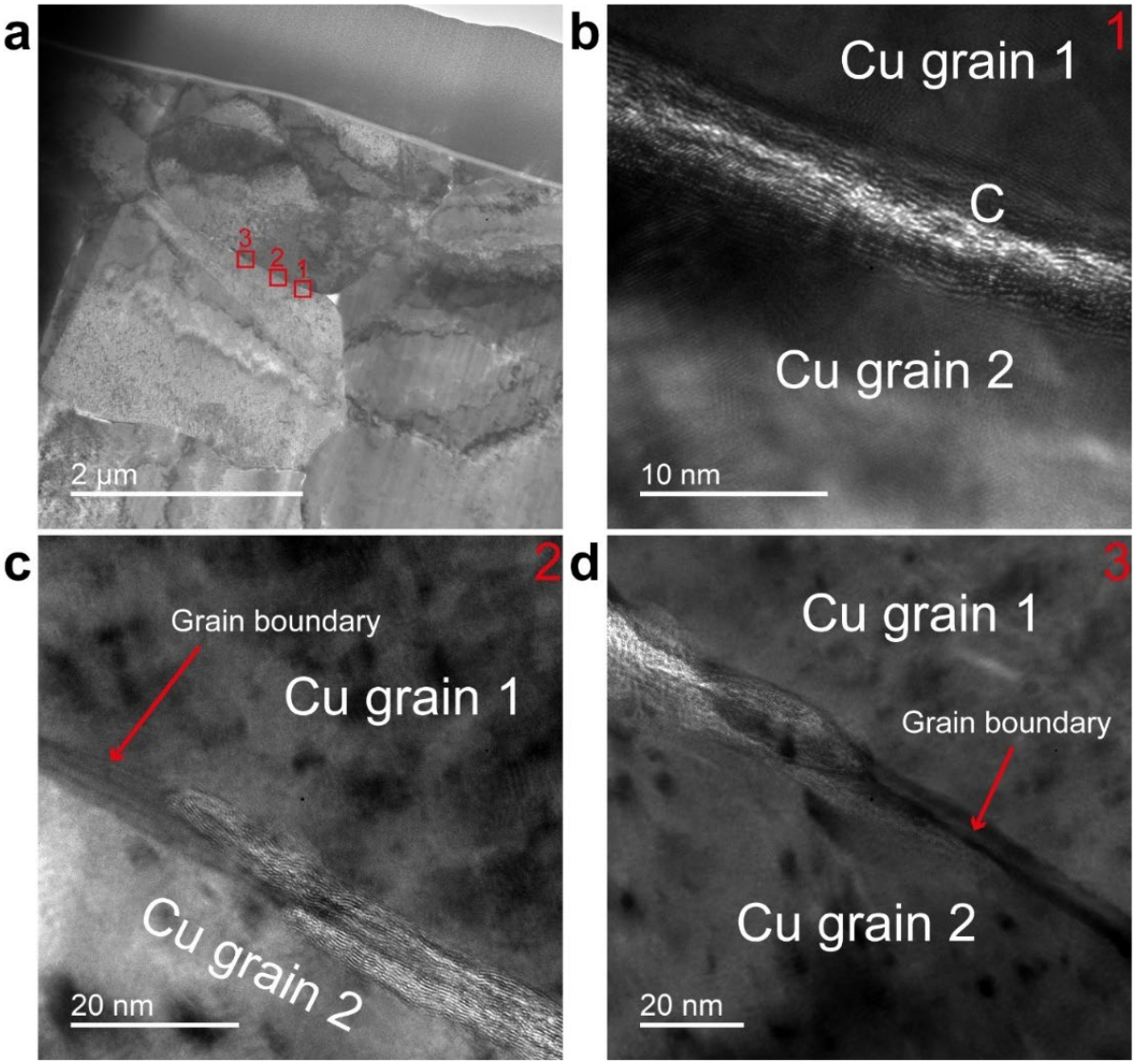

*Figure 3.11 – TEM observations of the nanostructure of rCu200C@0.65%: **a** broad view of the analyzed zone, **b** magnification of zone 1, **c** magnification of zone 2 and **d** magnification of zone 3*

Subsequent to the microstructural evaluations, High-Resolution Transmission Electron Microscopy (HRTEM) was employed to elucidate the behavior of carbon at the copper grain boundaries within the composite samples. A lamella for this detailed examination was prepared using FIB techniques, ensuring precision and maintaining the integrity of the sample's nanostructure.

Figure 3.11 delineates the HRTEM analysis of the rCu200C@0.65% sample, which

underwent sintering at 900°C and 100MPa. Figure 3.11 (a) provides a low-magnification view of a particular grain boundary within the sample. Marked by red squares, regions numbered 1, 2, and 3 indicate specific segments of the grain boundary selected for detailed scrutiny.

High-magnification images corresponding to these designated areas are presented in Figures 3.11 (b), (c), and (d), each elucidating different aspects of the carbon distribution and structure at the grain boundaries. In Figure 3.11 (b), the HRTEM image reveals carbon situated within the grain boundary, where approximately a dozen layers of carbon can be discerned, indicative of a degree of crystallization. This observation suggests that sintering not only impacts the localization of carbon within the composite but also promotes its crystallization at the grain boundaries.

Progressing along the grain boundary, Figure 3.11 (c) depicts a scenario where the carbon presence terminates abruptly, with the carbon layers adopting a U-shaped curvature at their termination point. This morphology could be interpreted as a manifestation of carbon segregation and expulsion from the grain boundary, transitioning into a region exhibiting typical copper grain boundary characteristics devoid of carbon incorporation.

Further along this boundary, Figure 3.11 (d) demonstrates that carbon reappears at the opposite end, reinforcing the notion of carbon segregation along the grain boundary. This pattern of carbon distribution supports the hypothesis that interfacial shear stresses experienced during sintering, compounded by the initial quality of the carbon used, contribute significantly to its localized segregation and morphological characteristics.

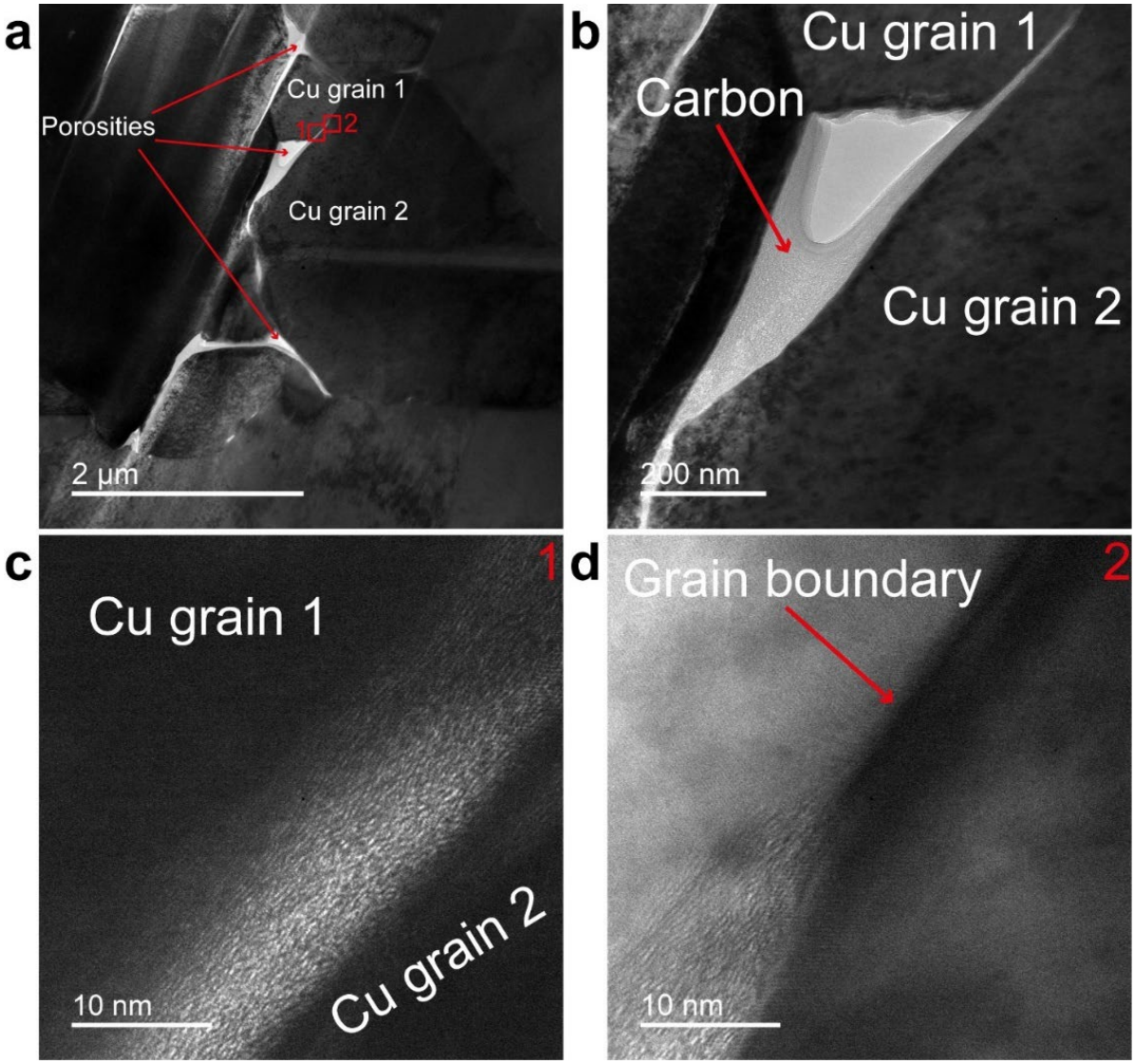

*Figure 3.12 – TEM observations of the nanostructure of rCu200C@2.00%: **a** broad view of the analyzed zone, **b** its associated magnification, **c** magnification of zone 1 and **d** magnification of zone 2*

Utilizing analogous methodologies, namely FIB for precise lamella preparation and HRTEM for in-depth nanostructural observations, Figure 3.12 furnishes an examination of the nanostructure inherent to the rCu200C@2.00% composite sample.

In Figure 3.12 (a), distinct porosities are observed within the sample's microstructure, a characteristic markedly different from the preceding observations. Notably, these porosities harbor substantial carbon accumulations, providing a plausible explanation for the reduced density observed in this particular composite variant.

The regions of interest within this nanostructure are demarcated as 1 and 2, with corresponding detailed images presented in Figures 3.12 (c) and 12 (d). As we traverse along a representative grain boundary, a similar phenomenon to that previously described is observable; however, the distinction lies in the substantially increased presence of carbon at and near the grain boundaries compared to the rCu200C@0.65%

sample.

This intensified carbon presence, as depicted in Figure 12(c) and (d), aligns with the previous narrative yet exhibits a more pronounced carbon aggregation. While the carbon structures show signs of organization, they do not fully achieve a graphitized state, indicating partial crystallization. The structural state of carbon, situated predominantly within the grain boundary porosities, underpins the segregation and agglomeration phenomena deduced from the microstructural analysis.

Furthermore, Figure 12(b) highlights the extensive carbon presence within the porosities, lending additional support to the segregation hypothesis. This visual evidence aligns with the concept that during sintering, carbon tends to migrate and concentrate within the existing microstructural voids, significantly impacting the material's overall density.

3.4 CONCLUSIONS

In this study, densification processes were systematically applied to pure copper powders, carbon-coated copper powders, and their mixtures utilizing SPS. The analysis of SPS curves indicated smooth densification processes for all sample types. Notably, the densification of pure copper samples was accompanied by gas release, potentially attributable to the liberation of hydrogen, suggesting prior absorption into the copper matrix.

The densification results yielded high densities for both pure copper and the rCu200C@0.65% composite samples, with values ranging from 8.79 g/cm^3 to 8.86 g/cm^3 for the former and between 8.85 g/cm^3 and 8.86 g/cm^3 for the latter. Conversely, the rCu200C@2.00% composite manifested lower densities, marked at 8.75 g/cm^3 and 8.74 g/cm^3, respectively. These findings underscore the significant impact of the proportion of carbon-coated copper particles integrated into pure copper powder on the resultant density and microstructural attributes.

Microstructural examinations revealed that elevating sintering parameters facilitated heightened density in pure copper samples but exhibited negligible effects on composite samples. This distinction was attributed to carbon presence at grain boundaries, which effectively inhibited grain growth within composite samples, a phenomenon not observed in pure copper counterparts. Moreover, subsequent dissolution of the copper matrix in composite samples unveiled defects within the carbon skeleton, indicative of underlying structural inconsistencies.

Nanostructural analysis provided further insights, revealing that sintering could potentially foster the crystallization of carbon at grain boundaries. However, segregation of carbon was observed, likely induced by high interfacial shear stresses during the sintering process. This segregation underscores the complex interplay between sintering conditions, material composition, and microstructural evolution within composite samples.

There is a clear imperative for further investigations to elucidate how composites incorporating higher-quality carbon, such as graphene grown on the particles, impact the microstructural and nanostructural dynamics. Subsequent research should focus on optimizing carbon quality and distribution within the copper matrix to enhance the composite's mechanical and electrical properties. Additionally, exploring alternative sintering parameters and incorporating advanced material characterization techniques may provide deeper insights into the interactions between copper and carbon components. Understanding these interactions will be crucial for tailoring the composite's properties to specific applications and for overcoming current limitations observed in the densification and structural integrity of carbon-coated copper powders.

This study lays an understanding but also opens avenues for enhancing composite materials' performance through control of material synthesis, densification processes, and microstructural optimization. The ultimate goal would be to develop copper-carbon composites with optimized density, minimized defect levels, and

improved functional properties suitable for advanced technological applications.

CHAPTER 4 – PHYSICAL PROPERTIES OF THE CARBON COPPER COMPOSITES

4.1 INTRODUCTION

Chapter 3 showed that the different power were successfully densified but the integrity of the carbon at the grain boundaries was compromised.

This chapter 4 delineates an analysis of the electrical conductivity and microhardness measurements conducted on the pure copper samples, identified as rCu200C and rCu300C. Initially, an examination of these samples establishes a baseline for comparison.

Subsequently, the focus shifts to the composite samples, where electrical conductivity and microhardness values are not only assessed but also juxtaposed with the baseline established by the pure copper samples. This comparative analysis aims to elucidate the impact of carbon incorporation on the electrical and mechanical properties of the copper matrix.

Following the evaluation of the composite samples, attention is directed towards the mixtures, encompassing varying proportions of carbon-coated copper particles within the pure copper matrix, designated as Cu-CuC@0.50%, Cu-CuC@1.00%, Cu-CuC@5.00%, and Cu-CuC@25.0%. The electrical conductivity and microhardness measurements of these mixtures are evaluated, providing insights into how different carbon concentrations influence the overall properties of the material, in comparison to both the pure and composite copper specimens.

The investigation further extends to the imaging of the indentation marks resulting from the microhardness tests. These indentations are analyzed using both Backscattered Electron (BSE) imaging and optical microscopy, offering a dual perspective that enhances the understanding of the material's response to mechanical stress. The BSE imaging provides high-resolution details on the microstructural context of the indentations, while optical imaging offers a broader view of the indentation quality and surface conditions.

Finally, the section culminates in presenting the fracture facies of the composite sample. This analysis is instrumental in understanding the fracture mechanics and failure modes of the composite materials, providing crucial information on their structural integrity and toughness. The examination of fracture surfaces, through imaging techniques, contributes to a comprehensive understanding of the material's behavior under stress and the impact of carbon integration on the mechanical properties of the copper-based composites.

4.2 METHODS AND MATERIALS

4.2.1 Materials

The evaluation of electrical conductivity was performed utilizing the Sigmacheck 2 apparatus provided by Ether NDE. Additionally, the assessment of microhardness was conducted employing the HMV-G Vickers microhardness tester, manufactured by Shimadzu.

The samples subjected to these testing protocols included pure copper specimens, designated as rCu200C and rCu300C, with the nomenclature reflecting the temperatures (200°C and 300°C, respectively) at which they were reduced prior to densification. Furthermore, composite samples, identified as rCu200C@0.65% and rCu200C@2.00%, were analyzed; these labels indicate the reduced copper powders at 200°C coated with varying concentrations of sucrose, resulting in differing levels of carbon coating.

In addition to the aforementioned specimens, mixtures consisting of pure copper and carbon-coated copper particles, denoted as Cu-CuC@0.50%, Cu-CuC@1.00%, Cu-CuC@5.00%, and Cu-CuC@25.0%, were also evaluated. These mixtures incorporated varying proportions of carbon-coated copper particles into the pure copper powder, specifically 0.50%, 1.00%, 5.00%, and 25.0%, aiming to elucidate the influence of carbon coated copper particles dispersed into a copper matrix on the mechanical and electrical properties of the resultant materials.

These samples underwent mechanical and electrical testing to assess their performance characteristics under standardized conditions. The evaluation aimed to discern the impact of reduction temperatures, carbon content, and composite formulation on the material properties, providing an understanding of the interplay between material composition, processing conditions, and resultant material characteristics.

4.2.2 Methods

For the electrical conductivity evaluations, a calibration process was employed using three cylindrical standards known for their distinct electrical conductivities: 102.54 %IACS, 62.5%IACS, and 8.18%IACS, each with an associated measurement uncertainty of ±0.35%IACS. This calibration was for ensuring the precision and reliability of the conductivity device prior to sample testing. Subsequently, each sample was subjected to multiple conductivity tests to derive an average value, thereby minimizing the influence of any anomalous readings and ensuring a robust assessment of the material's electrical properties. The measurements were conducted using a frequency of 60kHz. At this frequency the skin depth for copper is about 300µm.

In preparation for the microhardness testing, each sample underwent a rigorous surface preparation regimen to ensure a smooth and uniform testing area. This involved a sequence of mechanical polishing stages employing progressively finer grades of silicon carbide paper, followed by a polishing phase using a suspension containing 3.0µm diamond particles. The final stage of sample preparation involved chemical polishing utilizing an iron nitrate solution, enhancing the surface finish and eliminating superficial irregularities.

Microhardness testing was then executed with a standardized test load of 980.7 mN, applying five indentations with a dwell time of 15 seconds each across different regions of each sample. These indentations were systematically spaced to avoid interactions between successive tests. The resulting hardness values were then averaged to provide a representative measure of the material's microhardness.

Post-testing, the indentations and surrounding areas were subjected to detailed examination utilizing both Backscattered Electron (BSE) and optical microscopy techniques. The BSE imaging offered enhanced contrast and detailed examination of the indentation morphology and microstructural context, while optical observations provided a broader view of the surface conditions and indentation clarity. This dual approach allowed for a comprehensive assessment of the microhardness test sites, facilitating an in-depth understanding of the material's response to indentation, the presence of any surface anomalies, and the potential influences of underlying microstructural features.

4.3 Results and Discussions

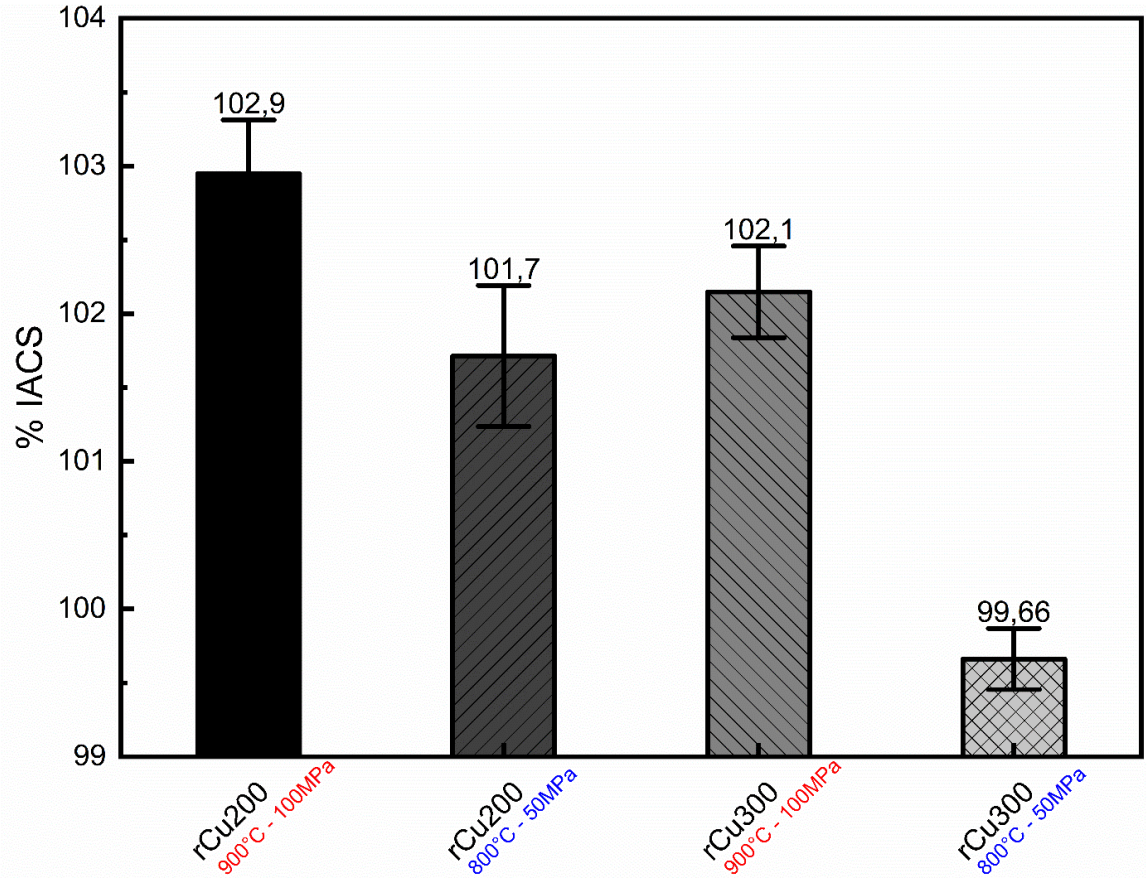

Figure 4.1 – Electrical conductivities of the pure copper samples

Figure 4.1 illustrates the electrical conductivity measurements for the reduced copper powders, designated as rCu200C and rCu300C, following SPS conducted at temperatures of 800°C and 900°C with an applied pressure of 50MPa and 100MPa, respectively. Notably, the highest electrical conductivity was recorded for the rCu200C sample sintered at 900°C – 100MPa, achieving an impressive 102.9% IACS. This is closely followed by the rCu300C sample subjected to the same sintering conditions, exhibiting a conductivity of 102.1% IACS. The results proceed to show conductivity for rCu200C sintered at 800°C – 50MPa at 101.7% IACS, and the rCu300C sintered under identical conditions manifesting a conductivity of 99.66% IACS.

These findings highlight the significant impact that pretreatment conditions and sintering parameters exert on the resultant electrical properties of the materials. Specifically, the reduction of copper powders at 300°C, presented challenges in subsequent grinding processes, thereby potentially introducing defects and impurities into the powders. This could elucidate the observed reduction in electrical conductivity for samples reduced at this higher temperature, as the presence of defects and impurities typically impedes electron flow, resulting in lower conductivity. Figure 4.2 (a) and (b) showcases the microstructures of rCu300 sintered at 800°C – 50MPa and 900°C – 100MPa, respectively. Figure 4.2 (a) clearly shows that the sample is highly porous so it could explain why the electrical conductivity for this sample is so low. On the other

hand, Figure 4.2 (b) shows less porosities which is coherent with the measured electrical conductivity of 102.1% IACS.

Moreover, these conductivity outcomes are corroborated by the microstructural and density analyses discussed in the preceding chapter. The interrelation between sintering parameters, microstructural integrity, and material densities plays a crucial role in determining the electrical performance of the sintered samples. The higher conductivity of rCu200C sintered at 900°C suggests that optimal sintering conditions can enhance microstructural ordering and reduce defects, thereby improving the electrical conductivity.

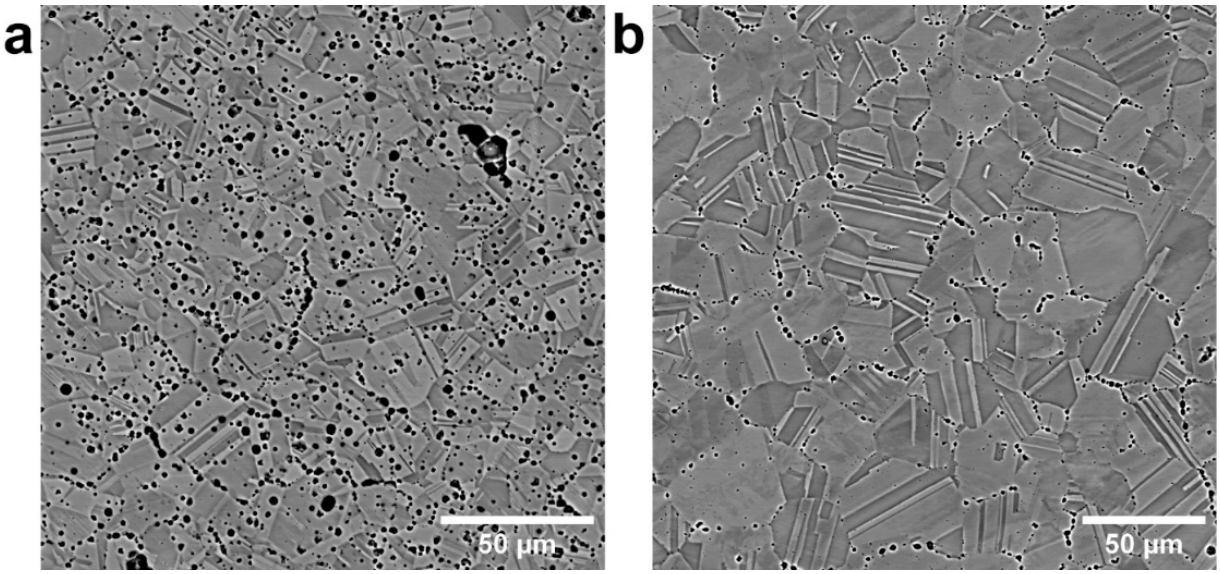

Figure 4.2 – Microstructure for rCu300C sintered under conditions: ***a*** *800°C - 50MPa and* ***b*** *900°C - 100MPa*

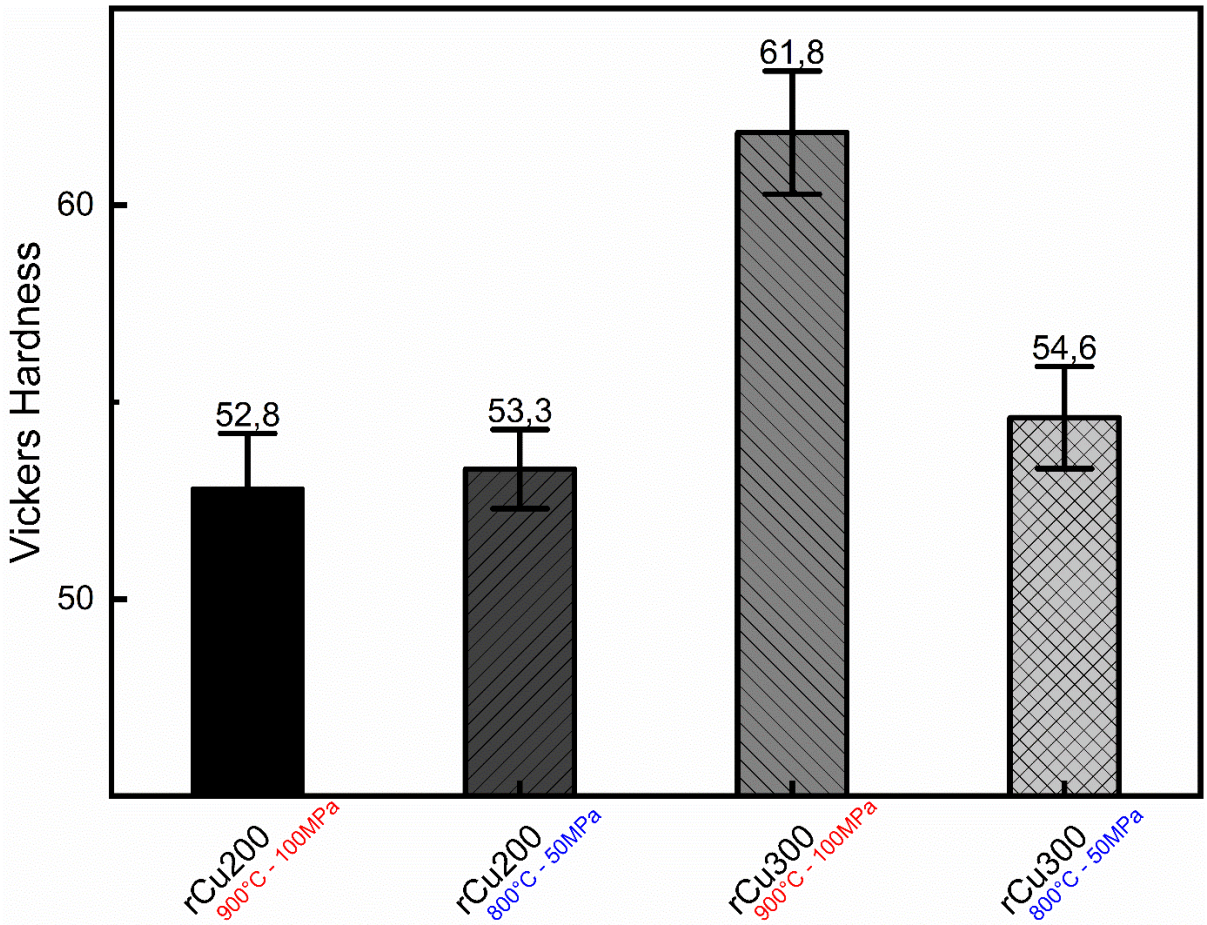

Figure 4.3 – Hardness of the pure copper samples

Figure 4.3 elucidates the microhardness measurements obtained for the pure copper samples. Contrary to the trends observed in electrical conductivity, the lowest microhardness values were recorded for the rCu200C samples, irrespective of the sintering conditions applied. Specifically, hardness values of 53.3 HV and 52.8 HV were measured for rCu200C samples subjected to sintering at 800°C – 50MPa and 900°C – 100MPa, respectively, demonstrating minimal variance between the two sets of parameters and indicating a relatively consistent hardness profile for this treatment temperature.

In contrast, the rCu300C samples exhibited a pronounced increase in hardness, particularly when sintered at 900°C – 100MPa, where a peak hardness value of 61.8 HV was observed. This is followed by a hardness value of 54.6 HV for rCu300C samples sintered at 800°C – 50MPa, suggesting that the elevated reduction temperature of 300°C, in conjunction with the sintering conditions, impacts the material's hardness.

This phenomenon suggests that the reduction temperature, coupled with the subsequent mechanical processing such as grinding, exerts a considerable influence on the microhardness of the material. It is postulated that the defects and impurities introduced during the grinding, particularly at the higher reduction temperature of 300°C, may inadvertently act to strengthen the material, potentially through mechanisms such as dislocation strengthening or grain boundary hardening.

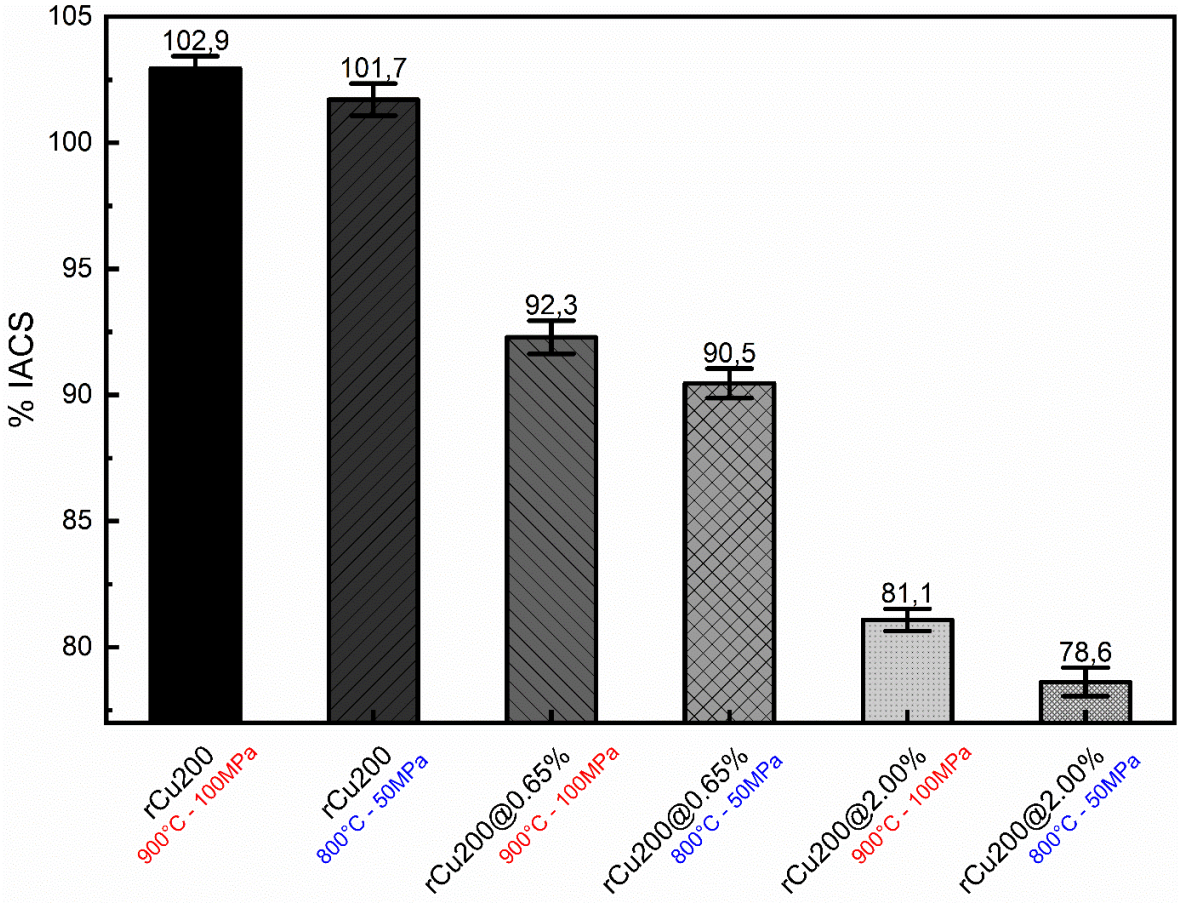

Figure 4.4 – Electrical conductivities of the composite samples

Following the assessment of the pure copper specimens, we turn our attention to the properties of the composite samples. Figure 4.4 elucidates the electrical conductivities of the composite specimens, namely rCu200C@0.65% and rCu200C@2.00%, which were subjected to sintering at 800°C – 50MPa and 900°C – 100MPa, respectively. These results are contextualized by comparison to the electrical conductivities of the rCu200C samples.

The electrical conductivity benchmarks are set by the rCu200C samples, exhibiting superior values of 103% IACS and 102.2% IACS under respective sintering conditions. Following these, the rCu200C@0.65% composite sintered at 900°C – 100MPa demonstrates a conductivity of 92.3% IACS, with a slight decrease to 90.5% IACS when sintered at 800°C – 50MPa. The rCu200C@2.00% composites manifest lower conductivities of 81.1% IACS and 78.6% IACS for sintering at 900°C – 100MPa and 800°C – 50MPa, respectively.

These findings align with previous microstructural and nanostructural analyses, wherein the carbon skeleton within the composites was observed to be perforated with voids and subjected to segregation. This microstructural characterization suggests that the presence of carbon, particularly in higher concentrations, acts detrimentally rather than beneficially towards the electrical properties of the composite. The interface between copper and carbon within these materials likely serves as a barrier to electron flow, leading to increased electron scattering and reduced conductivity since the

quality of the carbon is not met.

The distinct decrease in electrical conductivity observed in the composite samples, particularly as the carbon content increases, substantiates the hypothesis that carbon incorporation, in the form observed, is more of a defect than an enhancement concerning the material's electrical performance.

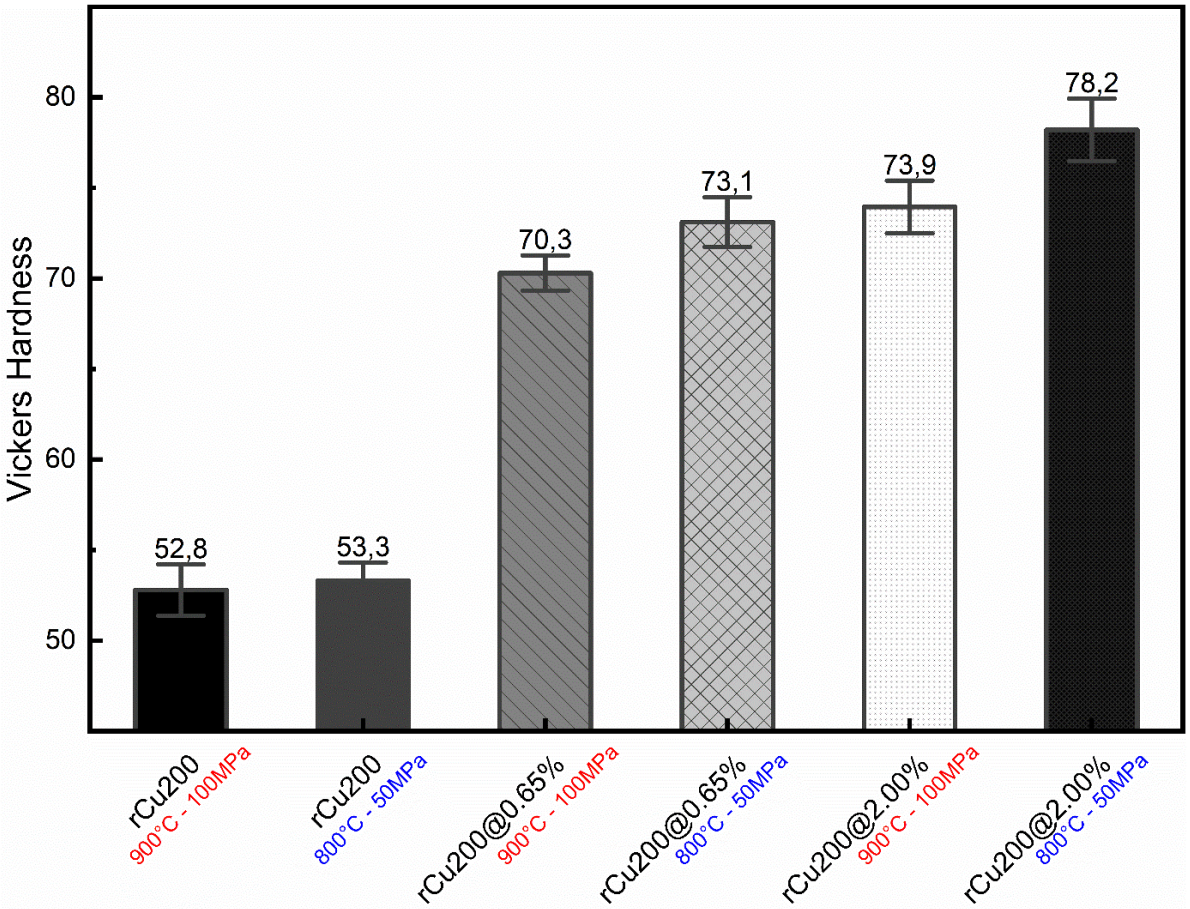

Figure 4.5 – Hardness of the composites samples

Figure 4.5 presents an analytical comparison of the microhardness measurements for the composite specimens, specifically rCu200C@0.65% and rCu200C@2.00%, following their respective sintering treatments at 800°C – 50MPa and 900°C – 100MPa. The findings are juxtaposed against the microhardness values of the rCu200C samples, facilitating a comprehensive evaluation of the material's mechanical properties post-sintering.

Contrary to the electrical conductivity trends previously discussed, the microhardness results reveal an inverse relationship, with the lowest hardness values observed in the rCu200C samples, registering at 53.3 HV and 52.8 HV under the two sintering conditions. In stark contrast, the composite samples demonstrate markedly higher hardness levels: rCu200C@0.65% exhibits hardness values of 70.2 HV and 73.1 HV, while rCu200C@2.00% displays even greater values of 73.9 HV and 78.2 HV,

respectively.

Notably, an unexpected trend emerges wherein the composites sintered at the lower temperature and pressure condition of 800°C - 50MPa exhibit higher hardness than those processed at 900°C – 100MPa. This phenomenon may be attributed to the differential impact of sintering conditions on carbon's structural behavior within the composite matrix. At the lower sintering temperature and pressure, it is plausible that the carbon experienced reduced interfacial shear stresses, thereby preserving its structural integrity at the grain boundaries and contributing to an increase in overall material hardness. Since the grain size distribution remained the same for all the composite sample we can postulate that here the grain size does not have significant impact on the hardness.

Furthermore, a clear correlation between carbon content and hardness is evident, with increased carbon levels corresponding to higher hardness values. This trend shows the significant role of carbon in reinforcing the composite matrix, likely through mechanisms such as load transfer and grain boundary strengthening.

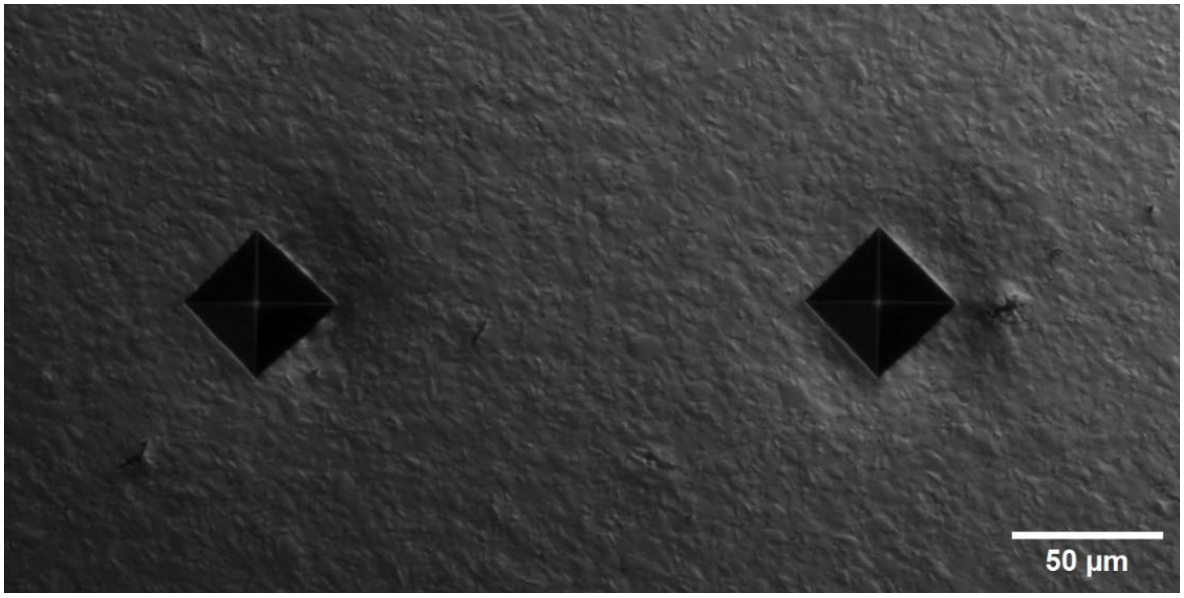

Figure 4.6 – Optical micrograph of the indentation of the rCu200C@0.65% sintered at 800°C - 50MPa

Figure 4.6 features optical micrographs showcasing two adjacent hardness indentations on the rCu200C@0.65% sample, which underwent sintering at 800°C and 50MPa. These indentations were strategically spaced 150µm apart to ensure that the plastic deformation zones associated with each indentation do not interfere with each other, thus maintaining the integrity of the individual test areas.

The micrographs reveal that the plastic deformation zones, or plastification zones, surrounding each indentation approximate a radius of about 40µm from the indentation's center. This observation provides insight into the extent of material deformation under the applied load. Notably, the absence of visible slip bands suggests that the carbon within the composite may be playing a significant role in absorbing the deformation induced by the hardness testing. This behavior is indicative of the carbon's

potential effectiveness in enhancing the composite's resistance to plastic deformation.

This analytical approach, utilizing optical micrography to observe the macroscopic effects of microhardness testing, offers a perspective on the deformation characteristics of the composite material under examination. The absence of slip bands around the indentations in the rCu200C@0.65% composite implies that the incorporated carbon, even at a relatively low percentage, contributes to the material's hardness and deformation response.

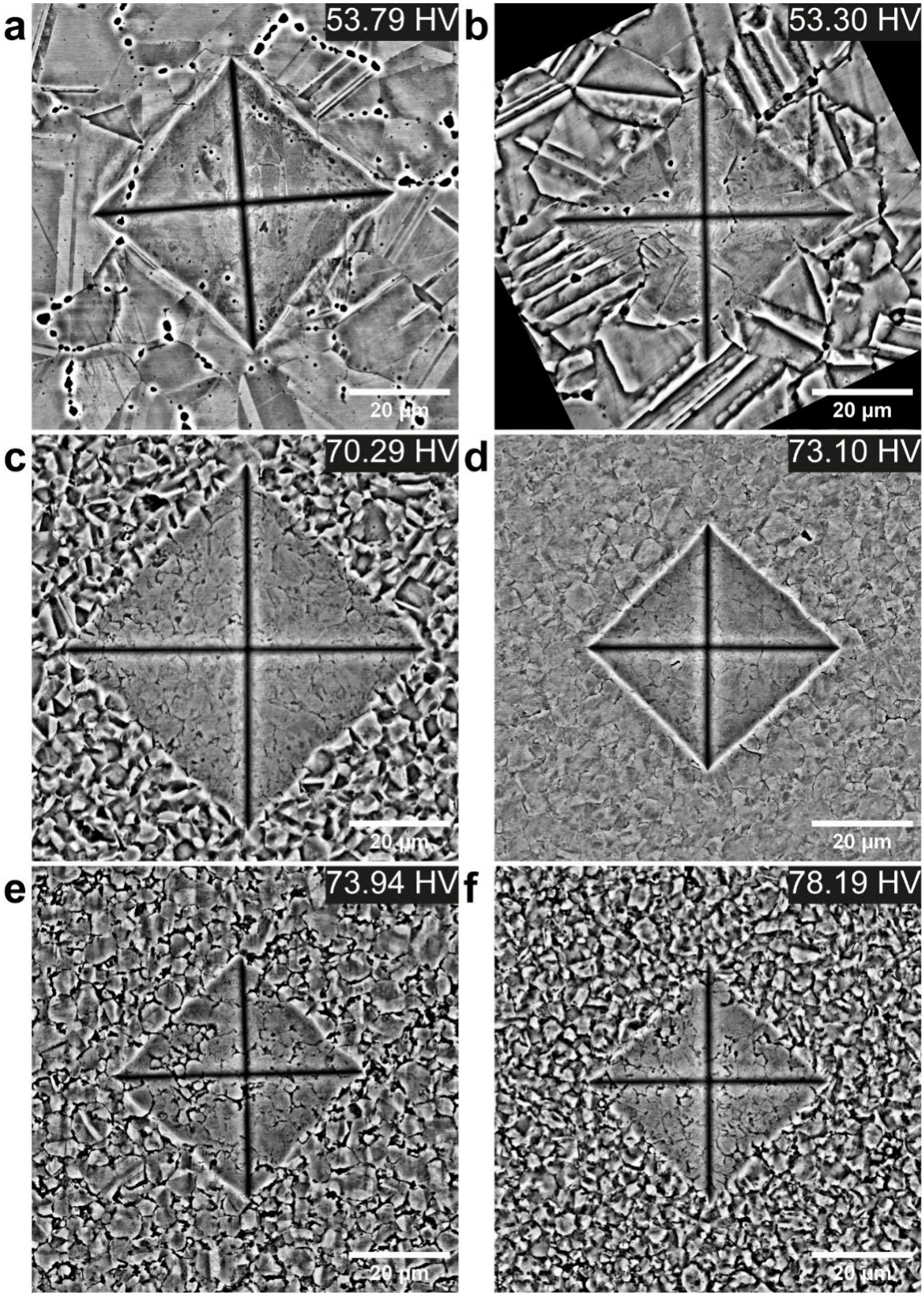

Figure 4.7 – SEM observations of the pure copper and composite samples: ***a*** *rCu200C sintered at 800°C - 50MPa,* ***b*** *Cu200C sintered at 900°C - 100MP,* ***c*** *Cu200C@0.65% sintered at 800°C - 50MPa,* ***d*** *Cu200C@0.65% sintered at 900°C - 100MPa* ***e*** *Cu200C@2.00% sintered at 800°C - 50MPa and* ***f*** *Cu200C@2.00% sintered at 900°C - 100MPa*

Figure 4.7 showcases the SEM observations using BSE mode of the indentations made during microhardness testing. This analytical approach was employed to gain detailed insights into the deformation characteristics surrounding the indentations, providing a more nuanced understanding of material response under applied loads.

In the pure copper samples, as depicted in Figures 4.7(a) and 4.5(b), subtle deformation features are observable around and within the indentations, discernible through variations in image contrast. These features suggest some degree of plastic deformation, although the material appears too malleable to manifest distinct slip bands, indicative of its relatively soft nature under the testing conditions employed.

Conversely, observations of the composite samples, presented in Figures 4.7(c), (d), (e), and (f), corresponding to rCu200C@0.65% and rCu200C@2.00% sintered at both 800°C – 50MPa and 900°C – 100MPa, respectively, reveal a different deformation response. Notably, there is a lack of discernible deformation features around the indentations; the material appears to have deformed uniformly without the formation of typical deformation artifacts such as pile-up or slip bands. This behavior suggests that the carbon within the composite is effectively absorbing and distributing the deformation stress, resulting in a 'softer' response akin to deformation 'like butter.'

This lack of visible deformation features in the composite samples, particularly in contrast to the pure copper, emphasizes the significant role of carbon in altering the material's response to indentation. The carbon's presence seems to mitigate the localization of plastic deformation, leading to a more homogenous deformation field around the indentations.

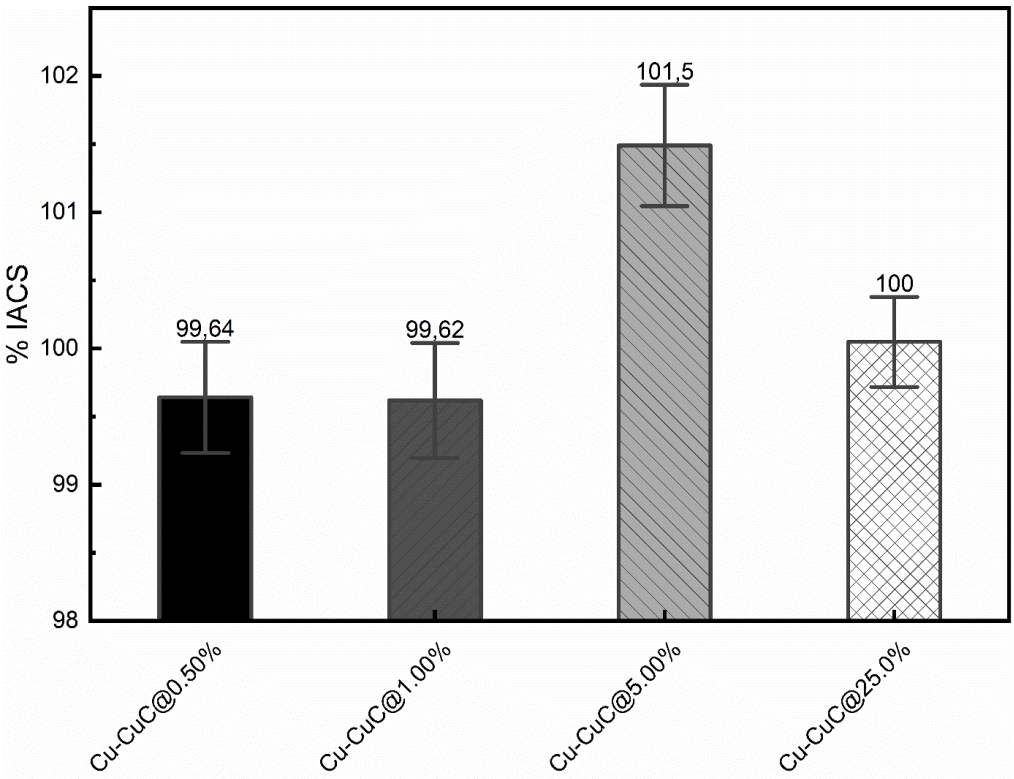

Figure 4.8 – Electrical conductivities of the mixtures

Figure 4.8 delineates the electrical conductivities observed in the four distinct mixtures of copper and carbon-coated copper powders. The conductivities were evaluated to ascertain the influence of varying carbon concentrations on the electrical properties of the resulting mixtures. Surprisingly, the highest electrical conductivity was recorded for mixture Cu-CuC@5.00%, which contains 5% carbon-coated copper particles, exhibiting a conductivity of 101.5%IACS. This result is particularly noteworthy given the significant incorporation of carbon, traditionally anticipated to reduce conductivity. Following Cu-CuC@5.00%, Cu-CuC@25.0%, which comprises an even higher carbon coated copper particles content of 25.0%, exhibited the next highest conductivity. Conversely, Cu-CuC@0.50% and Cu-CuC@1.00% both with lower carbon contents, displayed identical conductivity levels at 99.6% IACS. The conductivity results obtained for these mixtures are consistent with earlier findings pertaining to their densities. Specifically, Cu-CuC@0.50% and Cu-CuC@1.00% exhibited the lowest densities, suggesting suboptimal densification, which in turn could contribute to the reduced electrical conductivity observed. This correlation underpins the hypothesis that the level of densification significantly impacts the electrical properties of the material, with lower densification potentially interrupting the continuity necessary for optimal electrical conduction. In contrast, Cu-CuC@5.00% and Cu-CuC@25.0%, despite having higher carbon contents, demonstrated better densification, as reflected in their higher electrical conductivities. This suggests a complex interplay between carbon content, densification, and electrical conductivity, challenging traditional assumptions and indicating that under certain conditions, increased carbon content does not necessarily correlate with decreased conductivity.

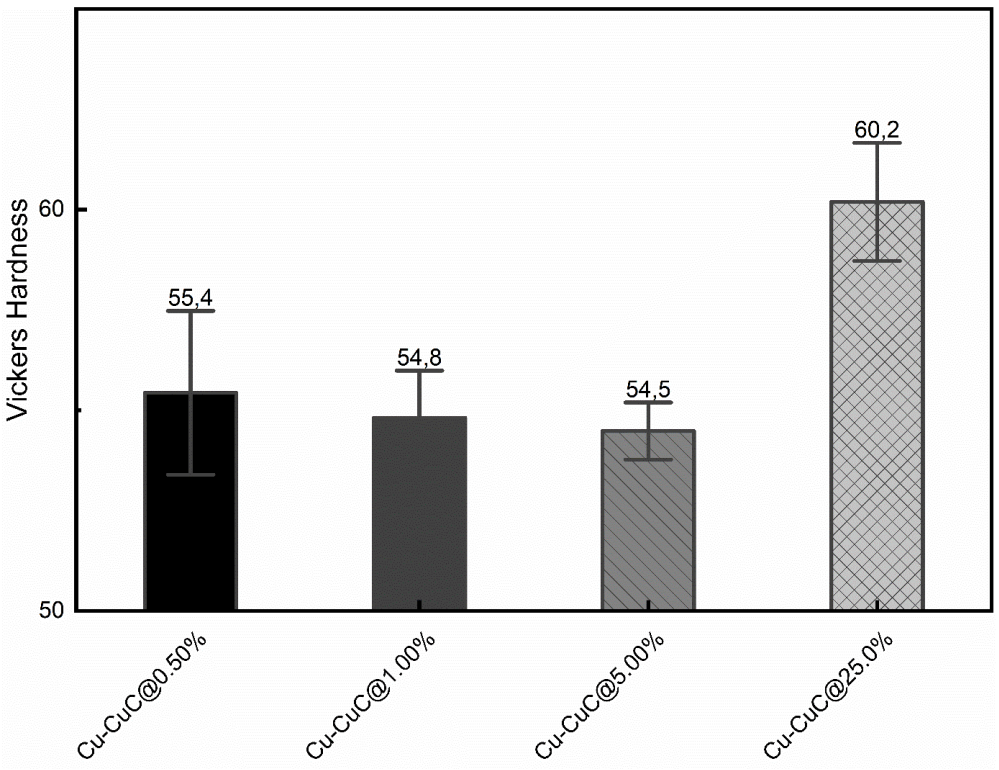

Figure 4.9 – Hardness of the mixtures

Figure 4.9 illustrates the microhardness measurements of the four distinct mixtures comprising varying proportions of copper and carbon-coated copper powders. These measurements are pivotal in understanding the relationship between composite formulation—specifically, the carbon content—and the resulting mechanical properties.

In this analysis, Cu-CuC@25.0%, which contains the highest proportion of carbon coated copper particles at 25%, exhibits the most substantial microhardness value at 60.2 HV. This result is consistent with the anticipated impact of increased carbon content, where the reinforcement provided by carbon is expected to enhance the material's resistance to indentation, thereby increasing its microhardness. The presence of a higher carbon content typically contributes to greater obstruction against plastic deformation, aligning with the observed increase in hardness.

Conversely, Cu-CuC@0.50%, Cu-CuC@1.00% and Cu-CuC@5.00% which incorporate lower quantities of carbon-coated copper particles, display microhardness values that are notably closer in range: 55.4 HV, 54.8 HV, and 54.5 HV, respectively. The relative uniformity in hardness among these three mixtures suggests that at lower carbon concentrations, the effect of carbon on hardness becomes less pronounced, resulting in a more homogenized material response to indentation.

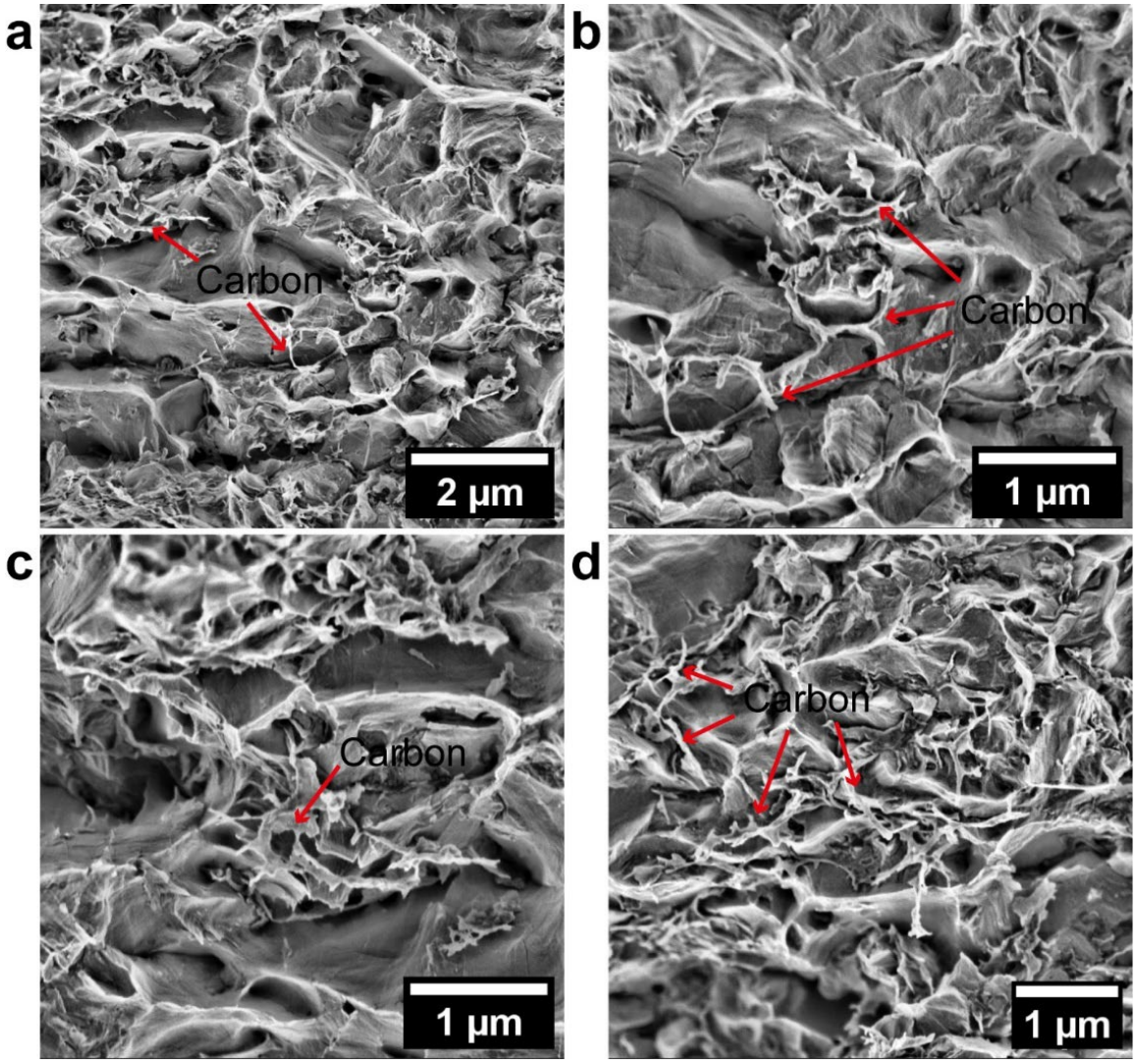

Figure 4.10 – Facies rupture of rCu200C@0.65% sintered at 900°C – 100MPa

Figure 4.10 provides a detailed examination of the fracture facies of the rCu200C@0.65% composite sample, with each subset illustrating the fracture morphology at different locations within the same sample. This multifaceted approach facilitates a comprehensive understanding of the fracture behavior exhibited by the composite.

The observed fracture characteristics suggest a brittle mode of failure, predominantly occurring along the grain boundaries. This fracture pattern aligns with the microstructural configuration, where carbon is ubiquitously situated at the grain boundaries. The presence of carbon in these regions is hypothesized to contribute to the brittleness observed, as it may impede the plastic deformation typically facilitated by grain boundary sliding during tensile stress.

Moreover, the images reveal carbon structures protruding from the fracture surfaces, appearing torn and rolled up. This manifestation of carbon at the fracture sites provides tangible evidence of the material's response to stress and the role of carbon in influencing the fracture mechanisms. The physical state of the carbon, particularly its dislodged and distorted appearance, accentuates the impact of carbon incorporation

on the material's structural integrity and cohesion during rupture.

These observations lead to the hypothesis that the ductility of the copper matrix is significantly compromised by the incorporation of carbon, particularly when localized at grain boundaries. The altered fracture morphology and the evident brittleness suggest that while carbon may enhance certain properties, its presence within the grain boundaries of the copper matrix can detrimentally affect the material's ability to undergo plastic deformation under stress.

4.4 CONCLUSIONS

This study has investigated the impact of the key processing conditions and carbon incorporation on the electrical and mechanical properties of copper-carbon composites. For pure copper specimens, it was observed that samples processed under the designation rCu200C exhibited superior electrical conductivities compared to their rCu300C counterparts, a phenomenon attributed to the preliminary reduction and sintering treatments. Specifically, elevated sintering parameters were correlated with enhanced electrical conductivity, underscoring the influence of processing conditions on material properties.

Conversely, the hardness assessment revealed an inverse trend, where rCu300C specimens demonstrated higher hardness values, indicating increased material resistance to deformation. This contrast between conductivity and hardness within pure copper samples punctuates the complex interplay between processing parameters and resultant material characteristics.

In the realm of composite samples, when juxtaposed with rCu200C benchmarks, a decrease in electrical conductivity was noted, primarily due to the inferior quality of the carbon incorporated within the matrix. Despite this, similar to pure copper, an increase in sintering temperature and pressure generally led to an enhancement in electrical conductivity for the composite specimens. However, the relationship between sintering conditions and hardness exhibited an inverse pattern, with higher sintering parameters potentially impairing the structural integrity of carbon at the grain boundaries. Indentation analyses further indicated that carbon presence at grain boundaries effectively absorbed deformation, impacting the overall hardness. The fracture facies analysis of the composites revealed a tendency towards brittle failure, further evidencing the significant role of carbon at grain boundaries.

For the mixed copper and copper-carbon specimens, electrical conductivity assessments demonstrated that Cu-CuC@5.00%, containing 5% carbon-coated copper particles, achieved the highest conductivity levels among the mixtures, with other mixtures exhibiting marginally lower conductivities. Interestingly, Cu-CuC@25.0% exhibited enhanced hardness, benefiting from its carbon content, which suggests a nuanced balance between conductivity and mechanical robustness in mixed compositions.

These findings collectively highlight that sintering parameters and carbon content exert significant, albeit sometimes counterintuitive, impacts on the electrical and mechanical properties of copper-carbon composites. The results undersline the necessity for engineering and optimization to develop high-quality copper-carbon composites tailored for specific applications. Future work should focus on refining the quality of carbon incorporation, exploring alternative processing techniques, and understanding the detailed mechanisms governing the interplay between carbon content, sintering conditions, and the resulting composite properties. This continued investigation will be important for advancing the application potential of copper-carbon composites in industrial and technological domains.

CHAPTER 5 – CONCLUSIONS AND PERSPECTIVES

This thesis has undertaken a detailed exploration into the synthesis, densification, and characterization of copper and copper-carbon composite materials, focusing on the effects of processing conditions and carbon incorporation on their electrical, mechanical, and microstructural properties. Across different chapters, distinct yet interrelated aspects of copper-based materials were investigated, revealing nuanced insights into their behavior and properties.

Initially, the synthesis of carbon-coated copper microparticles aimed to produce graphene-coated copper particles, aspiring towards high-quality copper-graphene composites. But the carbon remain amorphous. The study highlighted the role of reduction temperature and duration in effectively diminishing copper oxide layers, while underscoring the challenge of preventing premature particle sintering. A comparative synthesis approach indicated that the carbon structural quality markedly influences the material properties, advocating for optimization in synthesis routes for enhanced carbon structures. Adjustments in sucrose content and processing parameters were explored, delineating their significant impact on carbonization outcomes.

Subsequent chapters delved into the densification processes applied to these materials, utilizing SPS. The analyses stressed the smooth execution of densification. The findings pointed to a pronounced effect of carbon content on the densities and microstructural attributes of the composites, with particular emphasis on the role of carbon at grain boundaries in influencing material consolidation and integrity.

The investigation extended to the electrical and mechanical characterization of the composites. It was observed that while pure copper specimens exhibited superior electrical conductivities, the incorporation of carbon, especially when of inferior quality, led to reduced conductivities in composite samples. Interestingly, the microhardness assessments presented an inverse relationship to conductivity, with composite materials demonstrating increased hardness, attributed to carbon's influence on deformation absorption and grain boundary stabilization.

Fracture facies analysis provided additional context, revealing a predisposition towards brittle failure in carbon-enhanced composites, underscoring the significant yet complex role of carbon at the microstructural level.

Emerging from this comprehensive study are several directives for future research:

1. Optimization of copper oxide reduction processes, employing lower temperatures or alternative methodologies, to maintain particle integrity and prevent unwanted sintering when using spherical particles.
2. Enhanced control over the carbon supply during graphitization, particularly CVD deposition techniques, to promote the formation of high-quality graphene layers.
3. Working under atmospheric pressures during the CVD or the use of a PECVD setup while injecting methane migh help for the formation of high-quality graphene.
4. Using purer gas bottles to avoid oxygen contamination.
5. The utilization of ball milling to flatten the copper particles into flakes in order grow graphene on foil-like shapes (here flakes). Or the fabrication of micrometric flat copper (111) single-crystals. Those flakes would be coated with sucrose and carbonized under a flow of argon and hydrogen in a first step. In the case of the ball milled copper flakes, an annealing step would be required to induce recrystallization and grain growth hoping to obtain strong (111) orientation, to prevent any premature sintering the carbon layer must be present. The graphitization would take place under lowered pressures with maybe a methane flow. The idea here is to get locally a 2D architecture in the final composite. Prior to SPS, attention regarding the position of the flakes is required. The flakes must be flat on top of each other.
6. Exploration of sintering under reduced pressure and temperatures up to 1000°C to mitigate shear stress defects and improve carbon integrity.
7. More detailed mechanistic studies on the interplay between sintering conditions, carbon content and resusltant mechanical properties, load transfer modelizations between the copper matrix and the 3D graphene skeletton, severe plastic deformation resulting in the formation of texture, dislocation motion at grain boundaries.
8. In-depth electrical and electronic studies with the use of conductive AFM, grain boundaries electrical resistivity measurements, the use of angular resolved photo-electron spectroscopy at the grain boundaries to construct the band structure.

In conclusion, this thesis presents a framework for the development of copper-graphene composites, highlighting the critical balance required between processing conditions, material composition, and resultant properties. The insights gained pave the way for future advancements in the engineering of copper-based composite materials, aiming for optimized performance in electrical and mechanical applications. The proposed future research directions are poised to address existing challenges and

harness the potential of copper-graphene composites in technological and industrial applications.

REFERENCES

[1] J. Rodriguez, « The World Copper Factbook 2023 », 2023.

[2] « Electric Field Effect in Atomically Thin Carbon Films | Science ». Consulté le: 13 avril 2024. [En ligne]. Disponible sur: https://www-science-org.ezproxy.universite-paris-saclay.fr/doi/full/10.1126/science.1102896

[3] A. K. G. Kim Philip, « Carbon Wonderland », Scientific American. Consulté le: 13 avril 2024. [En ligne]. Disponible sur: https://www.scientificamerican.com/article/carbon-wonderland/

[4] C. J. Smithells, W. F. Gale, et T. C. Totemeier, *Smithells metals reference book*, 8th ed. / edited by W.F. Gale, T.C. Totemeier. Amsterdam ; Boston: Elsevier Butterworth-Heinemann, 2004.

[5] « Superior Thermal Conductivity of Single-Layer Graphene | Nano Letters ». Consulté le: 13 avril 2024. [En ligne]. Disponible sur: https://pubs-acs-org.ezproxy.universite-paris-saclay.fr/doi/abs/10.1021/nl0731872

[6] C. G. Lee, X. D. Wei, J. W. Kysar, et J. Hone, « Measurement of the Elastic Properties and Intrinsic Strength of Monolayer Graphene », *Science*, vol. 321, p. 385, 2008.

[7] « CSA - Discovery Guides, A Brief History of Copper ». Consulté le: 13 avril 2024. [En ligne]. Disponible sur: https://web.archive.org/web/20150203154021/http://www.csa.com/discoveryguides/copper/overview.php

[8] M. E. Schlesinger, K. C. Sole, W. Davenport, et G. R. F. Alvear Flores, *Extractive metallurgy of copper*, Sixth edition. Amsterdam Kidlington Cambridge, MA: Elsevier, 2022.

[9] United States. National Bureau of Standards, *Copper wire tables*. Washington Govt. Print. Off, 1914. Consulté le: 19 avril 2024. [En ligne]. Disponible sur: http://archive.org/details/copperwiretables31unituoft

[10] O. Bourgeois et H. Guillou, « Conduction électrique dans les solides - Introduction et théories élémentaires », *Conversion de l'énergie électrique*, nov. 2011, doi: 10.51257/a-v1-d2601.

[11] O. Bourgeois et H. Guillou, « Conduction électrique dans les solides - Transport et propriétés physiques des électrons de conduction », *Conversion de l'énergie électrique*, nov. 2011, doi: 10.51257/a-v1-d2602.

[12] W. D. Callister et D. G. Rethwisch, « Materials Science and Engineering ».

[13] P. M. Woodward, P. Karen, J. S. O. Evans, et T. Vogt, *Solid State Materials Chemistry*, 1re éd. Cambridge University Press, 2021. doi: 10.1017/9781139025348.

[14] Y. C. Cho *et al.*, « Copper Better than Silver: Electrical Resistivity of the Grain-Free Single-Crystal Copper Wire », *Crystal Growth & Design*, vol. 10, nº 6, p. 2780-2784, juin 2010, doi: 10.1021/cg1003808.

[15] « Materials_Properties_Thermal_Electrical_Characteri.pdf ».

[16] « Wrought Lightly Alloyed Copper:: MakeItFrom.com ». Consulté le: 19 avril 2024. [En ligne]. Disponible sur: https://www.makeitfrom.com/material-

group/Wrought-Lightly-Alloyed-Copper
[17] L. Lu, Y. Shen, X. Chen, L. Qian, et K. Lu, « Ultrahigh Strength and High Electrical Conductivity in Copper », *Science*, vol. 304, nº 5669, p. 422-426, avr. 2004, doi: 10.1126/science.1092905.
[18] A. Habibi, M. Ketabchi, et M. Eskandarzadeh, « Nano-grained pure copper with high-strength and high-conductivity produced by equal channel angular rolling process », *Journal of Materials Processing Technology*, vol. 211, nº 6, p. 1085-1090, juin 2011, doi: 10.1016/j.jmatprotec.2011.01.009.
[19] K. Surekha et A. Els-Botes, « Development of high strength, high conductivity copper by friction stir processing », *Materials & Design*, vol. 32, nº 2, p. 911-916, févr. 2011, doi: 10.1016/j.matdes.2010.08.028.
[20] B. Zhang et V. P. W. Shim, « Effect of strain rate on microstructure of polycrystalline oxygen-free high conductivity copper severely deformed at liquid nitrogen temperature », *Acta Materialia*, vol. 58, nº 20, p. 6810-6827, déc. 2010, doi: 10.1016/j.actamat.2010.09.009.
[21] V. Spuskanyuk *et al.*, « Effect of combining the equal-channel angular hydroextrusion, direct hydroextrusion and drawing on properties of copper wire », *Journal of Materials Processing Technology*, vol. 210, nº 13, p. 1709-1715, oct. 2010, doi: 10.1016/j.jmatprotec.2010.06.001.
[22] S. A. Hosseini et H. D. Manesh, « High-strength, high-conductivity ultra-fine grains commercial pure copper produced by ARB process », *Materials & Design*, vol. 30, nº 8, p. 2911-2918, sept. 2009, doi: 10.1016/j.matdes.2009.01.012.
[23] L. Ladani, J. Razmi, et T. C. Lowe, « Manufacturing of High Conductivity, High Strength Pure Copper with Ultrafine Grain Structure », *JMMP*, vol. 7, nº 4, p. 137, juill. 2023, doi: 10.3390/jmmp7040137.
[24] H. Yang *et al.*, « High strength and high conductivity Cu alloys: A review », *Sci. China Technol. Sci.*, vol. 63, nº 12, p. 2505-2517, déc. 2020, doi: 10.1007/s11431-020-1633-8.
[25] J. H. Warner, F. Schäffel, A. Bachmatiuk, et M. H. Rümmeli, Éd., *Graphene: fundamentals and emergent applications*, 1. ed. Amsterdam Heidelberg: Elsevier, 2013.
[26] C. Arya, K. K. H. De Silva, et M. Yoshimura, « Adlayer-free large-area single-crystal CVD graphene growth on copper », *J Mater Sci: Mater Electron*, vol. 31, nº 24, p. 21821-21831, déc. 2020, doi: 10.1007/s10854-020-04706-8.
[27] B. Deng, Z. Liu, et H. Peng, « Toward Mass Production of CVD Graphene Films », *Advanced Materials*, vol. 31, nº 9, p. 1800996, mars 2019, doi: 10.1002/adma.201800996.
[28] M. Bahri *et al.*, « Recent advances in chemical vapour deposition techniques for graphene-based nanoarchitectures: From synthesis to contemporary applications », *Coordination Chemistry Reviews*, vol. 475, p. 214910, janv. 2023, doi: 10.1016/j.ccr.2022.214910.
[29] H. Ji *et al.*, « Graphene Growth Using a Solid Carbon Feedstock and Hydrogen », *ACS Nano*, vol. 5, nº 9, p. 7656-7661, sept. 2011, doi: 10.1021/nn202802x.

[30] Z. Sun, Z. Yan, J. Yao, E. Beitler, Y. Zhu, et J. M. Tour, « Growth of graphene from solid carbon sources », *Nature*, vol. 468, n° 7323, p. 549-552, nov. 2010, doi: 10.1038/nature09579.
[31] A. C. Ferrari et D. M. Basko, « Raman spectroscopy as a versatile tool for studying the properties of graphene », *Nature Nanotech*, vol. 8, n° 4, p. 235-246, avr. 2013, doi: 10.1038/nnano.2013.46.
[32] M. Hu, Z. Yao, X. Wang, et Department of Chemical, Biological and Pharmaceutical Engineering, New Jersey Institute of Technology, Newark, NJ 07102, USA, « Characterization techniques for graphene-based materials in catalysis », *AIMS Materials Science*, vol. 4, n° 3, p. 755-788, 2017, doi: 10.3934/matersci.2017.3.755.
[33] S. J. Yoo, S. H. Han, et W. J. Kim, « A combination of ball milling and high-ratio differential speed rolling for synthesizing carbon nanotube/copper composites », *Carbon*, vol. 61, p. 487-500, sept. 2013, doi: 10.1016/j.carbon.2013.04.105.
[34] H. Deng, J. Yi, C. Xia, et Y. Yi, « Mechanical properties and microstructure characterization of well-dispersed carbon nanotubes reinforced copper matrix composites », *Journal of Alloys and Compounds*, vol. 727, p. 260-268, déc. 2017, doi: 10.1016/j.jallcom.2017.08.131.
[35] N. Nayan *et al.*, « Processing and characterization of spark plasma sintered copper/carbon nanotube composites », *Materials Science and Engineering: A*, vol. 682, p. 229-237, janv. 2017, doi: 10.1016/j.msea.2016.10.114.
[36] J.-H. Pak, G.-N. Kim, S.-G. Hwang, B.-S. Kim, J.-P. Noh, et S.-C. Huh, « Mechanical properties of Cu matrix composite fabricated by extrusion process », *Transactions of Nonferrous Metals Society of China*, vol. 26, n° 10, p. 2679-2686, oct. 2016, doi: 10.1016/S1003-6326(16)64356-X.
[37] A. K. Shukla *et al.*, « Processing copper–carbon nanotube composite powders by high energy milling », *Materials Characterization*, vol. 84, p. 58-66, oct. 2013, doi: 10.1016/j.matchar.2013.07.011.
[38] A. K. Shukla *et al.*, « Processing of copper–carbon nanotube composites by vacuum hot pressing technique », *Materials Science and Engineering: A*, vol. 560, p. 365-371, janv. 2013, doi: 10.1016/j.msea.2012.09.080.
[39] J. P. Tu, Y. Z. Yang, L. Y. Wang, X. C. Ma, et X. B. Zhang, « Tribological properties of carbon-nanotube-reinforced copper composites ».
[40] Z. Huang, Z. Zheng, S. Zhao, S. Dong, P. Luo, et L. Chen, « Copper matrix composites reinforced by aligned carbon nanotubes: Mechanical and tribological properties », *Materials & Design*, vol. 133, p. 570-578, nov. 2017, doi: 10.1016/j.matdes.2016.08.021.
[41] J. L. Song, W. G. Chen, L. L. Dong, J. J. Wang, et N. Deng, « An electroless plating and planetary ball milling process for mechanical properties enhancement of bulk CNTs/Cu composites », *Journal of Alloys and Compounds*, vol. 720, p. 54-62, oct. 2017, doi: 10.1016/j.jallcom.2017.05.208.
[42] H. Wang, Z.-H. Zhang, H.-M. Zhang, Z.-Y. Hu, S.-L. Li, et X.-W. Cheng, « Novel synthesizing and characterization of copper matrix composites reinforced with

carbon nanotubes », *Materials Science and Engineering: A*, vol. 696, p. 80-89, juin 2017, doi: 10.1016/j.msea.2017.04.055.
[43] S. Zhao *et al.*, « Cu matrix composites reinforced with aligned carbon nanotubes: Mechanical, electrical and thermal properties », *Materials Science and Engineering: A*, vol. 675, p. 82-91, oct. 2016, doi: 10.1016/j.msea.2016.08.044.
[44] E. Khaleghi, M. Torikachvili, M. A. Meyers, et E. A. Olevsky, « Magnetic enhancement of thermal conductivity in copper–carbon nanotube composites produced by electroless plating, freeze drying, and spark plasma sintering », *Materials Letters*, vol. 79, p. 256-258, juill. 2012, doi: 10.1016/j.matlet.2012.03.117.
[45] K. Rajkumar et S. Aravindan, « Tribological studies on microwave sintered copper–carbon nanotube composites », *Wear*, vol. 270, nº 9-10, p. 613-621, avr. 2011, doi: 10.1016/j.wear.2011.01.017.
[46] W. M. Daoush, B. K. Lim, C. B. Mo, D. H. Nam, et S. H. Hong, « Electrical and mechanical properties of carbon nanotube reinforced copper nanocomposites fabricated by electroless deposition process », *Materials Science and Engineering: A*, vol. 513-514, p. 247-253, juill. 2009, doi: 10.1016/j.msea.2009.01.073.
[47] L. Liu *et al.*, « Well-dispersion of CNTs and enhanced mechanical properties in CNTs/Cu-Ti composites fabricated by Molecular Level Mixing », *Journal of Alloys and Compounds*, vol. 726, p. 81-87, déc. 2017, doi: 10.1016/j.jallcom.2017.07.297.
[48] P.-C. Tsai, Y.-R. Jeng, J.-T. Lee, I. Stachiv, et P. Sittner, « Effects of carbon nanotube reinforcement and grain size refinement mechanical properties and wear behaviors of carbon nanotube/copper composites », *Diamond and Related Materials*, vol. 74, p. 197-204, avr. 2017, doi: 10.1016/j.diamond.2017.03.012.
[49] P.-C. Tsai et Y.-R. Jeng, « Experimental and numerical investigation into the effect of carbon nanotube buckling on the reinforcement of CNT/Cu composites », *Composites Science and Technology*, vol. 79, p. 28-34, avr. 2013, doi: 10.1016/j.compscitech.2013.02.003.
[50] M. E. Mendoza, I. G. Solórzano, et E. A. Brocchi, « Mechanical and electrical characterization of Cu-2wt.% SWCNT nanocomposites synthesized by in situ reduction », *Materials Science and Engineering: A*, vol. 544, p. 21-26, mai 2012, doi: 10.1016/j.msea.2012.02.052.
[51] Z. W. Xue, L. D. Wang, P. T. Zhao, S. C. Xu, J. L. Qi, et W. D. Fei, « Microstructures and tensile behavior of carbon nanotubes reinforced Cu matrix composites with molecular-level dispersion », *Materials & Design*, vol. 34, p. 298-301, févr. 2012, doi: 10.1016/j.matdes.2011.08.021.
[52] Ch. Guiderdoni, C. Estournès, A. Peigney, A. Weibel, V. Turq, et Ch. Laurent, « The preparation of double-walled carbon nanotube/Cu composites by spark plasma sintering, and their hardness and friction properties », *Carbon*, vol. 49, nº 13, p. 4535-4543, nov. 2011, doi: 10.1016/j.carbon.2011.06.063.
[53] K. T. Kim, J. Eckert, G. Liu, J. M. Park, B. K. Lim, et S. H. Hong, « Influence of embedded-carbon nanotubes on the thermal properties of copper matrix nanocomposites processed by molecular-level mixing », *Scripta Materialia*, vol. 64, nº 2, p. 181-184, janv. 2011, doi: 10.1016/j.scriptamat.2010.09.039.

[54] H. N. Kim, S. N. Chang, et D. K. Kim, « Enhanced microhardness of nanocrystalline carbon nanotube-reinforced Cu composite using planar shock-wave compaction », *Scripta Materialia*, vol. 61, nº 9, p. 871-874, nov. 2009, doi: 10.1016/j.scriptamat.2009.07.017.
[55] K. T. Kim, S. I. Cha, et S. H. Hong, « Hardness and wear resistance of carbon nanotube reinforced Cu matrix nanocomposites », *Materials Science and Engineering: A*, vol. 449-451, p. 46-50, mars 2007, doi: 10.1016/j.msea.2006.02.310.
[56] S. I. Cha, K. T. Kim, S. N. Arshad, C. B. Mo, et S. H. Hong, « Extraordinary Strengthening Effect of Carbon Nanotubes in Metal-Matrix Nanocomposites Processed by Molecular-Level Mixing », *Advanced Materials*, vol. 17, nº 11, p. 1377-1381, juin 2005, doi: 10.1002/adma.200401933.
[57] C. Arnaud *et al.*, « High strength – High conductivity double-walled carbon nanotube – Copper composite wires », *Carbon*, vol. 96, p. 212-215, janv. 2016, doi: 10.1016/j.carbon.2015.09.061.
[58] Ch. Guiderdoni *et al.*, « The preparation of carbon nanotube (CNT)/copper composites and the effect of the number of CNT walls on their hardness, friction and wear properties », *Carbon*, vol. 58, p. 185-197, juill. 2013, doi: 10.1016/j.carbon.2013.02.049.
[59] Ch. Guiderdoni, C. Estournès, A. Peigney, A. Weibel, V. Turq, et Ch. Laurent, « The preparation of double-walled carbon nanotube/Cu composites by spark plasma sintering, and their hardness and friction properties », *Carbon*, vol. 49, nº 13, p. 4535-4543, nov. 2011, doi: 10.1016/j.carbon.2011.06.063.
[60] Z. Wang, X. Cai, C. Yang, L. Zhou, et C. Hu, « An electrodeposition approach to obtaining carbon nanotubes embedded copper powders for the synthesis of copper matrix composites », *Journal of Alloys and Compounds*, vol. 735, p. 1357-1362, févr. 2018, doi: 10.1016/j.jallcom.2017.11.255.
[61] Y. Feng, G. E. McGuire, O. A. Shenderova, H. Ke, et S. L. Burkett, « Fabrication of copper/carbon nanotube composite thin films by periodic pulse reverse electroplating using nanodiamond as a dispersing agent », *Thin Solid Films*, vol. 615, p. 116-121, sept. 2016, doi: 10.1016/j.tsf.2016.07.015.
[62] Z. An, M. Toda, et T. Ono, « Comparative investigation into surface charged multi-walled carbon nanotubes reinforced Cu nanocomposites for interconnect applications », *Composites Part B: Engineering*, vol. 95, p. 137-143, juin 2016, doi: 10.1016/j.compositesb.2016.03.086.
[63] Y. L. Yang *et al.*, « Single-walled carbon nanotube-reinforced copper composite coatings prepared by electrodeposition under ultrasonic field », *Materials Letters*, vol. 62, nº 1, p. 47-50, janv. 2008, doi: 10.1016/j.matlet.2007.04.086.
[64] R. Sundaram, T. Yamada, K. Hata, et A. Sekiguchi, « The importance of carbon nanotube wire density, structural uniformity, and purity for fabricating homogeneous carbon nanotube–copper wire composites by copper electrodeposition », *Jpn. J. Appl. Phys.*, vol. 57, nº 4S, p. 04FP08, avr. 2018, doi: 10.7567/JJAP.57.04FP08.
[65] P.-M. Hannula, M. Junnila, D. Janas, J. Aromaa, O. Forsén, et M. Lundström,

« Carbon Nanotube Fiber Pretreatments for Electrodeposition of Copper », *Advances in Materials Science and Engineering*, vol. 2018, p. 1-8, 2018, doi: 10.1155/2018/3071913.

[66] R. Sundaram, T. Yamada, K. Hata, et A. Sekiguchi, « The influence of Cu electrodeposition parameters on fabricating structurally uniform CNT-Cu composite wires », *Materials Today Communications*, vol. 13, p. 119-125, déc. 2017, doi: 10.1016/j.mtcomm.2017.09.003.

[67] J. M. Tao, X. F. Chen, P. Hong, et J. H. Yi, « Microstructure and electrical conductivity of laminated Cu/CNT/Cu composites prepared by electrodeposition », *Journal of Alloys and Compounds*, vol. 717, p. 232-239, sept. 2017, doi: 10.1016/j.jallcom.2017.05.074.

[68] R. Sundaram, T. Yamada, K. Hata, et A. Sekiguchi, « Electrical performance of lightweight CNT-Cu composite wires impacted by surface and internal Cu spatial distribution », *Sci Rep*, vol. 7, nº 1, p. 9267, août 2017, doi: 10.1038/s41598-017-09279-x.

[69] J. Shuai, L. Xiong, L. Zhu, et W. Li, « Effects of ply-orientation on microstructure and properties of super-aligned carbon nanotube reinforced copper laminar composites », *Transactions of Nonferrous Metals Society of China*, vol. 27, nº 8, p. 1747-1758, août 2017, doi: 10.1016/S1003-6326(17)60197-3.

[70] P.-M. Hannula *et al.*, « Observations of copper deposition on functionalized carbon nanotube films », *Electrochimica Acta*, vol. 232, p. 495-504, avr. 2017, doi: 10.1016/j.electacta.2017.03.006.

[71] P.-M. Hannula *et al.*, « Carbon nanotube-copper composites by electrodeposition on carbon nanotube fibers », *Carbon*, vol. 107, p. 281-287, oct. 2016, doi: 10.1016/j.carbon.2016.06.008.

[72] J. Shuai, L. Xiong, L. Zhu, et W. Li, « Enhanced strength and excellent transport properties of a superaligned carbon nanotubes reinforced copper matrix laminar composite », *Composites Part A: Applied Science and Manufacturing*, vol. 88, p. 148-155, sept. 2016, doi: 10.1016/j.compositesa.2016.05.027.

[73] S. Sun *et al.*, « Vertically aligned CNT-Cu nano-composite material for stacked through-silicon-via interconnects », *Nanotechnology*, vol. 27, nº 33, p. 335705, août 2016, doi: 10.1088/0957-4484/27/33/335705.

[74] C. Subramaniam, A. Sekiguchi, T. Yamada, D. N. Futaba, et K. Hata, « Nano-scale, planar and multi-tiered current pathways from a carbon nanotube–copper composite with high conductivity, ampacity and stability », *Nanoscale*, vol. 8, nº 7, p. 3888-3894, 2016, doi: 10.1039/C5NR03762J.

[75] Y. Jin, L. Zhu, W. Xue, et W. Li, « Fabrication of superaligned carbon nanotubes reinforced copper matrix laminar composite by electrodeposition », *Transactions of Nonferrous Metals Society of China*, vol. 25, nº 9, p. 2994-3001, sept. 2015, doi: 10.1016/S1003-6326(15)63926-7.

[76] Z. An, M. Toda, et T. Ono, « Improved thermal interface property of carbon nanotube–Cu composite based on supercritical fluid deposition », *Carbon*, vol. 75, p. 281-288, août 2014, doi: 10.1016/j.carbon.2014.04.003.

[77] C. Subramaniam *et al.*, « Carbon nanotube-copper exhibiting metal-like thermal conductivity and silicon-like thermal expansion for efficient cooling of electronics », *Nanoscale*, vol. 6, nº 5, p. 2669-2674, 2014, doi: 10.1039/C3NR05290G.
[78] C. Subramaniam *et al.*, « One hundred fold increase in current carrying capacity in a carbon nanotube–copper composite », *Nat Commun*, vol. 4, nº 1, p. 2202, juill. 2013, doi: 10.1038/ncomms3202.
[79] G. Xu, J. Zhao, S. Li, X. Zhang, Z. Yong, et Q. Li, « Continuous electrodeposition for lightweight, highly conducting and strong carbon nanotube-copper composite fibers », *Nanoscale*, vol. 3, nº 10, p. 4215, 2011, doi: 10.1039/c1nr10571j.
[80] L. K. Randeniya, A. Bendavid, P. J. Martin, et C. Tran, « Composite Yarns of Multiwalled Carbon Nanotubes with Metallic Electrical Conductivity », *Small*, vol. 6, nº 16, p. 1806-1811, août 2010, doi: 10.1002/smll.201000493.
[81] Y. Chai et P. C. H. Chan, « High electromigration-resistant copper/carbon nanotube composite for interconnect application », in *2008 IEEE International Electron Devices Meeting*, San Francisco, CA, USA: IEEE, déc. 2008, p. 1-4. doi: 10.1109/IEDM.2008.4796764.
[82] T. J. Kang *et al.*, « Sandwich-Type Laminated Nanocomposites Developed by Selective Dip-Coating of Carbon Nanotubes », *Advanced Materials*, vol. 19, nº 3, p. 427-432, févr. 2007, doi: 10.1002/adma.200600908.
[83] H. Luo, Y. Sui, J. Qi, Q. Meng, F. Wei, et Y. He, « Copper matrix composites enhanced by silver/reduced graphene oxide hybrids », *Materials Letters*, vol. 196, p. 354-357, juin 2017, doi: 10.1016/j.matlet.2017.03.084.
[84] L. Dong, W. Chen, C. Zheng, et N. Deng, « Microstructure and properties characterization of tungsten–copper composite materials doped with graphene », *Journal of Alloys and Compounds*, vol. 695, p. 1637-1646, févr. 2017, doi: 10.1016/j.jallcom.2016.10.310.
[85] H. Yue *et al.*, « Effect of ball-milling and graphene contents on the mechanical properties and fracture mechanisms of graphene nanosheets reinforced copper matrix composites », *Journal of Alloys and Compounds*, vol. 691, p. 755-762, janv. 2017, doi: 10.1016/j.jallcom.2016.08.303.
[86] T. Wejrzanowski, M. Grybczuk, M. Chmielewski, K. Pietrzak, K. J. Kurzydlowski, et A. Strojny-Nedza, « Thermal conductivity of metal-graphene composites », *Materials & Design*, vol. 99, p. 163-173, juin 2016, doi: 10.1016/j.matdes.2016.03.069.
[87] T. Varol et A. Canakci, « Microstructure, electrical conductivity and hardness of multilayer graphene/Copper nanocomposites synthesized by flake powder metallurgy », *Met. Mater. Int.*, vol. 21, nº 4, p. 704-712, juill. 2015, doi: 10.1007/s12540-015-5058-6.
[88] J. Dutkiewicz *et al.*, « Microstructure and properties of bulk copper matrix composites strengthened with various kinds of graphene nanoplatelets », *Materials Science and Engineering: A*, vol. 628, p. 124-134, mars 2015, doi: 10.1016/j.msea.2015.01.018.
[89] W. Li, D. Li, Q. Fu, et C. Pan, « Conductive enhancement of copper/graphene

composites based on high-quality graphene », *RSC Adv.*, vol. 5, n° 98, p. 80428-80433, 2015, doi: 10.1039/C5RA15189A.
[90] W. J. Kim, T. J. Lee, et S. H. Han, « Multi-layer graphene/copper composites: Preparation using high-ratio differential speed rolling, microstructure and mechanical properties », *Carbon*, vol. 69, p. 55-65, avr. 2014, doi: 10.1016/j.carbon.2013.11.058.
[91] K. Chu et C. Jia, « Enhanced strength in bulk graphene–copper composites », *Physica Status Solidi (a)*, vol. 211, n° 1, p. 184-190, janv. 2014, doi: 10.1002/pssa.201330051.
[92] B. W. Wei *et al.*, « Synthesis and Physical Properties of Graphene Nanosheets Reinforced Copper Composites », *AMR*, vol. 833, p. 310-314, nov. 2013, doi: 10.4028/www.scientific.net/AMR.833.310.
[93] D. Qu *et al.*, « Preparation of Graphene Nanosheets/Copper Composite by Spark Plasma Sintering », *AMR*, vol. 833, p. 276-279, nov. 2013, doi: 10.4028/www.scientific.net/AMR.833.276.
[94] H. Luo, Y. Sui, J. Qi, Q. Meng, F. Wei, et Y. He, « Copper matrix composites enhanced by silver/reduced graphene oxide hybrids », *Materials Letters*, vol. 196, p. 354-357, juin 2017, doi: 10.1016/j.matlet.2017.03.084.
[95] R. Jiang, X. Zhou, et Z. Liu, « Electroless Ni-plated graphene for tensile strength enhancement of copper », *Materials Science and Engineering: A*, vol. 679, p. 323-328, janv. 2017, doi: 10.1016/j.msea.2016.10.029.
[96] D. Zhang et Z. Zhan, « Preparation of graphene nanoplatelets-copper composites by a modified semi-powder method and their mechanical properties », *Journal of Alloys and Compounds*, vol. 658, p. 663-671, févr. 2016, doi: 10.1016/j.jallcom.2015.10.252.
[97] D. Zhang et Z. Zhan, « Experimental investigation of interfaces in graphene materials/copper composites from a new perspective », *RSC Adv.*, vol. 6, n° 57, p. 52219-52226, 2016, doi: 10.1039/C6RA07606H.
[98] M. Li, J. Xie, Y. Li, et H. Xu, « Reduced graphene oxide dispersed in copper matrix composites: Facile preparation and enhanced mechanical properties », *Physica Status Solidi (a)*, vol. 212, n° 10, p. 2154-2161, oct. 2015, doi: 10.1002/pssa.201532038.
[99] Z. Jia, T. Chen, J. Wang, J. Ni, H. Li, et X. Shao, « Synthesis, characterization and tribological properties of Cu/reduced graphene oxide composites », *Tribology International*, vol. 88, p. 17-24, août 2015, doi: 10.1016/j.triboint.2015.02.028.
[100] J. Yang, X. Shen, Z. Ji, H. Zhou, G. Zhu, et K. Chen, « In-situ growth of Cu nanoparticles on reduced graphene oxide nanosheets and their excellent catalytic performance », *Ceramics International*, vol. 41, n° 3, p. 4056-4063, avr. 2015, doi: 10.1016/j.ceramint.2014.11.099.
[101] X. Li, Y. Zhao, W. Wu, J. Chen, G. Chu, et H. Zou, « Synthesis and characterizations of graphene–copper nanocomposites and their antifriction application », *Journal of Industrial and Engineering Chemistry*, vol. 20, n° 4, p. 2043-2049, juill. 2014, doi: 10.1016/j.jiec.2013.09.029.

[102] M. Li, H. Che, X. Liu, S. Liang, et H. Xie, « Highly enhanced mechanical properties in Cu matrix composites reinforced with graphene decorated metallic nanoparticles », *J Mater Sci*, vol. 49, nº 10, p. 3725-3731, mai 2014, doi: 10.1007/s10853-014-8082-x.
[103] Y. Tang, X. Yang, R. Wang, et M. Li, « Enhancement of the mechanical properties of graphene–copper composites with graphene–nickel hybrids », *Materials Science and Engineering: A*, vol. 599, p. 247-254, avr. 2014, doi: 10.1016/j.msea.2014.01.061.
[104] Y. Peng, Y. Hu, L. Han, et C. Ren, « Ultrasound-assisted fabrication of dispersed two-dimensional copper/reduced graphene oxide nanosheets nanocomposites », *Composites Part B: Engineering*, vol. 58, p. 473-477, mars 2014, doi: 10.1016/j.compositesb.2013.10.036.
[105] K. Zhang, « Fabrication of copper nanoparticles/graphene oxide composites for surface-enhanced Raman scattering », *Applied Surface Science*, vol. 258, nº 19, p. 7327-7329, juill. 2012, doi: 10.1016/j.apsusc.2012.04.002.
[106] Q. Chen, L. Zhang, et G. Chen, « Facile Preparation of Graphene-Copper Nanoparticle Composite by in Situ Chemical Reduction for Electrochemical Sensing of Carbohydrates », *Anal. Chem.*, vol. 84, nº 1, p. 171-178, janv. 2012, doi: 10.1021/ac2022772.
[107] X. Si *et al.*, « Effect of carbide interlayers on the microstructure and properties of graphene-nanoplatelet-reinforced copper matrix composites », *Materials Science and Engineering: A*, vol. 708, p. 311-318, déc. 2017, doi: 10.1016/j.msea.2017.10.015.
[108] L. Wang *et al.*, « Graphene-copper composite with micro-layered grains and ultrahigh strength », *Sci Rep*, vol. 7, nº 1, p. 41896, févr. 2017, doi: 10.1038/srep41896.
[109] D. Zhang et Z. Zhan, « Strengthening effect of graphene derivatives in copper matrix composites », *Journal of Alloys and Compounds*, vol. 654, p. 226-233, janv. 2016, doi: 10.1016/j.jallcom.2015.09.013.
[110] F. Chen, J. Ying, Y. Wang, S. Du, Z. Liu, et Q. Huang, « Effects of graphene content on the microstructure and properties of copper matrix composites », *Carbon*, vol. 96, p. 836-842, janv. 2016, doi: 10.1016/j.carbon.2015.10.023.
[111] D. Zhang et Z. Zhan, « Experimental investigation of interfaces in graphene materials/copper composites from a new perspective », *RSC Adv.*, vol. 6, nº 57, p. 52219-52226, 2016, doi: 10.1039/C6RA07606H.
[112] L. Wang *et al.*, « High apparent strengthening efficiency for reduced graphene oxide in copper matrix composites produced by molecule-lever mixing and high-shear mixing », *RSC Adv.*, vol. 5, nº 63, p. 51193-51200, 2015, doi: 10.1039/C5RA04782J.
[113] C. Zhao et J. Wang, « Fabrication and tensile properties of graphene/copper composites prepared by electroless plating for structrual applications: Fabrication and tensile properties of graphene/copper composites », *Phys. Status Solidi A*, vol. 211, nº 12, p. 2878-2885, déc. 2014, doi: 10.1002/pssa.201431478.
[114] L. Wang, Y. Cui, R. Li, G. Cao, B. Li, et W. Fei, « Effect of H2 Reduction Temperature on the Properties of Reduced Graphene Oxide and Copper Matrix Composites »,

Acta Metall. Sin. (Engl. Lett.), vol. 27, nº 5, p. 924-929, oct. 2014, doi: 10.1007/s40195-014-0146-z.

[115] J. Hwang *et al.*, « Enhanced Mechanical Properties of Graphene/Copper Nanocomposites Using a Molecular-Level Mixing Process », *Advanced Materials*, vol. 25, nº 46, p. 6724-6729, déc. 2013, doi: 10.1002/adma.201302495.

[116] Y. J. Mai, M. P. Zhou, H. J. Ling, F. X. Chen, W. Q. Lian, et X. H. Jie, « Surfactant-free electrodeposition of reduced graphene oxide/copper composite coatings with enhanced wear resistance », *Applied Surface Science*, vol. 433, p. 232-239, mars 2018, doi: 10.1016/j.apsusc.2017.10.014.

[117] Y. Raghupathy, A. Kamboj, M. Y. Rekha, N. P. Narasimha Rao, et C. Srivastava, « Copper-graphene oxide composite coatings for corrosion protection of mild steel in 3.5% NaCl », *Thin Solid Films*, vol. 636, p. 107-115, août 2017, doi: 10.1016/j.tsf.2017.05.042.

[118] A. Kamboj, Y. Raghupathy, M. Y. Rekha, et C. Srivastava, « Morphology, Texture and Corrosion Behavior of Nanocrystalline Copper–Graphene Composite Coatings », *JOM*, vol. 69, nº 7, p. 1149-1154, juill. 2017, doi: 10.1007/s11837-017-2364-0.

[119] H. S. Maharana, P. K. Rai, et A. Basu, « Surface-mechanical and electrical properties of pulse electrodeposited Cu–graphene oxide composite coating for electrical contacts », *J Mater Sci*, vol. 52, nº 2, p. 1089-1105, janv. 2017, doi: 10.1007/s10853-016-0405-7.

[120] G. Huang *et al.*, « Preparation and characterization of the graphene-Cu composite film by electrodeposition process », *Microelectronic Engineering*, vol. 157, p. 7-12, mai 2016, doi: 10.1016/j.mee.2016.02.006.

[121] G. Xie, M. Forslund, et J. Pan, « Direct Electrochemical Synthesis of Reduced Graphene Oxide (rGO)/Copper Composite Films and Their Electrical/Electroactive Properties », *ACS Appl. Mater. Interfaces*, vol. 6, nº 10, p. 7444-7455, mai 2014, doi: 10.1021/am500768g.

[122] C. L. P. Pavithra, B. V. Sarada, K. V. Rajulapati, T. N. Rao, et G. Sundararajan, « A New Electrochemical Approach for the Synthesis of Copper-Graphene Nanocomposite Foils with High Hardness », *Sci Rep*, vol. 4, nº 1, p. 4049, févr. 2014, doi: 10.1038/srep04049.

[123] K. Jagannadham, « Volume Fraction of Graphene Platelets in Copper-Graphene Composites », *Metall Mater Trans A*, vol. 44, nº 1, p. 552-559, janv. 2013, doi: 10.1007/s11661-012-1387-y.

[124] K. Jagannadham, « Electrical conductivity of copper–graphene composite films synthesized by electrochemical deposition with exfoliated graphene platelets », *Journal of Vacuum Science & Technology B, Nanotechnology and Microelectronics: Materials, Processing, Measurement, and Phenomena*, vol. 30, nº 3, p. 03D109, mai 2012, doi: 10.1116/1.3701701.

[125] K. Jagannadham, « Thermal Conductivity of Copper-Graphene Composite Films Synthesized by Electrochemical Deposition with Exfoliated Graphene Platelets », *Metall Mater Trans B*, vol. 43, nº 2, p. 316-324, avr. 2012, doi: 10.1007/s11663-011-

9597-z.
[126] K. Jagannadham, « Orientation dependence of thermal conductivity in copper-graphene composites », *Journal of Applied Physics*, vol. 110, n° 7, p. 074901, oct. 2011, doi: 10.1063/1.3641640.
[127] K. N. Subedi, K. Nepal, C. Ugwumadu, K. Kappagantula, et D. A. Drabold, « Electronic transport in copper–graphene composites », *Applied Physics Letters*, vol. 122, n° 3, p. 031903, janv. 2023, doi: 10.1063/5.0137086.
[128] M. Cao *et al.*, « Ultrahigh Electrical Conductivity of Graphene Embedded in Metals », *Adv Funct Materials*, vol. 29, n° 17, p. 1806792, avr. 2019, doi: 10.1002/adfm.201806792.
[129] Y. Kim *et al.*, « Strengthening effect of single-atomic-layer graphene in metal–graphene nanolayered composites », *Nat Commun*, vol. 4, n° 1, p. 2114, juill. 2013, doi: 10.1038/ncomms3114.
[130] J. Yang *et al.*, « Improving the electrical conductivity of copper/graphene composites by reducing the interfacial impurities using spark plasma sintering diffusion bonding », *Journal of Materials Research and Technology*, vol. 15, p. 3005-3015, nov. 2021, doi: 10.1016/j.jmrt.2021.09.100.
[131] J. Wang *et al.*, « The promising Cu/graphene composites in situ fabricated by solid organic carbon sources », *Materials Letters*, vol. 360, p. 136023, avr. 2024, doi: 10.1016/j.matlet.2024.136023.
[132] X. Li *et al.*, « Particle morphology dependence of the mechanical and electrical properties in the in-situ graphene reinforced Cu matrix composites », *Composites Part A: Applied Science and Manufacturing*, vol. 179, p. 108032, avr. 2024, doi: 10.1016/j.compositesa.2024.108032.
[133] S. Shu *et al.*, « Graphene-Reinforced Copper Matrix Composites as Electrical Contacts », *ACS Appl. Nano Mater.*, p. acsanm.4c00027, mars 2024, doi: 10.1021/acsanm.4c00027.
[134] B. Li, D. Lin, X. Zhang, D. Zhao, C. He, et N. Zhao, « Exceptional dynamic compressive properties of bio-inspired three-dimensional interlocking graphene network reinforced copper matrix composites », *Composites Part A: Applied Science and Manufacturing*, vol. 176, p. 107856, janv. 2024, doi: 10.1016/j.compositesa.2023.107856.
[135] D. Cakir, O. R. Caylan, et G. Cambaz Buke, « Synthesis and characterization of homogeneously dispersed graphene–copper heterostructures with enhanced thermal properties », *J Mater Sci*, vol. 59, n° 1, p. 105-113, janv. 2024, doi: 10.1007/s10853-023-09188-7.
[136] T. Li, Y. Wang, M. Yang, H. Hou, et S. Wu, « High strength and conductivity copper/graphene composites prepared by severe plastic deformation of graphene coated copper powder », *Materials Science and Engineering: A*, vol. 826, p. 141983, oct. 2021, doi: 10.1016/j.msea.2021.141983.
[137] T. Li, Y. Wang, M. Yang, H. Hou, et S. Wu, « High strength and conductivity copper matrix composites reinforced by in-situ graphene through severe plastic deformation processes », *Journal of Alloys and Compounds*, vol. 851, p. 156703,

janv. 2021, doi: 10.1016/j.jallcom.2020.156703.
[138] X. Zhang *et al.*, « A powder-metallurgy-based strategy toward three-dimensional graphene-like network for reinforcing copper matrix composites », *Nat Commun*, vol. 11, nº 1, p. 2775, juin 2020, doi: 10.1038/s41467-020-16490-4.
[139] T. Babul, M. Baranowski, N. Sobczak, M. Homa, et W. Leśniewski, « Thermophysical Properties of Cu-Matrix Composites Manufactured Using Cu Powder Coated with Graphene », *J. of Materi Eng and Perform*, vol. 25, nº 8, p. 3146-3151, août 2016, doi: 10.1007/s11665-016-2174-5.
[140] J. Y. Kim, J. A. Rodriguez, J. C. Hanson, A. I. Frenkel, et P. L. Lee, « Reduction of CuO and Cu_2O with H_2: H Embedding and Kinetic Effects in the Formation of Suboxides », *J. Am. Chem. Soc.*, vol. 125, nº 35, p. 10684-10692, sept. 2003, doi: 10.1021/ja0301673.